Pnictogenide and Chalcogenide Zintl Phases via Solid State and Solvothermal Syntheses

Dissertation
zur Erlangung des Doktorgrades (Dr. rer. nat.)
der
Mathematisch–Naturwissenschaftlichen Fakultät
der
Rheinischen Friedrich–Wilhelms–Universität Bonn

vorgelegt von
Frederik Simon Hermann
aus
Neuwied

Bonn, 2022

Angefertigt mit Genehmigung der Mathematisch-Naturwissenschaftlichen Fakultät der Rheinischen Friedrich-Wilhelms-Universität Bonn

1. Gutachter: Professor Dr. Johannes Beck
2. Gutachter: Professor Dr. Robert Glaum

Tag der Promotion: 26.08.2022
Erscheingungjahr: 2022

"*Basic research is like shooting an arrow in the air and,*
where it lands, painting a target."

Homer Burton Adkins

Contents

Abstract

This work concentrated on the synthesis of new Zintl phases, especially focusing on the synthesis of new polyarsenides and chalcogenides. Through high temperature synthesis, the compounds Ba_3As_4, Ba_3As_2O and $K_3Ba_7(As_3)_3O$ were successfully synthesised, whose structures are isotypical to known compounds. The main effort of this work was the synthesis of Zintl phases in liquid ammonia under mild and supercritical conditions. Advantage was taken of the fact that alkali metals and Europium form deep blue electride solutions of solvated electrons in liquid ammonia. These highly reactive solutions reacted with the chalcogens and pnictogens and formed polyanions. Thus, the phases $Rb_5(AsSe_3)Se\cdot 2\,NH_3$, $K_9Se_{2.88}(Se_2)_{1.12}OH$, and $[Eu(NH_3)_8]_2[Eu(NH_3)_3(As_7)_2]$ could be obtained.

A large number of the experiments were aimed at the synthesis of ternary compounds in the system A–M–As/Ch (A=Na-Cs; M=Cu, Ag, Au; Ch=S, Se). Rb_2AuAs_7, $Rb_3AuSe_2\cdot 1.5\,NH_3$, $K_2[AuSe]Se\cdot NH_3$ and $K_{10}CuSe_8Cl\cdot NH_3$ represent new members of this family. For the first time, the linear ion $CuSe_2^{3-}$ with an extremely short Cu-Se bond length of 2.23 Å was obtained. Rb_2AuAs_7 is the first representative in the ternary system Rb-Au-As and contains one-dimensional chains of condensed As_7 units. This polymeric anion $^1_\infty[As_7^{3-}]$ has not yet been reported.

As another important result of this work, the mixed chalcogenidoarsenates $[As_4S_6^{2-}]$ and $[As_2Se_6^{2-}]$, in $[Mn(NH_3)_6][As_4S_6]\cdot NH_3$ and $[Mn(NH_3)_6]_2[As_2Se_6]$ were isolated from liquid ammonia. The cyclic $[As_4S_6^{2-}]$ anion was observed in a new conformation. In parallel with these manganese-compounds, the polymeric solids As_3NS_3 and As_3NSe_3 formed, whose molecular structures are closely related to tris-(dimethylarsino)-amine $(Me_2As)_3N$.

Syntheses in ethylenediamine led to the framework structure $[Mn_2(HPO_3)_2(C_2H_8N_2)]$. Analogous the *spin-ladder* compounds $(NH_4)Fe_2S_3$ and $(NH_4)Fe_2S_3$ were obtained. In these compounds, Fe is present in the mixed oxidation state +2.5.

With the exception of two cases, the single crystal structures of all target compounds could be solved and refined. For $K_2[AuSe]Se\cdot NH_3$, a structural model could be presented despite pronounced twinning. For $Rb_3AuSe_2\cdot 1.5\,NH_3$, the q-vector for an incommensurable modulated structure model could be defined with satellites of first order. A solution of the incommensurability was not possible due to weak intensity of the satellites, therefore the structure model does not take the modulation into account.

Zusammenfassung

Diese Arbeit befasst sich mit der Synthese neuer Zintl Phasen. Dabei wurde der Fokus auf die Sythese neuer Polyarsenide und Chalkogenide gelegt. Durch Hochtemperatursynthese konnten die Verbindungen Ba_3As_4, Ba_3As_2O und $K_3Ba_7(As_3)_3O$ erfolgreich hergestellt werden, deren Strukturen isotyp zu bekannten Verbindungen sind. Der Schwerpunkt dieser Arbeit lag auf der Synthese von Zintl Phasen in flüssigem Ammoniak unter milden und superkritischen Bedingungen. Es wurde sich zu Nutze gemacht, dass Alkalimetalle und Europium in flüssigem Ammoniak tiefblaue Elektridlösungen solvatisierter Elektronen bilden. Diese hochreaktiven Lösungen reagierten mit den eingesetzten Chalkogenen und Pniktogenen zu Polyanionen. So konnten die Phasen $Rb_5(AsSe_3)Se\cdot 2\,NH_3$, $K_9Se_{2.88}(Se_2)_{1.12}OH$ und $[Eu(NH_3)_8]_2[Eu(NH_3)_3(As_7)_2]$ erhalten werden.

Eine Vielzahl der Experimente zielte auf die Synthese ternärer Verbindung im System A-M-As/Ch (A=Na-Cs; M=Cu, Ag, Au; Ch=S, Se) ab. Die Verbindungen Rb_2AuAs_7, $Rb_3AuSe_2\cdot 1.5\,NH_3$, $K_2[AuSe]Se\cdot NH_3$ und $K_{10}CuSe_8Cl\cdot NH_3$ stellen neue Vertreter dieser Familie dar. Dabei wurde das lineare Ion $CuSe_2^{3-}$ mit einer äußerst kurzen Bindungslänge von 2.23 Å erstmals erhalten. Rb_2AuAs_7 ist der erste Vertreter des ternären Systems Rb-Au-As und enthält eindimensionale Ketten aus kondensierten As_7-Einheiten. Dieses polymere Anion $^1_\infty[As_7^{3-}]$ wurde bisher nicht beschrieben.

Als weiteres wichtiges Ergebnis dieser Arbeit wurden erstmals die gemischten Chalkogenidoarsenate $[As_4S_6^{2-}]$ und $[As_2Se_6^{2-}]$ in $[Mn(NH_3)_6][As_4S_6]\cdot NH_3$ und $[Mn(NH_3)_6]_2[As_2Se_6]$ aus flüssigem Ammoniak isoliert. Dabei wurde das cyclische Anion $[As_4S_6^{2-}]$ in einer neuen Konformation erhalten. Parallel zu diesen Mangan-Verbindungen entstanden die polymeren Festkörper As_3NS_3 und As_3NSe_3, deren räumlicher Aufbau eng verwandt ist mit Tris-(dimethylarsino)-amin $(Me_2As)_3N$.

Synthesen in Ethylendiamin führten zur Framework-Struktur $[Mn_2(HPO_3)_2(C_2H_8N_2)]$. Analog ließen sich die *spin-ladder*-Verbindungen $(NH_4)Fe_2S_3$ und $(NH_4)Fe_2Se_3$ herstellen, in denen Eisen in der gemischen Oxidationsstufe +2.5 vorliegt.

Mit Ausnahme von zwei Fällen konnten die Einkristallstrukturen von allen Zielverbindungen gelöst und verfeinert werden. Für $K_2[AuSe]Se\cdot NH_3$ konnte trotz ausgeprägter Verzwilligung ein Strukturmodell gefunden werden. Bei $Rb_3AuSe_2\cdot 1.5\,NH_3$ konnte mit den Satelliten 1. Ordnung der q-Vektor für ein inkommensurable moduliertes Strukturmodell definiert werden. Eine Lösung der Inkommensurabilität war aufgrund schwacher Intensität der Satelliten nicht möglich, daher berücksichtigt das Strukturmodell diese Modulation nicht.

Chapter 1

Introduction

1.1 A Short Journey through the History of Zintl Phases

The first investigations of alkali metals in liquid ammonia go back to W. Weyl [1, 2]. He described the solution as deep blue and at high concentration as intensely copper coloured. The deep blue colour originates from the solvation of electrons [3]. This is the reason for the strong reducing effect of the solution. The solubility of alkali metals in ammonia and the reducing effect towards main group elements were further investigated by A. C. Joannis in 1891/92 [4, 5]. The alkali metal ammonia solution changes colour from blue to green when lead is added. C. A. Kraus and F. H. Smyth worked on further investigating these solutions in the first two decades of the 20th century and were able to determine on the basis of electrolytic investigations that corresponding solutions must contain alkali metal polyplumbides [6–8].

The term "Zintl phases" can be traced back to Eduard Zintl. As a student of Hönigschmid, Zintl was trained in potentiometric analysis and made important contributions in this area. During his time in Munich, Zintl dealt with intermetallic phases and investigated the transition from salt-like to intermetallic compounds. Zintl continued these investigations and made an important contribution by quantitatively characterising the composition of the ions present in solution. His most famous experiment is the titration of lead iodide to a solution of sodium in ammonia [9]. In this process, lead(II) is reduced to finely dispersed elemental lead. The finely dispersed lead then reacts further with sodium, which is manifested in the green colouring of the initially blue solution. The course of the titration was followed by measuring the potential and conductivity. The composition of the compound obtained was then finally determined from the turning point of the potential curve. The composition of the compounds, for example Na_4Pb_9, indicates anion clusters with homoatomic bonds. Zintl investigated the sodium compounds of the elements of main group 4 to 7 this

way. His investigations ultimately led to the discovery of the "polyanionic salts". Experiments were carried out with the elements to the left of main group 4, e.g. thallium, zinc, cadmium, mercury and gold [10]. However, the resulting products were insoluble in ammonia and had alloy-typical structures. This line between main group 3 and 4 was named the "Zintl line" by Fritz Laves in memory of Zintl [11]. Elements to the left of this line form alloy-like compounds with alkali metals and alkaline earth metals, and elements to the right of the line form stoichiometric salt-like compounds. This strict separation has been greatly softened at the present time, since in the meantime many representatives of polyanions of the tetrelide elements have been discovered [12]. Nevertheless, it should be noted that it was this very discovery by Zintl that laid the foundation for research into polyanionic salts up to the present day. In his obituary, Laves therefore demanded these polyanionic salts to be grouped under the term "Zintl phases" [11].

Zintl's concept was taken further by Wilhelm Klemm in the 1960s. For this purpose, he compared ionic radii [13] and the binding patterns of the anion partial structures. It became apparent that the density of the salts examined was greater than expected, which can be attributed to an electron transfer from the cation to the polyanion.

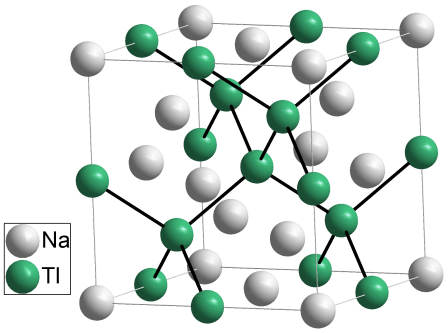

Figure 1.1: Unit cell of NaTl. The Tl^- anions form a diamond-like framework analogous to the iso-valence-electronic element silicon.

The example of the compound NaTl [14] (Fig. 1.1) discovered by Zintl shows this phenomenon well. Here, NaTl can be formulated as Na^+Tl^-. The thallium anions form a diamond-like framework in the anion partial structure of $^3_\infty[Tl^-]$ (Fig. 1.1). The sodium cations are embedded in the tetrahedral voids, which becomes possible due to the smaller atomic radius by 15 % compared to elemental sodium [13]. Zintl already determined in 1939 that Tl^- behaves similarly to the iso-valence-electronic element silicon. For this, an electron must be transferred from sodium to thallium making the formation of four covalent bonds possible. This explains the reduction of the radius of the sodium atoms, since the transfer of an electron is linked to the reduction of the atomic radius. As a result, thallium is four-bonded in the compound NaTl and behaves similarly to the iso-valence-electronic silicon, leading to a diamond-like framework.

Klemm's and Busmann's investigations on volume increments [13] in Zintl phases supported Zintl's assumption that the formally negatively charged particles, which

have the same number of electrons as the uncharged atoms of the element following in the periodic system, unite to form polyanions with a structure quite similar to that present in the corresponding elements. Today, these findings are summarised in the Zintl-Klemm-Busmann concept.

Already at the beginning of the 20th century, G.N. Lewis and W. Kossel published the $(8-N)$ rule as a contribution to conceptual chemistry, which is still used today [15, 16]. In 1973, H. Schäfer [17] extended the Zintl-Klemm-Busmann concept by this rule. After evaluating many Zintl phases known at that time, he came to the conclusion that the concept should not be limited to isosterism to elemental lattices of the same valence electron number, but that bonding should be taken into account as well. Therefore, he added the $(8-N)$ rule to the concept and further justified this with the general valence rule according to Pearson [18]. According to the $(8-N)$ rule, an atom with N valence electrons forms $(8-N)$ covalent bonds with its neighbours. N corresponds to the number of valence electrons of the atom plus the electrons transferred from the base metal.

From the 1980s onwards, Schäfer, together with B. Eisenmann, devoted himself to research on ternary Zintl phases. The $(8-N)$ rule proposed by Schäfer is equally useful here to describe the binding motifs of the polyanions. Thus, in the structure of Ba_3AlSb_3 [19] the dimeric groups of $Al_2Sb_6^{12-}$ (Fig. 1.2) are isostructural to the isovalence-electronic Al_2Cl_6 molecule. Polymeric chains of linked tetrahedra of $^1_\infty[AlAs_3^{6-}]$ (Fig. 1.2) are in the structure of Ca_3AlAs_3 [19], which are directly related to $^1_\infty[SiO_3^{2-}]$. According to the Zintl-Klemm-Busmann concept, the valence electrons of barium, re-

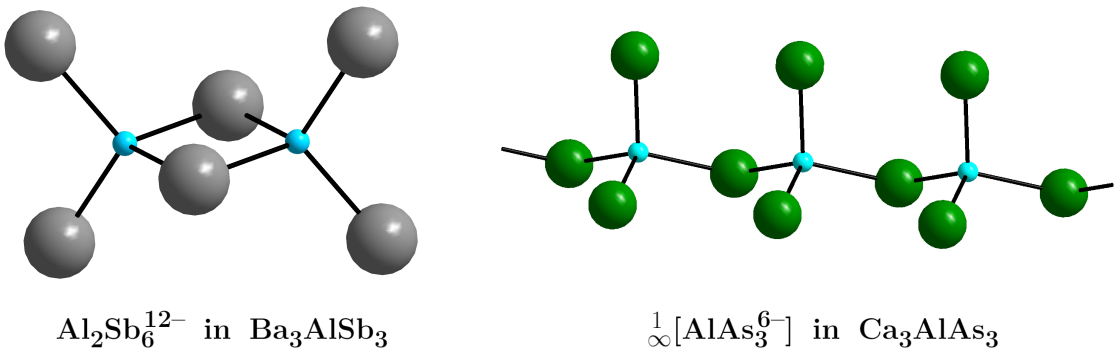

$\mathbf{Al_2Sb_6^{12-}}$ **in** $\mathbf{Ba_3AlSb_3}$ $\quad$ $\mathbf{^1_\infty[AlAs_3^{6-}]}$ **in** $\mathbf{Ca_3AlAs_3}$

Figure 1.2: Examples of anion structures in ternary Zintl phases.

spectively calcium, are completely transferred to the more electronegative elements. In both anions the aluminium atoms are negatively charged. Accordingly, the Al atoms show structurally four-bond behaviour. In case of the main group elements of group 5, arsenic and antimony, the bridging atoms have a negative formal charge and the

terminal antimony in $Al_2Sb_6^{12-}$ have a formal charge of -2. Due to the bonding pattern, all atoms in the anions are covalently saturated and confirm the $(8 - N)$ rule.

Nesper defined three criteria for Zintl phases [20]:
(1) a well-defined relationship exists between their chemical (geometrical) and electronic structures (i.e., certain aspects of their structures satisfy electron counting rules); (2) they are semiconductors (energy gaps less than 2 eV), or, at least, show increasing electrical conductivities with increasing temperature; and (3) Zintl phases are mostly diamagnetic. They should not show a temperature independent (Pauli-) paramagnetism.

Brauer published Zintl phases in the early 1970s that apparently contradicted the valence rule of the Zintl-Klemm-Busmann concept [21, 22]. Due to an excess of electropositive metal, the anions seemed to have too many electrons at their disposal. Thus, the initial description of the compounds A_2X (A=Ca, Sr, Ba, X=As, Sb, Bi) [21–24] turned out to be wrong. Shortly afterwards Y. Wang published the compound Eu_4As_2O [25] in the K_2NiF_4 structure type [26]. Wang noticed that the compound La_2Sb[27], which is isotypical to the alkaline earth compounds, has similar lattice parameters and the same space group type. Although this compound does not contain oxygen due to the trivalence of the lanthanum [28], it was the basis for a discussion with H.G. von Schnering about the possible oxygen content of compounds of the type A_2X (A=Ca, Sr, Ba, X=As, Sb, Bi). The composition of the compounds were consequently corrected to A_4X_2O (A=Ca, Sr, Ba, X=As, Sb, Bi) [29]. Since synthesis attempts with purified reactants were unsuccessful, however, with small amounts of metal oxide the "A_2X" compounds could be obtained, it became clear that oxygen contamination of the reactants had led to the formation of these double salts. The targeted, partial oxidation of Zintl phases was subsequently systematically investigated by Röhr [30–32], Nuss and Jansen [33] and yielded a number of interesting partially oxidised Zintl phases. In the meantime, besides the oxides, hydrides [34], bromides [35] and iodides [36] are known. In these double salts, the Zintl anions and oxides, or hydrides, iodides and bromides coexists in the lattice. In the double salt of the Zintl phase $Cs_{10}(Si_4)(Si_3O_9)$[37], in addition to the cyclotrisilicate ions $Si_6O_{17}^{10-}$ the Zintl anion Si_4^{4-} is present (Fig. 1.4), which is isosteric to white phosphorus.

In their publication of 1970, Kummer and Diehl [38] described the isolation and characterisation of ammoniates as impossible. The ammoniates decompose into alloys of the same composition with the release of ammonia, but these no longer contain

the complex polyanions as they do in solution. However, in order to obtain complex anions from solution, they used various amines as solvents to dissolve sodium-tin alloys. Hence, they succeeded in obtaining the compound $Na_4Sn_9 \cdot 8\,en$ (en $\widehat{=}$ ethylenediamine). Zintl phases, whose cations are complexed by aliphatic amines, are typically stable at room temperature and can be handled under inert gas conditions. With the introduction of the cryptand "2,2,2-crypt" (Fig. 1.3) to stabilise the cations, Corbett [39, 40] expanded the possibilities of synthesis from solutions. Since Zintl anions are generally strong reducing agents, stabilising the cations in the $[K–2,2,2\text{-crypt}]^+$ complex helps to prevent electrons from being transferred from the Zintl anion back to the cation. The use of cryptands, crown ethers and aliphatic amines is still widely used today in the study of new Zintl phases [41–43]. The size of the ligands used plays an important role, as this influences the packing in the crystal lattice significantly.

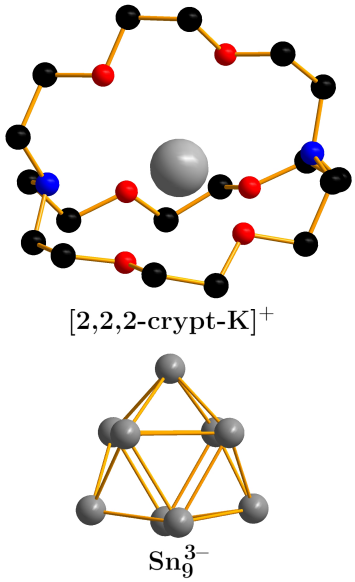

Figure 1.3: $[K–2,2,2\text{-crypt}]^+$ and Sn_9^{3-} in $[K–2,2,2\text{-crypt}]_3[Sn_9]$ [39].

Zintl's original synthesis method of reduction in liquid ammonia as solvent often leads to thermally unstable products. Due to the high content of crystal-bound ammonia, the products usually decompose already at a temperature above the boiling point of ammonia. In order to be able to examine the resulting ammoniates, the crystal therefore had to be kept at a constant low temperature from synthesis to measurement on the X-ray diffractometer. The set-up for crystal search under low temperatures by Kottke and Stalke [44] was therefore an important contribution to isolate ammoniates under a cooled nitrogen stream with the help of a microscope in order to select suitable crystals for the measurement by X-ray diffraction. With the help of this setup, Korber succeeded in 2001 in isolating the ammoniate $[Li(NH_3)_4][Pb_9] \cdot NH_3$ [45] from liquid ammonia. By single crystal diffractometry, the naked nido-Pb_9^{4-} cluster anion, firstly described by Zintl, could be verified in a crystal structure for the first time. The Pb_9^{4-} cluster has a single-capped square-antiprismatic structure. These naked anions are stable in little to non-protic solvents, such as liquid ammonia [9, 10, 14]. Zintl himself already discovered 18 of these naked polyanions [14]. They are called naked, because the outer electronic structure consists of electron pairs and not of a ligand

shell. Thus, there are no metal cation bonds to the anion. The formal charge of the anion clusters is generally comparatively low. None of the anion clusters obtained in solution so far exceeds the ratio 1:1 of cluster atom number to charge [46].

Among the polyanions, a great variety of bonding patterns is present. It ranges from simple one-dimensional bonding motifs to complex-branched three-dimensional frameworks. A few examples will be presented here to emphasise the diversity (Fig. 1.4): From simple P_2^{4-} dumbbells in NiP [47] to helical chains of $^1_\infty[As^{1-}]$ in LiAs [48]. Rings, for example, P_6^{6-} in InP_3, which is iso-valence-electronic to S_6 rings in elemental sulphur [49]. Anion clusters, such as As_7^{3-} in Li_3As_7 [50] and the already described Pb_9^{4-} in $[Li(NH_3)_4][Pb_9]\cdot NH_3$ [45]. Linked rings which form layers, such as the Si layer in $CaSi_2$ [51], the corrugated layers resemble those in α-arsenic. The Ca^{2+} cations are located between the Si layers. Cross-linked spiral chains with a fourfold symmetry axis are present in $SrSi_2$ [52]. A three dimensional framework of $^3_\infty[Si^-]$, build by Si^-, in which every atom has three covalent bonds. The cations are thereby enclosed by the framework structure. At high pressure, the structures of $SrSi_2$ and $CaSi_2$ transform into the α-$ThSi_2$ type. Further examples of three-dimensional structures are present in the diamond structure of Tl^- in the already described NaTl [14] or three-dimensional meshes of $^3_\infty[P_{12}^{8-}]$ in MMn_2P_{12} (M=Ti, Nb, Mo, W) [53, 54]. There is the possibility of different polyanions being present side by side, for example in Ca_2As_3 [55] with unbranched chains of As_4^{6-} and As_8^{10-} ions. In addition to these homoatomic Zintl anions, heteroatomic Zintl anions were further studied by Schäfer et al. [17]. As already mentioned, Ba_3AlSb_3 [19] and Ca_3AlAs_3 [19] are examples of heteroatomic Zintl phases, as well as the double salts, which can be produced by partial oxidation. For this purpose, the Zintl phase $Cs_{10}(Si_4)(Si_3O_9)$ [37] was previously described.

Despite a century of research in this field, this topic has not yet been exhausted. New methods of synthesis offer access to previously undiscovered Zintl phases. For example, syntheses in suitable solvents in autoclaves in a short reaction time of a few days already yield crystals of sufficient size for characterisation. Another current area of research is the synthesis of Zintl phases from ionic liquids. Through this synthesis route, phases are accessible at low temperatures that may not be stable at higher synthesis temperatures [56].

The main focus of this thesis is the investigation of arsenic and selenium-containing Zintl phases. Synthetic work carried out both as solid-state reactions and solvothermally in ammonia. For the mild solvothermal synthesis, the working methods of Kysliak [57] were followed. A detailed explanation of the preparation is documented in

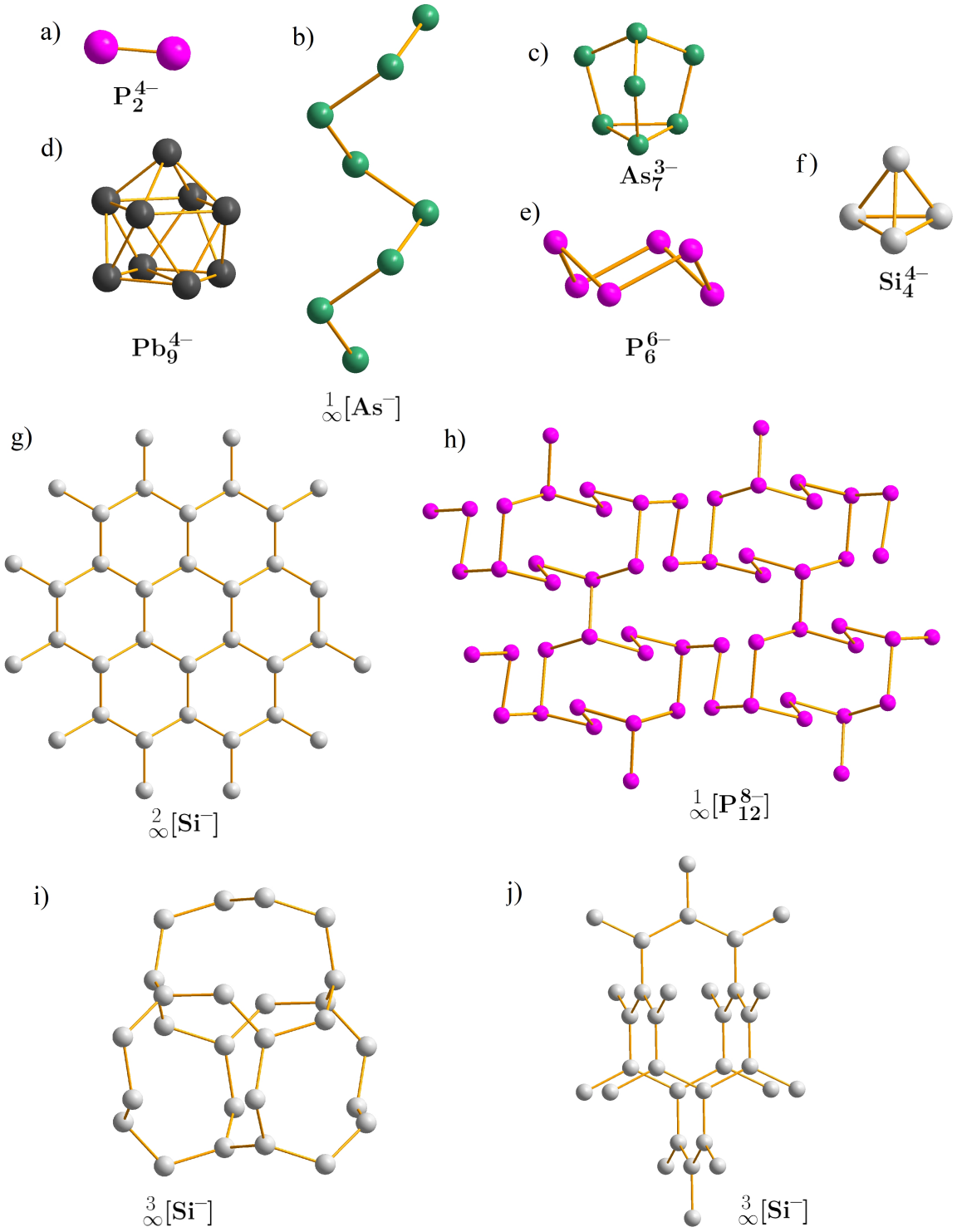

Figure 1.4: Structures of selected Zintl anions. **a)** NiP [47] **b)** LiAs [48] **c)** Li_3As_7 [50] **d)** $[Li(NH_3)_4][Pb_9]\cdot NH_3$ [45] **e)** InP_3 [49] **f)** $Cs_{10}(Si_4)(Si_3O_9)$ [37] **g)** $CaSi_2$ [51] **h)** MMn_2P_{12} (M=Ti, Nb, Mo, W) [53, 54] **i)** $SrSi_2$ [52] **j)** HP-$SrSi_2$ [52]

Section 2.2.3. In most cases, the reactants were inserted in elemental form in half ampoules, which were filled with dry ammonia to $\approx \frac{1}{3}$ of the volume of the ampoule. The filled ampoules were sealed under vacuum by melting. The glass thickness is chosen to achieve stability of the closed glass ampoules up to a pressure of ≈ 39 bar. This allows to keep the reaction mixture at temperatures of 55 °C, which, according to Van't Hoff's rule [58], should accelerate the reaction. This is an important aspect since sometimes it took months for suitable crystals to form. Higher temperatures in liquid ammonia can be realised in a closed system. With filling levels of 30 % to 50 %, temperatures just above room temperature are already sufficient to achieve pressures between 30-40 bar. The ampoules can withstand a pressure of about 39 bar. However, the ampoules are not always perfectly worked due to minor glass defects or contamination at the melting point. For this reason, work was carried out below the bursting limit at pressures around 23 bar, depending on the filling level. Therefore, the ampoules were kept at 55 °C. Bursting only occurred in rare cases. This allowed very mild reaction conditions to be routinely realised.

1.2 Access to Zintl Phases through Ammonothermal Syntheses

Ammonia is more basic than water ($pK_B(NH3) = 4.8$ and $pK_B(H2O) = 15.7$ [58]), less protic and less polar. Under standard conditions, ammonia is gaseous. Compared to water, ammonia has a higher vapour pressure at given temperatures. Moreover, ammonia has a smaller dielectric constant than water (NH_3: $\varepsilon_r = 16.90$, H_{20}: $\varepsilon_r = 79.30$ at 25 °C). Therefore, compounds with small polarity are dissolved better than salt-like ones. This inhibits nucleation and crystal growth, often resulting in crystals with poor quality for further investigations. Many of the investigated crystals obtained in the course of this work showed twinning and in some cases even powder rings appeared in the X-ray images.

The solubility of a solid depends on the relative permittivity of the solvent. If the energy of solvation compensates the lattice energy, the solid dissolves in the solvent. The relative permittivity increases with rising density, which occurs under higher pressure [59, 60]. This phenomenon is utilised under supercritical conditions. The critical parameters for ammonia are 405.40 K and 113.59 bar [61]. Above the critical point, there is a homogeneous supercritical fluid for which the liquid and gaseous state cannot be distinguished. The solubility of ionic salts is greatly improved under supercritical conditions because of the higher permittivity, which increases further with increasing

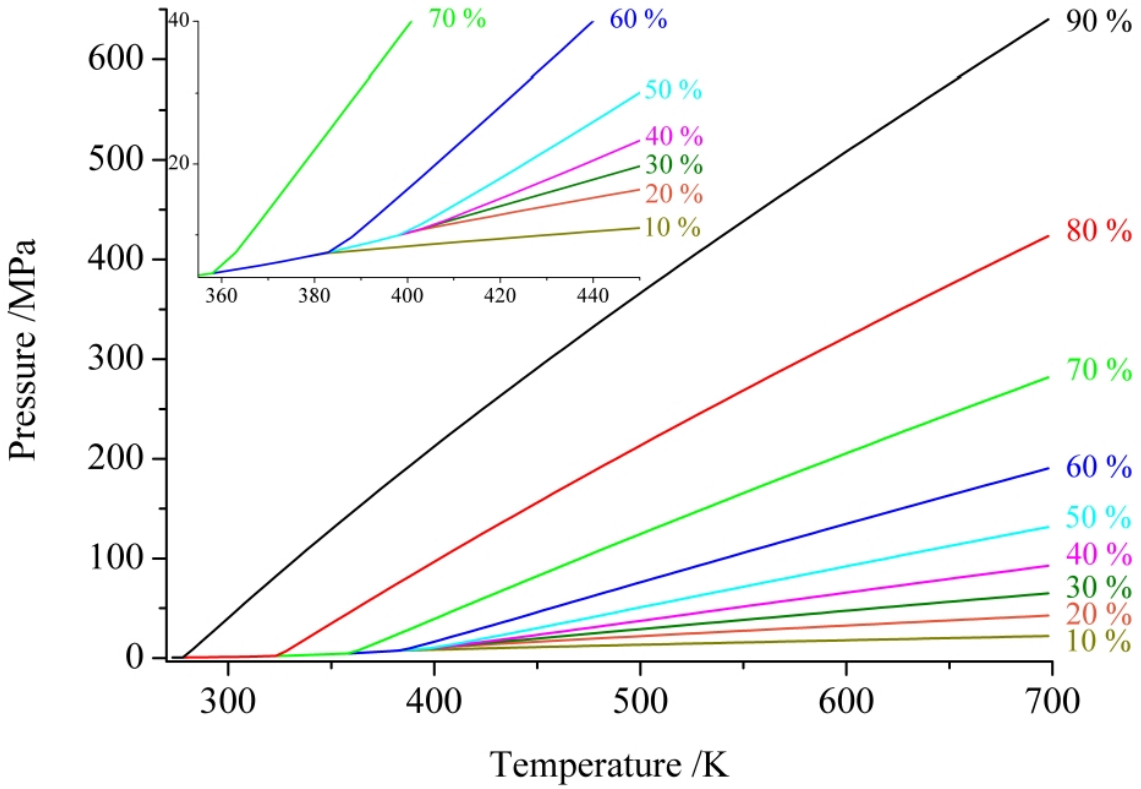

Figure 1.5: Pressure-temperature diagram of ammonia in dependence on the filling degree of the reaction vessel (in %). The inset shows an enlarged view in the range around the critical point ($T_{crit.}$ 405.2 K, $p_{crit.}$ =11.3 MPa). The figure has been reproduced from literature [62, 63].

pressure. Two parameters can easily be adjusted. The first is the amount of ammonia inside the ampoule, the second is the temperature. Both directly influence the density of the supercritical phase vice versa the solubility of ionic salts. The graph in Fig. 1.5 shows the pressure-temperature diagram of ammonia in dependence of the filling degree of the reaction vessel [62]. Filling degrees between 30 % to 50 % were chosen for the reaction vessels.

The results of the present research show that complex Zintl phases are thus accessible. The phases obtained in general do not need to contain ammonia and are consequently temperature stable.

Ammonothermal syntheses under supercritical conditions are used, for example, for the syntheses of high-purity gallium nitride and aluminium nitride. GaN and AlN are semiconductors with wide band gaps that are used as the basis for optoelectronic and electronic devices. Although the growth rate is lower than that of the large-scale process [64] from gaseous hydrogen chloride, gallium and ammonia, the high-purity crystals via ammonothermal synthesis are more resistant to thermal stress in technical applications as semiconductors [65] due to less crystallographic defects.

1.3 Polyarsenides

Due to its position in the periodic table, arsenic offers the possibility of forming one to three bonds per atom in Zintl phases. As a result of this ability, there is a multitude of possible bonding motifs. The chemistry of arsenides, with regard to the Zintl phases, is similar to that of phosphorus in many aspects. Binding patterns or building blocks can often be recognised in the modifications of phosphorus.

To date, only a few analogous structures to infinite two-dimensional polyanions are known, such as $^{2}_{\infty}[P^{3-}_{11}]$ in Ag_3P_{11} [66] or three-dimensional networks of $^{3}_{\infty}[P^{8-}_{12}]$ in MMn_2P_{12} (M=Ti, Nb, Mo, W) [53, 54]. Linked six-membered rings, forming a layered structure, are present in $Cu_{4,35(2)}Cd_{1,65(2)}As_{16}$ [67] in the structure type of Cu_5InP_{16} [68]. In MAs_3 (M=Ca, Sr, Ba, Eu) [69] two-dimensional infinite polyanionic $^{3}_{\infty}[As^{2-}_{3}]$ nets are derivatives of the black phosphorus structure. Mixed anions of phosphorus and arsenic have been described. Typically, the atoms occupy mixed positions. Thus, in $Pb_2As_xP_{14-x}$ ($x \sim 3.7$) [70], there is a polypnictogenide substructure consisting of rows of fused Pn_6 rings connected by cis- and trans-oriented P-bridges.

In contrast to the higher-dimensional structures, zero-dimensional polyarsenides contain isolated anions. These can be further divided into open-chain polyanions (e.g. As^{2-}_{2} in M_2As_2 (M=Ca, Sr, Eu) [71], $^{1}_{\infty}[As^{1-}]$ in MAs (M=Li, Na) [48, 73] and $BaAs_2$[81], As^{5-}_{3} and As^{7-}_{5} e.g. in HT−$LaAs_2$ [72]) and cyclic polyanions (As^{3-}_{3} three membered rings in CsAs [74], the aromatic As^{2-}_{4} in $(K(18\text{-crown-}6))_2As_4$ [82], the four-membered rings As^{4-}_{4} in the mineral skutterudite $CoAs_3$ [75], As^{5-}_{5} five-membered rings in $RbBa_2As_5$ [81], As^{4-}_{6} rings isoelectronic to elemental sulphur S_6 in the chair conformation e.g. in A_4As_6 (A=Rb,Cs) [83]). Polycyclic polyanions like As^{3-}_{7} are present in A_3As_7 (A=Li-Cs) [50, 74, 76, 77]. The first described member of compounds with this anion was Ba_3As_{14} [84]. The polycyclic anions As^{2-}_{10} and As^{4-}_{12} are known to date only from $[Na(18\text{-crown-}6)]_3[As_{10}]_{0.5}[As_{12}]_{0.5}\cdot 4THF$ [78]. The chiral so called "ufosane" anion As^{3-}_{11} occurs, for example, in A_3As_{11} (A=Rb, Cs) [79].

In phosphides, such as LiP_7 [85], KP_{15} [86], CsP_7 [87], Cu_2P_7 [88], LaP_7 [89], the anion framework can be understood as a condensate of the (poly-)cyclic anions. Thus, the condensed (poly-)cyclic anions can form chains, networks and layers. Many of these structures resemble sections of *Hittorf's* phosphorus, black phosphorus or grey arsenic. The polymeric anion in CsP_7 [87] can be derived from the isolated P^{3-}_{7} cage. Each cage forms a bond with the neighbouring cage, resulting in the one-dimensional infinite anion $^{1}_{\infty}[P^{1-}_{7}]$. CsP_7 was the first Zintl phase with a polymeric anion synthesised in liquid ammonia.

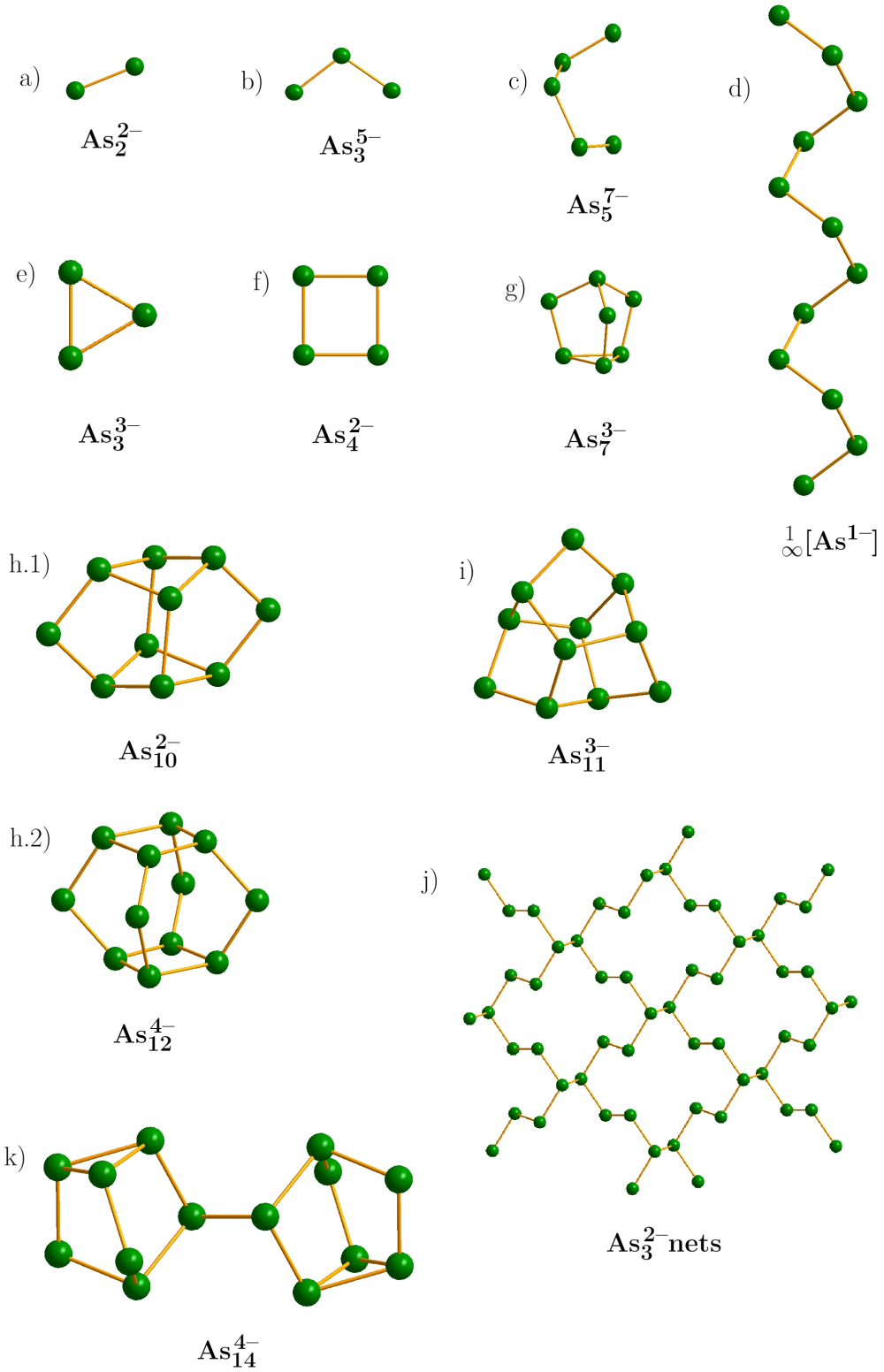

Figure 1.6: The structures of selected arsenic polyanions in the following Zintl phase compounds: **a)** M_2As_2 (M=Ca, Sr, Eu) [71] **b)** HT−$LaAs_2$ [72] **c)** HT−$LaAs_2$ [72] **d)**MAs (M=Li, Na) [48, 73] **e)** CsAs [74] **f)** $CoAs_3$ [75] **g)** A_3As_7 (A=Li-Cs) [50, 74, 76, 77] **h)** $[Na(18\text{-crown-6})]_3[As_{10}]_{0.5}[As_{12}]_{0.5}\cdot 4THF$ [78] **i)** A_3As_{11} (A=Rb, Cs) [79] **j)** MAs_3 (M=Ca, Sr, Ba, Eu) [69] **k)** $[Rb(18\text{-crown-6})]_4As_{14}\cdot 6NH_3$ [80]

This type of polymerisation has not yet been observed in arsenides. However, dimers of $[As_7]$ and $[As_{11}]$ cages are known. Two condensed $[As_7]$ cages are present in $[Rb(18\text{-crown-}6)]_4As_{14}{\cdot}6NH_3$ [80] as As_{14}^{4-} with a single bond present between the two cages. The As_{22}^{4-} anion is known from (Rb–2,2,2-crypt)$_4As_{22}$ · 4DMF [90]. It is a dimer formed from two As_{11} units with a single bond between the monomers. An exceptional representative of the polyanionic arsenides is the fullerene-type As_{20} in the anion $[As@Ni_{12}@As_{20}]^{3-}$. This fullerene-shaped arsenide with I_h symmetry is the first of its kind within the pnictogen group [91].

The clusters Pn_7^{3-}(Pn=P, As, Sb, Bi) [50, 92–94], as well as the clusters Pn_{11}^{3-} (Pn=P, As, Sb, Bi) [79, 92, 95, 96] are known for all heavy homologues of nitrogen. The cage-shaped polyanions are stable in solution. So far, no cages have been observed that exceed the charge to atom ratio=1:1. Higher charged Zintl anions have so far only been accessible by solid-state syntheses; it is presumed that higher charges cannot be stabilised in solvents [46]. The Pn_7^{3-} and Pn_{11}^{3-} cages are incongruently soluble in ammonia and other amines and are therefore popular as starting materials for syntheses. In the case of Pn_7^{3-}, it was frequently observed that the cages are linked by the cations present. This tendency is strong enough that even when crown ethers and cryptands are used, products are formed that still exhibit these linkage patterns. In the potassium compound $K_2(K\text{–}2,2,2\text{-crypt})_2Au_2(As_7)_2$, the cages are linked two-dimensionally [97]. Such compounds can be used to investigate the influence of the linkage on the band gap. The research group of P. S. Weiss [97, 98] investigated the band gaps of compounds containing As_7^{3-} clusters. In particular, the influence of ionic bonds between the clusters was investigated. By exchanging the cations (in this case the alkali metals K, Rb, Cs and the transition metals e.g. zinc and gold) the influence on the band gap could be investigated. The investigated compounds show one-, two- and three-dimensional linkage patterns [99].

The aim of this work was to obtain similar compounds without the use of cryptands, instead using ammonia as a solvent, in order to study the linkage of As_7^{3-} cages with transition metals. For this purpose, gold was specifically chosen. As a consequence of the high s-orbital contraction, due to relativistic effects, the electron affinity of gold (−2.31 eV) is much larger than that of Cu and Ag (–1.23/–1.30 eV) [58]. Gold thus behaves "iodine-like" in some respects and forms anionic Au^- in reaction with the strong reducing alkali metals Rb and Cs. This can be used to bring gold into solution in liquid ammonia in the presence of K, Rb and Cs [100]. In addition, an excess of arsenic can be used to obtain As_7^{3-} by direct reduction in ammonia [101–105]. Au^- can be reduced to Au^+ with the excess As, resulting in polyanionic arsenides. In this way it is possible to

work directly with the elements. A further aim was to link isolated polyanions together by the coordination of gold. Due to the possibility of formation of sterically demanding polyanions, like As_7^{3-} and As_{11}^{3-}, linear coordination of these anions is a suitable choice. The results obtained in this work show that the oxidation with arsenic is successful and the auride is oxidised to Au(I). It is not possible to judge whether the nortricylan cage is preferentially formed in the process.

The syntheses of linked heptaarsenides with cryptands and crown ethers has already been widely researched. The products can be well isolated, as they are usually temperature-stable. It is possible to purify the products using solvents. However, research into pure ammoniates has still been dealing with the same problems for over a hundred years. The temperature-unstable compounds have to be handled constantly at low temperatures after removal of the liquid ammonia. These working techniques are not widely used and are challenging to apply. The results presented in this thesis are essentially fundamental research. However, compared to applied research, the answers obtained are not less important, as the fundamental understanding of the reactivity of elements in ammonia contributes to a better understanding of possible reaction processes.

1.4 Coinage Metal Selenides

Chalcogens form a variety of compounds with coinage metals. These are often prepared from alkali metal chalcogenide melts by adding the coinage metal and additional chalcogen. Low temperatures around 350 °C are often sufficient in an alkali chalcogenide melt [106]. In the ICSD, no entries of ammoniates are present for the alkali metal coinage selenides. Interestingly, for the syntheses of the deposited alkali metal coinage metal selenides (Table 1.1), the precursor compounds A_2Se (A=Na, K, Rb, Cs) [107, 108] are obtained from liquid ammonia. In this process, the elements are reacted in elemental form in a stoichiometric approach. After removing the ammonia, the resulting powder is reacted as an educt for further reaction with the coinage metal and additional selenium. In these polyselenide melts, gold behaves far from a "noble" metal and yields a large number of compounds with interesting structural arrangements, in which the metal assembles to different coordination numbers and oxidation states [109]. Gold is known to dissolve in the presence of potassium, rubidium and caesium in ammonia as the auride ion Au^- [100]. Similarly, copper(II)chloride and silver(I)chloride are soluble in ammonia, forming the tetramine copper(II) complex and the diamine silver(I) complex, respectively. Since all the reactants for an alkali metal

selenide are soluble in ammonia, the question arose, what would happen in a one-pot synthesis.

The representatives of the $A_xAu_ySe_z$ compounds are listed in Table 1.1. It can be seen that both gold(I) and gold(III) compounds are known. The oxidation state influences the anion framework of the compound. The linear coordination in gold(I) compounds show infinite chains in the anion framework, but layered structures are present as well. The gold(III) compounds, on the other hand, show a square-planar coordination of the metal centre. Representatives for one-, two- and three-dimensional anion structures have been reported.

With the representatives of the $A_xCu_ySe_z$ compounds, layer structures can often be observed, in which the copper is tetrahedrally coordinated by selenium. $Cs(Cu_4Se_3)$ [110] is prepared in a hydrothermal synthesis and forms a layered structure comprising $CuSe_4$ tetrahedra that share five of their six sides to generate layers of $[Cu_4Se_3^-]_n$. These layers are alternating Se–Cu–Se–Cu–Se square networks and are separated by a layer of caesium cations. $Rb(CuSe_4)$ [111] and $Cs(CuSe_4)$ [110] comprises infinite one-dimensional chains of $[CuSe_4^-]_n$ that run along [100], separated by the alkali metal cations. KCu_2Se_2 [112] is built up of $^2_\infty[Cu_2Se_2^{2-}]$ layers that are separated by the K^+ cations. Every Cu atom is in a distorted tetrahedral environment of four selenium atoms. The layers are stacked onto each other parallel to the crystallographic c axis and are separated by the potassium cations. In KCuSe [113], the $^2_\infty[CuSe^-]$ anion framework appears graphite-like.

If the relatively small cations are exchanged for larger, soft cations such as the $[PPh_4]^+$, coinage metal selenium ring systems can be obtained from solution, compare Table 1.2. Even though the ammonia solvent shells "inflate" the cations, making them more easily polarised and space-demanding, no ring systems could be obtained. The representatives of the coinage metal-selenium compounds in Table 1.2 show the great variety of bonding patterns that are possible.

A	$A_xAu_ySe_z$	Anionic Structure
Na	$Na(AuSe_2)$ [109]	covalently bonded $[AuSe_2]_n^{n-}$ anionic layered network, polymerised $[Au_2Se_2]Se_{4/2}$ dimeric units with a central rhombic $[Au_2Se_2]^{2+}$ core; d(Au–Au) 3.73 Å
Na	$Na_5(Au(Se_3)_4)$ [107]	discrete $[Au(Se_3)_4]^{5-}$ anions
K	KAuSe [114]	one-dimensional chains of $^1_\infty[AuSe^-]$; d(Au–Au) 3.34 Å
K	$K(AuSe_5)$ [106, 109]	one-dimensional chains of $[AuSe_5]_n^{n-}$
K	$K(AuSe_2)$ [109]	one-dimensional chains of $[AuSe_2]_n^{n-}$
K	$K_3(Au(Se_5)_2(Se_3))$ [106]	$[Au(Se_3)(Se_5)_2]_n^{3n-}$; square-planar coordinated Au^{3+} with two trans-standing Se_5^{2-} and bridging Se_3^{2-} ligands
K	$K_3(AuSe_2)$ [115]	discrete, linear complex anions $[AuSe_2]^{3-}$
Rb	Rb(AuSe) [116, 117]	one-dimensional chains of $^1_\infty[AuSe^-]$; d(Au–Au) 3.37 Å
Rb	$Rb(Au_3Se_2)$ [108]	strongly corrugated anionic layers $^2_\infty[Au_3Se_2^-]$; d(Au–Au) 3.06 Å
Cs	Cs(AuSe) [117]	one-dimensional chains of $^1_\infty[AuSe^-]$; d(Au–Au) 3.43 Å
Cs	$Cs(AuSe_3)$ [109]	one-dimensional chains $[AuSe_3]_n^{n-}$
Cs	$Cs(Au_3Se_2)$ [108]	strongly corrugated anionic layers $^2_\infty[Au_3Se_2^-]$; d(Au–Au) 3.14 Å
Cs	$Cs_2(Au_2Se_3)$ [118]	one-dimensional chains of $[AuSeAuSe_2]_n^{2n-}$; discrete Au–Au pairs with a distance d(Au–Au) 3.20 Å; next nearest Au–Au contact is an interchain contact of 3.84 Å

Table 1.1: All alkali metal gold selenides $A_xAu_ySe_z$ known so far from the ICSD (Version 4.8.0 (build 20220419-1910) - Data Release 2022.1). There are no ammoniates in the database.

Compound	Anionic Structure
$(PPh_4)_4[Cu_2Se_{14}]$ [119]	$[(CuSe_4)Se_5(CuSe_5)]_4^-$; one of the two Cu atoms is part of a $CuSe_4$ five-membered ring, the other of a $CuSe_5$ six-membered ring. The two copper atoms are linked via a Se_5 chain, whereby each metal atom is surrounded by three selenium atoms in a planar fashion.
$(Ph_4P)_2[Cu_4(Se_4)_{2.4}(Se_5)_{0.6}]$ [120]	$[Cu_4(Se_4)_{2.4}(Se_5)_{0.6}]^{2-}$; A Cu_4 tetrahedron is surrounded by two sets of $[Se_4]^{2-}$ chains, the third chain consists of 41 % $[Se_4]^{2-}$ and 59 % $[Se_5]^{2-}$.
$[(Ph_3P)_2N]_2[Au_2Se_2(Se_4)_2]$ [121]	$[Au_2Se_2(Se_4)_2]^{2-}$; the planar $[Au_2Se_2]^{2+}$ core is coordinated by $[Se_4]^{2-}$ chelate ligands. The five-membered $AuSe_4$ rings develop the twist-boat conformation.
$(Ph_4P)_2[Au_2(Se_2)(Se_3)]$ [122]	$[Au_2(Se_2)(Se_3)]^{2-}$, envelope-shaped seven-membered ring containing two gold and five selenium atoms; d(Au–Au) 3.00 Å.
$(Ph_4P)_2[Au_2(Se_2)(Se_4)]$ [122]	$[Au_2(Se_2)(Se_4)]^{2-}$; the eight-membered ring is puckered; d(Au–Au) 3.13 Å

Table 1.2: Examples of copper or gold-containing polyselenides synthesised in solvents.

Chapter 2

Experimental Part

2.1 Analytical Methods

2.1.1 X-Ray Powder Diffraction

The samples measured were air-sensitive substances, so they were filled into glass capillaries (wall thickness 0.01 mm, diameter 0.1 mm to 0.3 mm) in a argon glove box and sealed with an electrically heated tantalum wire or applied to a surface carrier with adhesive film. The adhesive film is the brand "SCOTCH Magic Tape", the powder diffraction pattern is reproducible. For shorter measurements, the adhesive film turned out as sufficiently airtight. For the strongly X-ray absorbing substances, X-ray amorphous glass was mixed in. Measurements were made using a STOE-STADI-P diffractometer with cobalt Kα ($\lambda = 1.788\,96\,\text{Å}$) radiation. Reflections are detected with a Position Sensitive Device (PSD) detector. More recent measurements were taken with the DECTRIS MYTHEN 1K detector. The software suite "Win XPOW" [123] was used to control the diffractometer and the data was processed with "Match2" [124].

2.1.2 X-Ray Single Crystal Diffraction

Crystals for single crystal measurements were obtained from samples out of reaction vessels or ampoules filled with argon. The samples were transferred to polyfluorinated oil (FOMBLIN Y HVAC 140/13, Solvay, Brussels, BE) to protect them from moisture and air. Suitable crystals were selected using a stereomicroscope. Using the oil, the crystal was placed on a class fibre on a goniometer head. Inside the cold nitrogen stream (123 K) of the diffractometer the oil solidified. The crystal was then centred in the X-ray beam of the diffractometer. The κ-CCD four circle diffractometer (Bruker-Nonius, Delft, NL) was equipped with a molybdenum anode. The polychromatic radiation was monochromatised by a graphite single crystal to only use the MoK_α-radiation with the wavelength of $\lambda = 0.710\,73\,\text{Å}$. The reflections were detected by a CCD area detector

with a diameter of 95 mm. The detector consists of a photosensitive semiconductor element coated with gadolinium oxide sulphide, which fluoresces when irradiated. In this way the positions and the intensities of the reflexes can be determined. Low temperatures were ensured by a Cryostream 700 (Oxford Cryosystems, Oxford, UK). The programme "Collect" [125] was used for collecting the data. With "HKL-Scalepack" [126] the unit cell was determined. Integration and reduction of the data set was done by "HKL-Denzo" [126]. The structures were solved with direct methods and refined based on F^2 with anisotropic parameters for all atoms with SHELX-97 [127, 128]. The programme Multiscan [129] was used for semi-empirical absorption correction. This absorption correction by Blessing is based on the large redundancy of the given data set. The programmes were implemented in the programme suite WinGX [130]. The data of the modulated crystal structure was processed with "APEX4" [128]. For representation of crystal structures the programme Diamond [131] was used.

2.1.3 Low Temperature Single Crystal Manipulation

Synthesis in solvents often leads to cocrystallisation in the product. The high vapour pressure of the solvent inside the crystal lattice leads to diffusion and often ends in decomposition of the crystal or at least intensity decay of the reflections during data collection. Therefore it is always necessary to work below the decomposition temperature of the formed crystals. To gain access to the thermally unstable as well as air and moisture sensitive crystals, a modified form of the method of Kottke and Stalke [44] for low temperature manipulation of single crystals was used. A nitrogen gas flow is directed through a copper spiral immersed in liquid nitrogen. By means of a Teflon nozzle the cold nitrogen stream is directed into a specially manufactured round glass. This has a high rim with inlet and outlet opening and a cavity for X-ray amorphous, transparent, inert special oil (GALDEN HT 230, Solvay, Brussels, BE), which is highly viscous at low temperatures. The round glass is positioned on a Dewar vessel filled with nitrogen and is thus cooled from below. The reaction ampoules, which contain crystals and ammonia, are cooled in liquid nitrogen to freeze the solvent. They are opened in the cooled nitrogen stream. Using a steel spatula, previously cooled in liquid nitrogen, the crystals are transferred to the cold oil together with some solvent. The temperature can be controlled down to −40 °C via the flow rate of the nitrogen. Diffusion of ammonia out of the crystal lattice of solvent containing crystals is thus prevented, and thus their decomposition.

Crystals are observed through a stereo microscope. In the viscous oil, crystals suitable for single crystal X-ray structure examination can now be isolated with the aid of a glass needle. The crystals are either placed directly in front of the nozzle with a little oil or are placed directly from the oil-filled cavity onto a goniometer head with pre-centred glass fibre. In most cases, a crystal placed directly in front of the nozzle was easier to transfer to the glass fibre. In addition, less oil sticks to the glass fibre, which leads to better results in the X-ray experiment. The crystal is transported in the cold air cushion of a Dewar vessel. The glass fibre should not be placed in the liquid nitrogen. Cracks can form in the frozen oil and the crystal may fall from the glass fibre.

The crystal, cooled in the cold air cushion, is quickly removed from the Dewar vessel and placed into the cooling flow of the four-circuit diffractometer. The crystal is then centred. The round glass can be stored overnight in a Dewar vessel filled with dry ice and in the following day further crystals can be selected and examined.

With this method it was possible to gain access to thermally unstable crystals, which at room temperature are not manageable. This method was used to transfer crystals for elemental analysis to an EDX carrier.

2.1.4 Energy Dispersive X-Ray Spectroscopy (EDX)

All compounds were examined for the composition via energy dispersive electron-beam X-ray fluorescence. Selected crystals were fixed on a carbon coated sample holder and broken to obtain fresh surfaces to examine the bulk material. The sample holder is carbon coated to avoid static charging of the sample. Air sensitive samples were placed on the sample carrier under exclusion of air inside a glove box. These samples were transferred witch a special double chamber under exclusion of air into the chamber of a SPI Module Sputter Coater (Sputtermodul 11430, Fa. SPI Supplies), where the crystals were sputtered with carbon under low pressure (approx. 1×10^{-1} mbar, Edwards E2M5) using an argon plasma. The accelerating voltage was 25 kV. A second electron microscope with newer technique was used. The Hitachi SU3800 with a variable chamber pressure, sample introduction lock, SE, BSE and UVD detector as well as the X-ray detector EDAX EDS system "Octane Elect Super EDS". The sample preparation was analogous, but sputtering was no longer required. Whenever possible, the crystal from the previous X-Ray single crystal data collection was examined.

2.1.5 Raman Spectroscopy

The samples for vibrational Raman spectroscopy were analysed directly in the borosilicate glass reaction ampoule (diameter = 8 mm). Measurements were performed with an FT-Raman spectrometer (MuliRAM, Bruker, Karlsruhe) equipped with an Nd:YAG laser (DeniCAFC-LC-3/40, Laser Technologies, Klastech-Karpushko) (λ = 1064 nm) as excitation source and a liquid nitrogen cooled germanium detector. Bands occurring at 75 cm^{-1} and 78 cm^{-1} were assigned to the Nd:YAG laser. Measurements were performed at room temperature.

2.2 Preparative Methods

2.2.1 Working under Inert Gas Atmosphere

A Schlenk line was used for synthetic work under argon or vacuum. A pressure of 9.6×10^{-3} mbar was achieved with a rotary pump (RD4, Vacuubrand, Wertheim). The pressure was constantly monitored with a manometer (Combitron CM 300, Leybold, Cologne). Argon (Ar $\geq$ 99.996 %, $O_2 \leq$ 6 ppm, $N_2 \leq$ 20 ppm, $H_2O \leq$ 5 ppm; Praxair, Düsseldorf) was passed through several drying towers for further purification. Moisture was removed by silica gel, acidic impurities by potassium hydroxide pellets, water was absorbed by a 3 Å molecular sieve, phosphorus pentoxide neutralises basic impurities. To remove traces of oxygen and nitrogen, the gas was last passed through a titanium sponge heated to 650 °C. This reduces the proportion of oxygen and nitrogen to the partial vapour pressure of TiO or TiN. The Schlenk line is completely made of borosilicate glass. All joints were greased with high-vacuum grease (Leybonol LVO 870, Leybold GmbH, Cologne, GER). The pumped gas could be additionally passed through a cold trap, which was cooled by liquid nitrogen to protect the vacuum pump from volatile compounds and improving the vacuum. Other glass ware could be connected to the Schlenk line via glass joints. In order to free glass ware from oxygen and moisture residues before use, they were heated up to three times under vacuum with a Teclu burner. Between the steps, rinsing was carried out with purified argon. Ampoules were filled in argon countercurrent with a funnel. Ampoules that were to be filled with ammonia or ethylenediamine were tapered in the argon countercurrent to facilitate subsequent sealing. For this purpose, the ampoules, containing the educts, were cooled with liquid nitrogen in a vacuum to prevent premature reaction. The tapering of the ampoules was carried out with a hand torch at argon counterpressure. With the ampoule still connected to the argon vacuum system, the system was opened

to avoid overpressure during tapering. Following the tapering, the system was flushed several times with argon.

2.2.2 Glove Box

For preparation of air or moisture sensitive compounds, a glove box (Labmaster 130, MBraun, Garching) was used. Argon was used as inert gas. For purification, argon was passed through a molecular sieve (400 pm) and a BTS-Catalyst (Copper-Catalyst (SP), MBRAUN, Garching, GER). The oxygen and water content varied usually between 1 ppm and 10 ppm and was measured by an electrical analyser. Evacuation in the air lock was achieved with a rotary vane pump (RD4, Vacuubrand, Wertheim). In the front window, a microscope (MZ6, Leica Microsystems GmbH, Wetzlar) was integrated. A high-precision scale (BP61S, Sartorius AG, Göttigen) was used for weighing.

2.2.3 Working with Liquid Ammonia

The ammonia gas cylinder was connected with a hose to an evacuated Schlenk line. The ammonia gasflow was led through a drying tower filled with potassium hydroxide into a cold trap. The cold trap was cooled with an ethanol/dry ice bath. Sodium was previously placed in the cold trap for further purification of the ammonia. In order to fill reaction vessels, these were cooled in a vacuum in an ethanol/dry ice bath. The cooling bath at the ammonia storage vessel was removed. Ammonia now slowly condensed in the reaction ampoule. The internal pressure could be observed via mercury manometers, which helped to prevent the system from bursting in case of overpressure. As soon as sufficient ammonia condensed in the reaction ampoule, the ammonia storage vessel was cooled again and the connection was closed via a tap. The ammonia in the reaction ampoule was now frozen with liquid nitrogen and the ampoule was sealed under vacuum. The ampoule had an inner diameter of 8 mm and a wall thickness of 1 mm, with length of approx. 10 cm. NIST standard reference data was used to estimate the internal pressure of the ampoule with knowledge of the filling degree [63]. The burst pressure of the glass ampoule is calculated as approx. 39 bar. Thus the ampoules can be handled safely at room temperature and even at temperatures up to 55 °C, where the internal pressure reaches approx. 23 bar [63]. To protect against flying glass fragments in the event of a bursting ampoule, the ammonia ampoules were stored in polyethylene containers.

2.2.4 Reactions in Steel Autoclaves

In the previous section it was explained that liquid ammonia can be handled safely using thick-walled glass ampoules with a relatively small internal diameter of less than 10 mm. The equilibrium vapour pressure at room temperature (25 °C) is ≈ 9 bar. The ampoules used in the course of the synthetic work are able to withstand an internal pressure of up to 39 bar without bursting. Heating these glass ampoules up to 55 °C is therefore possible, provided that suitable safety precautions are ensured. For this purpose, the ampoules were heated in drying cabinets while being placed in steel tubes. However, if the synthesis conditions require heating above 55 °C, the only option for the use of glass ampoules is to work in an autoclave with suitable counterpressure.

Steel autoclaves with screw caps were used for this purpose. Tightening the screw cap with hard force causes a deformation at the sealing surface. This "cold seal" method [132] proved to be sufficient to keep the autoclaves tight. The counterpressure was adjusted using dry ice. The internal volume of the autoclave was determined, and the intrinsic volume of the reaction ampoules was subtracted. In the remaining volume, an internal pressure of about 180 bar was adjusted by adding dry ice. For this purpose, a weighed amount of solid CO_2 was added to the autoclave together with the filled reaction ampoules and the autoclave was quickly sealed to avoid loss of the volatile CO_2.

Nevertheless, many experiments resulted in bursting of the ampoules inside the autoclave.

Chapter 3

Syntheses

3.1 Polyarsenides

3.1.1 Ba_3As_2O

For the synthesis of Ba_3As_2O a mixture of Ba (285.5 mg, 2.079 mmol (Aldrich, 99 %)), As (69.9 mg, 0.933 mmol (MERCK, 99 %)) and As_2O_3 (46.1 mg, 0.233 mmol) was filled into a stainless steel ampoule. The ampoule was closed by welding with an argon arc and placed inside a quartz half ampoule under argon for protection against oxidation. The side with the joint at the end of the quartz half ampoule protruded from the furnace. By this method, it was possible to react several mixtures in different stainless steel ampoules under the same conditions in the absence of oxygen in the same furnace. The quartz half ampoule was reused several times, only the grease at the joint needed to be renewed every time. The reactants were heated at 200 °C h^{-1} to 800 °C. The temperature was kept for 10 h. At 5 °C h^{-1}, it was cooled to room temperature. The product was obtained as black crystals. Other phases identified from powder diffraction data were Ba_3As_4 and BaO. The composition was confirmed by energy-dispersive X-ray analysis (EDX). The powder diffraction pattern indicates, that Ba_3As_2O is present in the phase triangle of Ba_3As_4 and BaO.

3.1.2 $K_3Ba_7(As_3)_3O$

Reagents used were Ba (Aldrich, 99 %), K, As (MERCK, 99 %) and As_2O_3. The method analogous to the synthesis of Ba_3As_2O was applied. Mixtures of K, Ba, As, As_2O_3 with a molar ratio of 4:12:7:1 were heated with 200 °C h^{-1} to 800 °C for 3 h and cooled to room temperature with 10 °C h^{-1}. The product were black crystals of the new phase $K_3Ba_7As_9O$, respectively, in addition to unidentified phases. The potassium content was confirmed by energy-dispersive X-ray analysis (EDX) of the same crystal used for X-ray studies.

3.1.3 Ba_3As_4

For the synthesis of Ba_3As_4, a mixture of Ba (174.8 mg, 1.273 mmol) and As (127.5 mg, 1.702 mmol) was filled inside a stainless steel ampoule. The method analogous to the synthesis of Ba_3As_2O was applied. The reactants were heated with 200 °C h^{-1} up to 800 °C. The temperature was maintained for 10 h. At 5 °C h^{-1}, it was cooled to room temperature. The product was obtained as black crystals. The composition was confirmed by energy-dispersive X-ray analysis (EDX). The powder diffraction pattern indicates, that Ba_3As_4 is the main product of the synthesis.

3.1.4 $[Eu(NH_3)_8]_2[Eu(NH_3)_3(As_7)_2]$

A mixture of 30 mg (0.197 mmol) Eu and 70 mg (0.934 mmol) As was weighed into a borosilicate glass ampoule. The ampoule had an inner diameter of 8 mm and a wall thickness of 1 mm. With a length of 10 cm, the internal volume was 5 cm^3. Ammonia was condensed into the ampoule until a fill level of 25 % was reached. Then the ammonia was frozen with liquid N_2, the ampoule was evacuated and melted off. The ampoule was placed in an autoclave filled with dry ice pieces, and the autoclave was immediately sealed. The amount of CO_2 was calculated to build up a pressure of 180 bar at 150 °C. Using a gradient of 5 °C h^{-1}, the autoclave was heated to 150 °C and left at this temperature for 96 h. The slow heating rate was chosen to safely prevent overheating of the oven by the control system, otherwise too high pressures would occur, leading to destruction of the ampoule. The oven was brought to room temperature at a cooling rate of 5 °C h^{-1}. The product $[Eu(NH_3)_8]_2[Eu(NH_3)_3(As_7)_2]$ was obtained in the form of black needles. $[Eu(NH_3)_8]_2[Eu(NH_3)_3(As_7)_2]$ decomposed at room temperature and released a garlic smell, which could indicate the formation of AsH_3. The EDX spectrum confirmed the presence of Eu and As.

3.1.5 Rb_2AuAs_7

The compound was obtained by weighing a mixture of Rb, Au and As in a 2:1:1 ratio into a borosilicate ampoule under inert gas conditions. 11.6 mg (0.135 mmol) Rb, 5.1 mg (0.067 mmol) As and 13.3 mg (0.067 mmol) Au were used. The method analogous to the synthesis of $[Eu(NH_3)_8]_2[Eu(NH_3)_3(As_7)_2]$ was applied (Subsec. 3.1.4) and the ampoule was placed in an autoclave. The same temperature and time intervals from Subsec. 3.1.4 were used. The product was obtained as black, needle-shaped crystals. The composition was confirmed by energy-dispersive X-ray analysis (EDX).

3.2 Coinage Metal Selenides

3.2.1 $Rb_3AuSe_2 \cdot 1.5\,NH_3$

The compound was obtained by weighing a mixture of Rb (16.4 mg, 0.192 mmol), Au (12.6 mg, 0.064 mmol) and As_2Se_3 (16.5 mg, 0.043 mmol) into a borosilicate ampoule under inert gas conditions. The method analogous to the synthesis of $[Eu(NH_3)_8]_2[Eu(NH_3)_3(As_7)_2]$ was applied (Subsec. 3.1.4). The ampoule was placed in an oven at 55 °C and left there for 10 weeks. The product $Rb_3AuSe_2 \cdot 1.5\,NH_3$ was obtained as colourless, rhombic crystals and the composition was confirmed by energy-dispersive X-ray analysis (EDX). In the course of the synthetic work, it was observed that the use of As_2Se_3 instead of pure selenium enhanced the yield of well defined crystals significantly. If the reactants Rb, Au and Se were used in a ratio of 3:1:2, a colourless microcrystalline powder formed in a short time, which, however, did not contain suitable crystals and no structure determination could be carried out.

3.2.2 $K_{10}CuSe_8Cl \cdot NH_3$

The compound was obtained by weighing a mixture of K (9.0 mg, 0.23 mmol), CuCl (22.8 mg, 0.23 mmol) and Se (18.2 mg, 0.23 mmol) into a borosilicate ampoule under inert gas conditions. The method analogous to the synthesis of $[Eu(NH_3)_8]_2[Eu(NH_3)_3(As_7)_2]$ was applied (Subsec. 3.1.4). The ampoule was placed in an oven at 55 °C and left there for eight weeks. $K_{10}CuSe_8Cl \cdot NH_3$ was obtained as red crystals in the form of rhombic prisms and the composition was confirmed by energy-dispersive X-ray analysis (EDX).

3.2.3 $K_2[AuSe]Se \cdot NH_3$

The compound was obtained by weighing a mixture of K (4.5 mg, 0.115 mmol), Au (11.4 mg, 0.058 mmol) and Se (9.1 mg, 0.115 mmol) into a borosilicate ampoule under inert gas conditions. The method analogous to the synthesis of $[Eu(NH_3)_8]_2[Eu(NH_3)_3(As_7)_2]$ was applied (Subsec. 3.1.4). The synthesis was carried out under three different conditions and always yielded the target compound; at −18 °C for 6 weeks, at 55 °C in an oven for three weeks and at 150 °C in an autoclave for 96 h with a cooling ramp of 5 °C h^{-1}. Red crystals were found in all three reaction ampoules, but the crystal growth was significantly different. At −18 °C, only a few red crystals were formed, but the crystal shapes were regular. At 55 °C, star-shaped crystals with strong intergrowth were formed. The reaction in the autoclave provided the best results in terms of quantity and quality of the crystals, as well as the reaction time.

Nevertheless, even with different approaches, twin growth couldn't be prevented. EDX analysis confirmed the composition of $K_2[AuSe]Se \cdot NH_3$ for K, Au and Se.

3.3 *Spin-ladder* Compounds

3.3.1 $NH_4Fe_2S_3$

$NH_4Fe_2S_3$ was obtained by weighing a mixture of Fe (69.4 mg, 1.24 mmol) and S (80.5 mg, 2.51 mmol) into a borosilicate ampoule. Under argon, the ampoule was filled with ethylenediamine to a level of 50 %. The ampoule had an inner diameter of 8 mm and a wall thickness of 1 mm. The solution had an orange-red colour. After a week at 170 °C, black fine needles had formed. The product was washed with water and ethanol by decanting the solvent several times until it was colourless. The resulting substance was dried in a Schlenk flask at 50 °C under vacuum. Black metallic shiny acicular crystals were obtained as the product. The ratio of Fe and S was confirmed by energy-dispersive X-ray analysis (EDX).

3.3.2 $NH_4Fe_2Se_3$

A mixture of Fe (48.1 mg, 0.87 mmol) and Se (101.9 mg, 1.29 mmol) was weighed into a borosilicate ampoule. The method analogous to the synthesis of $NH_4Fe_2S_3$ was applied (Subsec. 3.3.1). $NH_4Fe_2Se_3$ was obtained as black metallic shiny acicular crystals. X-ray analysis (EDX) confirmed the ratio of Fe and Se in $NH_4Fe_2Se_3$.

3.4 $[Mn_2(HPO_3)_2(C_2H_8N_2)]$

For the synthesis of the compound Mn (13.1 mg, 0.23 mmol), Cu (15.2 mg, 0.23 mmol) and red P (51.7 mg, 1.7 mmol) were used. The already tapered ampoule was then filled to approx. 30 % with ethylenediamine in argon counter-stream. In order to remove possible impurities of the ethylenediamine, it was dried over calciumhydride and distilled prior to use. The ampoule with the solvent and the reactants was then cooled until frozen with a dry ice/ethanol bath. The ampoule was then evacuated and sealed by melting. The ampoule was kept in an oven at 170 °C for 7 days. $[Mn_2(HPO_3)_2(C_2H_8N_2)]$ was obtained in the form of colourless needle-shaped crystals. The composition was confirmed by energy-dispersive X-ray analysis (EDX).

3.5 Sulphur and Selenium Compounds Synthesised in Liquid Ammonia

3.5.1 $K_9Se_{2.88}(Se_2)_{1.12}OH$

A mixture of 100 mg of K (22.7 mg, 0.581 mmol), Ag (31.4 mg, 0.291 mmol), and Se (45.9 mg, 0.581 mmol) with the ratio 2:1:2 was weighed into a borosilicate glass ampoule. The method analogous to the synthesis of $[Eu(NH_3)_8]_2[Eu(NH_3)_3(As_7)_2]$ was applied (Subsec. 3.1.4). The ampoule was left for nine months at 55 °C. Yellow, hexagonal, flat crystals were isolated. In these crystals, no silver could be detected by EDX analysis. The structure refinement resulted in $K_9Se_{2.88}(Se_2)_{1.12}OH$.

3.5.2 $[Mn(NH_3)_6][As_4S_6]\cdot NH_3$ and As_3NS_3

100 mg of a mixture of Mn:As:S in a molar ratio of 1:2:3 was weighed into a borosilicate glass ampoule with 2 mg (0.016 mmol) of $MnCl_2$. 18.3 mg (0.333 mmol) Mn, 49.8 mg (0.666 mmol) As and 32.0 mg (0.999 mmol) S were used. The method analogous to the synthesis of $[Eu(NH_3)_8]_2[Eu(NH_3)_3(As_7)_2]$ was applied (Subsec. 3.1.4). At 55 °C the ampoule was left in an oven for six months. The product $[Mn(NH_3)_6][As_4S_6]\cdot NH_3$ was obtained in the form of yellow rod-shaped crystals, simultaneously red, hexagonal flat crystals of As_3NS_3 were formed. The ratio of As:S in As_3NS_3 was confirmed by EDX analysis as well as the composition of $[Mn(NH_3)_6][As_4S_6]\cdot NH_3$.

3.5.3 $[Mn(NH_3)_6][As_2Se_6]$ and As_3NSe_3

A mixture of 10.5 mg (0.191 mmol) Mn, 28.8 mg (0.384 mmol) As and 60.7 mg (0.769 mmol) Se were used in a molar ratio of 1:2:4 and weighed into a borosilicate glass ampoule. The method analogous to the synthesis of $[Eu(NH_3)_8]_2[Eu(NH_3)_3(As_7)_2]$ was applied (Subsec. 3.1.4). The ampoule was placed in an oven at 55 °C and was left there for six months. $[Mn(NH_3)_6][As_2Se_6]$ was obtained in the form of orange rod-shaped crystals, simultaneously black needles of As_3NSe_3 were present. Variation of the starting reactants showed, that adding 2 mg (0.016 mmol) of $MnCl_2$ the yield of As_3NSe_3 was increased. Synthesis at 150 °C in an autoclave for 96 h with a cooling ramp of 5 °C h^{-1} led to the same products. The ratio of As:Se in As_3NS_3 was confirmed by EDX analysis.

3.5.4 $Rb_5(AsSe_3)Se\cdot 2\,NH_3$

Rb (16.10 mg), Cu (3.99 mg) and As_2Se_3 (16.19 mg) were weighed into a borosilicate glass ampoule. The method analogous to the synthesis of $[Eu(NH_3)_8]_2[Eu(NH_3)_3(As_7)_2]$ was applied (Subsec. 3.1.4). After ten months at 55 °C, yellow transparent crystals were obtained. The EDX spectrum revealed that the compound didn't contain copper. The single crystal structure analysis revealed the formula $Rb_5(AsSe_3)Se\cdot 2\,NH_3$ for the crystals. Rb, As and Se were confirmed by energy-dispersive X-ray analysis (EDX).

Chapter 4

Results

4.1 Polyarsenides

4.1.1 Ba_3As_2O

Ba_3As_2O [133] crystallises as black rod-shaped crystals in the orthorhombic crystal system in the space group $Pmn2_1$ (No. 31) in the Ba_3Sb_2O [30] structure type. The lattice parameters of the unit cell are $a = 11.6333(9)$ Å, $b = 11.6391(7)$ Å, $c = 5.0004(3)$ Å. The volume of the unit cell is $V = 677.06(8)$ Å^3. The number of formula units is 4. The substance is sensitive to air and moisture.

The ternary phase Ba_3As_2O presented here is the second ternary arsenide oxide reported. In contrast to the first described member of compounds of this group, Ba_4As_2O [134], As_2^{4-} dumbbells are present instead of isolated As^{3-} anions. Ba_3As_2O shows strong similarities to the well-known Ba_3Sb_2O [30], where the pnictogenides are present as $[Sb_2^{4-}]$ dumbbells. The Sb atoms have a triple capped trigonal prismatic environment consisting of eight Ba atoms and the respective second atom of the Sb_2 group. The As_2^{2-} dumbbell As(1)–As(1)$^{\#1}$ in the structure of Ba_3As_2O has a bond length of 2.46 Å, while As(2)–As(2)$^{\#1}$ has a slightly longer bond of 2.49 Å. The dumbbells are in a coordination polyhedron of barium atoms, which can be described as a distorted cuboctahedron (Fig. 4.3). The deviations from the ideal cuboctahedron were calculated by the method of Continuous Symmetry Measures [135] using the program SHAPE [136]. The polyhedron deviates from the ideal cuboctahedron by 3.47 %, the centre of the dumbbell was chosen as the central body in this polyhedron. The deviation to the anticuboctahedron is 7.94 % and for the icosahedron 4.17 %. As another discrete anion, the oxide, on the Wyckoff position $4g$ with site symmetry $..m$, is surrounded by barium cations. At first sight, an octahedral environment of the oxide was assumed, but the calculation with SHAPE results in a deviation from the ideal octahedral of 1.23 %. Therefore, the 4+2 coordination is preferred. The bond difference

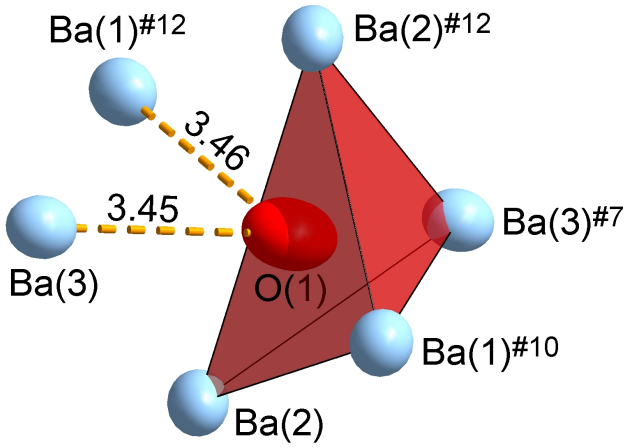

Figure 4.1: Representation of the coordination polyhedron of the oxygen atom in the structure of Ba_3As_2O. The barium atoms $Ba(1)^{\#12}$ and Ba(3) exhibit larger distances to the coordinated oxygen (red) with 3.45 Å and 3.46 Å. The other four distances are between 2.54 Å to 2.63 Å. A pseudo-octahedral environment is present with 4+2 barium (grey) coordinating to oxygen. Bond lengths in Å. Atoms are drawn as displacement ellipsoids representing a probability density of 90 %. Indices indicate the following symmetry operations: #7: -x+1/2,y+1/2,-z+1, #10: x-1/2,-y+3/2,z-1, #12: x,y,z-1.

between the shortest and longest Ba-O distance (0.92 Å) is another indicator. However, the octahedral environment of the oxide is mentioned here on purpose.

The immediate surroundings were described by Röhr [30] as a tetrahedron. However, calculations with SHAPE [136] show that a description as cis-divacant octahedral coordination (alternative: seesaw, sawhorse) is the better choice (Fig. 4.1). The calculated deviation for the cis-divacant octahedral coordination is 0.93 % compared to the tetrahedron with 5.20 %. These four barium atoms are located at a distance d(Ba-O) between 2.54 Å to 2.63 Å. In the immediate vicinity, two more barium atoms are present at a distance of 3.45 Å and 3.46 Å. In order to understand the 4+2 coordination of oxygen, the three crystallographically non-bonded barium positions must be considered. Two common features are outstanding. In each coordination sphere, both arsenic atoms and two oxygen atoms are present. The three different coordination polyhedra of the Ba positions are shown in Fig. 4.2. In every polyhedron, oxygen occupies the opposite corners of the polyhedron to each other, while the arsenic atoms are located in a plane. In the polyhedrons around Ba(1) and Ba(3), both atoms located on the Wyckoff positions 4*g*, the two longest distances between barium and oxygen are present (3.46 Å and 3.45 Å). For Ba(2), the oxygen distance is equidistant with 2.54 Å. For Ba(1) and Ba(3), the $[As_2]^{4-}$ dumbbells coordinate laterally, resulting in a higher charge density in the coordination polyhedron, which is why one of the two oxide ions evades

this charge further. Ba(2) is located in an almost ideal octahedron of coordinating oxygen and arsenic atoms, where in the square face the arsenic dumbbells coordinate over only one arsenic atom each. The charge density is thus lower, which is reflected in the oxygen atoms, which exhibit the same distances to Ba(2) atoms. The As-Ba distances d(As-Ba) are at an interval of 3.27 Å and 3.55 Å.

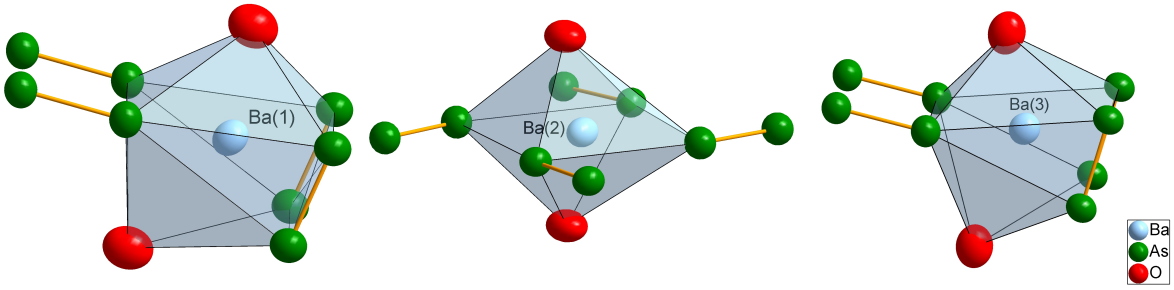

Figure 4.2: Illustration of the three crystallographically independent barium positions. In the case of the coordination polyhedra around Ba(1) and Ba(3), the lower oxygen atoms show larger distances to the central barium atoms. In the polyhedron around Ba(2), the oxygen atoms are equidistant to Ba(2). Atoms are drawn as displacement ellipsoids representing a probability density of 90 %.

It is noticeable that all octahedra are corner-linked on all sides, compare Fig. 4.4. The interstices form slightly distorted cuboctahedra, in which the two crystallographically independent $[As_2]^{4-}$ dumbbells are located (Fig. 4.3). This type of coordination suggests a relationship to perovskite, $CaTiO_3$. In perovskite [137] the $[TiO_6]$ octahedra are corner-linked on all sides and strontium is located in the cuboctahedral gaps. When transferred to the structure of $Ba_3As_2O = (As_2)OBa_3$, the cations are swapped with the anions, as can be seen from the molecular formula $CaTiO_3 \rightarrow (As_2)OBa_3$. In this scenario the arsenic dumbbell is considered as one "atom" and takes the place of the larger cation calcium. An indication of this relationship is the cuboctahedral environment of the dumbbells by barium. Another indicator for structural similarity comes from the refinement of the X-ray data. The measured crystal had to be refined as a twin with the twin law (0 1 0 / 1 0 0 / 0 0 -1 / -4). A

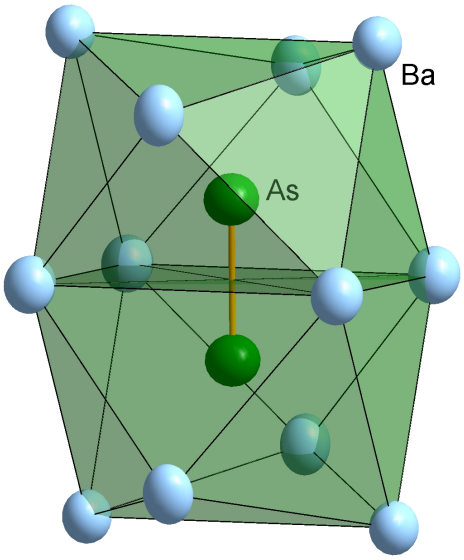

Figure 4.3: Surrounding of the $[As_2]^{4-}$ dumbbell by barium in the structure of Ba_3As_2O. Each arsenic atom is surrounded by a three-sided prism with capping of the faces. In each case, the opposite arsenic atom occupies an overcap of the prism. Overall, the coordinating barium atoms form a distorted cuboctahedron. Atoms are drawn as displacement ellipsoids representing a probability density of 90 %.

pseudo-tetragonal symmetry was present in the actual orthorhombic diffraction pattern. Precisely because of this pseudo-symmetry, the first solution in $P4/mbm$ was obtained. However, the strongly distorted displacement ellipsoids of oxygen and the already known structure of Ba_3Sb_2O by Caroline Röhr [30] indicated a lower symmetry. The occurrence of this twinning is an indication for a possible high-temperature phase with tetragonal symmetry. The symmetry of the higher symmetry space group is preserved in the domains and is reflected in the twin law. Another indication for the structural relationship is given by the lattice constants of Ba_3As_2O, which still preserve the cubic symmetry. Based on a cubic cell of $a = 5\,\text{Å}$, doubling of the a and b axes leads to a tetragonal cell with $a = b = 10\,\text{Å}$ and $c = 5\,\text{Å}$. In a second step, the tetragonal symmetry is slightly disturbed by a rotation of the corner-sharing $[OBa_6]$ octahedra. Taking into account the replacement of the spheric cations Ca^{2+} against the As_2^{4-} dumbbell shaped anions, which are all aligned parallel to the a-b plane, makes the elongation of the a and b axes to 11.6 Å understandable.

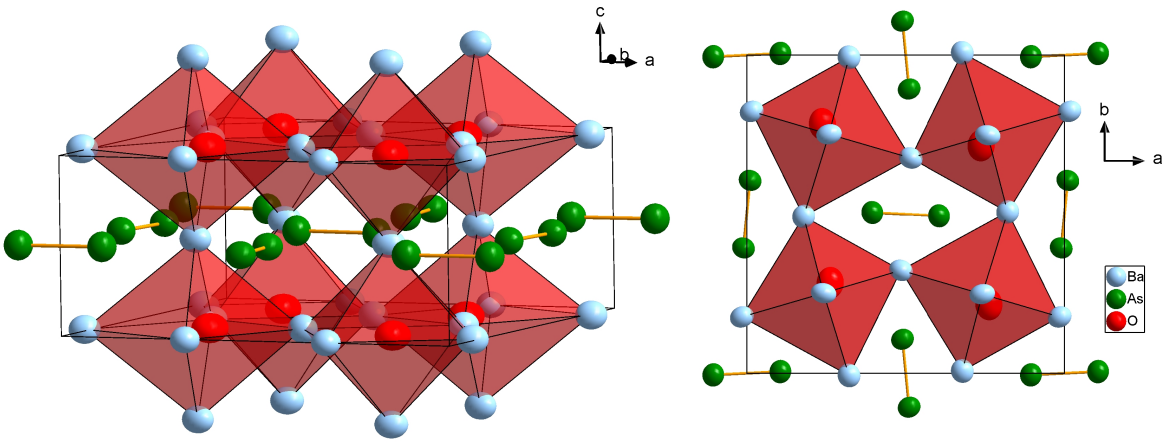

Figure 4.4: (Left) Extended unit cell of Ba_3As_2O along the crystallographic b-axis. (Right) Extended unit cell of Ba_3As_2O along the crystallographic c-axis. It can be seen that the oxide anion is not in the centre of the octahedron. However, the octahedra have been drawn in so that the relationship to perovskite can be seen. Atoms are drawn as displacement ellipsoids representing a probability density of 90 %.

4.1.2 $K_3Ba_7(As_3)_3O$

$K_3Ba_7(As_3)_3O$ crystallises as black rod-shaped crystals in the orthorhombic crystal system in the space group $P6_3/mcm$ (No. 193) in the $Na_3Sr_7(P_3)_3O$ structure type [138]. The lattice parameters of the unit cell are $a = b = 9.5260(1)$ Å, $c = 15.2003(3)$ Å. The volume of the unit cell is $V = 1194.55(3)$ Å^3 and the number of formula units is 2. The substance is sensitive to air and moisture. In the course of the structure refinement, the need to include a mixed atom position emerged. Initially, only a Ba atom was positioned in the Wyckoff position 12k. The resulting composition is $Ba_8K_2As_9O$, implying a non-integer negative charge $\{(As_3)_3\}^{16-}$ for the polyarsenide anions. The thermal displacement parameters, however, indicated that less electron density was located on position 12k. So finally a mixed occupation with 5/6 Ba and 1/6 K gave the best results and the lowest R values. The formula changed to a higher potassium content $K_3Ba_7(As_3)_3O$ and an integer number of negative charges $\{(As_3)_3\}^{15-}$ in the polyanionic structure part. Schnering has encountered the same difficulties with the refinement of the isotypical compounds $Na_3Sr_7(P_3)_3O$ and $Na_3Eu_7(P_3)_3O$ [138]. The isotropic refinement led to a site occupancy of 0.870(4) for the Sr(1) Position in $Na_3Sr_7(P_3)_3O$. In regards to the charge balance of the compound, it became apparent, that the position was not occupied entirely by strontium atoms alone, but strontium and sodium atoms with statistical distribution. Consequently, the position was refined with the same positional and displacement parameters for sodium and strontium. The site occupation factors (SOFs) of Sr1 and Na1 were refined to 0.837 and 0.163 under the constraint $SOF(Sr) + SOF(Na) = 1$, which is close to 5/6 and 1/6, therefore it was fixed at these fractions in the later refinement in order to account for the composition of $Na_3Sr_7(P_3)_3O$. After measuring the magnetic susceptibility of the isotypical structure of $Na_3Eu_7(P_3)_3O$, von Schnering could point the origin of the disorder concerning this 12-fold position to the statistical substitution by sodium atoms. The magnetic susceptibility showed no indications for valence variation of europium.

The structure contains two different anions, oxide ions and the chain-like Zintl anions As_3^{5-} (Fig. 4.5). The central As(1) atom occupies the Wyckoff position 6g with local symmetry $m2m$, the two symmetry related As(2) atoms are located on position 12k with local $..m$ symmetry. The point symmetry of the As_3^{5-} ion is C_{2v} with two equal As–As bonds of 2.46 Å. The bond lengths agree well with those in $Na_4Ba_3As_6$ (2.47 Å to 2.49 Å) [139]. The closest As$\cdots$As distances to the neighbouring As_3^{5-} ions amount to 3.88 Å in the c direction and 4.98 Å in the a-b plane and are larger than the sum of the van-der-Waals radii of As (3.70 Å [58]). No intermolecular bonds have to be considered.

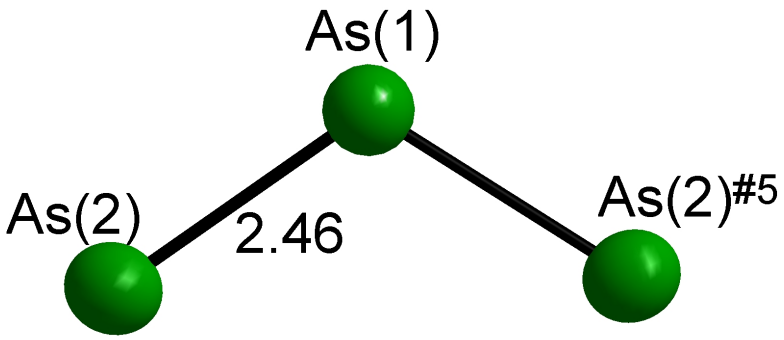

Figure 4.5: The As_3^{5-} ion in the structure of $K_3Ba_7(As_3)_3O$. Atoms are drawn as displacement ellipsoids representing a probability density of 90 %. Bond lengths are given in Å. Indices indicate the following symmetry operations: #2: -x+y+1,-x+1,z.

The As–As–As angle amounts to 112.9°. This is slightly smaller than the angles of As_3^{5-} in $Na_4Ba_3As_6$ (114.2° and 115.3°). Lower angles (101.9°) are in HT−$LaAs_2$ [72]. For comparison, the As–As–As angles in the infinite $[As^-]_n$ chain of KBa_2As_5 [140] are between 104° and 110° and are slightly smaller than in $K_3Ba_7(As_3)_3O$. In the arsenides Eu_4As_3 [141] and the isotypic Sr_4As_3 [142], both containing As_4^{6-} units, As–As–As angles of 115.8° and 116.3° are present. Within some limits, there is structural flexibility in the three-atomic arsenic chains.

The As_3^{5-} anions are surrounded solely by cations (Fig. 4.7). According to the local symmetry, the two independent As atoms have individual coordination polyhedral. Up to a limit of 4 Å, As(1) is surrounded by six Ba atoms, four Ba/K(2) and two Ba(1) in a trigonal prismatic fashion. As(2) has eight coordinating atoms, two K(1), two Ba(1) and four Ba/K(2) in form of a square antiprism. These polyhedra are connected via common square faces. In the unit cell, the polyhedra are stacked along the *c* axis. The highly charged As_3^{5-} ions are thus located in channels made up of Ba and K cations. Remarkably, neighbouring As_3^{5-} ions are not separated by empty polyhedra, instead all polyhedra are filled with As atoms. The closest contact is present between As(2) atoms in face-sharing square antiprisms. The distance (3.88 Å) is above the van-der-Waals radii, as mentioned above.

The other kind of anions in the structure are oxide anions. Analogous to the triarsenide anions, they are coordinated exclusively by cations. Six Ba/K(2) coordinate one O(1) atom in an almost undistorted octahedral fashion (Fig. 4.6). The six O(1)–Ba/K(2) bonds are of equal lengths (2.76 Å). The octahedron is slightly compressed, indicated by two different Ba/K(2)–O(1)–Ba/K(2) angles of 88.1° and 91.9°.
Fig. 4.8 depicts the extended unit cell of $K_3Ba_7(As_3)_3O$.

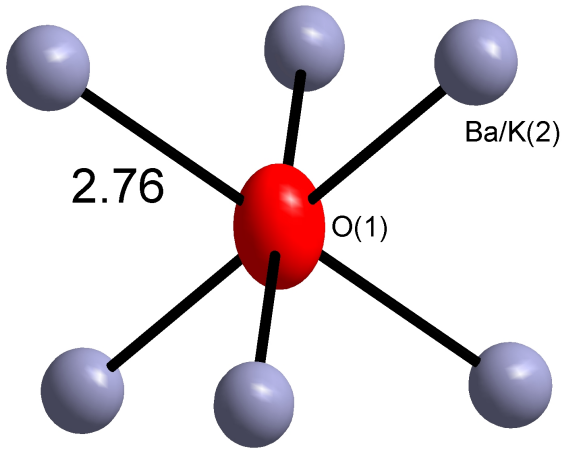

Figure 4.6: The coordination environment of the oxygen atom O(1) in the structure of $K_3Ba_7(As_3)_3O$. Atoms are drawn as displacement ellipsoids representing a probability density of 90 %. Bond lengths are given in Å.

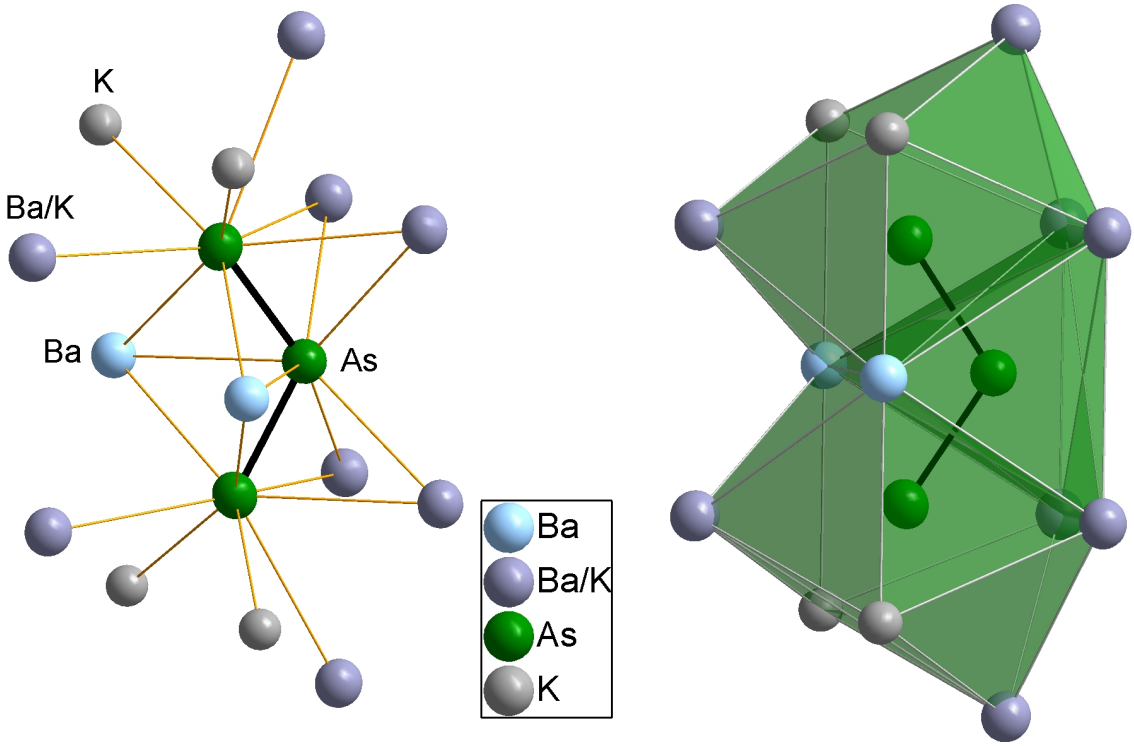

Figure 4.7: The coordination environment of the As_3^{5-} ion in the structure of $K_3Ba_7(As_3)_3O$. Left as a ball-stick model, right in a representation with interconnected polyhedra. Atoms are drawn as displacement ellipsoids representing a probability density of 90 %.

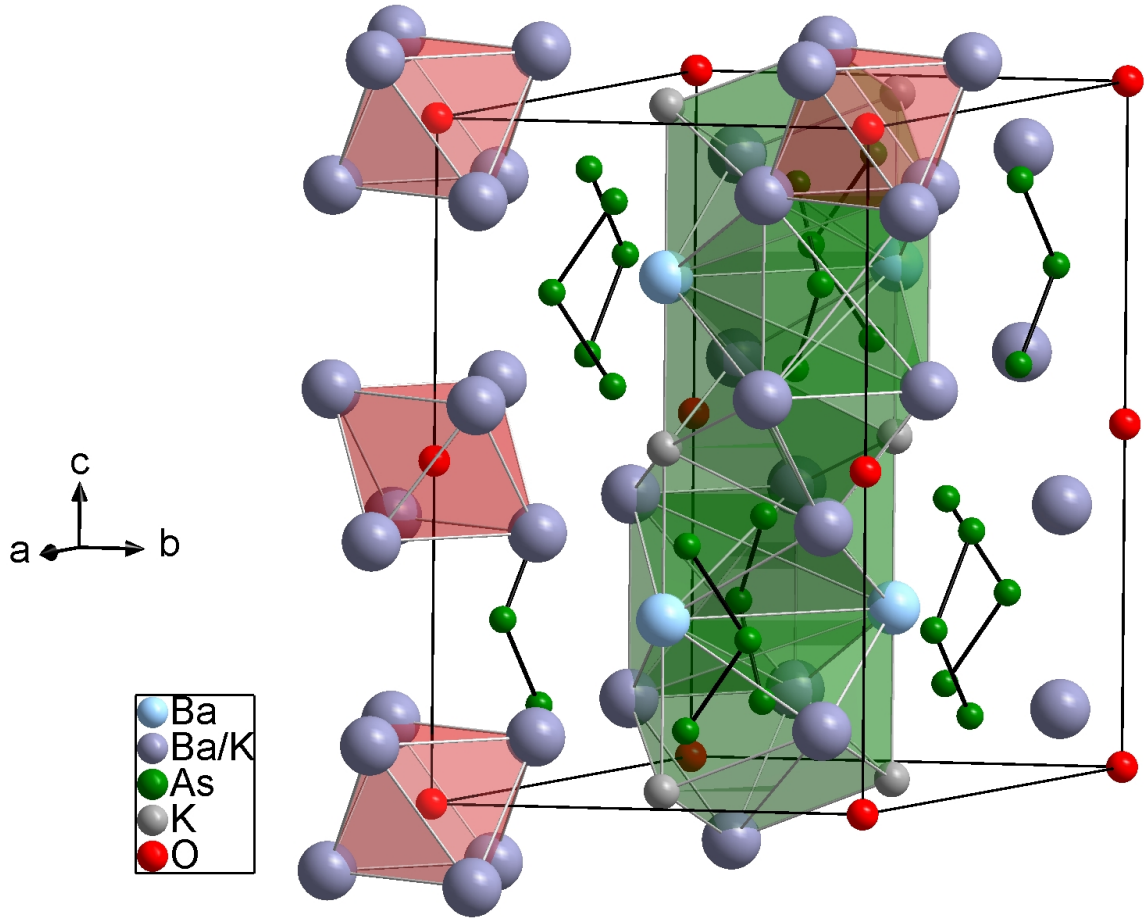

Figure 4.8: The unit cell of $K_3Ba_7(As_3)_3O$. Atoms are drawn as spheres of arbitrary radii. The coordination polyhedra of the As_3^{5-} and of the oxide ions are included.

4.1.3 Ba_3As_4

Ba_3As_4 [133] crystallises in the orthorhombic crystal system in the space group $Fdd2$ (No. 43), in the Sr_3As_4 structure type, which was first described by K. Deller and B. Eisenmann [142]. The lattice constants are $a = 15.3564(5)$ Å, $b = 18.7391(4)$ Å, $c = 6.2748(2)$ Å. The cell volume is $V = 1805.71(9)$ Å^3, the number of formula units is 8. Ba_3As_4 is a black brittle substance, which forms prismatic crystals. The substance is sensitive to air and moisture. Schnering published the cell parameters as early as 1984 [143], but he referred to unpublished data. The compound has not been registered in any database to this day. Since it originally appeared as a minor phase in the syntheses of Ba_3As_2O and $K_3Ba_7As_9O$, Ba_3As_4 was structurally characterised and will serve as a contribution to the phases in the Eu_3As_4 structure type in the context of this work.

The structure consists of As_4^{6-} chains embedded in a network of triangular prisms made up of the barium ions. There are two types of prisms, these are aligned parallel to each other or perpendicular to the prism three-fold axis. The prisms surrounding the arsenic chain are linked to each other via the square faces, and the neighbouring prisms are aligned either parallel or perpendicular to their three-fold axis of rotation, see Fig. 4.9. These columns are linked via the triangular faces of the prisms and thus form enantiomorphic polyhedra [141]. The Niggli formula can be expressed as ${}^3_\infty\{[AsBa_{6/8}]\}$. Due to this special linkage, 1/3 of all prisms are not occupied, compare Fig. 4.10. This results in a structure of the type $A_3B_4\square_2$. Thus, this structure can be derived from α-$ThSi_2$, as already described by Schnering [29]. In this AB_2 structure, all 16 prisms in the unit cell are occupied. Schnering describes the chain-like polyanions as fragments of the original three-dimensional infinite framework ${}^3_\infty\{Si\}$ in α-$ThSi_2$. The metric relationship between the unit cells is given by the matrix $Ba_3As_4 = (001, 330, \bar{1}10)$ α-$ThSi_2$. The Bärnighausen tree shown in Fig. 4.13 depicts the symmetry relationship to the α-$ThSi_2$ aristotype:
($ThSi_2$) $I4_1/amd \,-(\mathrm{t2})\rightarrow\, I2/a1d \,\hat{=}\, Fddd \,-(\mathrm{t2})\rightarrow\, Fdd2 \,-(\mathrm{k3})\rightarrow\, Fdd2$ (Ba_3As_4). In general, the α-$ThSi_2$ type is suitable as an aristotype of defect structures in which the metal atoms form trigonal prisms and finite polyanion chains are incorporated into them [144].

The As_4^{6-} chains consist of four As atoms with bond lengths d(As(1)–As(2)) = 2.46 Å for the terminal bond and d(As(2)–As(2')) = 2.55 Å for the central bond. The bond angles between the As atoms are 118.6°, the torsion angle is 86.8°. In comparison with the other two arsenic-containing compounds in the same structure type (Table 4.1), no particularly large deviations are noticeable. The angles between the arsenic

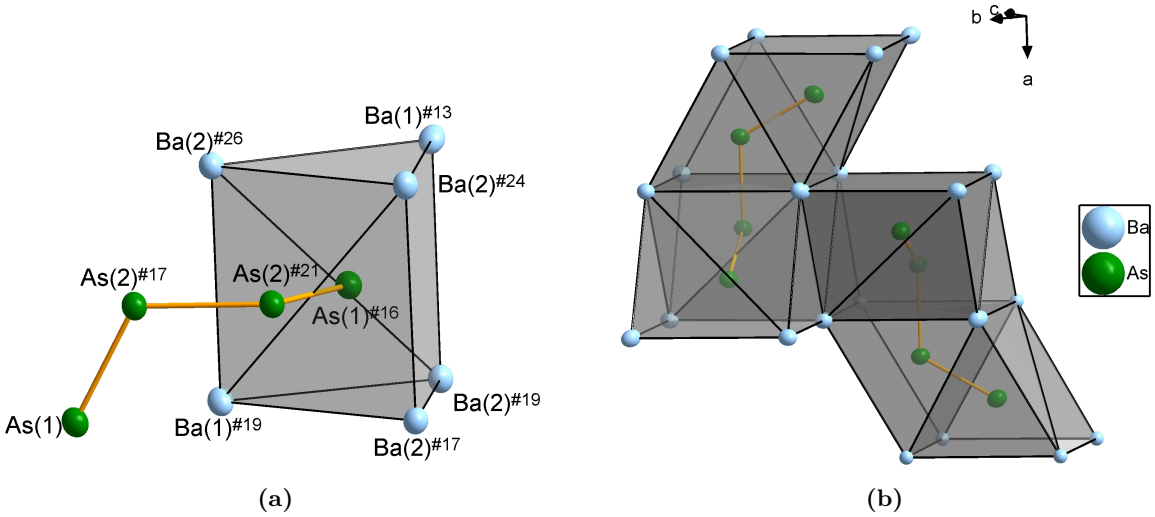

(a) (b)

Figure 4.9: (a) Representation of the arsenic chain As_4^{6-} in the structure of Ba_3As_4. The trigonal prismatic environment of the arsenic atoms is shown for one terminal arsenic atom of the chain. Indices indicate the following symmetry operations: #13: -x+3/4,y+1/4,z-1/4; #16: -x+1,-y,z; #17: -x+1,-y+1,z; #19: x+1/2,y,z-1/2; #21: x,y+1,z; #24: x+1/2,y,z+1/2; #26: x+1/4,-y+1/4,z+1/4. (b) The prisms surrounding the arsenic chain are linked to each other via the square faces. These columns are linked via the triangular faces of the prisms and form enantiomorphic polyhedra. The displacement ellipsoids represent a probability of 90 %.

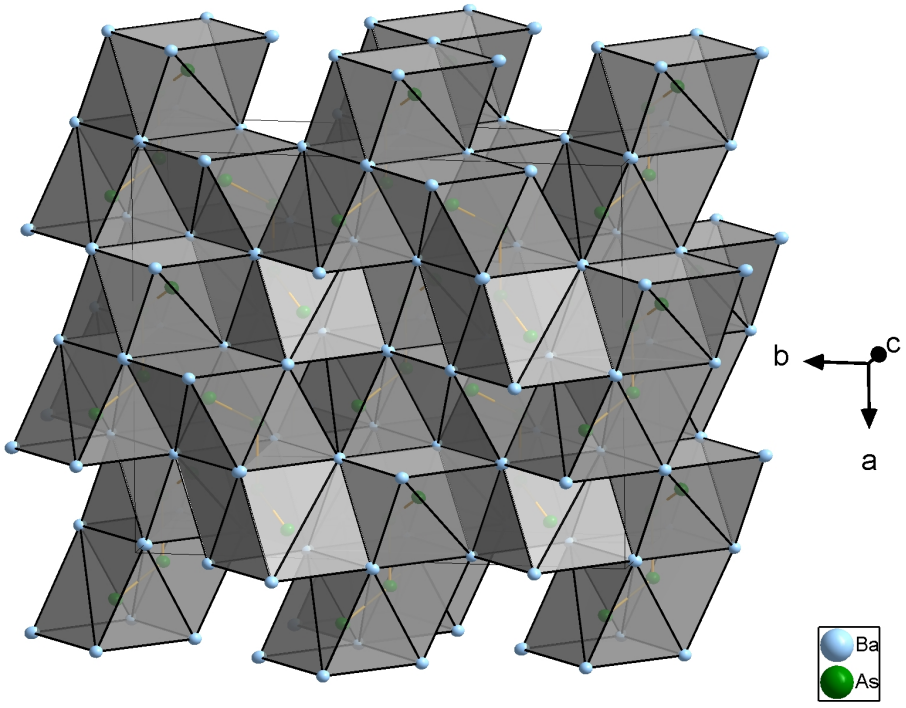

Figure 4.10: Extended unit cell of Ba_3As_4 with trigonal prismatic coordination polyhedra around the arsenic atoms. The structure can be derived from the α-$ThSi_2$-type. Ellipsoidal representation with a probability density of 90 %.

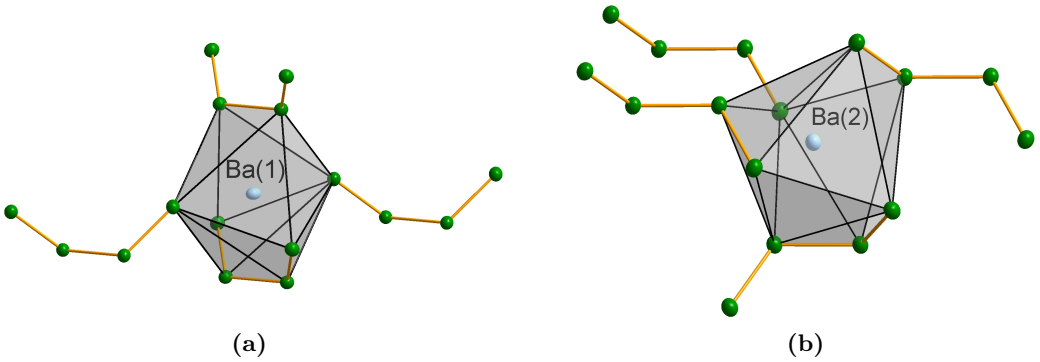

Figure 4.11: (a) Representation of the irregular coordination polyhedron around Ba(1). (b) Representation of the irregular coordination polyhedron around Ba(2). The displacement ellipsoids represent a probability of 90 %

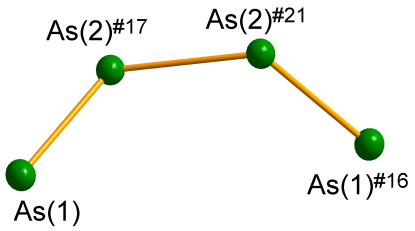

Figure 4.12: As_4^{6-} chain in compounds of the Eu_3As_4-structure type. Indices indicate the following symmetry operations: #16: -x+1,-y,z; #17: -x+1,-y+1,z; #21: x,y+1,z. The displacement ellipsoids represent a probability of 90 %

	Eu_3As_4 [143]	Sr_3As_4 [142]	Ba_3As_4
d(As1–As2) / Å	2.47	2.48	2.46
d(As2–As2') / Å	2.56	2.55	2.55
As–As–As / °	115.9	116.2	118.6
torsion / °	86.1	86.0	86.8
$d(M–M)^*_m$ / Å	4.16	4.22	4.42

Table 4.1: Average bond lengths, angles and torsion angles in compounds of the Eu_3As_4 type with As_4^{6-} tetraarsenide chains. * Mean, shortest cation distances d(M-M) (M = Eu, Sr, Ba) in the trigonal prismatic coordination of the arsenic atoms.

atoms increase with increasing radius of the cations. This is due to the increasing volume of the trigonal prismatic coordination polyhedron and the increasing distance d(M–M) in the series M = Eu, Sr, Ba.

The elongated As–As bond occurs where the trigonal Ba_6 prisms change the orientation of their three-fold axes. In the Si framework of α-$ThSi_2$, torsion angles of 0°, 90° and 180° occur at the Si–Si bonds. This applies to the arsenic chain formed by the defects, as can be seen from the torsion angles in Table 4.1, which are ≈ 86°. This is related to the orientation of the stretched central bond of the As_4 chains along the a-axis and, respectively, along the tetragonal c-axis of α-$ThSi_2$. The irregular coordination polyhedra (Fig. 4.11) are directly related to the 12-fold coordination in the α-$ThSi_2$ structure. The coordination polyhedra in Ba_3As_4 are a combination of tetragonal disphenoid and tetragonal prism. Here, the two barium positions are surrounded by 8 arsenic atoms each at a distance of 3.26 Å to 3.46 Å. In summary, the ordering of

the defects leads to the orientation of the As_4 chains and breaks the tetragonal symmetry. This ordering of the defects leads to a different packing and ultimately to the triplication of the $ThSi_2$ cell along the b-axis. This can be expressed by a sum formula including the defects: $ThSi_2 \times 3 = Th_3Si_6 \rightarrow Ba_3As_4\square_2$.

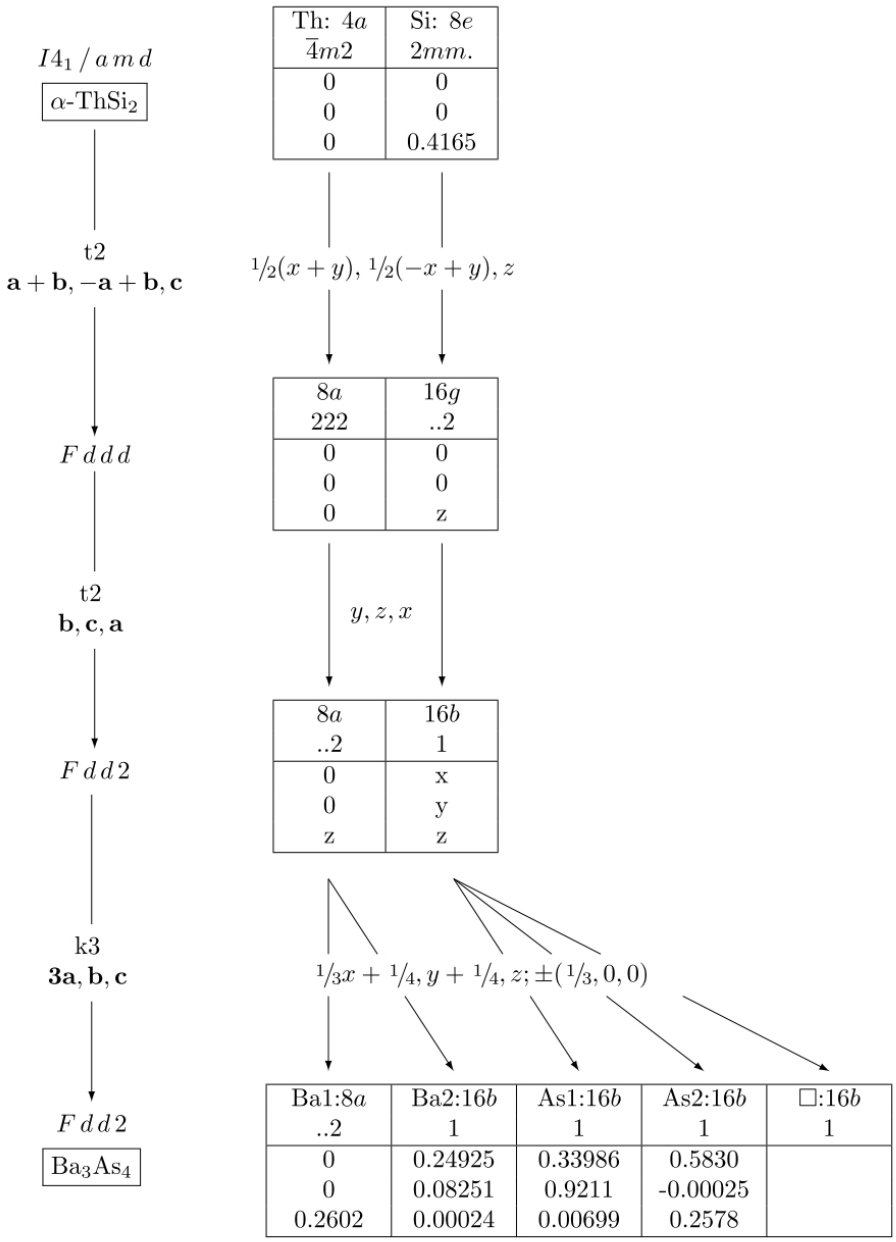

Figure 4.13: The Bärnighausen tree showing the symmetry relationship between Ba_3As_4 to the α-$ThSi_2$ aristotype. This can be expressed by a sum formula including the defects: $ThSi_2 \times 3 = Th_3Si_6 \rightarrow Ba_3As_4\square_2$.

4.1.4 $[Eu(NH_3)_8]_2[Eu(NH_3)_3(As_7)_2]$

Figure 4.14:
Black crystal of $[Eu(NH_3)_8]_2[Eu(NH_3)_3(As_7)_2]$ mounted on a glass capillary. Crystal dimensions are 0.130 × 0.084 × 0.026 mm^3.

$[Eu(NH_3)_8]_2[Eu(NH_3)_3(As_7)_2]$ forms black prismatic crystals (Fig. 4.14) and crystallises in the orthorhombic space group *Pccn* in a yet unknown structure type. The lattice parameters of the unit cell are $a = 32.3385(10)$ Å, $b = 9.1345(3)$ Å, $c = 12.9713(4)$ Å. The volume of the unit cell is $V = 3831.7(2)$ Å^3, the number of formula units is 4. The dataset contained 51411 reflections from which 8457 were unique. The quality factor R_{int} on averaging symmetry equivalent reflections amounted to 12.39 %.

In the structure of $[Eu(NH_3)_8]_2[Eu(NH_3)_3(As_7)_2]$, two crystallographically non equivalent europium cations and a heptaarsenide anion As_7^{3-} are present. Both europium cations form ammine complexes. Only ammonia ligands are present in the ligand sphere of Eu(1). Eu(2) has two heptaarsenide anions in its ligand sphere in addition to three ammonia molecules. Considering the different ligand spheres of the Eu^{2+} cations, the composition of the compound is as follows: $[Eu(NH_3)_8]_2[Eu(NH_3)_3(As_7)_2]$.

The structure is built up from $^1_\infty\{[Eu(NH_3)_3(As_7)_{2/2}]^{4-}\}$ strands. These strands run along the crystallographic *c*-axis and are separated from each other by the homoleptic octaammine complexes $[Eu(NH_3)_8]^{2+}$(Fig. 4.16).

The structure is built up of As_7^{3-} anions stacked along the crystallographic *c*-axis, which are connected via europium(II) cations. Eu(2) is linked via the atoms As(2), As(4), As(5), As(7) forming a η^4-coordination and the symmetry-generated atoms As(3)$^{\#1}$ and As(4)$^{\#1}$, see Figure 4.15. As(2), As(4), As(3)$^{\#1}$ and As(4)$^{\#1}$ are facing Eu(2). These arsenic atoms have two homonuclear bonds. The electron density is highest at these arsenic atoms, which is expressed in the short distance between the arsenic atoms with two homonuclear bonds and europium. Coordination across the square face formed by As(3)$^{\#1}$, As(4)$^{\#1}$, As(6)$^{\#1}$, As(7)$^{\#1}$ would have been conceivable as a second η^4 coordination to Eu(2), but the gap in bond lengths between 3.75 Å and 3.87 Å is clearly evident. For this reason, only As(3)$^{\#1}$ and As(4)$^{\#1}$ should be considered to take part in the coordination. The bond distances of Eu(2)–As to the arsenic atoms with two homonuclear bonds are significantly shorter than towards the As atoms with three homonuclear bonds. The electron density is enhanced at the arsenic atoms with two homonuclear bonds, which has a direct effect on the bond distance to the Eu(2) atom. The shortest bond distance is Eu(2)–As(2) with 3.18 Å, followed by

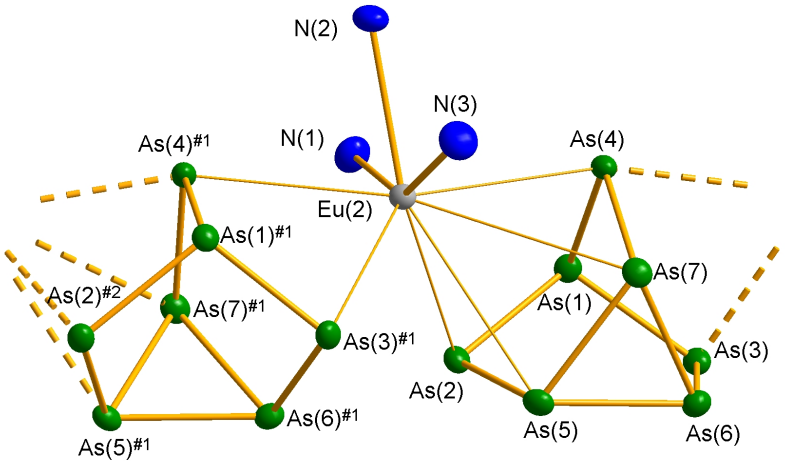

Figure 4.15: The europium atom Eu(2) is coordinated by two As_7^{3-} anions. Eu(2)–As bond lengths are shown up to 3.75 Å. The displacement ellipsoids represent a probability of 50 %. Symmetry transformations used to generate equivalent atoms: #1: -x+3/2,-y+1/2,z.

As(3)$^{\#1}$, As(4) and As(4)$^{\#1}$ with 3.21 Å, 3.25 Å and 3.32 Å, respectively. The distances towards As(5) and As(7) are significantly longer with 3.71 Å and 3.75 Å. The As(1) from the same molecule has an even longer distance to Eu(2) with 3.98 Å. The side of the heptaarsenide anion facing Eu(2) forms a five-membered ring. The anion does not offer a planar surface, which finds it's expression in the large distance from Eu(2) to As(1). The distances to As(6)$^{\#1}$ and As(7)$^{\#1}$, shown in Fig. 4.15 in the left As_7^{3-} anion, are again much longer with 3.87 Å and 3.90 Å. The longest Eu-As distance is to the As(1)$^{\#1}$ atom with 3.99 Å. The symmetry-related atoms As(1) and As(1)$^{\#1}$ form the point where the three five-membered rings of the anion converge and therefore, due to geometry, have the longest distances to Eu(2). The Eu(2)–N bond distances range from 2.69 Å to N(1) to 2.75 Å to N(3). The coordination is analogously assigned in the structure of $Ba_3P_{14}\cdot 18\,NH_3$ as a η^4 coordination [145]. In addition, arsenic atoms are present in the extended coordination. There is a clear gap between the bond lengths Eu(2)–As(7) and Eu(2)–As(5)$^{\#1}$, or Eu(2)–As(7)$^{\#1}$. A cut is therefore made at this point. Since the five-membered ring of the As_7^{3-} is not planar, this η^4 coordination results, as already observed in the related compound $Ba_3P_{14}\cdot 18\,NH_3$ by Korber and Daniels [145]. Other coordinations through the As_7^{3-} anion are conceivable, but a coordination involving the arsenic atoms with two homonuclear bonds is always preferred, as in this case.

The coordination sphere of Eu(1) is filled exclusively by ammonia molecules, forming a homoleptic octaammine complex $[Eu(NH_3)_8]^{2+}$ with a distorted square-antiprismatic arrangement (Fig. 4.17). The Eu-N bonds range from 2.73 Å to 2.79 Å. So far, two

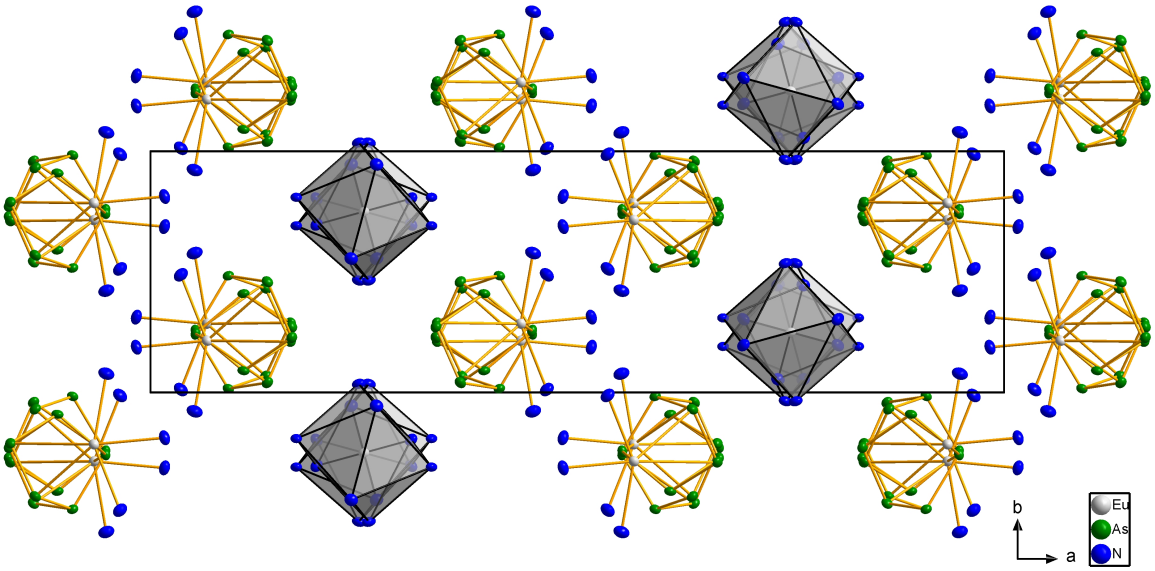

Figure 4.16: Section of structure of $[Eu(NH_3)_8]_2[Eu(NH_3)_3(As_7)_2]$; projection onto the a-b plane. $^1_\infty\{[Eu(NH_3)_3(As_7)_{2/2}]^{4-}\}$ strands run along the crystallographic *c*-direction separated by $[Eu(NH_3)_8]^{2+}$ cations (grey polyhedra). The displacement ellipsoids represent a probability of 50 %.

octaammine lanthanide complexes $M(NH_3)_8^{2+}$ (M = Eu, Yb) are known from the compounds $[M(NH_3)_8]I_2$ [146], obtained from $M(NH_2)_2$ (M = Eu, Yb) and NH_4I in liquid ammonia. The compounds $[M(NH_3)_8]I_2$ (M = Eu, Yb) crystallise isotypic to the compounds $[Ca(NH_3)_8]X_2$ (X = Br, I) [147] in the orthorhombic crystal system, space group *Pnma* and belong to the $[Ca(NH_3)_8]Cl_2$ [148] or $[Sr(NH_3)_8]Cl_2$ [149] structure type. In $[M(NH_3)_8]I_2$ (M = Eu, Yb) the metal centre is double-capped trigonally prismatic surrounded by ammonia molecules. In $[Eu(NH_3)_8]_2[Eu(NH_3)_3(As_7)_2]$, the homoleptic complex $[Eu(NH_3)_8^{2+}]$ is coordinated square-antiprismatically. A consideration of the angular difference supports this description. In 1995, Haigh established criteria to simplify the assignment of the coordination polyhedra of eightfold-coordinated complexes [150]. For this purpose, all the angles L–M–L between ligands are listed from the largest to the smallest in increasing order. The smallest angles within the coordination polyhedron are considered as well. One of Haigh's criteria states that if the difference between the 16th and 17th lowest L–M–L' angles is more than 20°, the structure is square-antiprismatic. The difference between the 16th and 17th lowest angle in this case is 25.77° (Table 4.2). According to Haigh, a difference greater than 20° corresponds to square-antiprismatic coordination, with the ideal angle being 27.24°. The gap between the 12th and 13th smallest angle is considered as well. The difference is 2.58°. As such, Haigh's criteria for a quadratic antiprismatic coordination are therefore fulfilled. Thus, the point symmetry is closer to D_{4d}, instead of the point symmetry of an ideal double-capped trigonal prism with C_{2v} symmetry. The SHAPE software

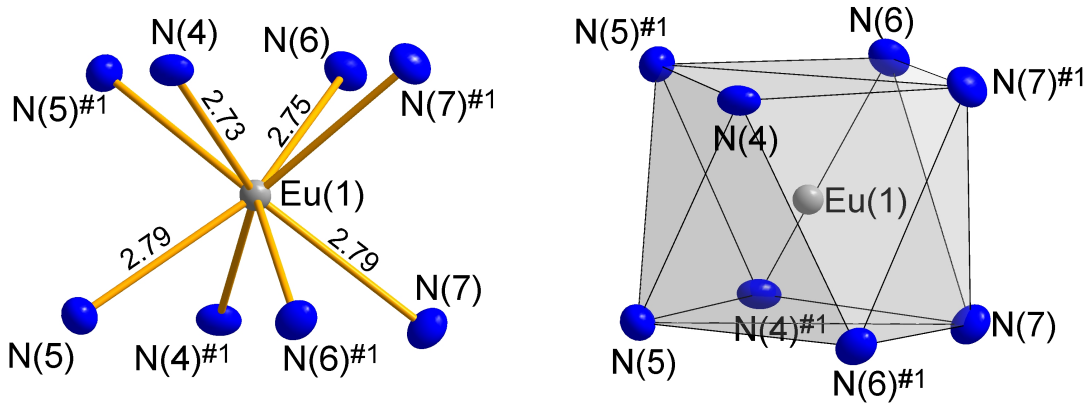

(a) (b)

Figure 4.17: (a) Bond length (in Å) in the coordination polyhedron of Eu(1). Symmetry transformations used to generate equivalent atoms: #1: -x+3/2,-y+1/2,z. (b) Square-antiprismatic environment of the Eu(1) atom by eight ammonia molecules. The displacement ellipsoids represent a probability of 50 %. Bond lengths in Å. Symmetry transformations used to generate equivalent atoms: #1: -x+3/2,-y+1/2,z.

[136] was used to calculate the deviation from the ideal square-antiprismatic coordination. The program calculates deviations from the ideal polyhedron by the method of Continuous Symmetry Measures [135] of polyhedral structures. The calculation with SHAPE results in a deviation from the ideal square antiprism of 0.7 %, for the ideal double-capped trigonal prism the calculation results in a value of 2.9 %. The energy difference of these two isomers was calculated by Blight and Kepert for $ML_4(L{-}L)_2$ complexes [151]. They concluded that the very similar energies of these isomers make it impossible to predict which one is preferred in a given situation. Other energy conditions such as crystal field stabilisation, covalent bonds and crystal packing or solvation forces must be taken into account [151].

Table 4.2: Selected bond lengths and angles of the environment of Eu(1) for $[Eu(NH_3)_8]_2[Eu(NH_3)_3(As_7)_2]$. Symmetry transformations used to generate equivalent atoms: #1: -x+3/2, -y+1/2 ,z.

No.	Atoms 1, 2	Angle / °	Atoms 1, 2	Distance / Å
1	N(6)-Eu(1)-N(5)#1	68.48(15)	Eu(1)-N(4)#1	2.727(5)
2	N(6)#1-Eu(1)-N(5)	68.48(15)	Eu(1)-N(4)	2.727(5)
3	N(4)#1-Eu(1)-N(7)	69.09(16)	Eu(1)-N(6)#1	2.750(5)
4	N(4)-Eu(1)-N(7)#1	69.09(16)	Eu(1)-N(6)	2.750(5)
5	N(6)#1-Eu(1)-N(7)	69.53(15)	Eu(1)-N(5)#1	2.784(5)
6	N(6)-Eu(1)-N(7)#1	69.53(15)	Eu(1)-N(5)	2.784(5)
7	N(4)-Eu(1)-N(5)#1	75.75(15)	Eu(1)-N(7)	2.790(5)
8	N(4)#1-Eu(1)-N(5)	75.75(15)	Eu(1)-N(7)#1	2.790(5)
9	N(4)#1-Eu(1)-N(5)#1	79.92(16)		
10	N(4)-Eu(1)-N(5)	79.92(16)		
11	N(4)#1-Eu(1)-N(6)	80.31(15)		
12	N(4)-Eu(1)-N(6)#1	80.32(15)		
13	N(5)#1-Eu(1)-N(5)	82.9(2)		
14	N(7)-Eu(1)-N(7)#1	83.3(2)		
15	N(6)-Eu(1)-N(7)	83.93(15)		
16	N(6)#1-Eu(1)-N(7)#1	83.93(15)		
17	N(5)-Eu(1)-N(7)	109.70(16)		
18	N(5)#1-Eu(1)-N(7)#1	109.70(16)		
19	N(4)#1-Eu(1)-N(6)#1	109.84(15)		
20	N(4)-Eu(1)-N(6)	109.84(15)		
21	N(4)-Eu(1)-N(7)	140.98(16)		
22	N(4)#1-Eu(1)-N(7)#1	140.98(16)		
23	N(5)-Eu(1)-N(7)#1	141.53(16)		
24	N(5)#1-Eu(1)-N(7)	141.54(16)		
25	N(6)#1-Eu(1)-N(6)	144.5(2)		
26	N(6)#1-Eu(1)-N(5)#1	145.43(15)		
27	N(6)-Eu(1)-N(5)	145.43(15)		
28	N(4)#1-Eu(1)-N(4)	147.4(2)		

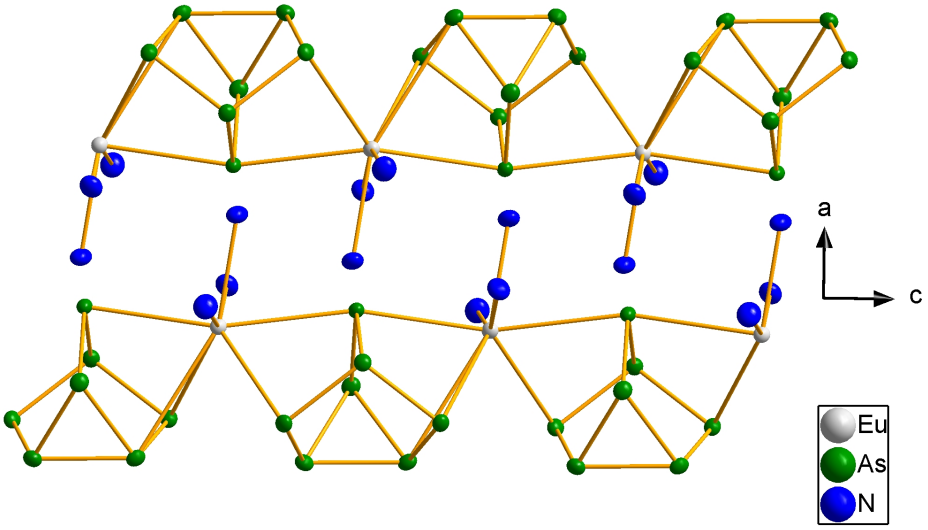

Figure 4.18: Interlocking of the Eu-As_7 chains viewed from the *b*-direction. The displacement ellipsoids represent a probability of 50 %.

The chains resulting from the linked As_7^{3-} are interlocked with an oppositely oriented chain of linked heptaarsenides, see Figure 4.18. The inversion centres lie on the Wyckoff position 4*a* on $(0,0,0);(1/2,1/2,0);(0,1/2,1/2);(1/2,0,1/2)$. The chains, which are linked in the crystallographic *c*-direction via Eu(II), are aligned alternately in an offset manner, or can be mapped onto each other by the inversion centre on 4*a*.

In the *b*-direction, the chains are mutually aligned and offset by 1/2. The interlocking of the chains by the ammonia can be observed from the top view along the chains (compare Fig. 4.16 and Fig 4.18), since N(2) points between two of the opposite chains. The centres of inversion lie between each of the diagonally opposite chains. N(1) and N(3) are each aligned with adjacent chains. The interlocking is given by the linking Eu(II) atom. This is surrounded by three ammonia molecules, which in turn are aligned towards the As(6) atom of the opposite chain. If the $[Eu(NH_3)_8^{2+}]$ polyhedra stacked along the *c*-axis are seen together as a rod, a hexagonal rod stacking results as the overall motive of this crystal structure with the ${}^1_\infty\{[Eu(NH_3)_3(As_7)_{2/2}]^{4-}\}$ chains, which run along the crystallographic *c*-axis.

Structural Comparison of the As_7^{3-} Anion in $[Eu(NH_3)_8]_2[Eu(NH_3)_3(As_7)_2]$ with Ammoniates Containing As_7^{3-} Anions

The ideal As_7^{3-} cluster has C_{3v} symmetry and can be viewed as a As_4 tetrahedron with three bridged edges, see Figure 4.19. "The bonding lengths in all ionic nortricyclane-cages show a characteristic distribution of three types of bonds, with $A > C > B$. The bonds A are defined by the three atoms of the triangular base, bonds B are those between the base atoms and the bridging atoms, and C refers to the bonds between the bridging atoms and the apical atom. The ratio $Q = H/A_m$ [152], where H is the height of the anion (from the base of the apical atom) and A_m is mean value of distances A, typically lies between 1.31 and 1.35 for ionic nortricyclane-like systems, in contrast to 1.42 for neutral, covalently substituted cages [104]."[101]

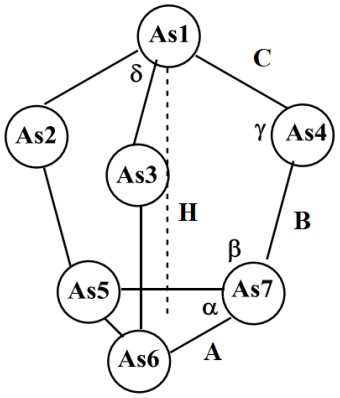

Figure 4.19: Structure of an 'ideal' As_7^{3-} cage anion. Three distances A, B, C and the height H of the cage are indicated.

When comparing the cage anion (Table 4.3), it can be seen that the height of the anion in $[Eu(NH_3)_8]_2[Eu(NH_3)_3(As_7)_2]$ is significantly lower with 3.33 Å than in the cage anion in Ba_3As_{14} (3.38 Å) [84]. Ba_3As_{14} was the first compound discovered to contain the cluster ion As_7^{3-} and was obtained in 1977 by Schmettow and Schnering by reaction of the elements Ba:As = 1:4-5 at 1000 K to 1100 K.

Complexation by ammonia leads to a more diffuse charge distribution in the cation Eu(1) as well as in the complex cation $[Eu(NH_3)_8]^{2+}$. This results in weaker Eu–As interactions in $[Eu(NH_3)_8]_2[Eu(NH_3)_3(As_7)_2]$, with the negative charges being more localised on the homonuclear divalent arsenic atoms. This leads to the compression of the cage, as As2, As3 and As4 distance from each other. The same behaviour can be observed in similar heptaarsenides obtained from solution, which exhibit comparable spatial arrangements in the crystal lattice. The structures used here for comparison are from Hanauer and Korber [101]. In $[Li(NH_3)_4]_3As_7{\cdot}NH_3$ (**2**), there is no direct contact between the cations Li^+. In $[Rb(18\text{-crown-}6)]_3As_7{\cdot}8\,NH_3$ (**3**), the rubidium cation is complexed by the crown ether. In addition, the Rb^+ coordinates to the two-bonded As in As_7^{3-}. $Cs_3As_7{\cdot}6\,NH_3$ (**4**) and $(Ph_4P)CsAs_7{\cdot}5\,NH_3$ (**5**) have direct contacts to the metal cation Cs^+. In compound **4**, these contacts lead to a framework structure. In $(Ph_4P)CsAs_7{\cdot}5\,NH_3$ (**5**), the presence of the large, non-coordinating Ph_4P^+ reduces the number of contacts between Cs^+ and As_7^{3-} ions, resulting in one-dimensional zig-zag

$^{1}_{\infty}\left\{[Cs(As_7)]^{2-}\right\}$ chains. Furthermore, in **5**, the heptaarsenide is coordinated from two sides by the metal ion.

	1 [84]	**2** [101]	**3** [101]	**4** [101]	**5** [101]	**6** (this work)
A_m / Å	2.498	2.50	2.524	2.515	2.522	2.487
B_m / Å	2.399	2.34	2.361	2.343	2.351	2.360
C_m / Å	2.431	2.4	2.421	2.404	2.424	2.407
δ_m / °	101.2	101.1	101.6	101.3	101.1	101.3
γ_m / °	99	99.5	99	99.5	99.4	99.3
β_m / °	105.6	105	105.2	104.9	105.1	105.2
H / Å	3.3789(4)	3.318(3)	3.3329(7)	3.320(1)	3.3395(5)	3.3318(6)
$Q = H/A_m$	1.35	1.33	1.32	1.32	1.31	1.34

Table 4.3: Average distances and angles in the As_7^{3-} units of compounds **1-6**. Compounds: Ba_3As_{14} (**1**), $[Li(NH_3)_4]_3As_7{\cdot}NH_3$ (**2**), $[Rb(18\text{-crown-6})]_3As_7{\cdot}8\,NH_3$(**3**), $Cs_3As_7{\cdot}6\,NH_3$ (**4**), $(Ph_4P)CsAs_7{\cdot}5\,NH_3$ (**5**), $[Eu(NH_3)_8]_2[Eu(NH_3)_3(As_7)_2]$ (**6**).

4.1.5 Rb_2AuAs_7

Figure 4.20: Black rod-shaped crystals of the new compound Rb_2AuAs_7 inside the reaction ampoule.

The compound Rb_2AuAs_7 [153] crystallises as black rods in the monoclinic crystal system in the space group $I2/a$ (No. 15) in a new structure type. The lattice parameters of the unit cell are $a = 7.4747(3)$ Å, $b = 12.6250(6)$ Å, $c = 12.0006(6)$ Å with the monoclinic angle of $\beta = 92.449(3)°$. The volume of the unit cell is $V = 1131.44(9)$ Å^3, the number of formula units is 2. Figure 4.20 shows the black crystals that grow rod-shaped inside the reaction ampoule. The substance is sensitive to air and moisture.

Rb_2AuAs_7 consists of cross-linked heptaarsenide anions with four independent arsenic atoms. The negative charge can be localised at the two-bonded arsenic atoms As(3), As(3)#2 and As(4), as can be seen in Fig. 4.21. A three-dimensional structure is formed by the formation of linear As–Au–As bridges (Fig. 4.22) between two adjacent $^1_\infty[As_7^{3-}]$ chains via the free bonding sites of the As(3) and its symmetry-equivalent generated atoms. This chain-like structure with the bridging gold atoms creates large cavities within the unit cell. The rubidium cations are embedded in these cavities to balance the charge (Figure 4.22).

When the entire structure is viewed along the c-axis (Fig. 4.22, right side), it can be seen that the polyanions are offset from each other by $^1/_2$ in a-direction. This perspective shows that the individual chains from one layer do not bind to each other, but are indirectly connected via the layer above and below via linear As–Au–As coordination. This results in an alternating sequence of anion and cation tunnels within the crystal, which make up an entire network. Finally, the binding situation of the gold atoms should be discussed. For this purpose, The Au–As bonds are compared with the known structure data of Na_2AuAs [154] and K_5AuAs_2 [155]. Table 4.4 compares the bond angles and bond lengths. The structural parameters are in good agreement with the literature values.

The comparison shows that the bonds of the new structure lie in the typical range of Au–As bonds. The As–Au–As bond angle shows the characteristic linear coordination behaviour for monovalent gold. It can be concluded, that in the Rb_2AuAs_7 structure the Au atom is present in the +I oxidation state. The displacement ellipsoid of gold

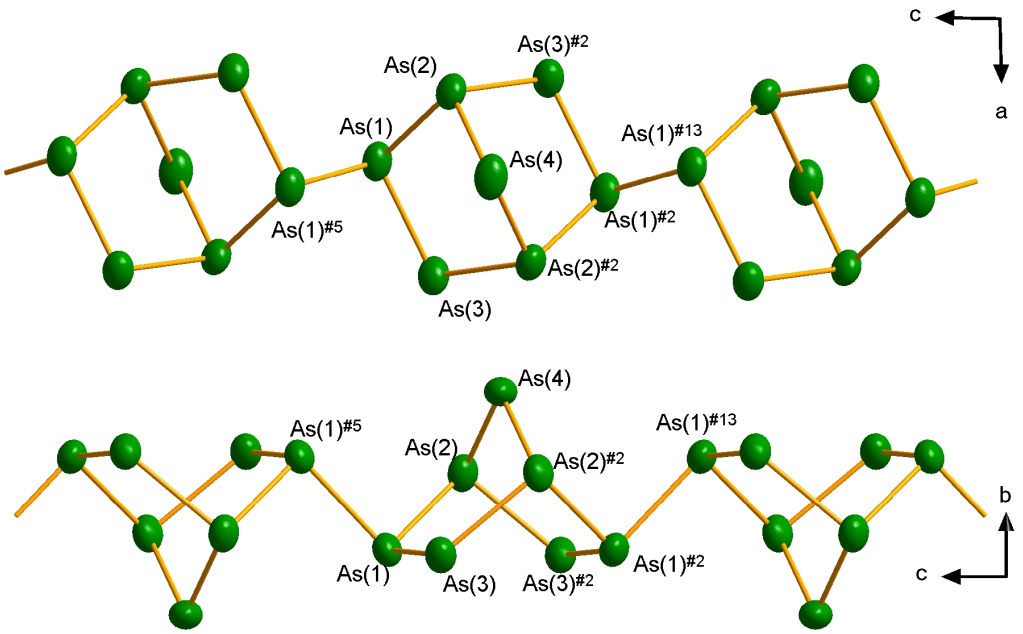

Figure 4.21: Section of the chains $^1_\infty[As_7^{3-}]$ in the structure of Rb_2AuAs_7. Two different views are given, both perpendicular to the *c*-axis. The displacement ellipsoids represent a probability of 90 %. Indices indicate the following symmetry operations: #2: -x+1/2,y,-z+1; #5: -x+1/2,-y+1/2,-z+3/2; #13: x,-y+1/2,z-1/2.

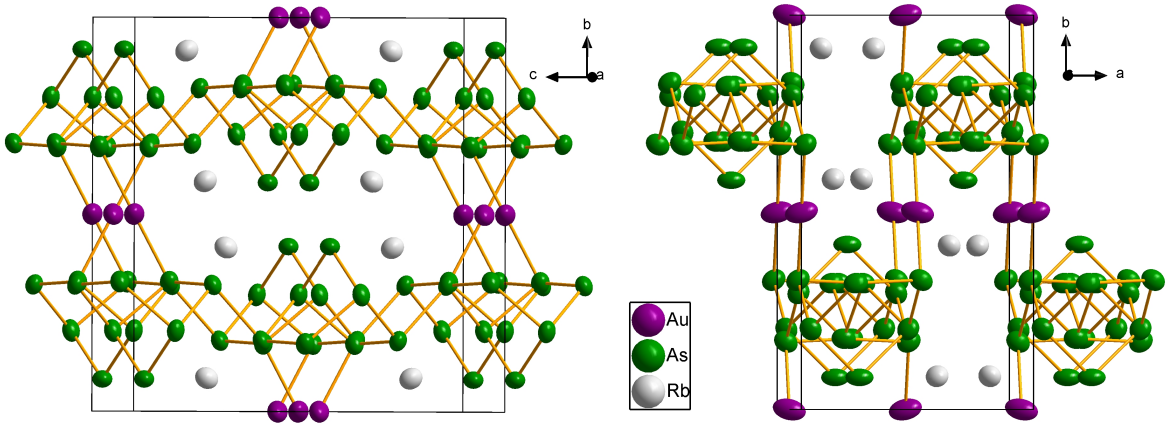

Figure 4.22: Extended unit cell of Rb_2AuAs_7 in a projection slightly tilted along the crystallographic *a*-axis (left) and along the crystallographic *c*-axis (right). The individual chains of $^1_\infty[As_7^{3-}]$ are linearly linked via gold atoms to form a three-dimensional structure with large cavities. The layers of the arsenic chains are offset by 1/2 in *a*-direction, resulting in a hexagonal tube stacking parallel to the *c*-axis. These cavities are occupied by rubidium to balance the charge. The displacement ellipsoids represent a probability of 90 %.

	Na_2AuAs	K_5AuAs_2	Rb_2AuAs_7
Bond length (Au–As)	2.501 Å	2.459 Å	2.451 Å
Bond angle (As–Au–As)	179.90°	180.00°	180.00°

Table 4.4: Comparison of bond lengths and angles in different alkali gold arsenides.

is aligned in the direction of the polyanions above and below and avoids displacement in direction of the positively charged rubidium atoms (Fig. 4.23, left side). Figure 4.22 (left) shows the unit cell as seen along the *a*-axis. Here, the linear structure of the As–Au–As bonds can be seen once more. The figure shows the alternating behaviour of the polyanions. It is striking that the apical As atoms or the square bases of the heptaarsenide are always opposite each other.

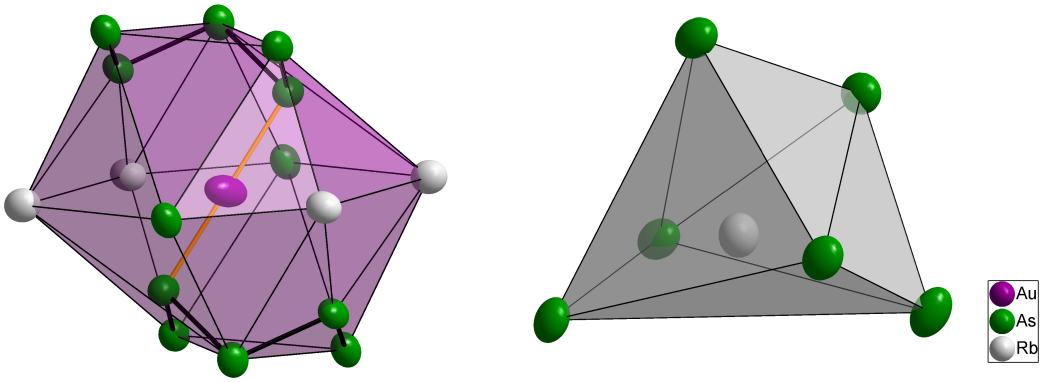

Figure 4.23: (Left) Coordination sphere up to 4.5 Å of gold in the structure of Rb_2AuAs_7. The displacement ellipsoid of gold is aligned in the direction of the polyanions above and below and avoids the positively charged rubidium atoms. (Right) The coordination sphere of rubidium up to 3.7 Å can best be described as a distorted trigonal prism. The displacement ellipsoids represent a probability of 90 %.

The coordination sphere of rubidium up to 3.7 Å does not make up a regular polyhedron. The depicted polyhedron can best be described as a distorted trigonal prism. The SHAPE software [136], which is a program for calculating Continuous Shape Measures of polyhedral structures, was used to calculate the deviation from the ideal polyhedron. The deviation from the ideal trigonal prism is 6.4 %. Four arsenic atoms span the base while two more are located on this base and thus span the trigonal prism in which rubidium is located. The structural motif of the arsenic chains and their linkage by gold atoms do not allow for a highly symmetrical cavity. The rubidium ion with its large radius of 1.66 Å (CN 6) [58] is classified as a soft base according to the HSAB concept and is located in this cavity, compensating the negative charge.

For arsenic no higher condensates of As_7 units have been described so far, except for As_{14}^{4-} [80]. However, for the lighter homologous phosphorus, one-dimensional infinite condensates of P_7 units are present. The anion in CsP_7 [87] can be interpreted as

condensates of P_7^{3-} cages. Each cage forms a bond with the neighbouring cage, resulting in the $^1_\infty[P_7^{1-}]$ anion (Fig. 4.24). In contrast to $^1_\infty[As_7^{3-}]$, the three-membered ring of the Pn_7 cage remains intact, since the links are located between two of the formerly double-bonded P atoms. The negative charge is localised on the remaining P atom with two homonuclear bonds. An $^1_\infty[P_7^{3-}]$ anion has not been detected so far. A detailed comparison of the $^1_\infty[As_7^{3-}]$ with the discrete As_7^{3-} anion is discussed in Subsection 4.1.5.

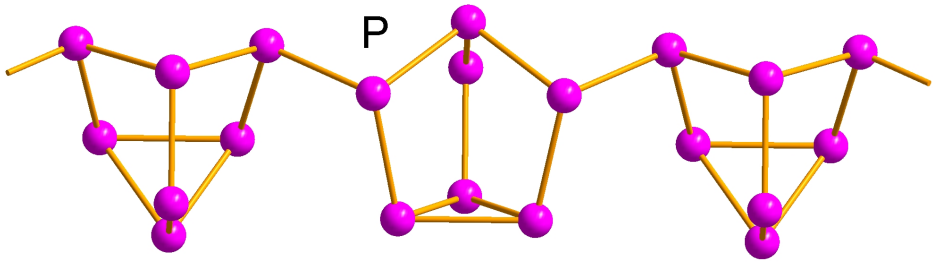

Figure 4.24: Section of the polymeric $^1_\infty[P_7^{1-}]$ in CsP_7.

Structural Comparison of the Polymeric $^1_\infty[As_7^{3-}]$ with the Discrete As_7^{3-} Anion

The known structure of the As_7^{3-} polyanion [50, 74, 76, 77] belongs to the substance class of heptapnictogenides. Figure 4.25 shows a sketch of As_7^{3-} (left) and $^1_\infty[As_7^{3-}]$ (right). In the following, the relationship between the two structures will be worked out.

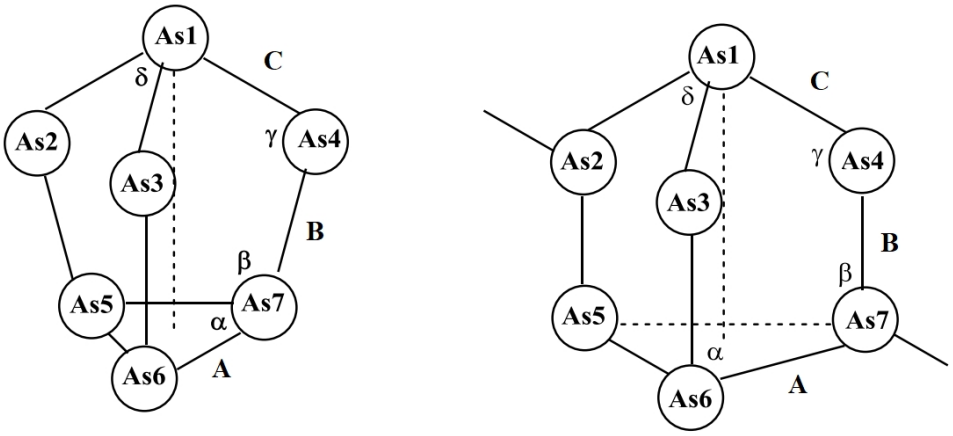

Figure 4.25: (Left) Schematic sketches of the known As_7^{3-} anion with markings of the bond lengths and angles. (Right) A section of the polymeric $^1_\infty[As_7^{3-}]$ with standardised labelling.

In comparison to the well known cage structure of the heptaarsenide As_7^{3-}, Rb_2AuAs_7 does not contain isolated As_7^{3-} anions, but a chain of covalently bound As clusters $^1_\infty[As_7^{3-}]$. A derivation of the polyanionic chain by cleaving the As5 and As7 bonds (Fig. 4.25). The links to the neighbouring cage are made by the As7–As2

bond. The negative charge is thus no longer localised at As2, but at As5. Furthermore, the symmetry is reduced. The C_3 rotation axis, which runs through the apical atom and is perpendicular to the trigonal base plane, is replaced by a C_2 rotation axis. This C_2 axis runs through the atom As3 and is perpendicular to the plane made up by the atoms As2, As4, As5 and As7. It is interesting to observe the effects of bond breaking and bond formation on the other bond lengths and angles (Table 4.5). When compar-

	1 [84]	**2** [101]	**3** [101]	**4** [101]	**5** [101]	**6** [74]	**7** (this work) (this work)	**8** (this work) (this work)
A_m / Å	2.498	2.50	2.524	2.515	2.522	2.511	2.487	2.440
B_m / Å	2.399	2.34	2.361	2.343	2.351	2.327	2.360	2.414
C_m / Å	2.431	2.4	2.421	2.404	2.424	2,404	2.407	2.428
δ_m / °	101.2	101.1	101.6	101.3	101.1	100.4	101.3	100.3
γ_m / °	99	99.5	99	99.5	99.4	99.1	99.3	101.3
β_m / °	105.6	105	105.2	104.9	105.1	105.1	105.2	103.7
α_m / °	60	60	60	60	60	60	60	96.3

Table 4.5: Average distances and angles in the As_7^{3-} units of compounds **1-8**. Compounds: Ba_3As_{14} (**1**), $[Li(NH_3)_4]_3As_7{\cdot}NH_3$ (**2**), $[Rb(18\text{-crown-6})]_3As_7{\cdot}8\,NH_3$(**3**), $Cs_3As_7{\cdot}6\,NH_3$ (**4**), $(Ph_4P)CsAs_7{\cdot}5\,NH_3$ (**5**), $RbAs_7$ (**6**), $[Eu(NH_3)_8]_2[Eu(NH_3)_3(As_7)_2]$ (**7**), Rb_2AuAs_7 (**8**).

ing the bond lengths, it is noticeable that the bonds B and C are slightly longer than those of the known cage structure. However, the bonds A of the trigonal base plane are shortened and are in the range of typical As–As bonds. The new structure has the bond length pattern (A > C > B) of the M_7^{3-} anions. The bond lengths As1–As3 and As6–As3 are interesting: with 2.376 Å, these are significantly shorter in the new chain structure than all other bonds. One reason might be that the As3 atom, as an apical atom above the chain structure, is located close to the voluminous rubidium cations (Fig. 4.22).

The angles β, γ and δ are comparable with each other in the structures (Table 4.5). The exception is the angle α, which is strongly widened due to the bond break. In summary, the polyanionic chain structure shows a clear similarity to the known cage structures of the heptapnictogenides. Therefore, the newly obtained chain structure can be described as a stretched, polymerised variant of the discrete, molecular As_7^{3-} anions.

It is the first of its kind. Rb_2AuAs_7 is the first compound in the ternary system Rb-Au-As. The special synthesis method in ammonia under supercritical conditions leads to this polymer. High pressure is obviously required for the discrete As_7^{3-} cages in solution to polymerise. The higher solubility of pnictogenide polyanions in supercritical ammonia [60, 62] plays a role, since this result could not be obtained at low pressures and temperatures. Due to the higher solubility, other possible compounds do not crystallise, for example phases consisting of rubidium and arsenic, whose solubility

product would already be exceeded in liquid ammonia. However, there is a lack of data on solubilities of Rb-As compounds in liquid ammonia to support this hypothesis. Another trick in the synthesis is the solubility of gold in ammonia in the presence of rubidium. It is generally known that alkali metals dissolve in ammonia. These solutions, consisting of positive alkali metal ions and solvated electrons, are very strong reducing agents and exhibit a deep blue colour, bronze-coloured at high concentrations. The redox potential is high enough to initially dissolve gold as an auride in ammonia [100]. With in excess of arsenic, Au^- is reduced to Au^+. Therefore all three reactants, rubidium, gold and arsenic, are in the same phase and favour the formation of the ternary system Rb_2AuAs_7.

4.2 Coinage Metal Selenides

4.2.1 $Rb_3AuSe_2 \cdot 1.5\,NH_3$

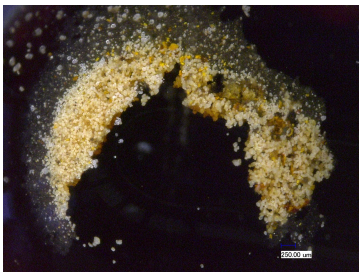

Figure 4.26: Colourless crystals of $Rb_3AuSe_2 \cdot 1.5\,NH_3$.

$Rb_3AuSe_2 \cdot 1.5\,NH_3$ crystallises as colourless, transparent, rhombic prisms (Fig. 4.26) in the monoclinic crystal system with the space group $P2_1/n$ (No. 14) in a new structure type. The lattice parameters of the unit cell are $a = 9.8884(2)$ Å, $b = 10.5592(2)$ Å, $c = 10.6585(2)$ Å with the monoclinic angle $\beta = 110.7780(10)°$. The volume of the unit cell is $V = 1040.51(4)$ Å^3, the number of formula units is 4. The dataset contained 7001 reflections, from which 3898 were unique. The quality factor R_{int} on averaging symmetry equivalent reflections amounted to 4.88 %.

The collected X-Ray data were inspected with the software *APEX4* [128] and the implemented tool *RLATT*. *RLATT* is used for a 3D visualisation of the lattice projected in the reciprocal space. Satellites of the first order with low intensities were present (Fig. 4.27). These satellites have a non-integral relationship to the primary lattice and require q-vectors for processing. It was possible to determine a q-vector of $q = -0.061, 0, +0.433$. Two components of the q-vector were irrational and could not be calculated with a simple fraction, which indicated an incommensurable modulated crystal. However, the intensities of these satellites were too weak to determine an incommensurable modulated structure model with the software JANA [156]. Therefore, these reflections were not taken into account. For this reason, the Fourier-transformed structure was based on the translation-symmetric mean structure. However, neglecting the modulation led to noticeable effects in the structure refinement, manifesting as unusually large anisotropic displacement parameters [157].

The asymmetric unit contains three rubidium atoms, two selenium atoms, one gold atom and one and a half ammonia molecules, with the N(2) position only half occupied. All atoms are located on general Wyckoff positions 4*e*. The three rubidium cations are each positively charged. The two selenium atoms build a linear complex anion with the gold atom. Au is in oxidation state +I in linear coordination. The two terminal selenium atoms have each two negative charges and fulfil the $(8-N)$ rule. Accordingly, this results in a triple negative charge for the linear complex anion $AuSe_2^{3-}$. Hence, the formula $Rb_3AuSe_2 \cdot 1.5\,NH_3$ is obtained.

Similar to the literature known discrete linear complex anion $AuSe_2^{3-}$ (d(Au–Se) 2.41 Å) in $K_3[AuSe_2]$ [115], a bond length of 2.40 Å is present. In difference to the

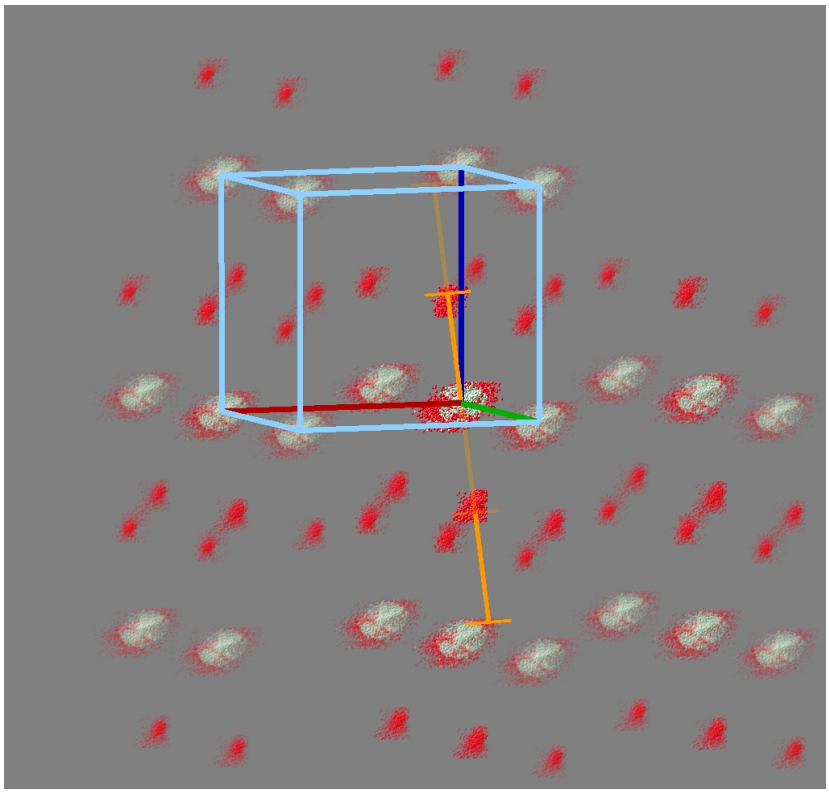

Figure 4.27: Picture created with the software *APEX4* [128] and the implemented tool *RLATT*. The unit lattice is drawn in light blue. a^* in red, b^* in green and c^* in blue. The modulation vector q (orange) connects the satellites of first order ($q = -0.061, 0, +0.433$). In this representation the q-vector connects the satellites 1 and $\overline{1}$, respectively, to the origin. The satellites show only weak intensities, but give the evidence of an incommensurable modulation in the structure of $Rb_3AuSe_2 \cdot 1.5\,NH_3$.

anion in the rhombohedral $K_3(AuSe_2)$ ($R\overline{3}c$), the anion is not perfectly linear, but has a angle of 176.1°. In the coordination sphere up to 4 Å, six rubidium atoms for Se(1) and five rubidium atoms for Se(2) are present. The distances d(Se–Rb) are in a range of 3.40 Å to 3.85 Å, which corresponds well to the literature [108, 116, 117]. In this way, the gold atom has four rubidium atoms in the range from 3.42 Å to 3.69 Å, which is consistent with distances in Rb(AuSe) (d(Au–Rb) 3.50 Å to 3.94 Å) [116, 117]. In the gold environment are three additional rubidium atoms in the range of 4.10 Å to 4.54 Å in addition to the two selenium atoms. In $Rb(Au_3Se_2)$ [108] the distance d(Au–Rb) amounts to 4.02 Å. These distances are shorter than the sum of the van-der-Waals radii and should be taken into consideration for the explanation of the somewhat unusual displacement ellipsoid of the gold atom. The displacement ellipsoid of Au is elongated in the direction, in which it has the least interaction with the surrounding rubidium atoms.

For the three independent Rb positions two different coordination numbers are present. The coordination numbers for Rb(1) are seven and six for Rb(2) and Rb(3). Rb(1) and Rb(3) have four $AuSe_2^{3-}$ anions in their environments, however Rb(2) has

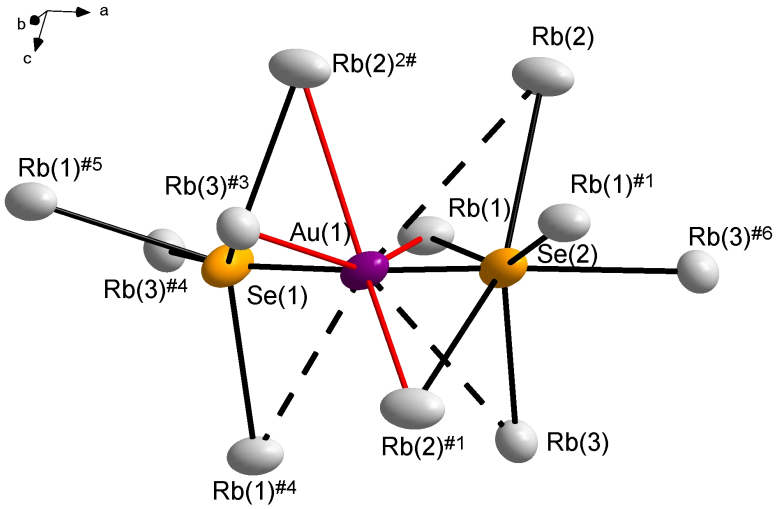

Figure 4.28: The $AuSe_2^{3-}$ anion in $Rb_3AuSe_2 \cdot 1.5\,NH_3$ and its coordination by Rb ions. The short Rb–Au distances are drawn in red (d(Au–Rb) 3.50 Å to 3.94 Å), the larger distances are characterised by fragmented bonds (d(Au–Rb) 4.10 Å to 4.54 Å). The displacement ellipsoids represent a probability of 90 % at 100K. Indices indicate the following symmetry operations: #1: -x+3/2,y+1/2,-z+1/2; #2: -x+1,-y+1,-z; #3: x-1/2,-y+3/2,z-1/2; #4: -x+1,-y+1,-z+1; #5: -x+1/2,y+1/2,-z+1/2; #6: -x+2,-y+1,-z+1.

only three anions in its coordination sphere. The different coordinations are shown in Fig. 4.29. The Rb–N distances are in a range of 3.06 Å to 3.41 Å, which is consistent with the literature [158].

Whether the unusual anisotropic displacement factors are due to a positional disorder of the heavy atoms or reflect their actual thermal vibrations can be determined by the temperature dependence of the displacement parameters [159]. For this purpose, the structure determination was repeated at 100 K to 160 K in steps of 10 K. No evidence of phase transformation was observed within this temperature range. The data sets were each treated with an absorption correction applying the Multiscan method of Blessing [129]. For the heavy atoms, the U_{ii} values were plotted against the absolute temperature to investigate any dynamic effects of the displacement for the respective atoms (Fig. 4.31). For thermally induced vibrations, the coefficients U_{ii} are expected to be approx. 0 at 0 K [160].

The U_{11} values of Rb(2) are particularly outstanding, since the displacement parameter U_{11} does not decrease with decreasing temperature. This is an important indicator for a disorder. However, there were no indications for a split position or a space group of lower symmetry. Hence, a disorder could not be included in the refinement. Overall, this is consistent with the suspected incommensurate modulation in the structure. This vibrational motion of the rubidium atom Rb(2) shifts the atom out of

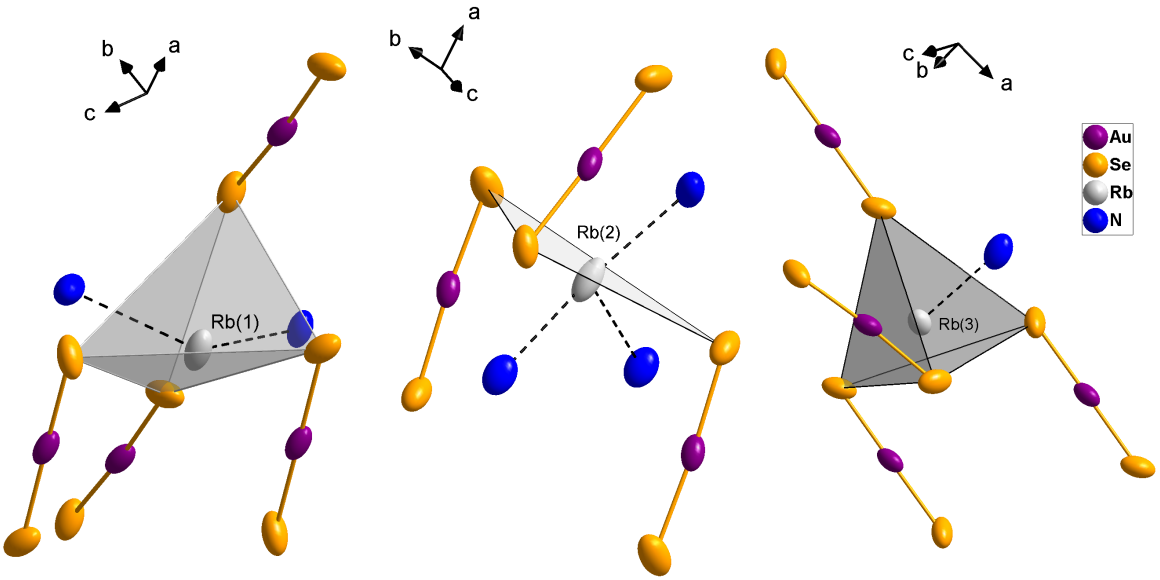

Figure 4.29: The three different rubidium positions in the asymmetric unit in $Rb_3AuSe_2 \cdot 1.5\,NH_3$. d(Rb–Se) 3.42 Å - 3.85 Å, d(Rb–N) 3.06 Å - 3.41 Å. The displacement ellipsoids represent a probability of 90 %.

the plane, which is spanned by 3 Se atoms (Fig. 4.29). Fixed by these heavy atoms, it is displaced in the direction towards the ammonia molecules. A look at the unit cell shows, that the network of ammonia molecules and rubidium atoms create channels, in which the discrete, linear $AuSe_2^{3-}$ anions are packed. An extended, doubled unit cell is given in Fig. 4.30. Bonds were drawn between nitrogen and rubidium to illustrate the network. Inside these channels, the linear $AuSe_2^{3-}$ molecules are oriented in the same direction. This leaves open the possibility that the linear molecules are periodically slightly tilted, which could lead to incommensurable modulation. These modulated displacements would therefore affect the coordinating atoms.

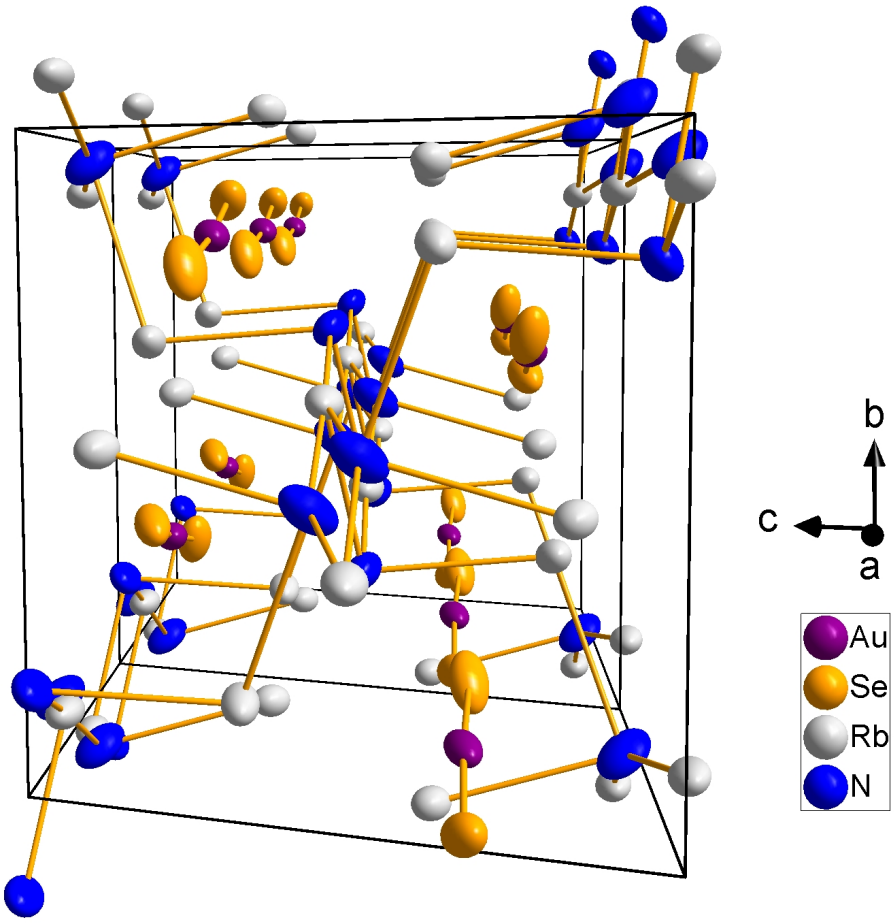

Figure 4.30: Perspective view of the extended, doubled unit cell of $Rb_3AuSe_2 \cdot 1.5\,NH_3$. N and Rb atoms were connected to show the channels, created by this network. Inside the channels, the discrete, linear $AuSe_2^{3-}$ anions are oriented in the same direction. The displacement ellipsoids represent a probability of 90 %.

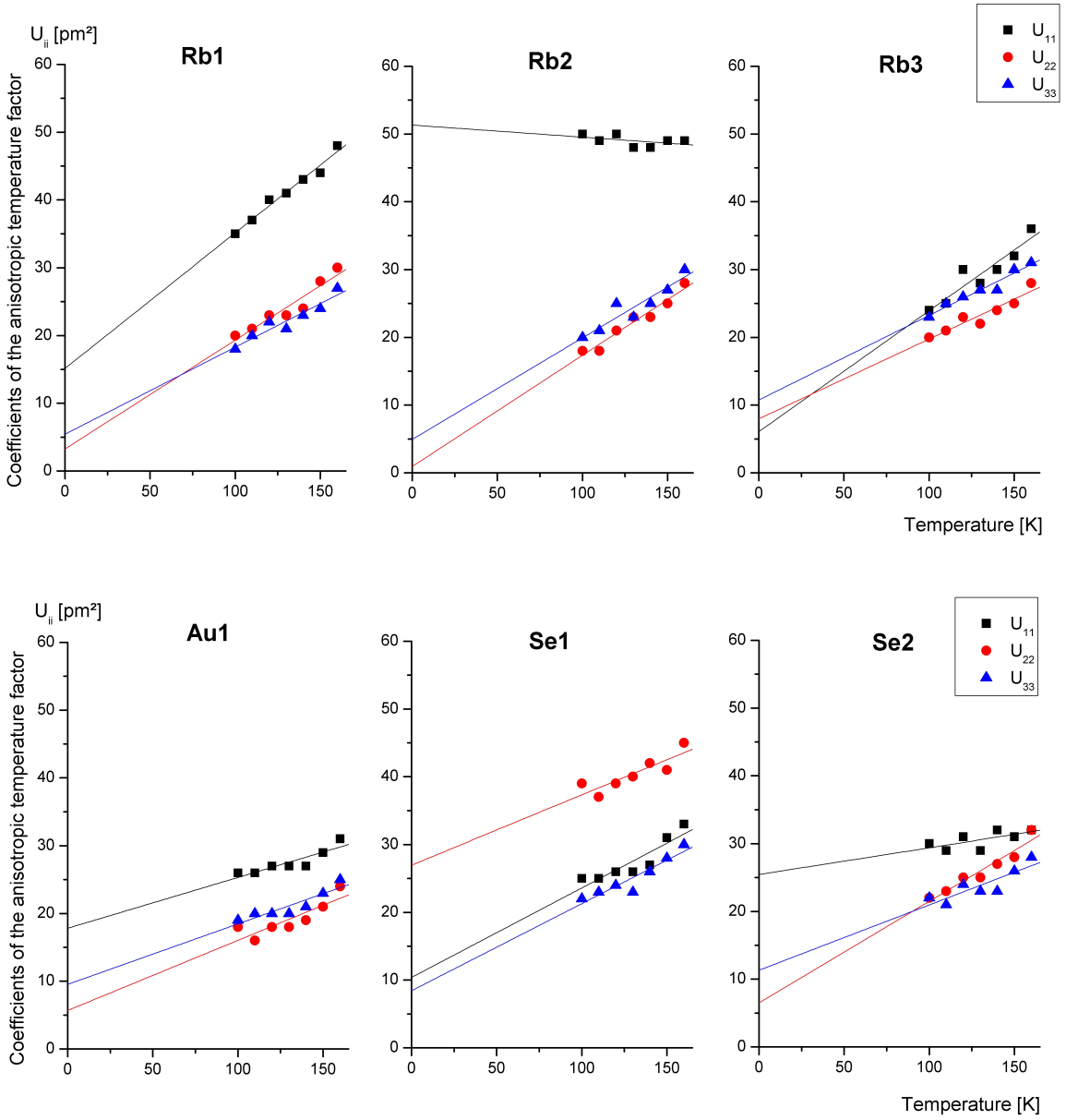

Figure 4.31: The coefficients U_{ii} of the anisotropic temperature factor of the heavy atoms in the structure of $Rb_3AuSe_2 \cdot 1.5\,NH_3$ as a function of absolute temperature. The data points are taken from the structural determinations at 100 K to 160 K in steps of 10 K. Linear extrapolations to 0 K are given as straight lines.

4.2.2 $K_{10}CuSe_8Cl \cdot NH_3$

$K_{10}CuSe_8Cl \cdot NH_3$ crystallises as red, transparent, rhombic prismatic crystals (Fig. 4.32) in the orthorhombic crystal system with the space group *Pbcn* (No. 60) in a new structure type. The lattice parameters of the unit cell are $a = 13.0315(3)$ Å, $b = 11.9464(4)$ Å, $c = 16.8078(5)$ Å. The volume of the unit cell is $V = 2616.63(13)$ Å^3 and the number of formula units is 4.

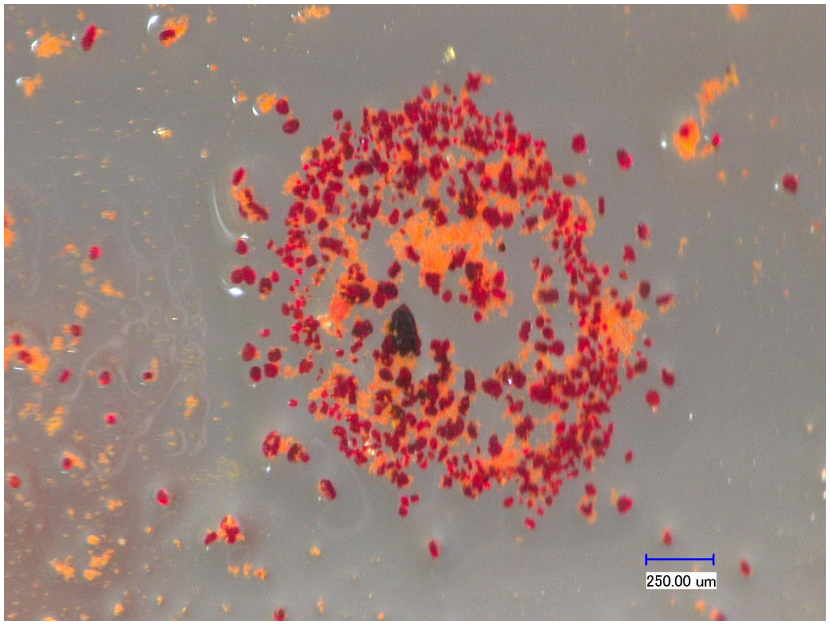

Figure 4.32: Red crystals of $K_{10}CuSe_8Cl \cdot NH_3$.

Three types of anions are present in the asymmetric unit. A chloride anion is located on the Wyckoff position 4*c* with .2. local symmetry. Selenium occurs in two anion types with different bonding situations. Se(2) and Se(3) form a dumbbell Se_2^{2-}, isoelectronical to Br_2. This anion is already known from Zintl phases such as A_2Se_2 (A=Na, K, Rb) [161, 162]. The bond length is 2.41 Å, which is consistent with the literature. One half of the second dumbbell in the asymmetric unit is build up by Se(4), which occupies the general position 8*b*. The inversion centre on 4*b* is in the centre of the dumbbell. The bond length between Se(4) and the symmetry equivalent $Se(4)^{\#10}$ is 2.41 Å. In addition to the dumbbells, the selenium atom Se(1) and its symmetry equivalent atom coordinate the copper atom Cu(1) in the linear complex anion $[CuSe_2]^{3-}$ (Fig. 4.33). The Cu(1) atom is located on the Wyckoff position 4*k* in an inversion centre. This is the first time that the linear complex anion $[CuSe_2]^{3-}$ is reported. According to the Zintl-Klemm concept, a triple negative charge is assigned to this anion. The Se(1)–Cu(1) distance amounts to 2.23 Å. This bond is unusually short, since bond lengths around 2.40 Å are present in other alkali-copper-selenium compounds [110–113]. In most cases, the environment of copper is tetrahedral. In the graphite-like $^2_\infty[CuSe^-]$

anion framework in KCuSe [113], copper is trigonal planar surrounded by selenium and vice versa, the bond length amounts to 2.41 Å. However, in the linear complex anion $[CuSe_2]^{3-}$, strong electrostatic interactions between the copper(I) cation and the two terminal, negatively charged selenium atoms contribute to the shortening of the bond length. In addition to five symmetry independent potassium ions, a disordered ammonia molecule is present in the asymmetric unit. The ammonia molecule on 8*d* is located close to the two fold axis on Wyckoff position 4*c* with .2. local symmetry.

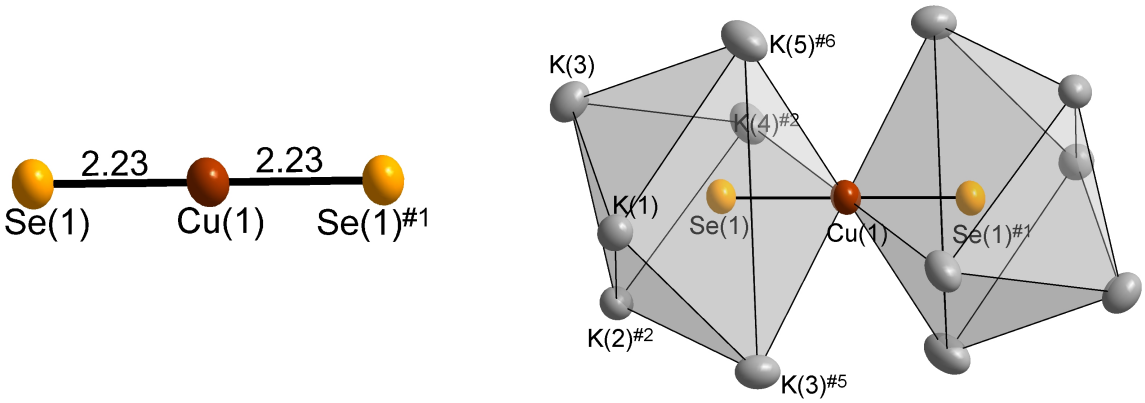

Figure 4.33: (Left) Linear complex anion $CuSe_2^{3-}$ in $K_{10}CuSe_8Cl \cdot NH_3$. (Right) Coordination of Se(1) and symmetry equivalent Se(1)$^{\#1}$ by potassium and copper. Bond lengths in Å. The displacement ellipsoids represent a probability of 90 %. Indices indicate the following symmetry operations: #1: -x+1,-y+1,-z; #2: x,-y+1,z-1/2; #5: -x+3/2,y+1/2,z; #6: -x+3/2,y-1/2,z.

Additionally to the coordination by Cu(1), Se(1) is coordinated by six K cations with K–Se distances reaching from 3.24 Å to 3.32 Å. The K and Cu atoms form a distorted single-capped trigonal-prismatic environment around Se(1) (Fig. 4.33). K(4) overcaps the square face of this prism. Se(2) is surrounded by seven K ions and the disordered ammonia (Fig. 4.34). Six K ions form a trigonal prism. Two of the square faces are occupied by the seventh K atom and the disordered ammonia molecule. The third square face is shared with the coordination polyhedra surrounding Se(3). The environment of the Se(4)–Se(4)$^{\#10}$ dumbbell is nearly identical to the environment of the Se(2)–Se(3) dumbbell (Fig. 4.34). At the overcapping position of the square face, the ammonia molecule is replaced with an additional K ion. Therefore, each Se atom is surrounded by eight K atoms. In the middle of the Se(4)–Se(4)$^{\#10}$ bond an inversion centre is located. The environment of the dumbbells as a whole can be described as a cuboctahedron. For the cuboctahedron coordination of Se(4)–Se(4)$^{\#10}$ the program SHAPE [136] calculated a deviation of 2.7 % from the ideal O_h symmetry, respectively 3.4 % for the cuboctahedron coordination of Se(2)–Se(3).

The chloride ion is coordinated by six potassium ions. The smallest deviations from the ideal coordination polyhedra were calculated by the method of Continuous

Symmetry Measures [135] using the program SHAPE [136] with the best result and a deviation of 5.3 % from the trigonal prism with D_{3h} symmetry. For an octahedron with O_h symmetry, the deviation amounts to 6.4 %. Therefore, the description as a distorted trigonal prism is the best one. Compared to KCl (d(K–Cl)=3.14 Å) the K–Cl bond lengths differ slightly.

The complex anion and the Se(4)–Se(4)$^{\#10}$ dumbbell are located at the same height in the *a*-*b* plane. Between the complex anions there is one Se_2^{2-} anion each. The distances are too long (4.74 Å) for selenium to be described as a Se_4^{2-} chain. An alternative molecular formula, which takes the the discrete anions into consideration, is $K_{10}(CuSe_2)(Se_2)_3Cl$, respectively as $(K^+)_{10}[Cu(I)Se_2^{2-}](Se_2^{2-})_3(Cl^-)$. Fig. 4.35 shows a perspective view of the extended unit cell.

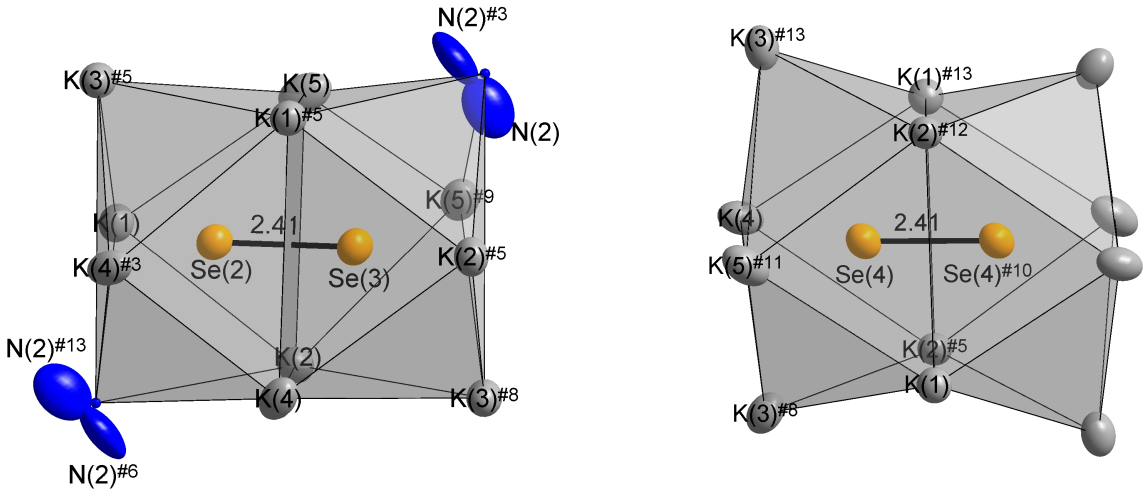

Figure 4.34: (Left) Potassium coordination polyhedron around the dumbbell anion Se_2^{2-} formed by Se(2) and Se(3). Selenium is trigonally prismatically surrounded by potassium. The prism is triple-capped by the opposite selenium atom and K(3)$^{\#5}$, respectively K(3)$^{\#8}$ and the disordered ammonia. It was not possible to locate the hydrogen atoms of the ammonia molecule. N(1) is located close to the Wyckoff position 4*c* with .2. local symmetry, therefore it is half occupied. (Right) The coordination polyhedron around the dumbbell anion Se_2^{2-} is eight K ions. Each Se atom surrounded trigonal prismatic by K ions. The prism is triple-capped by the opposite Se atom and K(3), and its symmetry-generated positions. Bond lengths in Å. The displacement ellipsoids represent a probability of 90 %. Indices indicate the following symmetry operations: #3: -x+1,y,-z+1/2; #5: -x+3/2,y+1/2,z; #6: -x+3/2,y-1/2,z; #8: x,-y+1,z+1/2; #9: -x+2,y,-z+1/2; #10: -x+1,-y+2,-z+1; #11: -x+3/2,-y+3/2,z+1/2; #12: x-1/2,-y+3/2,-z+1; #13 x-1/2,y+1/2,-z+1/2.

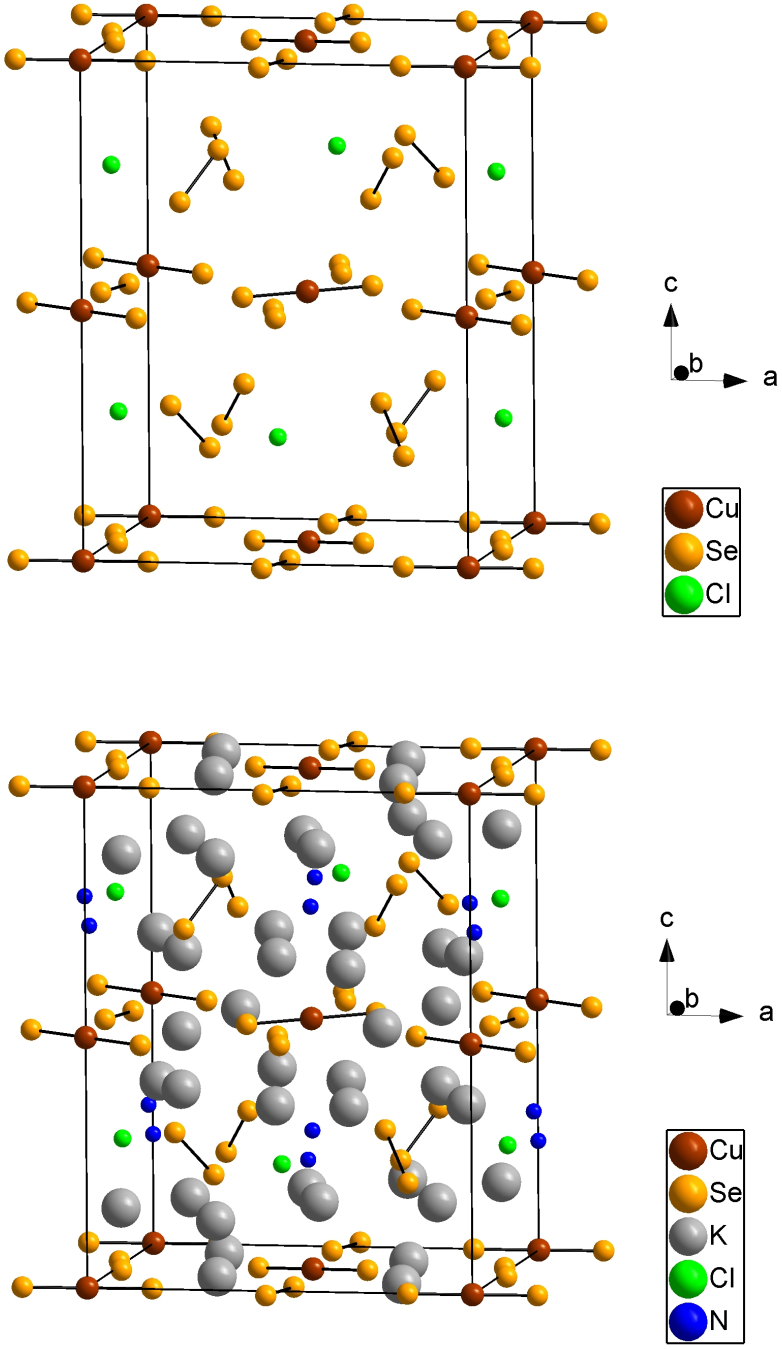

Figure 4.35: (Top) A perspective view of the extended unit cell of $K_{10}CuSe_8Cl \cdot NH_3$. Potassium ions and ammonia molecules have been omitted for improved clarity. (Bottom) The same perspective view of the extended unit cell of $K_{10}CuSe_8Cl \cdot NH_3$ with all atoms visible. Atoms are drawn as spheres of arbitrary radii.

4.2.3 $K_2[AuSe]Se\cdot NH_3$

$K_2[AuSe]Se\cdot NH_3$ crystallises as red needles in the monoclinic crystal system with the space group $P2_1$ (No. 4) in a new structure type. The lattice parameters of the unit cell are $a = 11.6351(8)$ Å, $b = 6.2587(3)$ Å, $c = 11.6322(9)$ Å with the monoclinic angle $\beta = 119.990(3)°$. The volume of the unit cell is $V = 544.17(16)$ Å^3. The number of formula units is 4. Figure 4.36 shows the red crystals that grow in the form of bow ties due to systematic twinning.

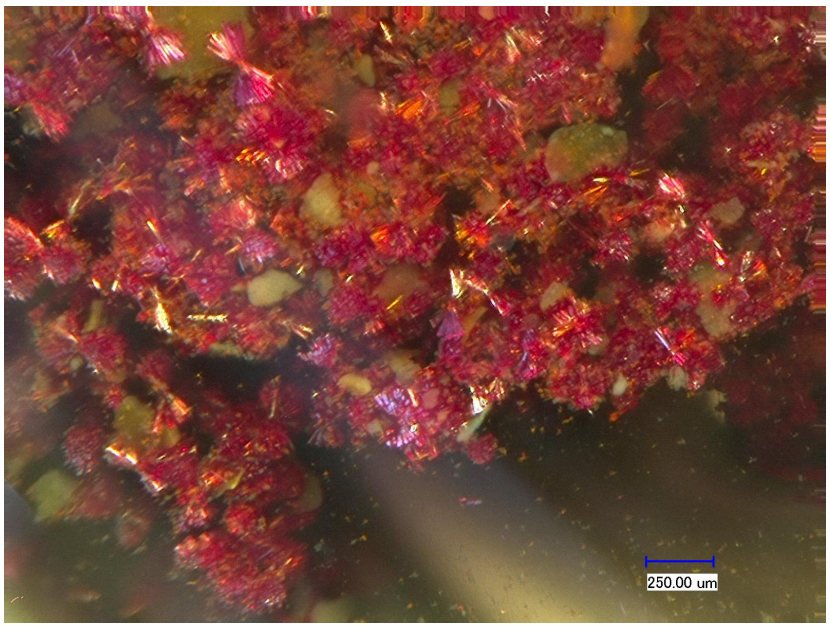

Figure 4.36: The red needles are the compound $K_2[AuSe]Se\cdot NH_3$. Synthesised at 55 K in ammonia. Due to systematic twinning, the compound grows in the shape of a bow tie.

The structure of $K_2[AuSe]Se\cdot NH_3$ was first refined in the non-centrosymmetric space group $P6_3$ using the hexagonal unit cell parameters $a = 11.6455(12)$ and $c = 6.2657(7)$ Å. From the 12656 collected reflections, 1448 were unique, resulting in the quality factor $R_{int} = 7.74\,\%$. Refinement was performed as an inversion twin with an batch scale factor of 0.467. In the asymmetric unit two Se atoms, one Au atom, two K atoms and one N atom are present. The N atom was refined with an isotropic displacement parameter. The displacement ellipsoids for K(2) are flat, which was the reason to look further into twinning. A monoclinic system in space groups $P2_1$ or $P2_1/m$ with a and c approximately equal and β approximately 120° may emulate a hexagonal cell [163]. In such a case, the diffraction pattern could give absences and possibly intensity statistics corresponding to $P6_3$. The twin would have three domains, in this case called "Drilling". The solution of SHELXT [127] in the monoclinic crystal system recommended the non-centrosymmetric space group $P2_1$. Using the twin matrix (0 0 1 / 0 1 0 / -1 0 -1 / 3) resulted in better wR_2 values (wR_2 = 0.1182)

than in the hexagonal system (wR_2=0.1721). Additionally, the program suggested an inversion twin. The twin matrix was adjusted to (0 0 1 / 0 1 0 / -1 0 -1 / -6), meaning that there were not three, but six different domains in this merohedral twinned crystal. Crystal growth and shape indicated the possibility of such twinning (Fig. 4.36). Nevertheless, the monoclinic refinement needed restrains to prevent individual atoms from becoming "non-positive-definite". However, the best solution for this problematic crystal structure has not yet been presented. Since the bond lengths and angles in both solutions differ only slightly from each other, the structure model is sufficient to describe the structure.

The structure consists of zig-zag chains $[AuSe^-]_n$ and chains of equidistant selenium atoms $[Se^-]$, assuming gold is present exclusively in the +I oxidation state. Four K atoms and one ammonia molecule are present in the asymmetric unit of the unit cell, leading to the formula $K_2[AuSe]Se\cdot NH_3$. Regarding the discussion on bond lengths and angles, data from the hexagonal cell (Fig. 4.37) will be taken. The ammonia molecule is in close distance to K(1) (2.61 Å). The shorter distance in the $[AuSe^-]_n$ chain (2.38 Å) is in good agreement with the $[AuSe^-]_n$ zig-zag chain in KAuSe (2.41 Å) [114], but the other bond length is significantly longer with 2.48 Å. In $K_3(Au(Se_5)_2(Se_3))$ [106], Au is in the oxidation state +III, with distances to Se of 2.46 Å to 2.48 Å. The equidistant chain of Se atoms (3.13 Å) may have Se–Se interactions, but it is possible, that the long Au–Se distance (2.48 Å) is due to the presence of Au(III) cations to some extent. The short Au$\cdots$Au distances (3.13 Å) give reason to suspect interactions between the Au atoms. On the other hand, Au-Mössbauer spectroscopy of the compounds AAuCh (A=K, Rb, Cs; Ch=S, Se, Te) showed no evidence for d^{10}–d^{10} interactions [164]. In CsAuTe [117] the Au–Au distance is 3.11 Å, which is close to d(Au–Au) 3.13 Å in $K_2[AuSe]Se\cdot NH_3$. Bronger [164] concludes that the interactions must be much weaker than all other binding interactions. Possibly the observed "short" Au–Au distances correspond to van-der-Waals contacts.

At this point, it is not possible to judge with certainty whether an infinite chain of singly charged Se atoms or separated doubly negatively charged Se atoms are present. In the second case, Au would have to be present as Au(I) and Au(III) in the same environment. An infinite chain of equidistant $^1_\infty[Se^-]$ would be a hitherto unobserved structural feature. Infinite chains of $[Te^-]$ are known in literature [165, 166]. For TlTe, a Peierls distortion was observed. The room temperature modification shows an equidistant $^1_\infty[Te^-]$ chain (d(Te–Te) 3.08 Å), whereas in the low temperature modification (LT, 127 K) the chain shows alternating distances [165]. Park et al. describe longer selenide chains to be more potent oxidisers and therefore lead to Au(III) [106]. The short N–K

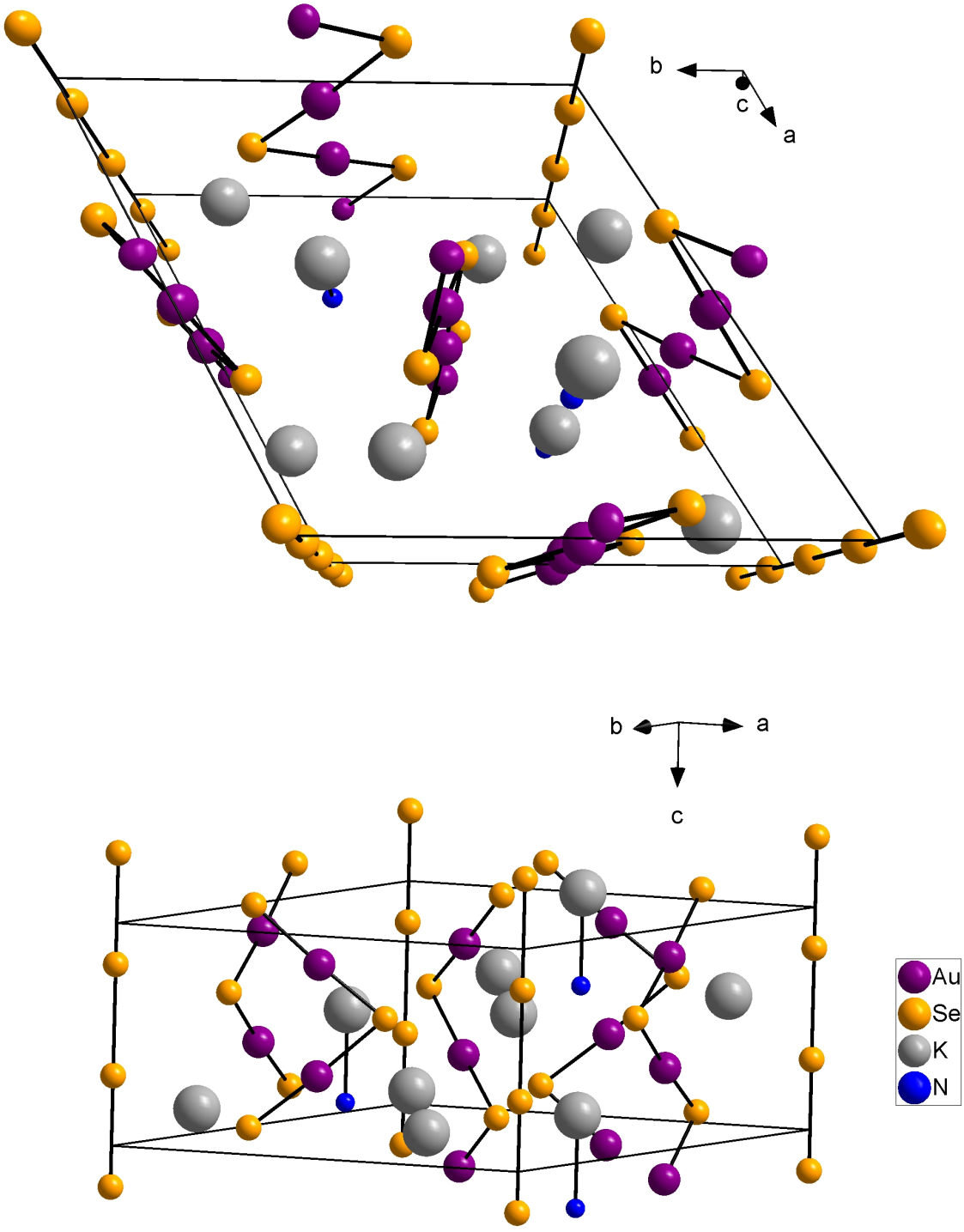

Figure 4.37: Two perspective views of the hexagonal unit cell of $K_2[AuSe]Se \cdot NH_3$. A equidistant chain of selenium atoms is present in addition to the zig-zag chain $[AuSe^-]_n$. Atoms are drawn as spheres of arbitrary radii.

distance (2.61 Å) is the reason to interpret the nitrogen position as ammonia and not as an ammonium cation. Similar bond lengths are present in $[K(NH_3)](Se_2)$ [167].

However, the true character of $K_2[AuSe]Se \cdot NH_3$ is still unsolved. With the underlying data, it has not yet been possible to create a structural model which satisfactorily describes the compound without leaving open questions. This gives rise to the need for further research.

The crystallographically difficult analysis of the crystal structure contrasts with the conceivably simple preparation of $K_2[AuSe]Se \cdot NH_3$. Within minutes, the educts reacted rapidly in liquid ammonia. After an hour the first red crystals formed. Different approaches were tried out to get better crystal qualities. Moreover, lower amounts of reactants were chosen to reduce nucleation. Reaction vials were stored at different temperatures (−18 °C, 25 °C and 55 °C) as well as under supercritical conditions at 150 °C. The crystallographic problems occurred for crystals isolated from all runs.

4.3 *Spin-ladder* Compounds

4.3.1 $(NH_4)Fe_2S_3$

$(NH_4)Fe_2S_3$ [168] crystallises as black, metallically lustrous, acicular crystals in the orthorhombic crystal system with the space group *Cmcm* (No. 63) in the $CsCu_2Cl_3$-structure type. It is isotypical to the mineral rasvumite KFe_2S_3 [169]. The lattice parameters of the unit cell are $a = 9.0986(15)$ Å, $b = 10.982(2)$ Å, $c = 5.4440(8)$ Å. The volume of the unit cell is $V = 544.17(16)$ Å^3 and the number of formula units is 4.

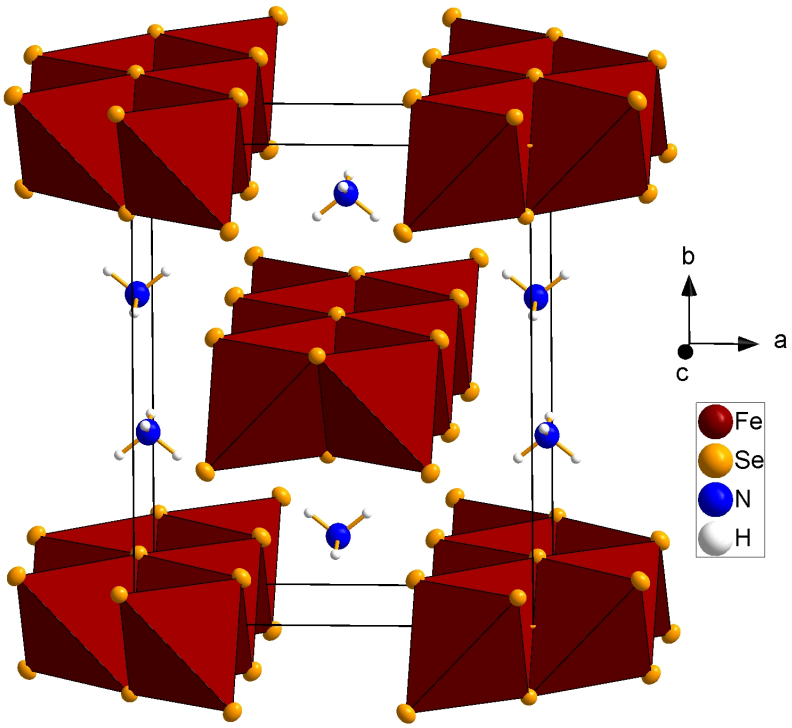

Figure 4.38: Extended unit cell of $(NH_4)Fe_2S_3$ with tetrahedral coordination of the iron atoms. Displacement ellipsoids are scaled with a probability of 90 %.

In the course of the refinement of the crystal structure, the hydrogen atoms attached to nitrogen could not be located in the difference Fourier map of the electron density. However, the position would have to be occupied by a monovalent cation to achieve charge balance. Additionally, it can be ruled out that the crystals contain neat ammonia, since no decomposition occurred upon increasing the temperature to 50 °C. Finally, by comparing the ionic radii of the monovalent cations with similar substances, it can be concluded that ammonium ions are present. In the course of the structure determination of the isotypic $(NH_4)Fe_2Se_3$, the hydrogen atom positions could be located in the difference Fourier maps.

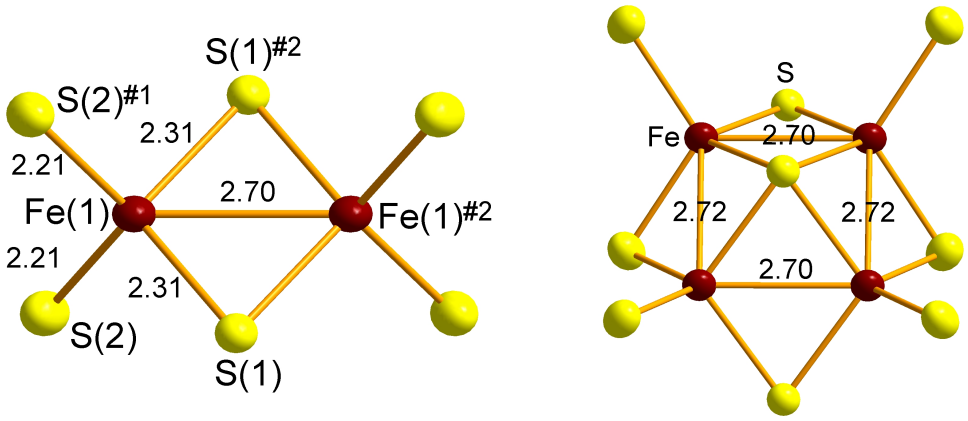

Figure 4.39: (Left) Representation of the FeS_4 tetrahedra with bond lengths in Å. (Right) Representation of the linkage of the FeS_4 tetrahedra to form an Fe_4S_9 unit with bond lengths in Å. The displacement ellipsoids represent a probability of 90 %. Indices indicate the following symmetry operations: #1: x,-y+1,-z+1; #2: -x+1,-y+1,-z+1.

The structure (Fig. 4.38) consists of chains of double edge-sharing $FeSe_4$ tetrahedra running along the *c*-axis and face-sharing pairs of $(NH_4)Se_{10}$ polyhedra that form double chains parallel to *c*. Since two longer and two shorter Fe–S bonds are present the FeS_4 tetrahedra are slightly distorted. The bond length between Fe and a bridging sulphur atom S(1) is 2.31 Å, the bond length to the terminal S(2) is shorter (2.21 Å). The ammonium ions are located between the chains of double edge-sharing $FeSe_4$ tetrahedra. The ammonium ions form NH_4Se_{10}-polyhedra, which form double chains in the *c*-direction. These are linked to the next layer in the *a*-direction via edges-sharing. Sulphur can be assigned the oxidation state -II. Due to the charge of the ammonium ion, Fe must assume an oxidation state between +II and +III in order to obtain a charge balanced compound. One possibility would be to assign an oxidation state of +II to half of the iron ions and an oxidation state of +III to the other half. However, the bonding of the iron ions suggests that an electron is constantly moving between the two iron atoms and that the oxidation state of the iron changes dynamically. The Fe atom in the oxidation state +II and +III cannot be distinguished crystallographically, since it is on the same crystallographic site. The question of the oxidation state of the Fe atom is taken up again in Section 4.3.4. Fig. 4.39 shows the linkage of four iron ions. The four iron atoms are all in one plane, and the angle between three iron atoms is 90°. The two opposite Fe–Fe bonds have the same length, but there is one slightly longer (2.72 Å) and one slightly shorter (2.70 Å) Fe–Fe bond.

Analogous to the compounds KFe_2S_3 and $BaFe_2S_3$, the iron atoms are arranged in a ladder shape. This atomic order is a prerequisite for the special cooperative magnetism of a *spin-ladder* structure. $BaFe_2S_3$ was found to be a superconductor [170]

at about 11 GPa, followed by the appearance of superconductivity below $T_c = 14$ K. Density functional theory calculations (DFT) for KFe_2S_3 showed similar behaviour under pressure like $BaFe_2S_3$, with a critical pressure of ≈ 23 GPa [171]. In order to find out whether $(NH_4)Fe_2S_3$ forms a *spin-ladder* structure, magnetic measurements must first be carried out, since the appropriate atomic arrangement does not necessarily lead to the formation of this magnetic phenomenon.

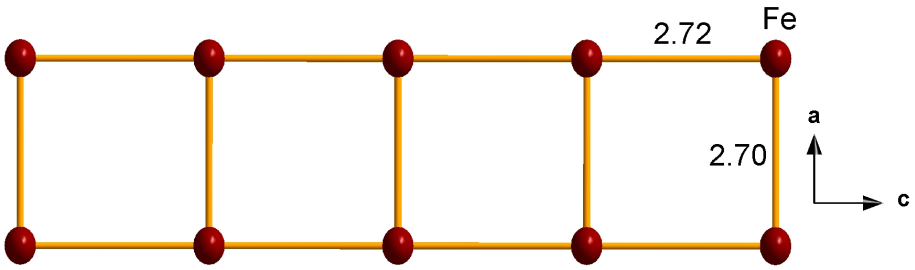

Figure 4.40: Arrangement of the Fe atoms in the structure of $NH_4Fe_2S_3$. The ladder of Fe atoms with almost perfect square rings is planar. Bond lengths are given in Å. Displacement ellipsoids are scaled with a probability of 90 %.

4.3.2 $(NH_4)Fe_2Se_3$

$(NH_4)Fe_2Se_3$ [168] crystallises as black, metallically lustrous, acicular crystals in the orthorhombic crystal system with the space group *Cmcm* (No. 63). It is isotypical to the previously described $(NH_4)Fe_2S_3$. The lattice parameters of the unit cell are $a = 9.0986(15)$ Å, $b = 10.982(2)$ Å, $c = 5.4440(8)$ Å. The volume of the unit cell is $V = 544.17(16)$ Å^3 and the number of formula units is 4.

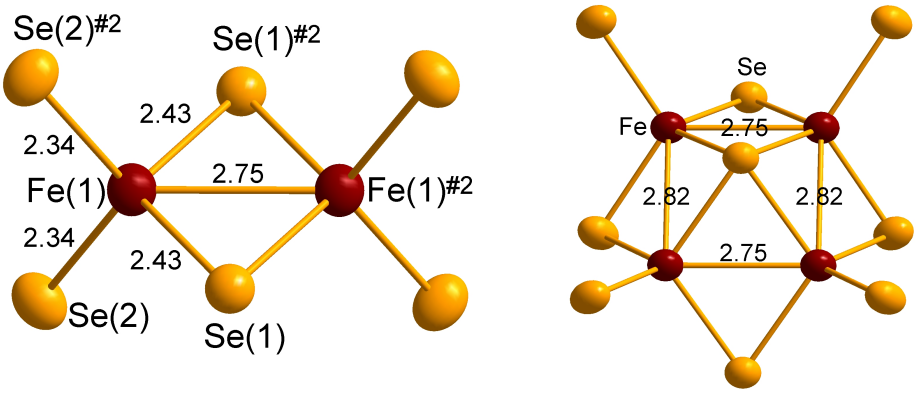

Figure 4.41: (Left) Representation of the $FeSe_4$ tetrahedra with bond lengths in Å. (Right) Representation of the linkage of the $FeSe_4$ tetrahedra to form an Fe_4Se_9 unit with bond lengths in Å. The displacement ellipsoids represent a probability of 90 %. Indices indicate the following symmetry operations: #1: x,-y+1,-z+1; #2: -x+1,-y+1,-z+1.

The $FeSe_4$ tetrahedra are slightly distorted. The shorter bond between iron and selenium is 2.34 Å. Figure 4.41 shows two selenium atoms (Se(1)) bonded to two iron atoms each. At 2.43 Å, this bond is 0.1 Å longer than the iron-selenium bond to the terminal selenium atoms (Se(2)). The regular ladder arrangement of the Fe atoms is preserved when replacing S by Se. The Fe–Fe bonds, however, increase significantly. The Fe–Fe bonds perpendicular to the ladder direction increase from 2.70 Å to 2.75 Å, in the ladder direction from 2.72 Å to 2.82 Å. The ladder-like arrangement of the iron ions in the structure is shown in the following Fig. 4.42.

Analogous to the corresponding sulphide $(NH_4)Fe_2S_3$, the Se atom has the oxidation state -II, therefore the iron atom must have an oxidation state between +II and +III.

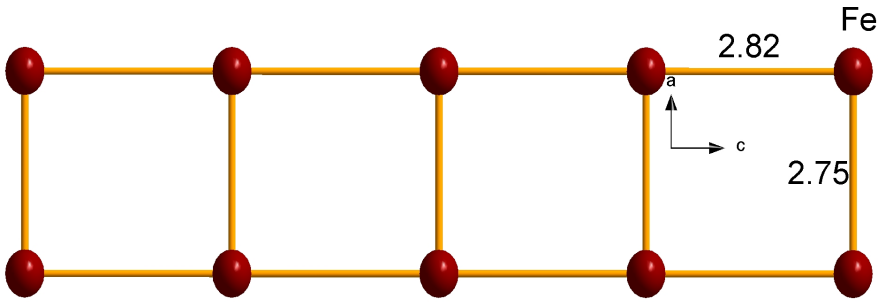

Figure 4.42: Arrangement of the Fe atoms in the structure of $NH_4Fe_2S_3$. The ladder of Fe atoms with almost perfect square rings is planar. Bond lengths are given in Å. Displacement ellipsoids are scaled with a probability of 90 %.

4.3.3 Comparison of $(NH_4)Fe_2S_3$ and $(NH_4)Fe_2Se_3$ with Isostructural Compounds

The two newly synthesised compounds $(NH_4)Fe_2S_3$ and $(NH_4)Fe_2Se_3$ are isostructural to KFe_2S_3 [169] and $BaFe_2S_3$ [172]. NH_4^+ ions are located at the position of the K^+ and Ba^{2+} ions, respectively, in the crystal lattice. Besides the two there are other compounds with iron and sulphur/selenium, which crystallise in the $CsCu_2Cl_3$ structure type: KFe_2Se_3 [173], $RbFe_2S_3$ [174], $RbFe_2Se_3$ [175], $CsFe_2S_3$ [174], $CsFe_2Se_3$ [175] and $TlFe_2S_3$ [176]. Table 4.6 shows the ionic radii and electronegativities of the various cations in the compounds above.

Cation	Ion radius [Å]	Electronegativity according to Pauling
NH_4^+	1.43	
Ba_2^+	1.36	0.89
K^+	1.38	0.82
Rb^+	1.49	0.82
Cs^+	1.67	0.79
Tl^+	1.50	2.04

Table 4.6: Ionic radius [177] and electronegativity [178] of the cations.

The compounds are described with the general molecular formula AFe_2S_3 and AFe_2Se_3. A comparison of the ionic radii of the cation A with the volume of the

cell provides an almost linear relationship. The compounds with monovalent A cations from the first main group and ammonium are compared. The larger lattice parameters are due to a larger volume of the AS_{10} and ASe_{10}-polyhedra, while the volumes of the FeS_4 and $FeSe_4$ tetrahedra remain almost the same. Furthermore, it can be observed that the larger the volume of the AS_{10} and ASe_{10}-polyhedra, the more the A cation deviates along the *b*-axis from the centre of the polyhedron [174].

	AFe_2S_3		AFe_2Se_3
	V (cell) [Å^3]		V (cell) [Å^3]
K^+	538.00	K^+	594.23
NH_4^+	543.97(16)	NH_4^+	608.44(9)
Rb^+	564.44	Rb^+	620.85
Cs^+	604.44	Cs^+	662.56
	V AS_{10}-polyhedra [Å^3]		V ASe_{10}-polyhedra [Å^3]
K^+	88.68	K^+	95.44
NH_4^+	89.41	NH_4^+	98.84
Rb^+	93.42	Rb^+	101.47
Cs^+	101.53	Cs^+	109.66
	V FeS_4-polyhedra [Å^3]		V $FeSe_4$-polyhedra [Å^3]
K^+	5.910	K^+	7.081
NH_4^+	5.914	NH_4^+	6.957
Rb^+	6.00	Rb^+	6.937
Cs^+	6.04	Cs^+	7.054
	d(Fe–Fe) along *a*-axis [Å]		d(Fe–Fe) along *a*-axis [Å]
K^+	2.734	K^+	2.751
NH_4^+	2.698	NH_4^+	2.752
Rb^+	2.716	Rb^+	2.765
Cs^+	2.699	Cs^+	2.754
	d(Fe–Fe) along *c*-axis [Å]		d(Fe–Fe) along *c*-axis [Å]
K^+	2.709	K^+	2.800
NH_4^+	2.722	NH_4^+	2.819
Rb^+	2.723	Rb^+	2.819
Cs^+	2.741	Cs^+	2.845

Table 4.7: Volume of unit cells and polyhedra, Fe–Fe bond lengths along the *a*- and *c*-axis of selected AFe_2S_3/AFe_2Se_3 compounds.

The distances between the iron ions in the edge-linked FeS_4 tetrahedra decrease along the *a*-axis and increase along the *c*-axis as the ionic radius of the A cation increases, compare Table 4.7. Looking at the Fe–Fe distances in the compounds AFe_2Se_3, the increase of the distance with larger ionic radius of the A cation can be observed along the *c*-axis. However, there is no linear relationship between the ionic radius of the A cation and the distance of the iron ions along the *a*-axis. The change in the spacing of the iron ions in the compound changes the bond character of the Fe–Fe bond [174].

4.3.4 The Oxidation State of Iron

Compounds that contain an element in different oxidation states are called mixed-valent compounds and are widespread, especially in the field of transition metals. A common feature of these mixed-valent compounds is their colour, which is attributed to a cooperative metal-metal interaction. Among the best-known substances of this class with iron in the oxidation state +II and +III is the Prussian blue $Fe_4[Fe(CN)_6]_3$ with its characteristic blue colour [177]. Mixed-valent compounds have an important role in biological processes. The ferredoxins are iron- and sulphur-containing proteins in which iron is tetrahedrally surrounded by sulphur. In metabolic reactions, these proteins act as electron transmitters [179]. A classification of mixed-valence compounds was introduced by Robin and Day [180]. Class 1 includes compounds in which the metal centres with different oxidation states can be clearly distinguished due to different chemical environments. No electronic interactions occur between the metal atoms. In compounds assigned to class 2, the chemical environment of the metals is similar. Therefore, the energy barrier for electronic interactions is low. If the oxidation states of the metals cannot be distinguished from each other because they have an identical chemical environment, the compound is classified in class 3. The valence electrons are delocalised and no fixed oxidation state can be assigned to the metals. In $(NH_4)Fe_2S_3$ and $(NH_4)Fe_2Se_3$, the iron atoms always have the identical chemical environment at room temperature. However, it cannot be ruled out that the lattice vibration occurring at room temperature exceeds the energy barrier for electronic interactions, causing the electrons to jump between the iron atoms in a dynamic process. If the temperature is reduced to the point where almost no lattice vibrations are present, a different chemical environment of the two iron atoms can be detected. Therefore, $(NH_4)Fe_2S_3$ and $(NH_4)Fe_2Se_3$ may belong to the 2nd or 3rd class of mixed-valent compounds.

The compounds AFe_2S_3 and AFe_2Se_3 are particularly interesting because of the intermediate oxidation state on iron. Ionic bonds are predominantly found between the A cation and sulphur or, respectively, the A cation and selenium. However, the bonds between iron and sulphur/selenium in the FeS_4/$FeSe_4$ tetrahedra are mainly covalent. The electrons are delocalised, therefore no exact oxidation state can be assigned to the iron atoms [174]. Investigations of the oxidation state of iron in $BaFe_2S_3$ by means of Mössbauer spectroscopy showed that instead of an oxidation state of +II, iron has the intermediate oxidation state +2.5 [181]. The results of the calculations of Hoggins and Steinfink [182] support this observation: based on the Fe-S bond lengths, an oxidation state of +2.64 was calculated for Fe. Data from Mössbauer spectroscopy for KFe_2S_3 gave an empirical oxidation state of +2.62 instead of the formal oxidation

state +2.5 [175]. The oxidation states of iron in the compounds AFe_2S_3 (with A=K, Rb, Cs) calculated in this way increase from +2.62 in KFe_2S_3 to +2.77 in $CsFe_2S_3$ [181]. A higher oxidation number of iron affects the bond lengths of the chains of the FeS_4 tetrahedra [175]. The Fe–Fe bond length along the *c*-axis becomes longer as the empirical oxidation state on the iron increases.

An explanation for the calculated oxidation numbers is provided by Goodenough's bond model [183]. The observed longer Fe–Fe distances are related to delocalised electrons of the iron ions parallel to the FeS_4 tetrahedral chains. The remaining electrons are localised between two iron ions orthogonal (along the *a*-axis) to the direction of the FeS_4 tetrahedral chains. The investigation of barium, rubidium and caesium selenoferrates yields similar correlations [175]. For these selenoferrates, a correlation between a higher oxidation state of the iron and a longer distance of the iron atoms parallel to the *c*-axis could be found. The observed effect is significantly greater for the AFe_2Se_3 compounds than for the AFe_2S_3 compounds. However, the oxidation state of iron is not only dependent on the bond length of the Fe-S or Fe–Se bonds, but is influenced by the cation located between the tetrahedra [181]. Therefore, it must be assumed that there are interactions between the cations of the AS_{10} or $A_{10}Se_{10}$ polyhedra and the FeS_4 tetrahedra. A larger volume of the AS_{10}/ASe_{10} polyhedra leads to a weakening of the ionic bond between Fe–S/Fe–Se [184]. This slightly weaker bond could lead to a better overlap of the orbitals of the iron atoms and sulphur/selenium atoms as well as a stronger repulsion of the iron atoms. The exact bonding character of the Fe–S/Fe–Se bond has not yet been sufficiently investigated. To determine the exact electron configuration of the iron, detailed Mössbauer spectra and magnetic susceptibility measurements would have to be carried out.

The empirical oxidation state of the iron of $(NH_4)Fe_2S_3$ and $(NH_4)Fe_2Se_3$, newly synthesised in the course of this work can be estimated from the oxidation states of similar compounds given in the literature. Since the ionic radius for ammonium is between that of a potassium ion and rubidium ion, it can be assumed that the oxidation state of the iron in $(NH_4)Fe_2S_3$ is between the oxidation states of the single atoms in the compounds KFe_2S_3 and $RbFe_2S_3$. Therefore, the iron atoms in $(NH_4)Fe_2S_3$ probably have an oxidation state between +2.66 and +2.77. An oxidation state for the compounds with selenium has not yet been determined.

A comparison of the length of the Fe–Fe bonds along the FeS_4 tetrahedral chains shows that the Fe–Fe bond in $(NH_4)Fe_2Se_3$ is significantly longer than the Fe–Fe bond in $(NH_4)Fe_2S_3$. Therefore, from the general trend of a higher oxidation state on iron with a larger Fe–Fe distance along the FeS_4 tetrahedral chains, a higher oxidation state

should result for iron in $(NH_4)Fe_2Se_3$ than in $(NH_4)Fe_2S_3$.

On the basis of the structural parameters, R. Roß und T. Bredow [185] calculated the conductivity and the magnetic state of $NH_4Fe_2S_3$ and $NH_4Fe_2Se_3$ with the programme *CRYSTAL* [186] using the *pob-TZVP-rev2* basis set [187] and the GGA-hybrid-method M06-D3 [188, 189]. A band gap of 2.96 eV was calculated for $NH_4Fe_2S_3$, which is in the range of a semiconductor. At an external pressure of 20 GPa the conductivity of the ferromagnetic state increases abruptly to a weak conductor. The calculation for $NH_4Fe_2Se_3$ concluded, that $NH_4Fe_2Se_3$ is in the range of a semiconductor with a band gap of 2.71 eV. Above 15 GPa the ferromagnetic state becomes electrically conductive and corresponds to the order of magnitude of a weak conductor. At 25 GPa, the ferromagnetic state becomes energetically more stable than the configuration of the ground state.

4.4 $[Mn_2(HPO_3)_2(C_2H_8N_2)]$

$[Mn_2(HPO_3)_2(C_2H_8N_2)]$ [168] forms colourless needles and crystallises in the orthorhombic space group *Pnnm* in a yet unknown structure typ. The lattice parameters of the unit cell are $a = 15.610(7)$ Å, $b = 4.9805(11)$ Å, $c = 6.0094(14)$ Å. The volume of the unit cell is $V = 467.20(26)$ Å^3. The asymmetric unit of the unit cell has the composition $MnPO_2NCH_3$. The dataset contained 999 reflections from which 587 were unique. The quality factor R_{int} on averaging symmetry equivalent reflections amounted to 1.13 %. The hydrogen atoms of ethylenediamine were placed in geometrically calculated positions, refined using a "riding model" [127]. The hydrogen of the phosphite anion could be identified from the Fourier difference map.

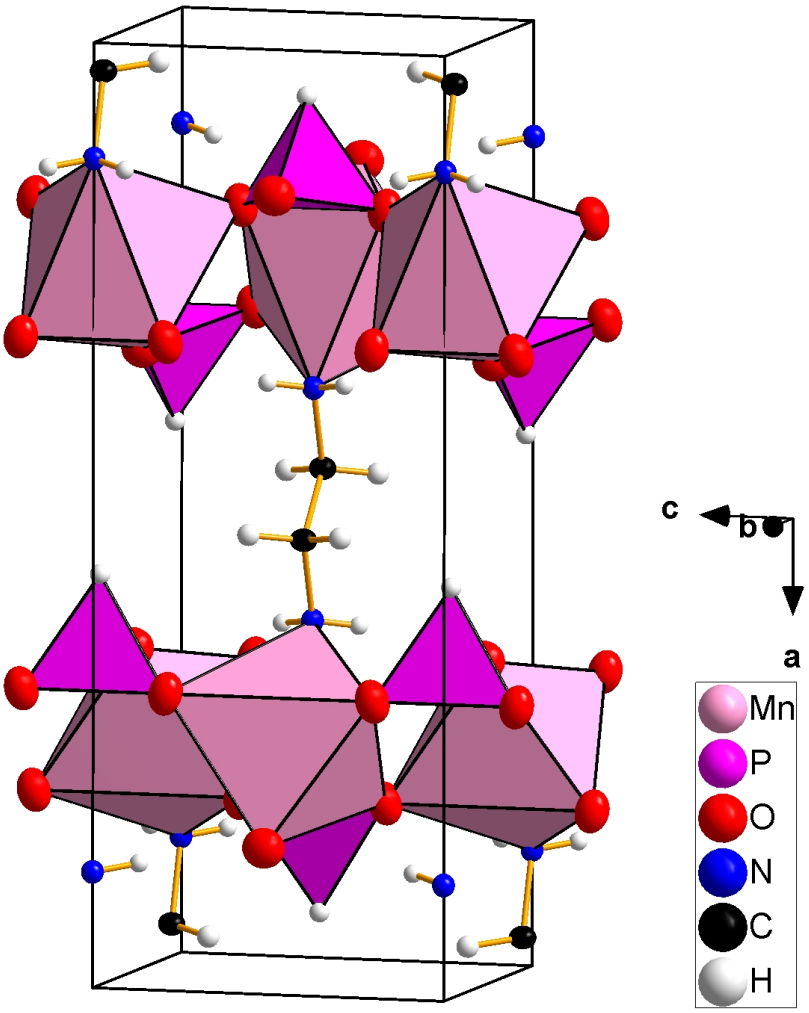

Figure 4.43: Extended unit cell of $[Mn_2(HPO_3)_2(C_2H_8N_2)]$ with octahedral coordination of the manganese atoms and tetrahedral coordination of the phosphorus atoms. Ellipsoids represent a probability of 90 %. Hydrogen atoms are drawn with arbitrary radii.

The structure (Fig. 4.43) contains layers built up from $Mn(O_5N)$ octahedra (Fig. 4.44). These layers stack on top of each other orthogonally to the *a*-axis. Between the layers of distorted-octahedrally surrounded Mn^{2+} are ethylenediamine molecules that coordinate with the nitrogen atom to the Mn^{2+} (Fig. 4.45). The dis-

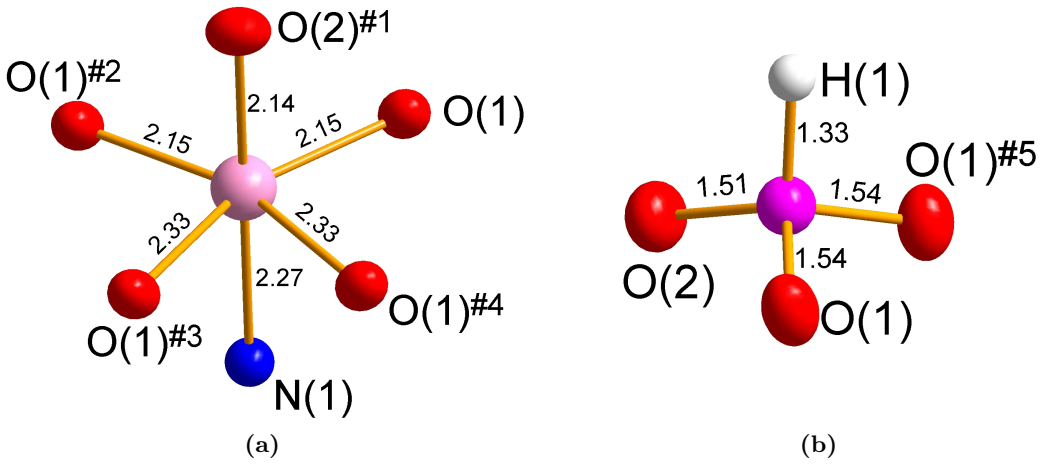

Figure 4.44: (a) Representation of the $Mn(O_5N)$ octahedron with bond lengths in Å. (b) Representation of the HPO_3 tetrahedron with bond lengths in Å. The displacement ellipsoids represent a probability of 90 % and 40 % for the hydrogen atom. Indices indicate the following symmetry operations: #1: -x+1/2,y-1/2,-z+1/2; #2: x,y,-z+1; #3: -x+1/2,y+1/2,z+1/2; #4: -x+1/2,y+1/2,-z+1/2; #5: x,y,-z.

torted $Mn(O_5N)$ octahedra are linked to each other via corners. A total of four phosphite anions $(HPO_3)^{2-}$ (IUPAC recommendation: phosphonate) and one nitrogen atom of ethylenediamine coordinate to one Mn^{2+} ion. Three phosphite anions $(HPO_3)^{2-}$ coordinate to Mn^{2+} via one oxygen atom (O(1), $O(1)^{\#1}$ and $O(1)^{\#2}$) and the fourth $(HPO_3)^{2-}$ coordinates to Mn^{2+} with two oxygen atoms ($O(1)^{\#4}$ and $O(1)^{\#3}$), so that the central Mn atom is surrounded by five oxygen atoms. The Mn–$O(1)^{\#3}$ and Mn–$O(1)^{\#4}$ bond lengths are 0.18 Å longer than the average Mn–O bond lengths (2.15 Å) of the phosphite anions that coordinate to Mn^{2+} via one oxygen atom. The bond lengths Mn–O and Mn–N are shown in Figure 4.44. Moreover, the angle between $O(1)^{\#3}$–Mn–$O(1)^{\#4}$ is 64.0°, which is much smaller than the other angles between Mn and O, which amount to 87.1° for O(1)–Mn–$O(1)^{\#4}$ and 111.1° for O(1)–Mn–$O(1)^{\#2}$.

A comparison between the Mn–O bond lengths in the Mn(O5N) octahedra of $[Mn_2(HPO_3)_2(C_2H_8N_2)]$ with Mn–O bond lengths of structurally related compounds from the literature shows that the shorter Mn–O(1)/–$O(1)^{\#2}$/–$O(2)^{\#1}$ bonds are slightly below the average (2.22 Å) [190]. However, the longer Mn–$O(1)^{\#3}$/–$O(1)^{\#4}$ bonds of the $Mn(O_5N)$ octahedron are above the average. Due to the phosphite anion coordinating to the Mn^{2+} ion via two oxygen atoms, the coordination polyhedron is strongly distorted, which is reflected in the different Mn–O bond lengths. In similar

compounds such as $(C_2H_{10}N_2)[Mn_3(HPO_3)_4]$ [190] and $Mn(HPO_3)$ [191], only one oxygen atom of the phosphite anion coordinates to the central Mn atom. As a result, the octahedra are less distorted and the Mn–O bond lengths do not differ as much. The phosphite anion $(HPO_3)^{2-}$ is a representative of the phosphorus oxo anions and can be called the simplest compound of the class of phosphites $(RPO_3)_2$ with R = H. Phosphorus is present in the +III oxidation state. Various compounds of the light transition metals with phosphite are known in the literature [190], among with Mn(II) phosphite compounds. Phosphorus is tetrahedrally surrounded by three oxygen atoms and one hydrogen atom in $(HPO_3)^{2-}$. The oxygen atoms of a phosphite ion coordinate to two Mn^{2+}. The bond length between phosphorus and the two oxygen atoms coordinating to the same Mn^{2+} is 0.02 Å longer than the other P–O(1)$^{\#3}$/–O(1)$^{\#4}$ bond lengths. The bond lengths between phosphorus and oxygen or hydrogen are given in Figure 4.44.

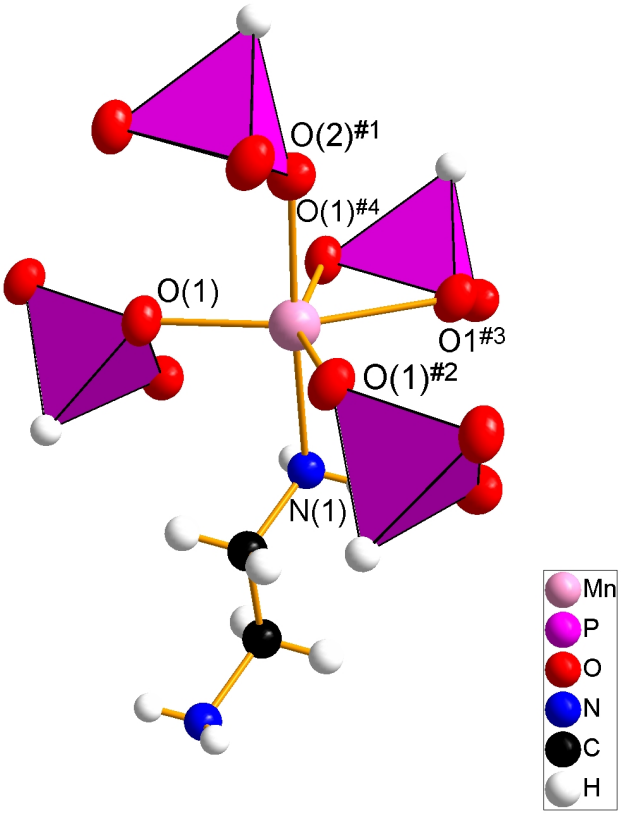

Figure 4.45: Representation of the octahedral environment of manganese with (HPO_3) tetrahedra. Ellipsoids represent a probability of 90 %. Hydrogen atoms are drawn with arbitrary radii. Indices indicate the following symmetry operations: #1: -x+1/2,y-1/2,-z+1/2; #2: x,y,-z+1; #3: -x+1/2,y+1/2,z+1/2; #4: -x+1/2,y+1/2,-z+1/2.

Redox reactions often take place in solvothermal syntheses. In this case, the manganese is oxidised so that Mn^{2+} ions are formed in the solution. Some divalent metal ions, including Mn^{2+}, Fe^{2+}, Co^{2+}, Ni^{2+} and Zn^{2+}, show a strong tendency to form

metal-ethylenediamine complexes [192]. Three ethylenediamine ligands coordinate to the central Mn atom, resulting in an octahedral coordination polyhedron. It can be assumed that Mn^{2+} can form further complexes in ethylenediamine.

A complex of manganese and ethylenediamine that is particularly interesting with regard to the structure of the product formed is the $[\{Mn(en)_2(enH)\}_2(\mu{-}en)]^{6+}$ cation [193]. In this complex, Mn^{2+} is surrounded by two ethylenediamine ligands, each occupying two coordination sites. The two other ethylenediamine ligands are bonded to manganese via a nitrogen atom, whereby one of the two ligands is bridged to the next Mn^{2+} cation. This results in a binuclear complex cation. The structure of $[Mn_2(HPO_3)_2(C_2H_8N_2)]$ contains a bridging ethylenediamine ligand linking two manganese ions. This suggests that the $[\{Mn(en)_2(enH)\}_2(\mu{-}en)]^{6+}$ cation (Fig. 4.46) is partially incorporated into the structure of the product as a structure-directing template. In general, it can be stated that metal-ethylenediamine complexes are often incorporated into the final compound as a structure-directing template. Therefore, molecular structures or chain structures result [192].

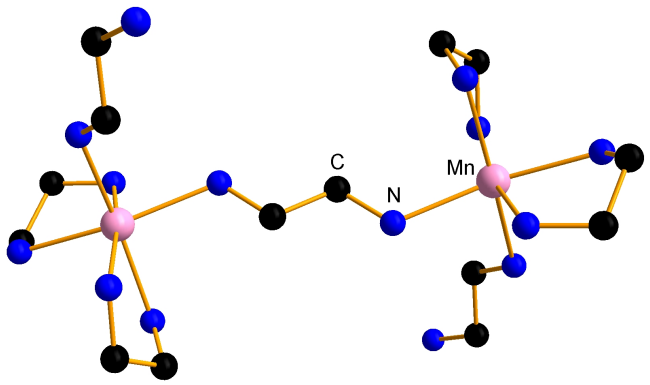

Figure 4.46: Representation of the $[Mn(en)_2(enH)_2(\mu{-}en)]^{6+}$ cation in $(enH_2)[Mn(en)_2(enH)_2(\mu{-}en)](Ge_2Se_7)_2$ [193].

The compound $[Mn_2(HPO_3)_2(C_2H_8N_2)]$ contains a large amount of oxygen. During the synthesis, apart from weighing in the reactants, work was carried out under argon and vacuum. Nevertheless, contamination by oxygen or water from the air cannot be excluded. One reactant used for the synthesis was red phosphorus.

The phosphorus used for the synthesis was stored in air for a long period, so it cannot be ruled out that the phosphorus reacted with oxygen from the air. To increase the reactivity of the phosphorus, it was mortared in air, which could contribute to the formation of further phosphorus-oxygen compounds. In addition, it should be noted that manganese metal reacts slowly and superficially with oxygen when stored for a longer period of time.

4.5 Sulphur and Selenium Compounds Synthesised in Liquid Ammonia

4.5.1 $K_9Se_{2.88}(Se_2)_{1.12}OH$

$K_9Se_{2.88}(Se_2)_{1.12}OH$ forms yellow, hexagonal, flat crystals and crystallises in the monoclinic space group $C2/m$ in a yet unknown structure type. The lattice parameters of the unit cell are $a = 9.2535(3)$ Å, $b = 16.5172(5)$ Å, $c = 18.0434(7)$ Å with the monoclinic angle $\beta = 98.595(2)°$. The volume of the unit cell is $V = 2726.82(16)$ Å^3. The number of formula units is 4, the dataset contained 5397 reflections from which 3141 were unique. The quality factor R_{int} on averaging symmetry equivalent reflections amounted to 5.12 %.

The asymmetric unit consists of nine potassium atoms, seven selenium atoms and one hydroxide molecule. Four selenium form dumbbell like Se_2^{2-} anions. During the refinement it became apparent that the Se(5) position was not occupied by the Se^{2-} anion alone but the Se_2^{2-} dumbbell position of Se(6)–Se(7). Se(5) is approximately half-way between the bond of Se(6)–Se(7). A statistical distribution was calculated for Se(5) and Se(6)–Se(7). Consequently, the disorder of the Se_2^{2-}, formed by Se(6)–Se(7), and the isolated Se^{2-} (Se(5)) was refined under the constraint $SOF(Se(6) + Se(7)) + SOF(Se(5)) = 1$. The site occupation factors were refined to 0.12 for Se(6)–Se(7) and 0.88 for Se(5).

The fact that the O(1) position is oxygen, and not nitrogen from the ammonia, is supported by the noticeable alignment of the hydrogen with the nearby doubly negatively charged selenium Se(2), thus achieving charge balance. The hydrogen atom H(1) could be identified from the Fourier difference map and is located at a distance of 1.11 Å from the oxygen O(1). The hydroxide ion is octahedrally surrounded by potassium. The selenium atom (Se(2)) is located on the $4i$ position with positional symmetry m. The hydroxide hydrogen is aligned to it with a distance of 2.56 Å with an O–H–Se angle of 174.8°. A Se$\cdots$H–O hydrogen bond can be interpreted.

The anion polyhedra are shown in Fig. 4.47. In the dumbbell anion of Se(6)–Se(7), the atom Se(6) is surrounded by eight potassium ions. The bond lengths of 2.39 Å are consistent with the literature e. g. K_2Se_2 [161]. Often, when coordinated by monovalent cations, double-capped trigonal prismatic environments, or square prismatic environments are described for selenium (compare Subsection 4.2.2). Here, the description of a square prismatic environment with idealised D_{4d} symmetry fits best. The pyramidal environment of the Se(7) atom, with coordination number 5 and idealised D_{5h} symmetry, is unusual. This is a result of the statistical distribution of the anions. Since

all K atoms participating in the coordination of Se(7) (12 %) coordinate Se(5) (88 %), the pentagonal pyramid is the compromise within the packing of the structure. The deviations from the ideal polyhedron around Se(5) was calculated by the method of Continuous Symmetry Measures [135] using the program SHAPE [136]. The coordination of Se(5) is close to the C_{4v} symmetry of the spherical capped square antiprism (1.83 %), but even closer to the C_s symmetry of the muffin-like polyhedron (1.53 %) with nine potassium atoms at a distance of 3.33 Å to 3.87 Å.

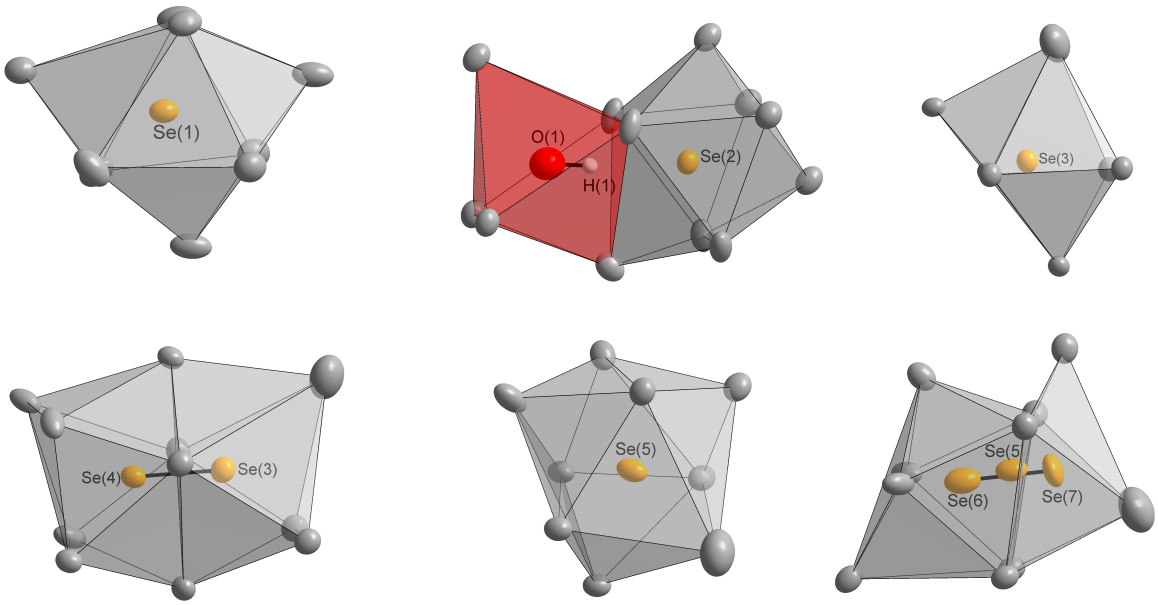

Figure 4.47: The different anion polyhedra in $K_9Se_{2.88}(Se_2)_{1.12}OH$. Potassium in grey, oxygen in red and selenium in orange. The displacement ellipsoids represent a probability of 90 %. Indices indicate the following symmetry operations: #1: -x+1,-y+1,-z; #2: x,-y+1,z-1/2; #5: -x+3/2,y+1/2,z; #6: -x+3/2,y-1/2,z.

Another discrete doubly negatively charged Se(1) is located on the 8*j* site on a general position. Se(1) and Se(5) have a similar environment by K ions. Thus, both selenium atoms are surrounded by nine potassium atoms each. In the case of Se(2), the hydroxide hydrogen is present in the coordination sphere, forming a hydrogen bond with 2.56 Å. The coordination octahedron around O(1) (OK_6) shares a triangular face with the coordination polyhedra of Se(2). Across this triangular face, the hydroxide hydrogen coordinates to Se(2). Se(3) and Se(4) are present as a $[Se_2]^{2-}$ dumbbell. The bond distance within the dumbbell is 2.42 Å.

The coordination sphere of K(9) was investigated in more detail because the displacement ellipsoid is significantly larger compared to the other potassium atoms (Fig. 4.48). In addition, there is a very short distance to Se(7) with 2.41 Å. Within the potassium coordination polyhedron, two different types of anions are present, Se^{2-}

and $(Se_2)^{2-}$ anions. The two opposite corners of the polyhedron are statistically occupied. 12 % of these positions are occupied by Se(7) (dumbbell) and 88 % by Se(5) (d(Se(5)–K(9)) 3.43 Å).

The remaining four corners of the octahedron are occupied by Se(3) from the Se dumbbell Se(3)–Se(4) and its symmetry generated positions. Due to the mixed occupation by the Se dumbbell Se(6)–Se(7) and the single Se(5), K(9) must therefore adapt to the environment and thus manifests itself in the enlarged displacement ellipsoid. Since the bond distances Se(5)–K(9) and Se(7)–K(9) vary considerably, the influence is correspondingly large (d(Se(5)–K(9)) = 3.43 Å, d(Se(7)–K(9)) = 2.42 Å, Δ = 1.21 Å). Attempts were made to refine K(9) with a disorder as well. However, these attempts were unsuccessful because no second potassium position was presented for K(9) in the Fourier difference map and thus a refinement with a disorder model was not possible. The displacement of the potassium atom is probably too small in this case, and the occupation of the second position can be assumed to be very small with a maximum of 12 %.

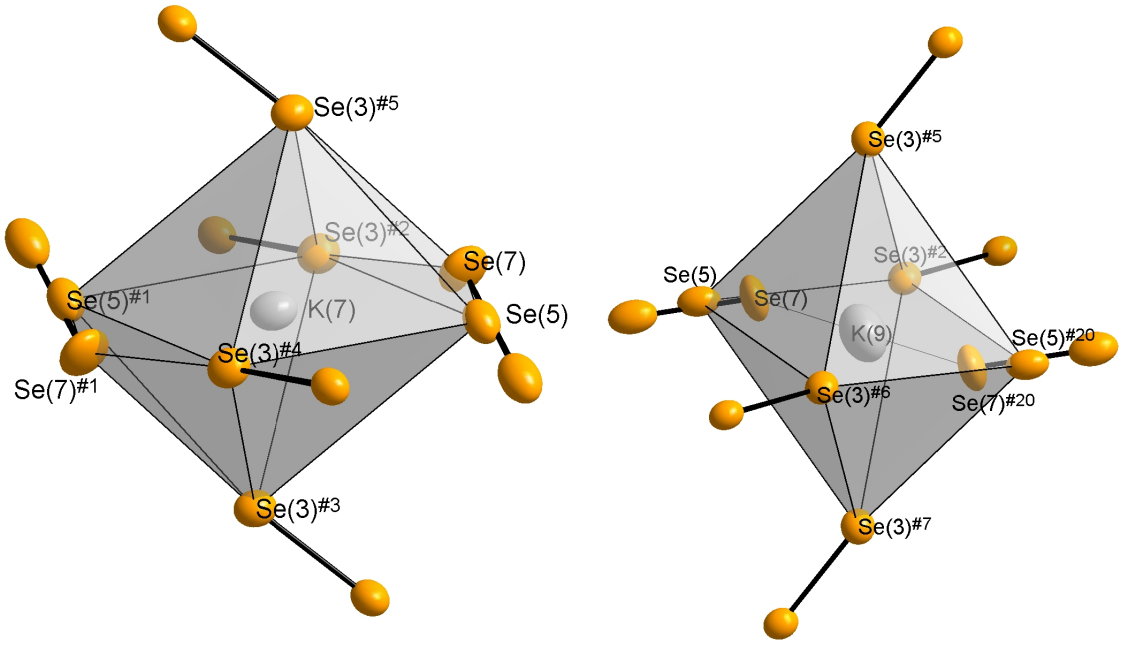

Figure 4.48: The polyhedra around K(7) and K(9). The displacement ellipsoids represent a probability of 90 %. Indices indicate the following symmetry operations: #1: 1-x,y,-z; #2: 1/2-x, 12-y, -z; #3: 1/2+x, 1/2-y, z; #4: 1/2+x, -1/2+y, z; #5: 1/2-x, -1/2+y, -z; #6: -1/2+x, -1/2+y, z; #7: -1/2+x, 1/2-y, z; #8 -x, y, -z; #20: -x,y,-z.

The two mixed Se positions are present in the coordination polyhedron of K(7) (Fig. 4.48). Again, the mixed anion positions occupy opposite corners of the octahedron. The distance K(7)–Se(7) (3.22 Å) is similar to the distances present in the structure of K_2Se_2 [161]. On the other hand, the distance d(K(9)–Se(7)) with 2.41 Å

is unusually short. This distance is only approximately 0.3 Å longer than the longest Se–Se distance in Se_5^{2-} chains [194–196]. If it is assumed that the K(9) position is partially occupied by selenium, a Se_5^{2-} chain would result, which, however, is only present to 12 %. The charge balance could then be achieved if the oxygen position were interpreted as a water molecule, but only for 12 %. K(9) is additionally coordinated by four fully occupied Se positions and is octahedrally coordinated, similar to K(7). The partial occupation of the K(9) position is therefore electrostatically unfavourable. Starting from a Se_5^{2-} chain, the middle Se atom at the K(9) position would be coordinated just by selenium and only at a distance of 4.3 Å would other K atoms be present. The EDX spectrum shows no other elements present in the crystals except Se and K, besides oxygen, carbon and fluorine. The latter elements are caused by polyfluorinated oil and the carbon coated sample holder. A different element instead of potassium at the K position is therefore excluded. Only 12 % of the dumbbell of Se(6)–Se(7) is present. Therefore, it can be assumed that the short bond of 2.41 Å occurs at this position due to packing effects. The displacement ellipsoids of K(9) and Se(7) are aligned in the same way.

In the unit cell (Fig. 4.49), it can be seen that the hydroxide ions and discrete Se^{2-} anions are located in one plane. Likewise, the doubly negatively charged anions are in one plane.

The source of oxygen is not known. Probably, by contamination of the glove box atmosphere, the potassium metal was partially oxidised. The oxide layer was removed by cutting it off with a knife. Small traces of potassium oxide nevertheless could have found their way into the reaction vessel. Without this fortunate mishap, this unusual chalcogenide-hydroxide, synthesised in liquid ammonia, would not have been discovered.

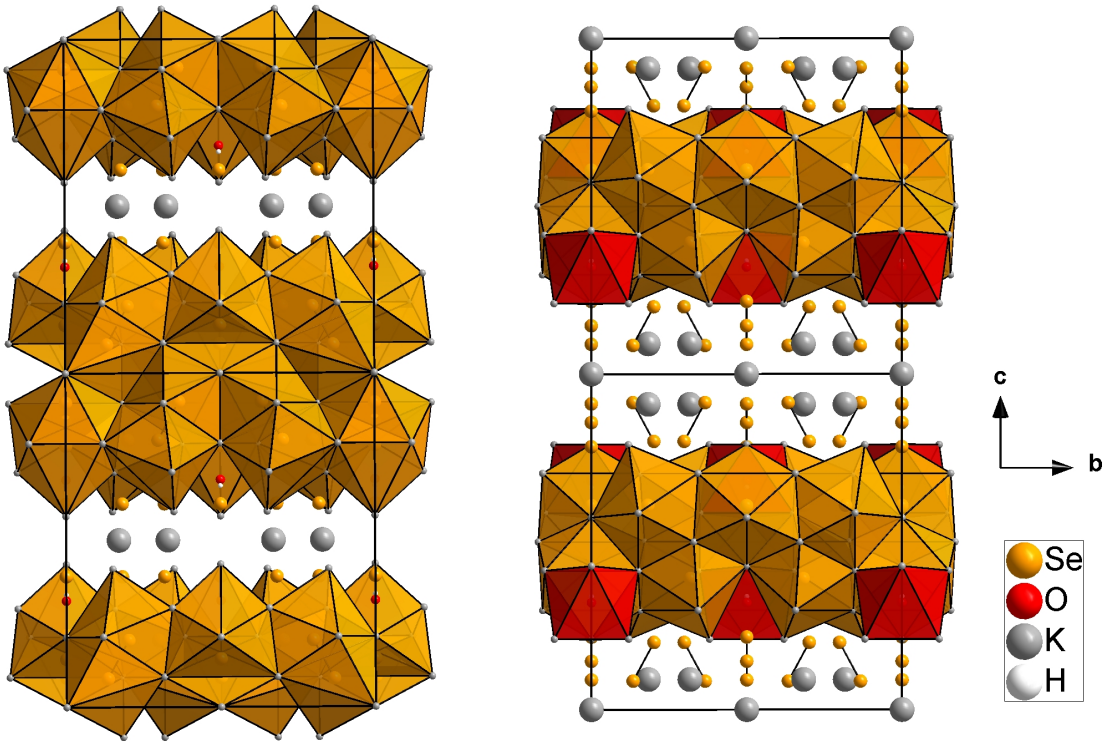

Figure 4.49: (Right) View of the extended unit cell of $K_9Se_{2.88}(Se_2)_{1.12}OH$ in *a*-direction with polyhedra around Se(5) and the dumbbell anions Se(2)–Se(3), Se(6)–Se(7). (Left) View of the extended unit cell of $K_9Se_{2.88}(Se_2)_{1.12}OH$ in *a*-direction with polyhedra around Se(1), Se(2), Se(3) and the hydroxide anion. Atoms are drawn as spheres of arbitrary radii.

4.5.2 As_3NS_3

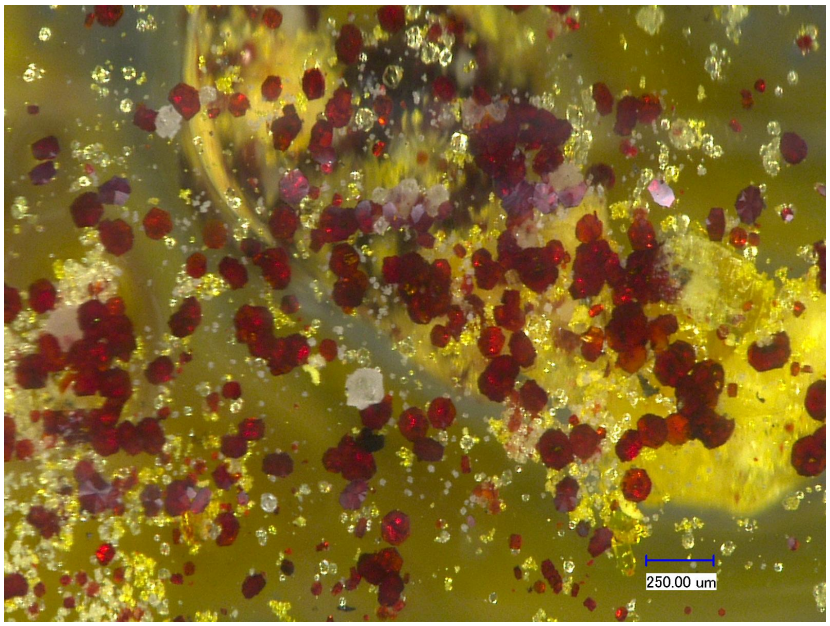

Figure 4.50: Red hexagonal crystals of As_3NS_3 with bright yellow rod-shaped crystals of $Mn(NH_3)_6As_4S_6 \cdot NH_3$ (Subsection 4.6.2).

As_3NS_3 crystallises as red, hexagonal, flat crystals (Fig. 4.50). For the structure analysis a suitable crystal of As_3NS_3 was selected. The X-ray diffraction data collection was performed at room temperature and revealed a hexagonal crystal system with the space group $P6_3/m$. The lattice parameters of the unit cell are $a = b = 10.7386(6)$ Å, $c = 3.2941(2)$ Å. The volume of the unit cell is $V = 328.97(4)$ Å^3, the number of formula units is 2. The dataset contained 998 reflections from which 294 were unique. The quality factor R_{int} on averaging symmetry equivalent reflections amounted to 4.95 %.

After refinement of the structure model with only As, N and S, electron density remained on the c-axis. The largest difference Fourier map peak of 1.46 e$^-$/Å^3 was located at (0 / 0 / 1/4). The second largest peak amounted to 0.67 e$^-$/Å^3. To investigate whether solvents might be involved, the measurement was repeated with the same crystal at 100 °C. The largest difference Fourier map peak of 1.27 e$^-$/Å^3 was located at (0 / 0 / 1/4). The second largest peak was of 1.18 e$^-$/Å^3 , the third largest peak of 0.97 e$^-$/Å^3. The difference between the largest peaks came out as somewhat smaller. After cooling to 20 °C, a third X-ray diffraction data collection was performed. The largest difference Fourier map peak of 1.13 e$^-$/Å^{3}was located at (0.64 / 0.69 / 3/4), the second largest of 0.67 e$^-$/Å^3. The gap was still present, but the electron density was no longer located on the c-axis. Therefore a solvent molecule was finally excluded from the structure model. The compound can be stored in air.

Only limited data could be collected in direction of the c^*-axis, since already from the second layer ($hk2$) onwards only few reflection intensities are recognisable, the third ($hk3$) and fourth layers ($hk4$) provide little to no reflection intensities (Fig. 4.51). This is due to the flat crystal growth. This additionally complicates the evaluation of very low electron density on the c-axis.

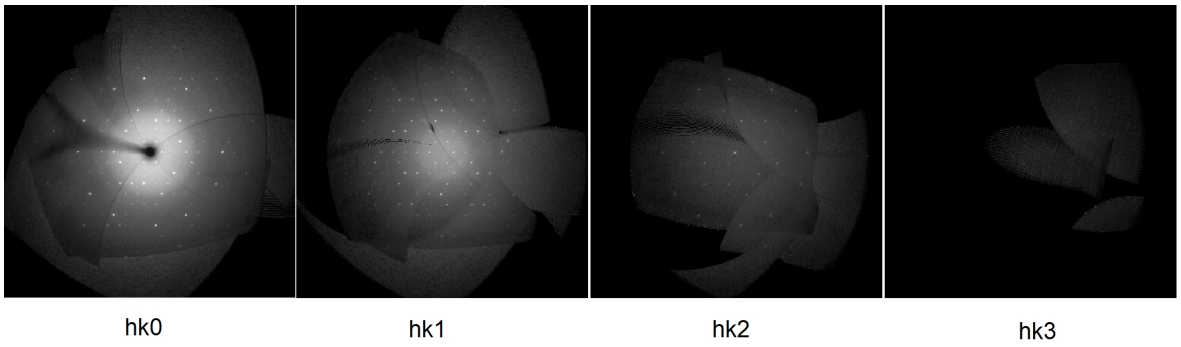

Figure 4.51: X-ray diffraction images of As_3NS_3 at 293 K along c^*-direction, layers $hk0$, $hk1$, $hk2$ and $hk3$ are shown. The X-ray single crystal reflection data of As_3NS_3 of the third ($hk3$) and fourth layers show hardly any ($hk3$) to no reflection intensities for $hk4$.

In the same reaction ampoule the compound $[Mn(NH_3)_6][As_4S_6]\cdot NH_3$ (Subsection 4.6.2) was present. When a catalytic amounts of $MnCl_2$ was added to the mixture of Mn, As, S, the formation of As_3NS_3 was positively affected. Without the use of $MnCl_2$, As_3NS_3 was still present in the reaction ampoule, but in smaller amounts. The same phenomenon was observed for the isotypic structure As_3NSe_3 (Subsection 4.5.3), which formed alongside of $[Mn(NH_3)_6]_2[As_2Se_6]$ (Subsection 4.6.3). N, As and sulphur are present in the asymmetric unit. The nitrogen atom is located on the Wyckoff position $2c$ with local symmetry $\overline{6}$. With a bond distance of 1.85 Å it is linked to three arsenic atoms. The bond angle is 120°. The arsenic atom on $6h$, with local symmetry m, is linked to sulphur with a bond length of 2.28 Å. Sulphur is located on the Wyckoff position $6h$, with local symmetry m. This linkage results in a polymeric chain along the c-axis (Fig. 4.52). The bond length As–N and As–S are in a good agreement with an average value for the As–N (1.85 Å) and As–S (2.28 Å) single bond length, as derived from a statistical survey of the Cambridge Structural Database (CSD) [197].

Within the unit cell two of these one-dimensional chains run along the c-axis with an offset of ½ with respect to the c-axis (Fig. 4.53). The hexagonal structure is in the nature of the described bonding pattern, as is the 6_3 helical axis, which passes through the centre of gravity of the one-dimensional chain, the three-bonded nitrogen. Nitrogen is trigonal-planar surrounded by arsenic. This binding situation can be interpreted as a sp^2 hybridisation of the nitrogen. The nitrogen has the highest electronegativity in this compound with $\mathcal{X}_N = 3.04$ [178] and is covalently bonded to three arsenic

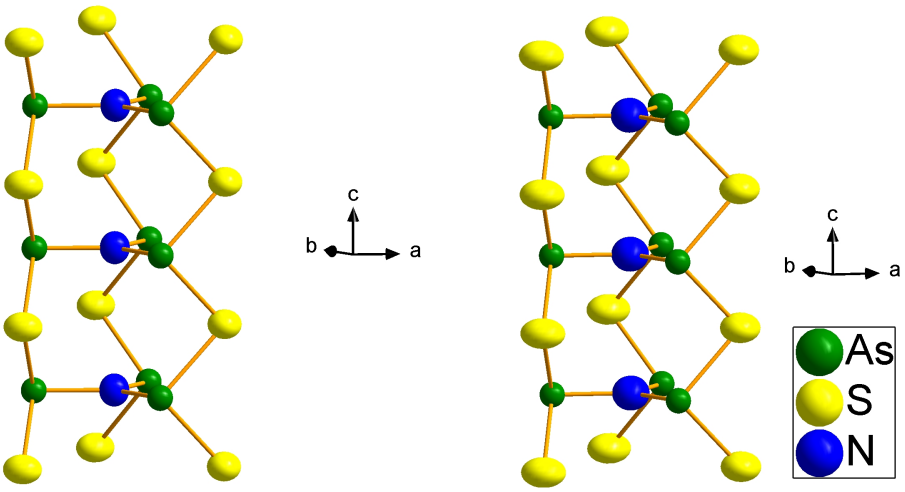

Figure 4.52: (Left) One-dimensional chain in As_3NS_3 at 293 K, (right) respectively As_3NS_3 at 373 K. Displacement ellipsoids are scaled with a probability of 90 %.

atoms. Sulphur with an electronegativity of $\mathcal{X}_S = 2.58$ [178] binds with two arsenic atoms ($\mathcal{X}_As = 2.18$ [178]). The angle As–S–As is 92.4°, deviating strongly from a tetrahedral angle. According to the VSEPR [198], this can be explained by two free electron pairs on the sulphur atom, which point outwards of the chain. The trivalent trigonal-pyramidal coordinated As can be interpreted as AX_3E (A=As, X=ligands, E=lone pair) with an expressed lone pair [198]. The binding situation results in the formula As_3NS_3. The small Pauling electronegativity differences support the covalent nature of the one-dimensional polymeric chain in As_3NS_3.

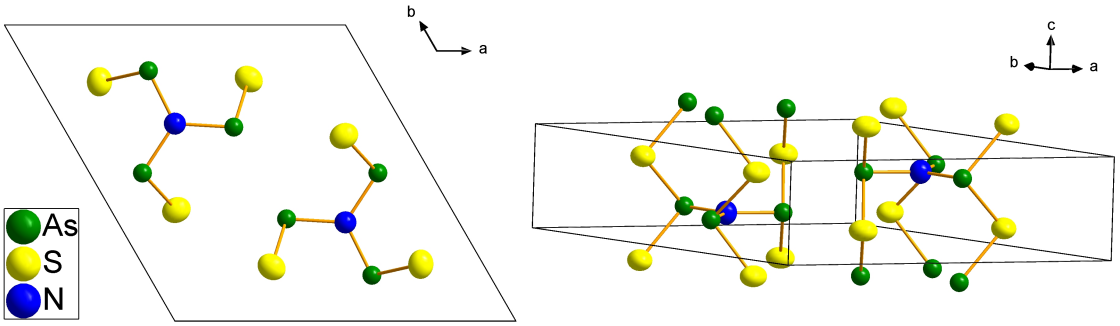

Figure 4.53: (Left) View in *c*-direction of the unit cell of As_3NS_3 at 293 K. (Right) Perspective view of the extended unit cell of As_3NS_3 at 293 K. Displacement ellipsoids are scaled with a probability of 90 %.

As_3NS_3 can be decomposed into As_2S_3 [199] and AsN. AsN was first detected in 1934 by Spinks [200] by using UV spectroscopy. Only recently has it been achieved to produce crystalline AsN [201] under high pressure conditions generated by diamond anvil cells (DACs) and high temperature-quenching rate inherent to laser heating technique. AsN was formed after heating up to 1400 K at a pressure of 25 GPa. AsN

crystallises in the the cubic space group $P2_13$. The N–As–N angles in AsN (98.5° to 103.8°) are slightly larger than the N–As–S angles in As_3NS_3 (92.49° to 99.57°). The N–As–N angles differ greatly. While in AsN the NAs_3 units form trigonal pyramids with angles 103.4° to 112.7°, the NAs_3 unit in As_3NS_3 is trigonal planar. However, As_3NS_3 is related to tris-(dimethylarsino)-amine $(Me_2As)_3N$ [202]. In the structure of $(Me_2As)_3N$ (Fig. 4.54), N is trigonal planar surrounded by As (N–As–N=119.6° to 120.2°, d(As–N)=1.84 Å to 1.86 Å). Two methyl groups bind to each of the three arsenic atoms. As is present in the trigonal pyramid with As at the top of the pyramid. By replacing the methyl group with S, which again binds to a second As, the chain structure of As_3NS_3 can be derived. The planar NAs_3 moiety as a central and typical structural feature, however, is present in both structures.

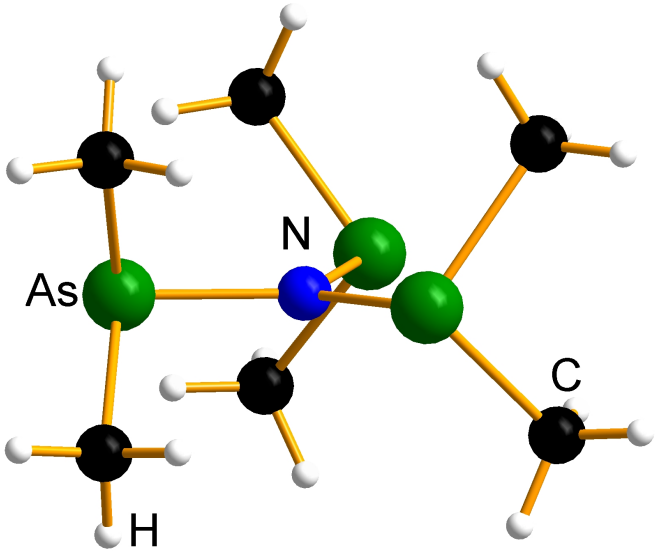

Figure 4.54: The molecular structure of $(Me_2As)_3N$. Atoms are drawn as spheres of arbitrary radii.

4.5.3 As_3NSe_3

As_3NSe_3 crystallises as metallic, rod-shaped crystals. For the structure analysis a suitable crystal of As_3NSe_3 was selected. The X-ray diffraction data collection was performed under a cold nitrogen gas flow (123 K) and revealed a hexagonal crystal system with the space group $P6_3/m$. The lattice parameters of the unit cell are $a = b = 10.8641(16)$ Å, $c = 3.4651(12)$ Å. The volume of the unit cell is $V = 354.19(16)$ Å^3, the number of formula units is 2. The dataset contained 4880 reflections from which 316 were unique. The quality factor R_{int} on averaging symmetry equivalent reflections amounted to 24.36 %. The crystal was of poor quality, therefore the X-ray diffraction data were integrated with the software *APEX4* [128].

As_3NSe_3 is isotypic to As_3NS_3 (see Subsection 4.5.2). The asymmetric unit contains N, As, and Se. These three atoms form an one-dimensional polymeric chain along [001] (Fig. 4.55). The N–As bond length is 1.85 Å, and the As–Se bond length is 2.42 Å, which is consistent with data of the Cambridge Structural Database (CSD) [197] and the As–Se bond lengths present in $Rb_5(AsSe_3)Se \cdot 2\,NH_3$ (Subsection 4.6.1) and $[Mn(NH_3)_6]_2[As_2Se_6]$ (Subsection 4.6.3). The N–As–Se angles in As_3NSe_3 (91.37° to 99.10°) are in the same range compared to As_3NS_3 (N–As–S: 92.49° to 99.57°).

As_3NSe_3 was obtained as a by-product in the synthesis of $[Mn(NH_3)_6]_2[As_2Se_6]$ (Subsection 4.6.3). By adding catalytic amounts of $MnCl_2$, the yield of As_3NSe_3 could be increased.

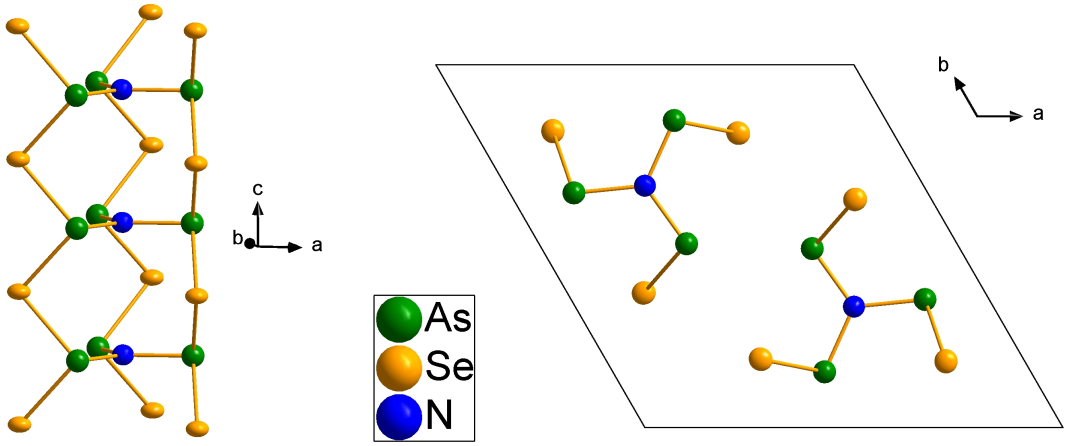

Figure 4.55: (Left) One-dimensional chain in As_3NSe_3 with displacement ellipsoids are scaled with a probability of 90 %. (Right) View in *c*-direction of the unit cell of As_3NSe_3. Displacement ellipsoids are scaled with a probability of 90 %.

4.6 Chalcogenidoarsenates

4.6.1 $Rb_5(AsSe_3)Se\cdot 2\,NH_3$

$Rb_5(AsSe_3)Se\cdot 2\,NH_3$ crystallises as orange prismatic crystals. For the single crystal structure analysis a suitable crystal was selected and fixed on the goniometer head of the diffractometer. X-Ray diffraction data collection was performed under a cold nitrogen gas flow (123 K) and revealed an orthorhombic crystal system with the non-centrosymmetric space group $P2_12_12_1$ (No. 19). The lattice parameters of the unit cell are $a = 8.7877(7)$ Å, $b = 10.7419(7)$ Å, $c = 17.4683(10)$ Å. The volume of the unit cell is $V = 1648.95(19)$ Å^3 with 4 formula units. The dataset contained 6352 reflections from which 3616 were unique. The quality factor R_{int} on averaging symmetry equivalent reflections amounted to 16.21 %. The displacement parameters of the nitrogen atoms were refined isotropic. SHELXL [127] suggested an inversion twin. The refinement of the inversion twin resulted in a relative batch scale factor (BASF) of 0.39(12). Accordingly, the measured crystal was not enantiopure. The crystals were weakly reflecting, which is the reason for the high R_{int}.

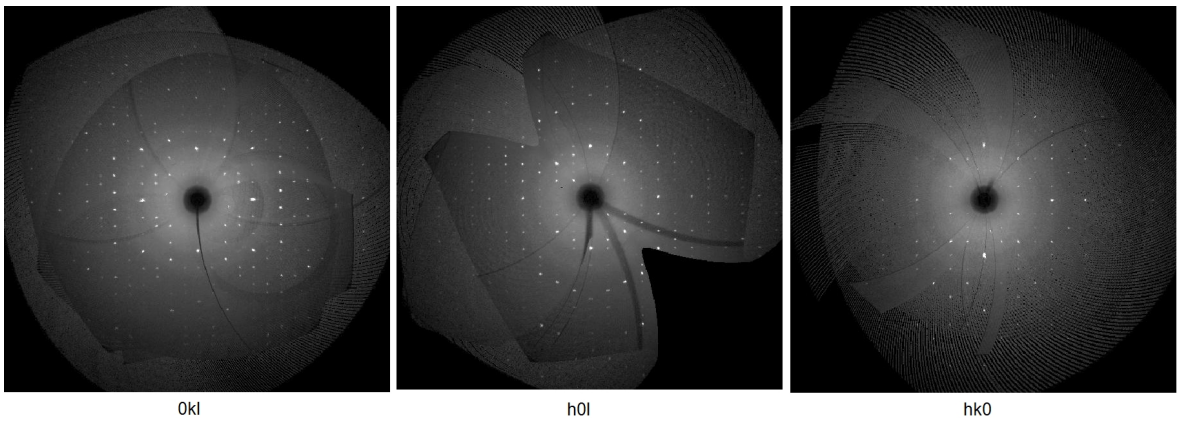

Figure 4.56: X-ray diffraction images of the zero layers $0kl$, $h0l$ and $hk0$. The X-ray single crystal reflection data of $Rb_5(AsSe_3)Se\cdot 2\,NH_3$ show weak reflection intensities in a^* and b^*-direction.

The two $AsSe_3^{3-}$ anions were localised directly in the asymmetric unit in the structural solution with SHELXL [127]. Since the crystals outgas at room temperature, the two nitrogen positions present in the asymmetric unit are interpreted as ammonia molecules. The remaining electron densities are interpreted by SHELXL [127] as rubidium. The resulting molecular formula $Rb_6(AsSe_3)\cdot 2\,NH_3$, however, indicates four negative charges for the $AsSe_3$ anion,which seems highly unlikely, since this anion is known from the literature with three negative charges as $AsSe_3^{3-}$ [203]. Since Rb (37 electrons) and Se (34 electrons) are hard to distinguish via X-ray diffraction, chemically the most reasonable position for a further selenium atom in the asymmetric

unit was determined by its most reasonable surrounding. Thus, the molecular formula $Rb_5(AsSe_3)Se\cdot 2\,NH_3$ was obtained. With five positive charges provided by Rb^+, the anions come out as Se^{2-} and $AsSe_3^{3-}$, thus the $(8-N)$ rule of the anions is fulfilled and the charge balance of the compound is correct, considering that ammonia molecules are present and not ammonium ions.

After the diffraction data collection, the entire crystal was examined for the composition via an EDX spectrum. Due to the high sensitivity of the compound, hydrolysis occurred in the short period of time when the crystal was exposed to air before entering the vacuum chamber of the EDX spectrometer. The analysis gave a substantial content of sodium in the sample, which could not be disregarded. In the following, attempts to include Na in the refinement of the crystal structure were undertaken. First, Na was placed on the Rb positions, in both ways, fully occupied and with Na/Rb in mixed occupation. For the positions that were refined with sodium, a non-positive definite warning was issued for the displacement ellipsoids and the structural model yielded significantly worse R-values. Therefore, this structural model was discarded. The used rubidium metal was examined for traces of sodium, but none could be detected. Therefore, the already developed structural model was kept.

Since the compound is highly sensitive to hydrolysis, it is assumed that the reaction with atmospheric moisture will yield hydroxides reacting with the soft glass of the glass tube carrying the crystal, resulting in a reaction when the crystal was transferred to the EDX carrier. This allows sodium to be dissolved from the glass and explains the traces of sodium detected. The small traces of sulphur are due to an impurity of the selenium used. The selenium was purified by sublimation, but obviously sulphur was volatile and contaminated the deposited Se. The traces are so small, however, that no improvement in the refinement could be observed when the selenium positions were partly occupied with sulphur.

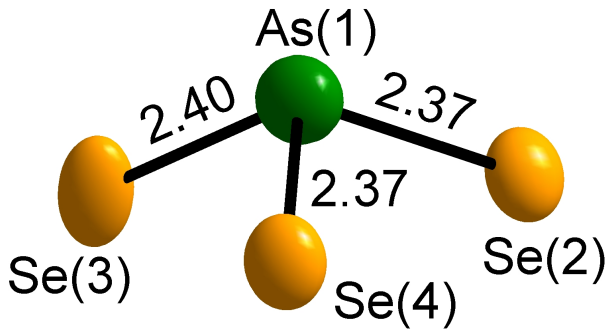

Figure 4.57: The $AsSe_3^{3-}$ anion in $Rb_5(AsSe_3)Se\cdot 2\,NH_3$. The Se–As–Se angles are between 103.4 Å to 105.8 Å. Bond lengths in Å. The displacement ellipsoids represent a probability of 90 %.

In the anion $AsSe_3^{3-}$ (Fig. 4.57), three different bond lengths are present in the range of 2.36 Å to 2.40 Å with Se–As–Se angles of 103.4 Å to 105.8 Å. The bond lengths and angles are close to those in A($AsSe_3$) (A=Na, K) [203]. The degree of pyramidalisation is comparable to similar compounds also containing an $AsSe_3$ molecule. For this purpose, the distance between the arsenic atom and the plane spanned by the three selenium atoms was measured representing the height of the trigonal pyramid. In $A_3(AsSe_3)$ (A=Na, K) [203], a distance of 1.05 Å is present in $Na_3(AsSe_3)$ and a distance of 1.00 Å in $K_3(AsSe_3)$. In $Rb_5(AsSe_3)Se\cdot 2\,NH_3$ the distance is 0.98 Å. Thus, the $AsSe_3$ molecule fits well into the series of trivalent triselenoarsenates(III).

The isolated selenium atom is coordinated by seven rubidium atoms in a slightly distorted capped octahedron (Fig. 4.58), with idealised C_{3v} symmetry. The deviations from the ideal polyhedron was calculated by the method of Continuous Symmetry Measures [135] using the program SHAPE [136] and resulted in a deviation of 0.5 %. The Se(1)–Rb distances are between 3.32 Å to 3.52 Å.

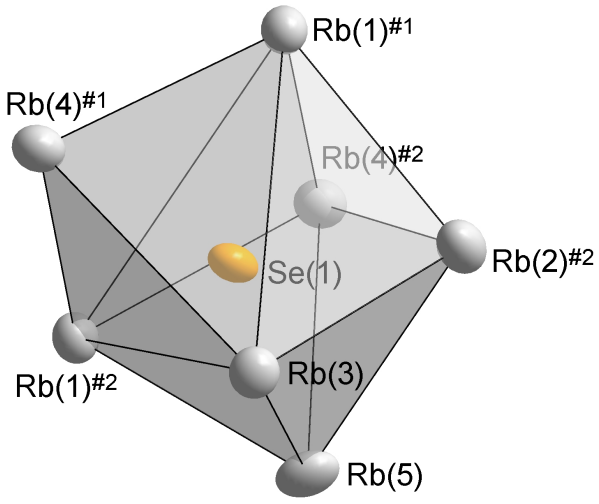

Figure 4.58: The coordination sphere of Se(1) in $Rb_5(AsSe_3)Se\cdot 2\,NH_3$. The polyhedron is best described as an capped octahedron with distances between d(Se–Rb) 3.32 Å to 3.52 Å. The displacement ellipsoids represent a probability of 90 %. Indices indicate the following symmetry operations: #1: -x+1,y-1/2,-z+1/2; #2: -x+1/2,-y+1,z-1/2.

In contrast, the selenium atoms in the $AsSe_3^{3-}$ anion have different surroundings. Se(2) has six rubidium ions, Se(3) five, and Se(4) again six rubidium ions in distances d(Se–Rb) between 3.46 Å to 3.69 Å, which is consistent with the literature [108, 116, 117]. The different coordination polyhedra are shown in Fig. 4.59. The extended unit cell of $Rb_5(AsSe_3)Se\cdot 2\,NH_3$ is shown in Fig. 4.60.

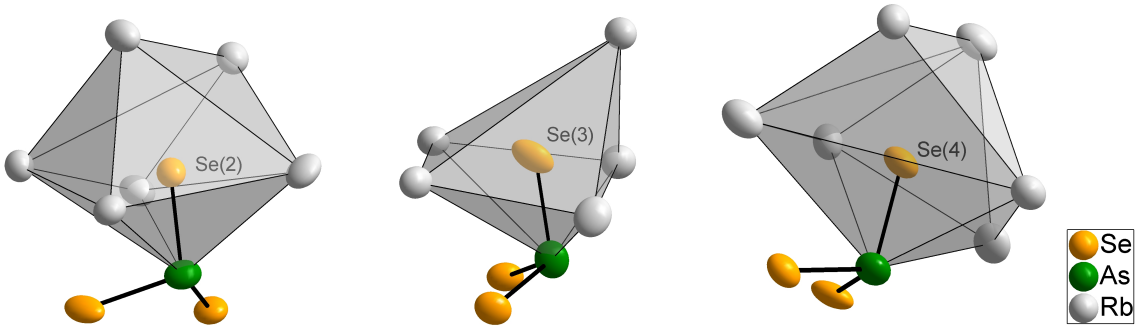

Figure 4.59: The $AsSe_3^{3-}$ anion in $Rb_5(AsSe_3)Se \cdot 2\,NH_3$. The different coordination polyhedra of Se(2), Se(3) and Se(4) are shown with distances d(Se–Rb) between 3.46 Å to 3.69 Å. The displacement ellipsoids represent a probability of 90 %.

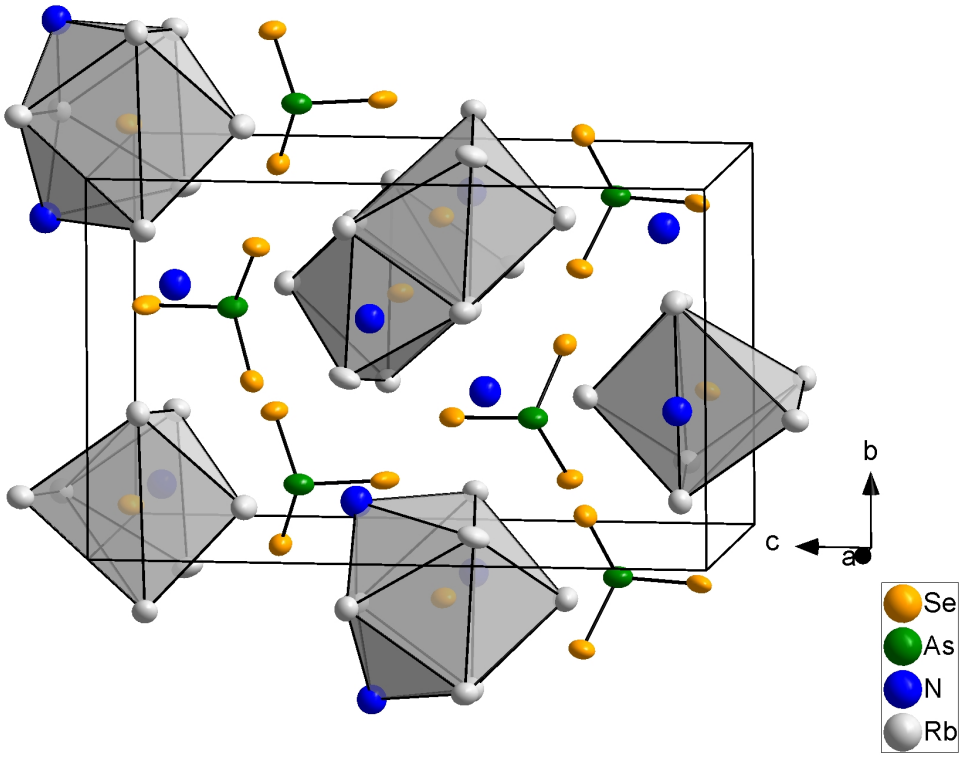

Figure 4.60: A perspective view of the extended unit cell of $Rb_5(AsSe_3)Se \cdot 2\,NH_3$. The displacement ellipsoids represent a probability of 90 %.

4.6.2 $[Mn(NH_3)_6][As_4S_6]\cdot NH_3$

$[Mn(NH_3)_6][As_4S_6]\cdot NH_3$ crystallises as bright yellow rod-shaped crystals (Fig. 4.61). For the structure analysis a suitable crystal was selected and fixed on the goniometer head of the diffractometer. X-Ray diffraction data collection was performed under a cold nitrogen gas flow (123 K) and revealed an orthorhombic crystal system. The systematic extinctions lead to the space groups $Pmna$ and $Pmn2_1$, of which the acentric latter one was confirmed in the course of the structure determination. The lattice parameters of the unit cell are $a = 8.1474(2)$ Å, $b = 11.5618(3)$ Å, $c = 10.8145(3)$ Å. The volume of the unit cell is $V = 1018.71(5)$ Å^3, the number of formula units is 2. The dataset contained 8065 reflections from which 2353 were unique. The quality factor R_{int} on averaging symmetry equivalent reflections amounted to 13.01 %. Hydrogen atoms were placed in geometrically calculated positions, refined using a "riding model" [127]. Polarity is present in the measured crystal, reflected in an absolute structure parameter of 0.020(14).

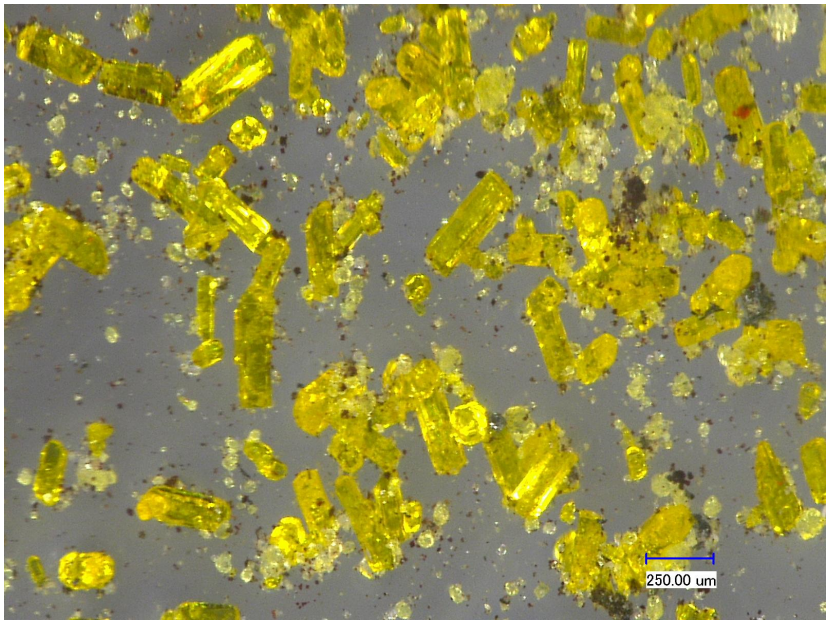

Figure 4.61: Bright yellow rod-shaped crystals of $Mn(NH_3)_6As_4S_6\cdot NH_3$ with red crystals of As_3NS_3 (Subsection 4.5.2).

The asymmetric unit consists of half of an $[As_4S_6]^{2-}$ anion, half of a $[Mn(NH_3)_6]^{2+}$ complex as well as one ammonia solvent molecule (Fig. 4.62). The nitrogen atoms N(3) and N(5) occupy the Wyckoff position 2a with m.. local symmetry. Hence, the bonded hydrogen atoms site occupation factor is set to one half. The Mn–N bonds in the $[Mn(NH_3)_6]^{2+}$ cation are in the range of 2.26 Å to 2.29 Å, which is consistent with other hexammine-manganese(II) complexes [57, 204, 205]. With N–Mn–N angles

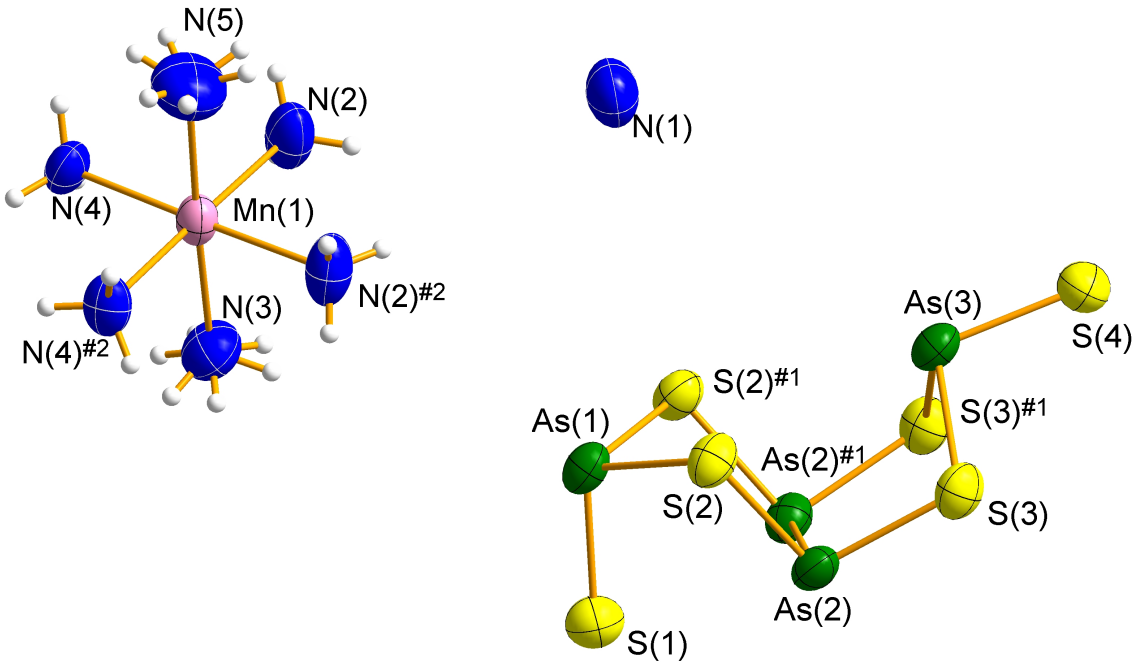

Figure 4.62: The molecules in the structure of $[Mn(NH_3)_6][As_4S_6]\cdot NH_3$ consisting of $[As_4S_6]^{2-}$ anions, octahedral $[Mn(NH_3)_6]^{2+}$ as well as ammonia solvent molecules. Hydrogen atoms are placed on geometrically calculated positions, refined using a "riding model" [127] and drawn with arbitrary radii. The displacement ellipsoids represent a probability of 90 %. The hydrogen atoms of the free solvent molecule could neither be obtained by residual electron density nor by calculation. Indices indicate the following symmetry operations: #1: -x+1,y,z; #2: -x,y,z.

89.1° - 94.2° and 178.6° - 177.8°, the coordination environment around the Mn atom is an almost ideal octahedron.

In the polyanion hexathiotetraarsenate $[As_4S_6]^{2-}$ the atoms S(1), As(1), As(3) and S(4) occupy the Wyckoff position 2*a* with *m*.. local symmetry, the atoms S(2), S(3) and As(2) are located on the general position. The polyanion is classified in the low-symmetric point group C_s. Arsenic and sulphur are alternately linked. Sulphur occurs in the polyanion both terminal and with two bonds to arsenic. The Zintl anion consists of two five-membered rings with terminal sulphur atoms. The five rings are connected by the As(2)–As(2)$^{\#1}$ bond, with a bond length of 2.57 Å. The angles between S(2)–As(2)–S(3) and S(2)$^{\#1}$–As(2)$^{\#1}$–S(3)$^{\#1}$ are 98.7° and 98.6°. Similarly, the bond angles of the other S–As–S bonds are all close to 100°. It should be mentioned that this molecule shows different possibilities of folding [206–209]. The conformer found in the structure of $[Mn(NH_3)_6][As_4S_6]\cdot NH_3$ was observed for the first time for anions of the formula $As_4S_6^{2-}$. However, the conformer is known for the isostructural anion $As_4Se_6^{2-}$ [210]. The anion can be derived from the Realgar cage. When the As–As bond in the cage is exchanged for terminal As–S$^-$ groups, the $As_4S_6^{2-}$ Anion is obtained [211]. The other conformer of the $As_4S_6^{2-}$ anion has higher symmetry with point group C_{2v},

with the As–As bond located in an additional mirror plane. Comparing the bond length with existing structures, the bond lengths in this new conformer do not differ much. Table 4.8 shows a comparison of the bond lengths with the conformer known from literature. These two conformers are the only known conformers for anions of the formula $As_4S_6^{2-}$ so far.

Bond No.	$[(C_3H_7)_2NH_2]_2[X]$ [206]	$[TMDPH_2][X]$ [209]	$[C_5H_{12}N]_2[X]$ [207]	$[Ph_4P]_2[X]$ [208]	$[Mn(NH_3)_6][X]$ this work
1	2.15	2.15	2.18	2.13	2.16
6	2.15	2.15	2.18	2.12	2.15
2	2.31	2.29	2.30	2.28	2.30
10	2.31	2.29	2.30	2.31	2.30
3	2.21	2.22	2.23	2.19	2.25
9	2.21	2.22	2.23	2.21	2.25
4	2.21	2.22	2.23	2.20	2.24
8	2.21	2.22	2.23	2.22	2.24
5	2.31	2.29	2.30	2.34	2.30
7	2.31	2.29	2.30	2.33	2.30
11	2.56	2.55	2.58	2.62	2.57

Table 4.8: Comparison of the bond lengths with the known *cis*-conformer of the $[As_4S_6]^{2-}$ anion ([X]≙$[As_4S_6]$). The bond lengths are all in the same range and there is no irregularity. All registered $[As_4S_6]^{2-}$ anions from the CCDC (last reviewed 2022-06-04).

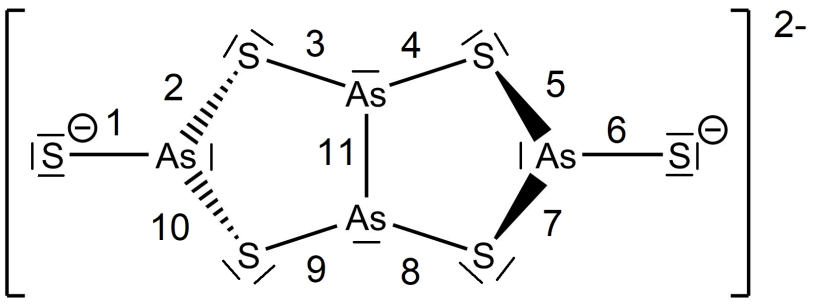

Figure 4.63: Lewis structure of the hexathiotetraarsenate $As_4S_6^{2-}$ in $[Mn(NH_3)_6][As_4S_6]\cdot NH_3$. The bonds are numbered in order to compare the different conformers in Table 4.8, disregarding the stereochemistry of the different conformers.

Moreover, it is important to mention, that the short distances N···S (2.67 Å to 2.93 Å) are an indicator for N–H···S hydrogen bonds. The shortest and longest distances are found towards the terminal sulphur atoms S(1) and S(4). Four ammonia molecules are located close to S(1) (d(N···S)=3.51 Å to 3.56 Å), respectively five nitrogen atoms were found near S(4) (d(N···S)=3.57 Å to 3.62 Å). The four bridging sulphur atoms show larger distances to nitrogen (d(N···S)=3.61 Å to 3.71 Å). The shortest distance is present to the free ammonia molecule (3.63 Å). A closer look at the Lewis structure of the anion, see Fig. 4.63, explains the different situation of the bridging and terminal

sulphur atoms. The partial negative charge at the terminal sulphur atoms is higher, therefore smaller distances are present.

In addition, the packing of the $[Mn(NH_3)_6]^{2+}$ octahedra and the $[As_4S_6]^{2-}$ anions indicates the same. The complex cations are closest to the terminal sulphur atoms of the anions. The anions are located in one layer, alternately tilted by the 2_1 screw axes in *c*-direction, pointing with the terminal sulphur atoms in *b*-direction. The *a*-*c* plane, in which the anions are located, is situated between the corrugated sheet build up by octahedra (Fig.4.64). The polarity of the structure is caused by the arrangement of the anions. The anion itself has no inversion centre and there is no inversion centre in the unit cell. The trigonal pyramidal arrangement of the AsS_3 units within the anion point uniformly in the positive *c*-direction with the tip of the pyramid, which is the arsenic atom. The red arrows in Fig. 4.64 illustrate the orientation of the trigonal pyramidal arrangement and highlight the polarity of the structure.

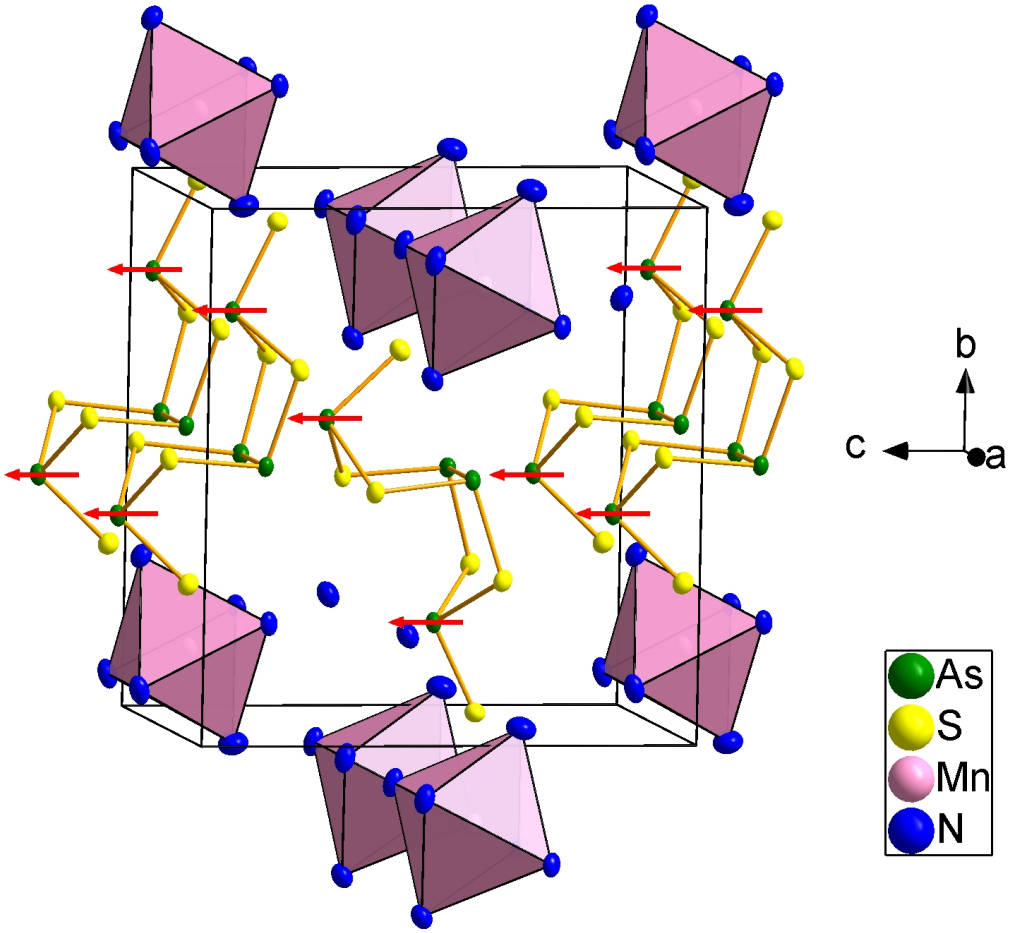

Figure 4.64: Extended unit cell of $[Mn(NH_3)_6][As_4S_6]\cdot NH_3$ in the direction of the *a*-axis. The $[Mn(NH_3)_6]^{2+}$ octahedra are located in a corrugated sheet. $[As_4S_6]^{2-}$ anions occupy the sheet in between. The free ammonia molecule, which does not coordinate to manganese, is filling the void between the cations and anions. The red arrows highlight the polarity of the structure. The hydrogen atoms have been omitted for clarity. The displacement ellipsoids represent a probability of 50 %.

Since $[Mn(NH_3)_6][As_4S_6]$ is sensitive to loss of volatile ammonia, Raman spectra of the yellow crystals were recorded with the crystals in the reaction vessel. The $As_4S_6^{2-}$ anion has C_s symmetry. Based on the structural data, a Raman spectrum was calculated with *ORCA* [212, 213] with the orbital basis set *def2-TZVP* [214] and *AuxJ* basis set *def2/J* [215].

The Raman spectrum of $[Mn(NH_3)_6][As_4S_6]$ is shown in Fig. 4.66. The band at $362\,cm^{-1}$ and $352\,cm^{-1}$ can be assigned to the terminal S–As stretching vibrations. In the calculated Raman spectrum (Fig. 4.67) the terminal S–As stretching vibrations are at $362\,cm^{-1}$ and $428\,cm^{-1}$. The bands between $120\,cm^{-1}$ to $230\,cm^{-1}$ are in good agreement with the calculated spectrum, but at $186\,cm^{-1}$ the two different vibrations cannot be distinguished. C. Pantano investigated the gelation of As_2S_3 in amine solvents [216]. He postulated on basis of Raman data the As_2S_3/ethylenediamine chelation to occur as depicted in Fig. 4.65. The conformation of the As_4S_6 group is isosterical to the $As_4S_6^{2-}$ present in $[Mn(NH_3)_6][As_4S_6]$. In the spectra of this compound the intense $438\,cm^{-1}$ is associated with the =As–S–S–As= resonance. This bond links the As_4S_6 units and is present in $[Mn(NH_3)_6][As_4S_6]$. But this is important evidence for the formation of the $As_4S_6^{2-}$ anion in amine solvents, like ammonia. But it leaves the question why this conformer has not yet been isolated in ethylenediamine.

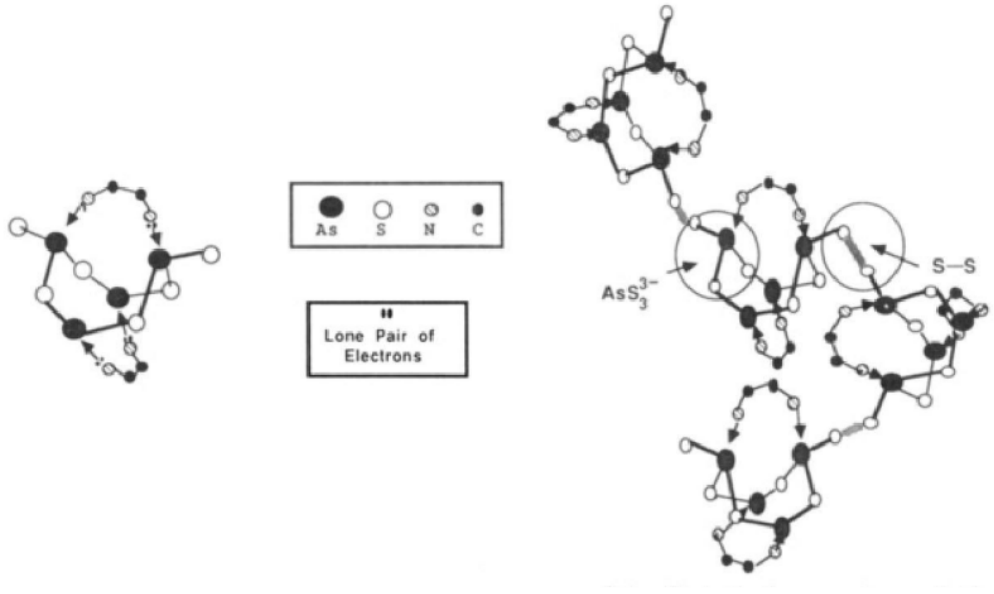

Figure 4.65: Proposed As_2S_3/ethylenediamine solution species: (left) Lewis-base chelation model (As_4S_6+$H_2NCH_2CH_2NH_2$); (right) branched chains. The Figure has been reproduced from literature [216].

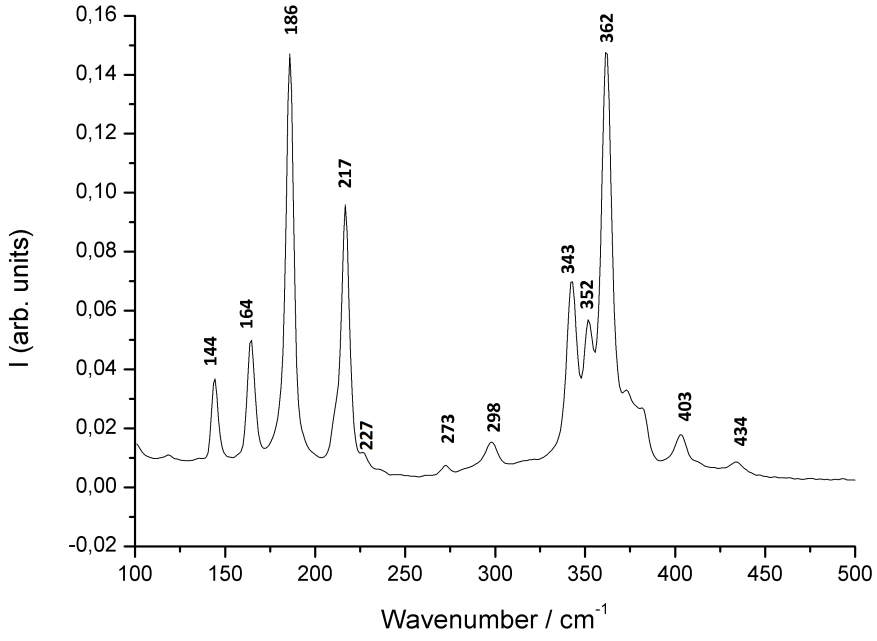

Figure 4.66: The Raman spectrum of $[Mn(NH_3)_6][As_4S_6]$ in the range $100 - 500$ cm^{-1}.

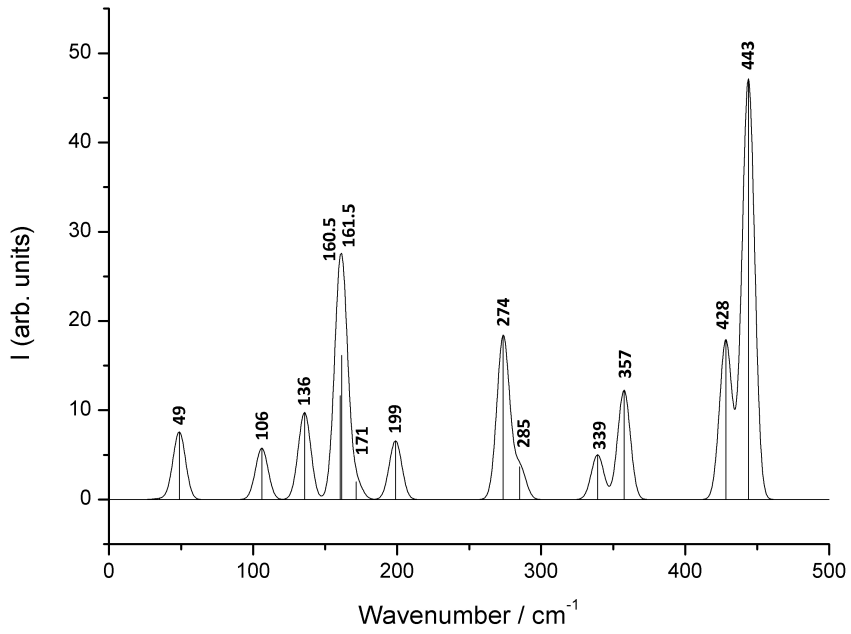

Figure 4.67: Calculated Raman spectrum of $[Mn(NH_3)_6][As_4S_6]$ in the range $100 - 500$ cm^{-1}. Calculated with ORCA [212, 213] with the orbital basis set *def2-TZVP* [214] and *AuxJ* basis set def2/J [215].

4.6.3 $[Mn(NH_3)_6][As_2Se_6]$

$[Mn(NH_3)_6]_2[As_2Se_6]$ crystallises as bright yellow rod-shaped crystals. For the structure analysis a suitable crystal of $[Mn(NH_3)_6][As_2Se_6]$ was selected and fixed on the goniometer head of the diffractometer. The X-ray diffraction data collection was performed under a cold nitrogen gas flow (123 K) and revealed a monoclinic crystal system with the space group $P2_1/n$ (No. 14). The lattice parameters of the unit cell are $a = 6.7484(4)$ Å, $b = 12.3781(8)$ Å, $c = 10.8297(6)$ Å with the monoclinic angle of $\beta = 102.940(4)°$. The volume of the unit cell is $V = 881.66(9)$ Å^3, the number of formula units is 2. The dataset contained 5599 reflections from which 1835 were unique. The quality factor R_{int} on averaging symmetry equivalent reflections amounted to 7.88 %. Hydrogen atoms were placed in geometrically calculated positions, refined using a "riding model" [127].

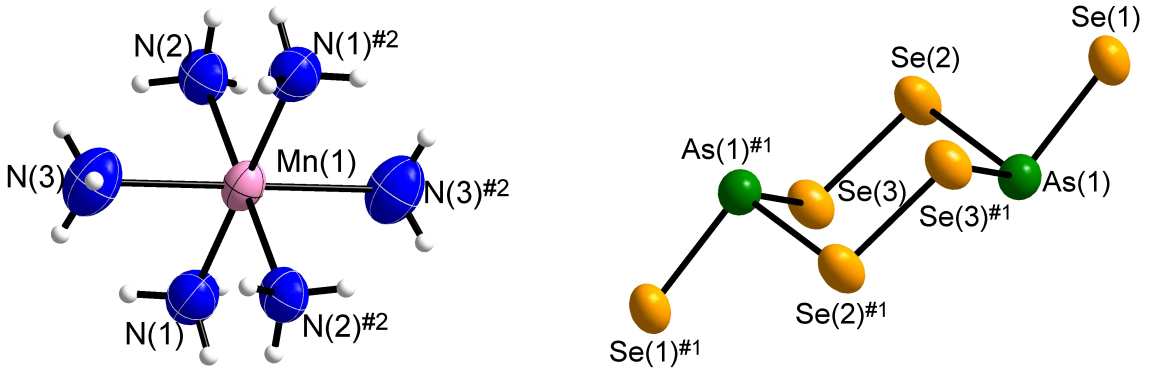

Figure 4.68: The molecules in the structure of $[Mn(NH_3)_6][As_2S_6]$: (right) $[As_2S_6]^{2-}$ anion and the octahedral $[Mn(NH_3)_6]^{2+}$ cation (left). Hydrogen atoms are placed in geometrically calculated positions and drawn with arbitrary radii. The displacement ellipsoids represent a probability of 90 %. Indices indicate the following symmetry operations: #1: -x+1,-y+1,-z+1; #2: -x+1,-y+1,-z.

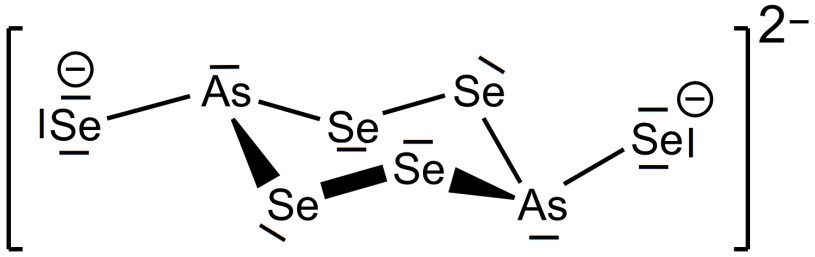

Figure 4.69: Lewis structure of the selenidoarsenate(III) [1,4-As_2Se_6]$^{2-}$ with idealised C_{2h} symmetry.

With the manganese atom placed in an inversion centre, the asymmetric unit contains a half $[Mn(NH_3)_6]^{2+}$ complex cation with three independent ammonia ligands. The centre of gravity of the selenidoarsenate(III) anion is located in an inversion centre. Accordingly, the asymmetric unit holds one half of the $[As_2Se_6]^{2-}$ anion (Fig. 4.68).

The manganese atom Mn(1) is located on the Wyckoff position 2*b* with local symmetry $\bar{1}$. This inversion centre is the centre of the octahedral coordination sphere by ammonia molecules. The Mn–N bonds within the $[Mn(NH_3)_6]^{2+}$ cation are in the range of 2.24 Å to 2.29 Å, which is agreeable with other hexammine-manganese(II) complexes [57, 204, 205]. The coordination sphere around Mn(1) is almost ideal octahedral, with N–Mn–N angles 86.9° - 93.1° and 180°.

In the selenidoarsenate $[1,4\text{-}As_2Se_6]^{2-}$ the atoms As(1), Se(2), Se(3) and their symmetry equivalent positions form six membered rings with chair conformation. The Se(1) atom and its symmetry equivalent atom occupy the equatorial positions 1 and 4 of the six-membered rings. The negative charge is mainly located at these terminal selenium atoms (Fig. 4.69). The molecule is of crystallographic C_i symmetry. The higher molecular symmetry C_{2h} is almost fulfilled. The As–Se bonds in the $[1,4\text{-}As_2Se_6]^{2-}$ anion are between 2.32 Å and 2.42 Å. The shortest As–Se bond (2.32 Å) is located between the terminal selenium atom and the bonded arsenic atom. The homonuclear Se–Se bond length is 2.34 Å. The Se–As–Se angles are between 95.4° to 99.0°, the Se–Se–As angles are 99.5° and 101.4°. All angles and distances are consistent with $[1,4\text{-}As_2Se_6]^{2-}$ polyanions known from literature [217–219].

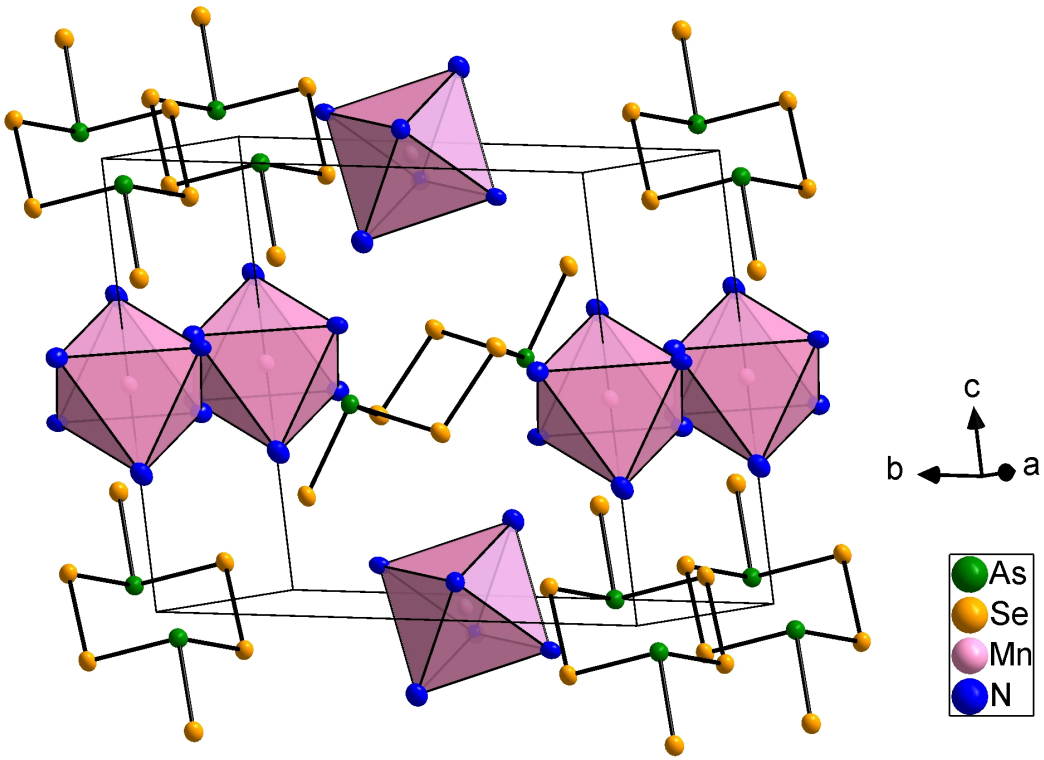

Figure 4.70: A perspective view of the extended unit cell of $[Mn(NH_3)_6][As_2Se_6]$. The hydrogen atoms have been omitted for improved clarity. Atoms are drawn as displacement ellipsoids representing a probability density of 50 %.

The extended unit cell is shown in Fig. 4.70. The distances N···S (3.47 Å to 4.07 Å) indicate possible N–H···S hydrogen bonds. The sum of the van-der-Waals radii of hydrogen ($r(H) = 1.4$ Å) and selenium ($r(Se) = 1.9$ Å) [58] is 3.3 Å. Distances of N–H···S between 2.81 Å and 3.18 Å are present in the structure. These short H···S distances give reason to assume that not only ionic interactions occur between the hexamminmaganese(II)-complex and the selenidoarsenate(III). These hydrogen bonds influence the orientation of the octahedral complex, but keeping in mind that the hydrogen positions were calculated and refined using a "riding model" [127].

The arrangement of the cations and anions is related to the simple structure of CsCl. In Fig. 4.71 the ammonia ligands of the $[Mn(NH_3)_6]^{2+}$ complex have been omitted for clarity. The central manganese atoms are connected, for a better understanding of the packing. Inside the middle of these distorted cubes of cations, the $[1,4\text{-}As_2Se_6]^{2-}$ anions are located. Because of the *n*-gliding plane and the 2_1 screw axis, the anions show two different orientations. In this view, the anions and cations gain the coordination number 8 in form of a distorted cubic environment. This arrangement of the ions in the structure of $[Mn(NH_3)_6][As_2S_6]$ is thus analogous to the arrangement of the ions in the structure of CsCl.

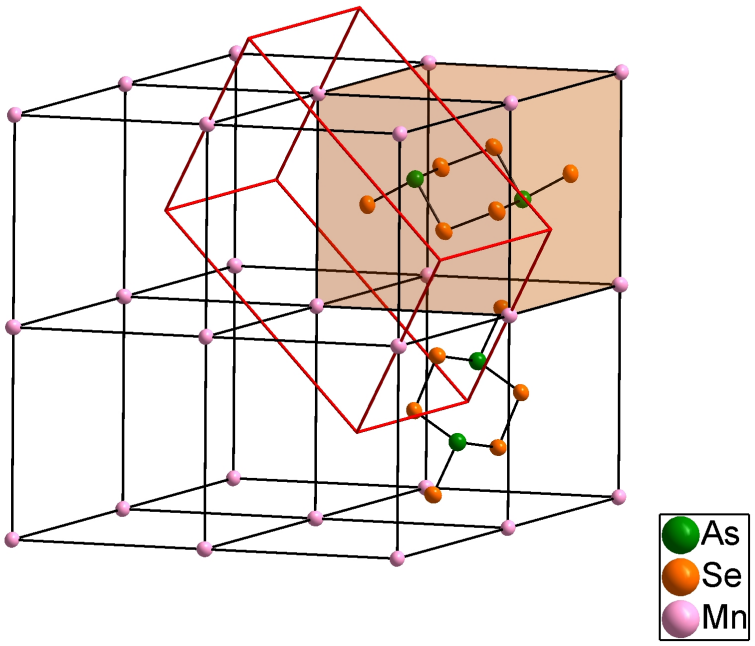

Figure 4.71: The connected manganese atoms form a distorted cubic environment with the anions in the centre of the cube. The different orientations of the anions result from the symmetry operations. Coordination number is 8 for both cation and anion. The ammonia molecules have been omitted for improved clarity. The cell edges are in red. Atoms are drawn with standardised atom radii.

Chapter 5

Summary and Outlook

In the course of this work, a large number of new Zintl phases were presented. The synthesis went back to the origins of the Zintl phases and often took place directly in liquid ammonia. The fact that even after 90 years of research on Zintl phases, synthesis in liquid ammonia still provides exciting findings is due to the sophisticated low temperature single crystal manipulation, since the products are often thermally unstable.

The successful synthesis of Rb_2AuAs_7 is a representative of a three-dimensionally linked structure. Due to the demanding synthesis and low yields, the substance has not been further characterised in terms of conductivity. Nevertheless, it is an example of a three-dimensional linkage. The infinite chains of ${}^{1}_{\infty}[As_7]^{3-}$ units are the first observed complex arsenic polyanions consisting of condensed As_7^{3-} cages. It is the first polymeric polyarsenide via solution chemistry. Due to the linearly coordinated gold, the chains are linked to each other in three dimensions.

The good solubility of europium in ammonia led to the reduction of arsenic to the well-known nortricyclane-analogue ion As_7^{3-} under ammonothermal, supercritical conditions and formed $[(Eu(NH_3)_8)]_2[Eu(NH_3)_3(As_7)_2]$. In this structure, infinite, one-dimensional chains of cages linked by europium are present alongside $[Eu(NH_3)_8]^{2+}$ cations stacked between the chains.

In addition to the ammonothermal syntheses, partially oxidised Zintl phases were investigated. The three phases Ba_3As_4, Ba_3As_2O and $K_3Ba_7(As_3)_3O$ were thus obtained by conventional high-temperature solid state synthesis. All of them contained open-chain arsenides ($[As_2]^{4-}$, $[As_3]^{5-}$ and $[As_4]^{6-}$). Ba_3As_4 is not a partially oxidised Zintl phase, but always occurred as a by-product in the syntheses of the other two compounds and could finally be obtained in medium purity.

The synthesis of a copper-containing selenide and two gold-containing selenides in liquid ammonia were successful. For the silver compounds, no representative could be characterised so far. Often, elemental silver was subsequently recognisable in the

reaction vessels. The known linear complex anion $[AuSe_2]^{3-}$ [115] could be found in the compound $Rb_3(AuSe_2)\cdot 1.5NH_3$. Under similar conditions, the linear complex anion $CuSe_2^{3-}$, was synthesised for the first time, which is present alongside Se_2^{4-} and chloride anions in the compound $K_{10}CuSe_8Cl\cdot NH_3$. In $K_2[AuSe]Se\cdot NH_3$ in addition to an infinite chain of equidistant Se^{2-} anions, the well-known $^1_\infty[AuSe^{1-}]$ zig-zag chain is present, but with alternating bond lengths.

Replacing the solvent ammonia against ethylenediamine led to unexpected reactions. By decomposing the solvent, the two new compounds $NH_4Fe_2S_3$ and $NH_4Fe_2Se_3$ were obtained and joined the family of the compounds with the *spin-ladder* structures and iron in the averaged oxidation state +2.5. In $NH_4Fe_2Ch_3$ (Ch=S,Se) Fe(II) and Fe(III) cannot be distinguished crystallographically. The comparison with the compounds KFe_2S_3 and $BaFe_2S_3$ suggest that the new representatives of this structure type should be investigated for magnetic and conductive properties under pressure. Unfortunately, within the scope of this work, it was not possible to obtain the two compounds in high purity to pursue these additional investigations.

Equally gratifying was the discovery of the framework compound $[Mn_2(HPO_3)_2(C_2H_8N_2)]$. Contrary to the expectation of a $[Mn(en)_3]^{2-}$ complex, ethylenediamine acts as a crosslinker, connecting the metal atoms and thus forming a framework structure.

It was shown that the anions $As_4S_6^{2-}$ [206–209] and $As_2Se_6^{2-}$ [217–219], which so far had been obtained from organic solvents, could in fact be crystallised from ammonia for the first time, both with the complex cation $[Mn(NH_3)_6]^{2+}$. The $As_4S_6^{2-}$ anion was observed for the first time in a different conformation as already described for the respective selenium compound with the anion $As_4Se_6^{2-}$ [210]. As secondary products, the unusual compounds As_3NS_3 and As_3NSe_3 appeared. The yield of As_3NS_3, respectively As_3NSe_3, could be increased by adding catalytic amounts of $MnCl_2$. The structures of As_3NS_3 and As_3NSe_3 are closely related to $(Me_2As)_3N$ [202]. Especially the bonding motif As_3N stands out with the sp^2 hybridisation of nitrogen.

The conducted experiments with manganese, arsenic and sulphur, or selenium, raise the expectation that a great variety of further compounds could be discovered by varying the transition element.

In $K_9Se_{2.88}(Se_2)_{1.12}OH$ the Zintl anions Se_2^{2-} are present in addition to Se^{2-} and OH^-. It is conceivable that similar compounds are accessible from liquid ammonia through the targeted use of oxides.

Experiments with the easily oxidisable transition metals (Mn, Fe, Zn) with pnictogens and, or chalcogenes and noble metals (Cu, Ag, Au) and their chlorides were

not successful. Despite many attempts, it was not possible to obtain further alkali metal-coinage metal-arsenic compounds. So far, the compound Rb_2AuAs_7 is the only representative of this family. A reproduction of this compound with crystals of sufficient quality and size has not been successful.

The first ammoniates in the A-Au/Cu-Se system were synthesised. With suitable synthesis conditions and modified element ratios, new ammoniates including these metals will be possible in the future. In experiments with silver, crystals were observed, but their structure could not be sufficiently determined due to a high degree of twinning. However, this is a lead for further experiments.

A.1 Data of Single Crystal Structure Determinations

A.1.1 Ba_3As_2O

Table A.1: Crystal data and structure refinement for Ba_3As_2O.

Empirical formula	Ba_3As_2O
Formula weight / $g \cdot mol^{-1}$	577.86
Temperature / K	123(2)
Crystal system; space group	Orthorhombic; *Pbam*
Lattice constants / $Å$	$a = 11.6333(9)$
	$b = 11.6391(7)$
	$c = 5.0004(3)$
Volume / $Å^3$	677.06(8)
Z; F(000); calc. density / $g \cdot cm^{-3}$	4; 968; 5.669
Wavelength	$Mo_{K\alpha}(\lambda = 0.710\,73\,Å)$
Crystal size / mm^3	$0.100 \times 0.015 \times 0.010$
Theta range for data collection / °	$3.501 \leq \theta \leq 27.392$
Limiting indices	$-15 \leq h \leq 15$; $-15 \leq k \leq 15$; $-6 \leq l \leq 6$
Reflections collected / unique	11248 / 864
Completeness to $\theta = 25.242°$	99.9%
R_{int}	0.1253
Absorption coefficient / mm^{-1}	26.835; Semi-empirical from equivalents
Max. / min. transmission	0.0168 / 0.0432
Refinement method	Full-matrix least-squares on F^2
Data / restraints / parameters	864 / 0 / 40
R indices (all data) R_1; wR_2	0.0715; 0.0799
R indices $[[n]I > 2\sigma(I)]$ R_1; wR_2	[599] 0.0400; 0.0730
Goodness-of-fit for F^2	1.062
Largest diff. peak / $e^- \cdot Å^{-3}$	+1.333
Largest diff. hole / $e^- \cdot Å^{-3}$	-1.768

Table A.2: Atomic coordinates ($\times 1 \times 10^4$) and equivalent isotropic displacement parameters U_{eq} / $Å^2$ $\times 1 \times 10^3$ for the independent atoms in the structure of Ba_3As_2O.

Atom	Wyck.	Site	x / a	y / b	z / c	U_{eq} / $Å^2$
Ba(1)	4*g*	..m	5154(5)	6769(4)	10000	27(1)
Ba(2)	4*h*	..m	2586(2)	7516(6)	5000	27(1)
Ba(3)	4*g*	..m	1787(4)	4930(10)	0	27(1)
As(1)	4*h*	..m	3945(7)	5052(8)	5000	28(2)
As(2)	4*h*	..m	5104(4)	8935(6)	5000	25(1)
O(1)	4*g*	..m	2380(20)	7836(16)	0	41(5)

Table A.3: Anisotropic displacement parameters U_{ij} / $Å^2$ $\times 1 \times 10^3$ for the independent atoms in the structure of Ba_3As_2O.

Atom	U_{11}	U_{22}	U_{33}	U_{23}	U_{13}	U_{12}
Ba(1)	30(2)	25(2)	26(2)	0	0	-3(1)
Ba(2)	35(2)	22(1)	24(1)	0	0	3(2)
Ba(3)	28(2)	30(2)	22(2)	0	0	1(1)
As(1)	25(4)	29(3)	29(4)	0	0	-1(1)
As(2)	28(3)	24(3)	24(3)	0	0	2(1)
O(1)	40(11)	55(15)	28(9)	0	0	-1(10)

Table A.4: Selected bond lengths for Ba_3As_2O. Symmetry transformations used to generate equivalent atoms: #1: x+1/2,-y+3/2,z+1; #2: -x+1,-y+1,-z+1; #3: -x+1,-y+1,-z+2; #4: x,y,z+1; #5: x+1/2,-y+3/2,z; #6: x-1/2,-y+3/2,z; #7: -x+1/2,y+1/2,-z+1; #8: -x+1/2,y+1/2,-z; #9: -x+1/2,y-1/2,-z; #10: x-1/2,-y+3/2,z-1; #11: -x+1/2,y-1/2,-z+1; #12: x,y,z-1; #13: -x+1,-y+2,-z+1.

Atoms 1, 2	Distance / $Å$	Atoms 1, 2	Distance / $Å$
Ba(1)-O(1)#1	2.63(3)	Ba(2)-As(2)#6	3.344(8)
Ba(1)-As(1)#2	3.441(5)	Ba(2)-As(2)	3.364(7)
Ba(1)-As(1)#3	3.441(5)	Ba(2)-As(1)#7	3.448(5)
Ba(1)-As(1)	3.496(5)	Ba(2)-Ba(3)#7	3.831(5)
Ba(1)-As(1)#4	3.496(5)	Ba(2)-Ba(3)#8	3.831(5)
Ba(1)-As(2)#4	3.551(6)	Ba(3)-O(1)#9	2.62(3)
Ba(1)-As(2)	3.551(6)	Ba(3)-As(2)#10	3.440(5)

continued on next page

Atoms 1, 2	Distance / Å	Atoms 1, 2	Distance / Å
Ba(1)-Ba(2)#1	3.866(7)	Ba(3)-As(2)#6	3.440(5)
Ba(1)-Ba(2)#5	3.866(7)	Ba(3)-As(2)#9	3.526(4)
Ba(1)-Ba(2)#4	3.992(7)	Ba(3)-As(2)#11	3.526(4)
Ba(1)-Ba(2)	3.992(7)	Ba(3)-As(1)#12	3.546(8)
Ba(1)-Ba(3)#2	4.071(7)	Ba(3)-As(1)	3.546(8)
Ba(2)-O(1)	2.539(3)	As(1)-As(1)#2	2.457(16)
Ba(2)-O(1)#4	2.539(3)	As(2)-As(2)#13	2.492(14)
Ba(2)-As(1)	3.275(5)		

Table A.5: Selected bond angles for Ba_3As_2O. Symmetry transformations used to generate equivalent atoms: #1: x+1/2,-y+3/2,z+1; #2: -x+1,-y+1,-z+1; #3: -x+1,-y+1,-z+2; #4: x,y,z+1; #5: x+1/2,-y+3/2,z; #6: x-1/2,-y+3/2,z; #7: -x+1/2,y+1/2,-z+1; #8: -x+1/2,y+1/2,-z; #9: -x+1/2,y-1/2,-z; #10: x-1/2,-y+3/2,z-1; #11: -x+1/2,y-1/2,-z+1; #12: x,y,z-1; #13: -x+1,-y+2,-z+1.

Atoms 1, 2, 3	Angle / °	Atoms 1, 2, 3	Angle / °
Ba(2)-O(1)-Ba(2)#12	159.9(7)	Ba(1)-As(1)-Ba(3)#4	78.66(7)
Ba(2)-O(1)-Ba(3)#8	95.8(6)	Ba(1)#12-As(1)-Ba(3)#4	144.3(2)
Ba(2)#12-O(1)-Ba(3)#8	95.8(6)	Ba(3)-As(1)-Ba(3)#4	89.7(2)
Ba(2)-O(1)-Ba(1)#10	96.8(6)	As(2)#13-As(2)-Ba(2)#5	125.9(2)
Ba(2)#12-O(1)-Ba(1)#10	96.8(6)	As(2)#13-As(2)-Ba(2)	113.8(2)
Ba(3)#8-O(1)-Ba(1)#10	101.6(6)	Ba(2)#5-As(2)-Ba(2)	120.3(2)
As(1)#2-As(1)-Ba(2)	121.7(5)	As(2)#13-As(2)-Ba(3)#1	70.92(18)
As(1)#2-As(1)-Ba(1)#2	70.5(2)	Ba(2)#5-As(2)-Ba(3)#1	72.70(16)
Ba(2)-As(1)-Ba(1)#2	133.34(9)	Ba(2)-As(2)-Ba(3)#1	133.20(8)
As(1)#2-As(1)-Ba(1)#3	70.5(2)	As(2)#13-As(2)-Ba(3)#5	70.92(18)
Ba(2)-As(1)-Ba(1)#3	133.34(9)	Ba(2)#5-As(2)-Ba(3)#5	72.70(16)
Ba(1)#2-As(1)-Ba(1)#3	93.21(19)	Ba(2)-As(2)-Ba(3)#5	133.20(8)
As(1)#2-As(1)-Ba(2)#11	118.3(5)	Ba(3)#1-As(2)-Ba(3)#5	93.25(17)
Ba(2)-As(1)-Ba(2)#11	120.0(2)	As(2)#13-As(2)-Ba(3)#8	67.19(16)
Ba(1)#2-As(1)-Ba(2)#11	68.3(2)	Ba(2)#5-As(2)-Ba(3)#8	134.79(8)
Ba(1)#3-As(1)-Ba(2)#11	68.3(2)	Ba(2)-As(2)-Ba(3)#8	67.52(14)
As(1)#2-As(1)-Ba(1)	68.1(2)	Ba(3)#1-As(2)-Ba(3)#8	138.1(2)

continued on next page

Atoms 1, 2, 3	Angle / °	Atoms 1, 2, 3	Angle / °
Ba(2)-As(1)-Ba(1)	72.2(2)	Ba(3)#5-As(2)-Ba(3)#8	73.36(16)
Ba(1)#2-As(1)-Ba(1)	138.5(3)	As(2)#13-As(2)-Ba(3)#7	67.19(16)
Ba(1)#3-As(1)-Ba(1)	73.14(15)	Ba(2)#5-As(2)-Ba(3)#7	134.79(8)
Ba(2)#11-As(1)-Ba(1)	134.20(9)	Ba(2)-As(2)-Ba(3)#7	67.52(14)
As(1)#2-As(1)-Ba(1)#12	68.1(2)	Ba(3)#1-As(2)-Ba(3)#7	73.36(16)
Ba(2)-As(1)-Ba(1)#12	72.2(2)	Ba(3)#5-As(2)-Ba(3)#7	138.1(2)
Ba(1)#2-As(1)-Ba(1)#12	73.14(15)	Ba(3)#8-As(2)-Ba(3)#7	90.30(14)
Ba(1)#3-As(1)-Ba(1)#12	138.5(3)	As(2)#13-As(2)-Ba(1)	135.08(11)
Ba(2)#11-As(1)-Ba(1)#12	134.20(9)	Ba(2)#5-As(2)-Ba(1)	68.1(2)
Ba(1)-As(1)-Ba(1)#12	91.32(17)	Ba(2)-As(2)-Ba(1)	70.5(2)
As(1)#2-As(1)-Ba(3)	134.84(13)	Ba(3)#1-As(2)-Ba(1)	75.6(2)
Ba(2)-As(1)-Ba(3)	72.12(15)	Ba(3)#5-As(2)-Ba(1)	140.8(4)
Ba(1)#2-As(1)-Ba(3)	71.25(7)	Ba(3)#8-As(2)-Ba(1)	137.9(4)
Ba(1)#3-As(1)-Ba(3)	134.7(2)	Ba(3)#7-As(2)-Ba(1)	75.2(3)
Ba(2)#11-As(1)-Ba(3)	66.42(14)	As(2)#13-As(2)-Ba(1)#12	135.08(11)
Ba(1)-As(1)-Ba(3)	144.3(2)	Ba(2)#5-As(2)-Ba(1)#12	68.1(2)
Ba(1)#12-As(1)-Ba(3)	78.66(7)	Ba(2)-As(2)-Ba(1)#12	70.5(2)
As(1)#2-As(1)-Ba(3)#4	134.84(13)	Ba(3)#1-As(2)-Ba(1)#12	140.8(4)
Ba(2)-As(1)-Ba(3)#4	72.12(15)	Ba(3)#5-As(2)-Ba(1)#12	75.6(2)
Ba(1)#2-As(1)-Ba(3)#4	134.7(2)	Ba(3)#8-As(2)-Ba(1)#12	75.2(3)
Ba(1)#3-As(1)-Ba(3)#4	71.25(7)	Ba(3)#7-As(2)-Ba(1)#12	137.9(4)
Ba(2)#11-As(1)-Ba(3)#4	66.42(14)	Ba(1)-As(2)-Ba(1)#12	89.5(2)

A.1.2 $K_3Ba_7(As_3)_3O$

Table A.6: Crystal data and structure refinement for $K_3Ba_7(As_3)_3O$.

Empirical formula	$K_3Ba_7(As_3)_3O$
Formula weight / $g \cdot mol^{-1}$	1768.96
Temperature / K	123(2)
Crystal system; space group	Hexagonal; $P6_3/mcm$
Lattice constants / $Å$	$a = b = 9.52600(10)$
	$c = 15.2003(3)$
Volume / $Å^3$	1194.55(3)
Z; F(000); calc. density / $g \cdot cm^{-3}$	2; 1508; 4.918
Wavelength	$Mo_{K\alpha}(\lambda = 0.710\,73\,Å)$
Crystal size / mm^3	$0.124 \times 0.06 \times 0.032$
Theta range for data collection / °	$3.645 \leq \theta \leq 27.467$
Limiting indices	$-12 \leq h \leq 12$; $-12 \leq k \leq 12$; $-19 \leq l \leq 19$
Reflections collected / unique	20831 / 528
Completeness to $\theta = 25.242°$	99.5%
R_{int}	0.0899
Absorption coefficient / mm^{-1}	24.229; Semi-empirical
	from equivalents
Max. / min. transmission	0.057 / 0.013
Refinement method	Full-matrix least-squares on F^2
Data / restraints / parameters	528 / 0 / 25
R indices (all data) R_1; wR_2	0.0225; 0.0474
R indices $[[n]I > 2\sigma(I)]$ R_1; wR_2	[473] 0.0186; 0.0462
Goodness-of-fit for F^2	1.120
Extinction coefficient	0.00081(10)
Largest diff. peak / $e^- \cdot Å^{-3}$	+1.024
Largest diff. hole / $e^- \cdot Å^{-3}$	-0.792

Table A.7: Atomic coordinates ($\times 1 \times 10^4$) and equivalent isotropic displacement parameters U_{eq} / $Å^2$ $\times 1 \times 10^3$ for the independent atoms in the structure of $K_3Ba_7(As_3)_3O$.

Atom	Wyck.	Site	*SOF*	*x / a*	*y / b*	*z / c*	U_{eq} / $Å^2$
Ba(1)	4*c*	..m	1.00002	6667	3333	2500	22(1)
Ba(2)	12*k*	..m	0.83334	7598(1)	7598(1)	3987(1)	24(1)
K(2)	12*k*	..m	0.16666	7598(1)	7598(1)	3987(1)	24(1)
As(1)	6*g*	..m		2692(1)	2692(1)	2500	22(1)
As(2)	12*k*	..m		4120(1)	4120(1)	3849(1)	23(1)
K(1)	4*d*	..m	0.50001	3333	6667	5000	19(1)
O(1)	2*b*	..m	0.499981	10000	10000	5000	37(3)

Table A.8: Anisotropic displacement parameters U_{ij} / $Å^2$ $\times 1 \times 10^3$ for the independent atoms in the structure of $K_3Ba_7(As_3)_3O$.

Atom	U_{11}	U_{22}	U_{33}	U_{23}	U_{13}	U_{12}
Ba(1)	22(1)	22(1)	22(1)	0	0	11(1)
Ba(2)	24(1)	24(1)	25(1)	0(1)	0(1)	13(1)
K(2)	24(1)	24(1)	25(1)	0(1)	0(1)	13(1)
As(1)	22(1)	22(1)	22(1)	0	0	10(1)
As(2)	22(1)	22(1)	24(1)	-1(1)	-1(1)	11(1)
K(1)	19(1)	19(1)	19(1)	0	0	10(1)
O(1)	29(4)	29(4)	54(7)	0	0	14(2)

Table A.9: Selected bond lengths for $K_3Ba_7(As_3)_3O$. Symmetry transformations used to generate equivalent atoms: #1: -y+1,x-y,z; #2: -x+y+1,-x+1,z; #3: -y+1,x-y,-z+1/2; #4: -x+y+1,-x+1,-z+1/2; #5: x,y,-z+1/2; #6: -x+1,-y+1,z-1/2; #7: -x+1,-y+1,-z+1; #8: -y+1,x-y+1,z; #9: y,-x+y+1,-z+1; #10: x-y+1,x,-z+1; #11: -y+2,x-y+1,z; #12: -x+y,-x+1,-z+1/2; #13: -x+y,-x+1,z; #14: y,x,-z+1/2; #15: x-y,x,-z+1; #16: -x+2,-y+2,-z+1; #17: -x+y+1,-x+2,z.

Atoms 1, 2	Distance / *Å*	Atoms 1, 2	Distance / *Å*
Ba(1)-As(1)	3.5207(6)	As(1)-Ba(2)#3	3.3250(5)
Ba(1)-As(1)#1	3.5207(6)	As(1)-Ba(2)#1	3.3250(5)
Ba(1)-As(1)#2	3.5207(6)	As(1)-Ba(2)#13	3.3250(5)
Ba(1)-As(2)	3.5309(4)	As(1)-Ba(1)#14	3.5206(6)

continued on next page

Atoms 1, 2	Distance / Å	Atoms 1, 2	Distance / Å
Ba(1)-As(2)#3	3.5309(4)	As(2)-K(1)#7	3.3656(3)
Ba(1)-As(2)#2	3.5309(4)	As(2)-K(1)	3.3657(3)
Ba(1)-As(2)#1	3.5309(4)	As(2)-Ba(2)#13	3.4209(5)
Ba(1)-As(2)#4	3.5309(4)	As(2)-Ba(2)#1	3.4209(5)
Ba(1)-As(2)#5	3.5309(4)	As(2)-Ba(1)#14	3.5309(4)
Ba(1)-K(1)#6	3.80007(8)	As(2)-Ba(2)#7	3.6740(7)
Ba(1)-K(1)#7	3.80007(8)	K(1)-As(2)#13	3.3657(4)
Ba(1)-Ba(2)	4.3357(3)	K(1)-As(2)#9	3.3657(4)
Ba(2)-O(1)	2.7577(4)	K(1)-As(2)#15	3.3657(4)
Ba(2)-As(2)	3.3200(8)	K(1)-As(2)#8	3.3657(4)
Ba(2)-As(1)#2	3.3250(5)	K(1)-As(2)#7	3.3657(3)
Ba(2)-As(1)#8	3.3250(5)	K(1)-Ba(1)#7	3.80008(8)
Ba(2)-As(2)#2	3.4209(5)	K(1)-Ba(1)#14	3.80007(8)
Ba(2)-As(2)#8	3.4209(5)	K(1)-Ba(2)#15	4.0071(3)
Ba(2)-As(2)#7	3.6740(7)	K(1)-Ba(2)#8	4.0071(3)
Ba(2)-Ba(2)#9	3.8357(7)	O(1)-Ba(2)#16	2.7576(4)
Ba(2)-Ba(2)#10	3.8357(7)	O(1)-Ba(2)#11	2.7576(4)
Ba(2)-Ba(2)#11	3.9630(7)	O(1)-Ba(2)#9	2.7576(4)
As(1)-As(2)	2.4601(8)	O(1)-Ba(2)#17	2.7576(4)
As(1)-As(2)#5	2.4601(8)	O(1)-Ba(2)#10	2.7576(4)
As(1)-Ba(2)#12	3.3250(5)		

Table A.10: Selected bond angles for $K_3Ba_7(As_3)_3O$. Symmetry transformations used to generate equivalent atoms: #5: x,y,-z+1/2, #9: y,-x+y+1,-z+1; #10: x-y+1,x,-z+1; #11: -y+2,x-y+1,z; #12: -x+y+1,-x+2,z.

Atoms 1, 2, 3	Angle / °
As(2)-As(1)-As(2)#5	112.87(5)
Ba(2)#10-O(1)-Ba(2)	88.129(12)
Ba(2)#12-O(1)-Ba(2)	91.871(12)
Ba(2)#11-O(1)-Ba(2)#9	180

A.1.3 Ba_3As_4

Table A.11: Crystal data and structure refinement for Ba_3As_4.

Empirical formula	Ba_3As_4
Formula weight / $g \cdot mol^{-1}$	711.70
Temperature / K	123(2)
Crystal system; space group	Orthorhombic; $Fdd2$
Lattice constants / $Å$	$a = 15.3564(5)$
	$b = 18.7391(4)$
	$c = 6.2748(2)$
Volume / $Å^3$	1805.71(9)
Z; F(000); calc. density / $g \cdot cm^{-3}$	8; 2400; 5.236
Wavelength	$Mo_{K\alpha}(\lambda = 0.710\,73\,Å)$
Crystal size / mm^3	0.070 × 0.034 × 0.020
Theta range for data collection / °	$3.431 \leq \theta \leq 27.468$
Limiting indices	$-19 \leq h \leq 19$; $-24 \leq k \leq 24$; $-8 \leq l \leq 8$
Reflections collected / unique	7962 / 1034
Completeness to $\theta = 25.242°$	100%
R_{int}	0.0948
Absorption coefficient / mm^{-1}	27.394; Semi-empirical from equivalents
Max. / min. transmission	0.2302 / 0.1432
Refinement method	Full-matrix least-squares on F^2
Data / restraints / parameters	1034 / 1 / 34
R indices (all data) R_1; wR_2	0.0295; 0.0487
R indices $[[n]I > 2\sigma(I)]$ R_1; wR_2	[929] 0.0238; 0.0468
Goodness-of-fit for F^2	1.055
Absolute structure parameter	0.03(5)
Extinction coefficient	0.000226(16)
Largest diff. peak / $e^- \cdot Å^{-3}$	+1.962
Largest diff. hole / $e^- \cdot Å^{-3}$	-1.325

Table A.12: Atomic coordinates ($\times 1 \times 10^4$) and equivalent isotropic displacement parameters U_{eq} / $Å^2$ $\times 1 \times 10^3$ for the independent atoms in the structure of Ba_3As_4.

Atom	Wyck.	Site	x / a	y / b	z / c	U_{eq} / $Å^2$
Ba(1)	8*a*	..2	0	0	2603(1)	11(1)
Ba(2)	16*b*	1	2493(1)	825(1)	3(1)	10(1)
As(1)	16*b*	1	3399(1)	9211(1)	69(3)	11(1)
As(2)	16*b*	1	5831(1)	-3(1)	2577(3)	10(1)

Table A.13: Anisotropic displacement parameters U_{ij} / $Å^2$ $\times 1 \times 10^3$ for the independent atoms in the structure of Ba_3As_4.

Atom	U_{11}	U_{22}	U_{33}	U_{23}	U_{13}	U_{12}
Ba(1)	10(1)	14(1)	8(1)	0	0	-1(1)
Ba(2)	9(1)	11(1)	11(1)	1(1)	-1(1)	0(1)
As(1)	10(1)	12(1)	11(1)	1(1)	-1(1)	-1(1)
As(2)	9(1)	12(1)	10(1)	0(1)	0(1)	-1(1)

Table A.14: Selected bond lengths for Ba_3As_4. Symmetry transformations used to generate equivalent atoms: #1: -x+1/2,-y+1,z+1/2; #2: x-1/2,y-1,z+1/2; #3: x-1/2,y,z+1/2; #4: -x+1/2,-y,z+1/2; #5: -x+1/2,-y,z-1/2; #6: x-1/2,y,z-1/2; #7: -x+1/4,y-3/4,z+1/4; #8: x-1/4,-y+3/4,z+1/4; #9: x-1/4,-y+1/4,z+3/4; #10: -x+1/4,y-1/4,z+3/4; #11: x,y-1,z; #12: -x+3/4,y-3/4,z-1/4; #13: -x+3/4,y+1/4,z-1/4; #14: -x+1/2,-y+1,z-1/2; #15: x-1/4,-y+1/4,z-1/4; #16: -x+1,-y,z; #17: -x+1,-y+1,z.

Atoms 1, 2	Distance / $Å$	Atoms 1, 2	Distance / $Å$
Ba(1)-As(1)#1	3.2598(14)	Ba(2)-As(1)#11	3.3288(8)
Ba(1)-As(1)#2	3.2598(14)	Ba(2)-As(1)#12	3.3462(14)
Ba(1)-As(2)#3	3.372(2)	Ba(2)-As(2)#6	3.3521(14)
Ba(1)-As(2)#4	3.372(2)	Ba(2)-As(2)#13	3.3792(7)
Ba(1)-As(2)#5	3.401(2)	Ba(2)-As(1)#14	3.386(2)
Ba(1)-As(2)#6	3.401(2)	Ba(2)-As(2)#15	3.3972(7)
Ba(1)-As(1)#7	3.4913(6)	Ba(2)-As(2)#16	3.4083(15)
Ba(1)-As(1)#8	3.4913(6)	Ba(2)-As(1)#1	3.461(2)
Ba(1)-Ba(2)#9	4.3939(6)	Ba(2)-Ba(2)#5	4.4051(6)

continued on next page

Atoms 1, 2	Distance / Å	Atoms 1, 2	Distance / Å
Ba(1)-Ba(2)#10	4.3939(6)	Ba(2)-Ba(2)#4	4.4051(6)
Ba(1)-Ba(2)#4	4.4143(4)	As(1)-As(2)#17	2.4655(10)
Ba(1)-Ba(2)#3	4.4143(4)	As(2)-As(2)#16	2.5506(15)

Table A.15: Selected bond angles for Ba_3As_4. Symmetry transformations used to generate equivalent atoms: #16: -x+1,-y,z; #17: -x+1,-y+1,z.

Atoms 1, 2, 3	Angle / °
As(1)#17-As(2)-As(2)#16	118.55(3)

A.1.4 $[Eu(NH_3)_8]_2[Eu(NH_3)_3(As_7)_2]$

Table A.16: Crystal data and structure refinement for $[(Eu(NH_3)_8)_2][Eu(NH_3)_3(As_7)_2]$.

Empirical formula	$[(Eu(NH_3)_8)_2][Eu(NH_3)_3(As_7)_2]$
Formula weight / $g \cdot mol^{-1}$	1700.90
Temperature / K	123(2)
Crystal system; space group	Orthorhombic; $Pccn$
Lattice constants / $Å$	$a = 32.3385(10)$
	$b = 9.1345(3)$
	$c = 12.9713(4)$
Volume / $Å^3$	677.06(8)
	3831.7(2)
Z; F(000); calc. density / $g \cdot cm^{-3}$	4; 2996; 2.948
Wavelength	$Mo_{K\alpha}(\lambda = 0.710\,73\,Å)$
Crystal size / mm^3	0.130 × 0.084 × 0.026
Theta range for data collection / °	$3.004 \leq \theta \leq 35.162$
Limiting indices	$-52 \leq h \leq 52$; $-14 \leq k \leq 14$; $-20 \leq l \leq 21$
Reflections collected / unique	51411 / 8457
Completeness to $\theta = 25.242°$	99.6%
R_{int}	0.1239
Absorption coefficient / mm^{-1}	16.865; Semi-empirical from equivalents
Max. / min. transmission	0.4952 / 0.3022
Refinement method	Full-matrix least-squares on F^2
Data / restraints / parameters	8457 / 0 / 142
R indices (all data) R_1; wR_2	0.0892; 0.1054
R indices $[[n]I > 2\sigma(I)]$ R_1; wR_2	[5459] 0.0442; 0.0927
Goodness-of-fit for F^2	0.976
Extinction coefficient	0.00041(4)
Largest diff. peak / $e^- \cdot Å^{-3}$	+3.059
Largest diff. hole / $e^- \cdot Å^{-3}$	-2.149

Table A.17: Atomic coordinates ($\times 1 \times 10^4$) and equivalent isotropic displacement parameters U_{eq} / $Å^2$ $\times 1 \times 10^3$ for the independent atoms in the structure of $[(Eu(NH_3)_8)_2][Eu(NH_3)_3(As_7)_2]$.

Atom	Wyck.	Site	x / a	y / b	z / c	U_{eq} / $Å^2$
As(1)	8*e*	1	5912(1)	5160(1)	3782(1)	18(1)
As(2)	8*e*	1	6349(1)	5692(1)	5234(1)	18(1)
As(3)	8*e*	1	6370(1)	5407(1)	2348(1)	19(1)
As(4)	8*e*	1	5528(1)	7437(1)	3649(1)	18(1)
As(5)	8*e*	1	6641(1)	7892(1)	4633(1)	19(1)
As(6)	8*e*	1	6657(1)	7722(1)	2733(1)	20(1)
As(7)	8*e*	1	6090(1)	9099(1)	3573(1)	19(1)
Eu(1)	4*d*	..2	7500	2500	5600(1)	16(1)
Eu(2)	8*e*	1	5662(1)	7851(1)	6116(1)	17(1)
N(1)	8*e*	1	5356(2)	5123(6)	6262(4)	30(1)
N(2)	8*e*	1	4835(2)	8123(6)	6430(4)	28(1)
N(3)	8*e*	1	5518(2)	10781(6)	5876(5)	34(1)
N(4)	8*e*	1	6708(2)	1909(5)	5009(4)	23(1)
N(5)	8*e*	1	7649(2)	551(6)	3991(4)	25(1)
N(6)	8*e*	1	7559(2)	5360(5)	6245(4)	25(1)
N(7)	8*e*	1	8053(2)	1964(6)	7207(4)	26(1)

Table A.18: Anisotropic displacement parameters U_{ij} / $Å^2$ $\times 1 \times 10^3$ for the independent atoms in the structure of $[(Eu(NH_3)_8)_2][Eu(NH_3)_3(As_7)_2]$.

Atom	U_{11}	U_{22}	U_{33}	U_{23}	U_{13}	U_{12}
As(1)	20(1)	14(1)	19(1)	-1(1)	0(1)	-2(1)
As(2)	20(1)	18(1)	18(1)	1(1)	-1(1)	4(1)
As(3)	20(1)	19(1)	18(1)	-4(1)	0(1)	4(1)
As(4)	15(1)	22(1)	16(1)	-2(1)	-1(1)	2(1)
As(5)	18(1)	18(1)	23(1)	-4(1)	-4(1)	-1(1)
As(6)	17(1)	20(1)	22(1)	1(1)	3(1)	-2(1)
As(7)	23(1)	13(1)	23(1)	-1(1)	-2(1)	2(1)
Eu(1)	18(1)	13(1)	18(1)	0	0	-1(1)

continued on next page

Atom	U_{11}	U_{22}	U_{33}	U_{23}	U_{13}	U_{12}
Eu(2)	17(1)	17(1)	18(1)	-2(1)	0(1)	1(1)
N(1)	30(3)	29(3)	32(3)	1(2)	4(2)	-8(2)
N(2)	19(3)	34(3)	31(3)	-3(2)	-2(2)	5(2)
N(3)	40(3)	24(3)	38(3)	-1(2)	-1(3)	6(2)
N(4)	21(2)	14(2)	35(3)	-2(2)	-3(2)	0(2)
N(5)	28(3)	25(3)	23(2)	-2(2)	1(2)	2(2)
N(6)	29(3)	16(2)	31(3)	-2(2)	5(2)	-4(2)
N(7)	24(3)	24(3)	29(3)	2(2)	-8(2)	-5(2)

Table A.19: Selected bond lengths for $[(Eu(NH_3)_8)_2][Eu(NH_3)_3(As_7)_2]$. Symmetry transformations used to generate equivalent atoms: #1: x,-y+3/2,z-1/2; #2: -x+3/2,-y+1/2,z; #3: x,-y+3/2,z+1/2.

Atoms 1, 2	Distance / Å	Atoms 1, 2	Distance / Å
As(1)-As(3)	2.3883(8)	As(6)-As(7)	2.4753(8)
As(1)-As(2)	2.4042(8)	Eu(1)-N(4)#2	2.727(5)
As(1)-As(4)	2.4278(8)	Eu(1)-N(4)	2.727(5)
As(2)-As(5)	2.3533(8)	Eu(1)-N(6)	2.750(5)
As(2)-Eu(2)	3.1835(6)	Eu(1)-N(6)#2	2.750(5)
As(3)-As(6)	2.3620(8)	Eu(1)-N(5)	2.785(5)
As(3)-Eu(2)#1	3.2122(6)	Eu(1)-N(5)#2	2.785(5)
As(4)-As(7)	2.3682(9)	Eu(1)-N(7)	2.790(5)
As(4)-Eu(2)	3.2509(6)	Eu(1)-N(7)#2	2.790(5)
As(4)-Eu(2)#1	3.3248(6)	Eu(2)-N(1)	2.688(6)
As(5)-As(6)	2.4691(8)	Eu(2)-N(2)	2.717(5)
As(5)-As(7)	2.5071(8)	Eu(2)-N(3)	2.734(6)
As(5)-Eu(2)	3.7049(7)		

Table A.20: Selected bond angles for $[(Eu(NH_3)_8)_2][Eu(NH_3)_3(As_7)_2]$. Symmetry transformations used to generate equivalent atoms: #1: x,-y+3/2,z-1/2; #2: -x+3/2,-y+1/2,z; #3: x,-y+3/2,z+1/2.

Atoms 1, 2, 3	Angle / °	Atoms 1, 2, 3	Angle / °
As(3)-As(1)-As(2)	103.11(3)	N(1)-Eu(2)-N(3)	148.48(18)

continued on next page

Atoms 1, 2, 3	Angle / °	Atoms 1, 2, 3	Angle / °
As(3)-As(1)-As(4)	100.41(3)	N(2)-Eu(2)-N(3)	76.10(18)
As(2)-As(1)-As(4)	100.53(3)	N(1)-Eu(2)-As(2)	73.03(12)
As(5)-As(2)-As(1)	98.58(3)	N(2)-Eu(2)-As(2)	142.90(12)
As(5)-As(2)-Eu(2)	82.54(2)	N(3)-Eu(2)-As(2)	133.18(13)
As(1)-As(2)-Eu(2)	89.81(2)	N(1)-Eu(2)-As(3)#3	133.35(12)
As(6)-As(3)-As(1)	99.36(3)	N(2)-Eu(2)-As(3)#3	125.54(11)
As(6)-As(3)-Eu(2)#1	86.65(2)	N(3)-Eu(2)-As(3)#3	72.15(13)
As(1)-As(3)-Eu(2)#1	89.58(2)	As(2)-Eu(2)-As(3)#3	89.339(17)
As(7)-As(4)-As(1)	99.22(3)	N(1)-Eu(2)-As(4)	84.97(11)
As(7)-As(4)-Eu(2)	82.20(2)	N(2)-Eu(2)-As(4)	91.56(11)
As(1)-As(4)-Eu(2)	87.83(2)	N(3)-Eu(2)-As(4)	88.80(12)
As(7)-As(4)-Eu(2)#1	84.82(2)	As(2)-Eu(2)-As(4)	70.544(15)
As(1)-As(4)-Eu(2)#1	86.31(2)	As(3)#3-Eu(2)-As(4)	129.938(17)
Eu(2)-As(4)-Eu(2)#1	164.71(2)	N(1)-Eu(2)-As(4)#3	79.00(11)
As(2)-As(5)-As(6)	106.54(3)	N(2)-Eu(2)-As(4)#3	74.37(11)
As(2)-As(5)-As(7)	105.74(3)	N(3)-Eu(2)-As(4)#3	99.66(12)
As(6)-As(5)-As(7)	59.66(2)	As(2)-Eu(2)-As(4)#3	113.409(16)
As(2)-As(5)-Eu(2)	58.43(2)	As(3)#3-Eu(2)-As(4)#3	68.930(15)
As(6)-As(5)-Eu(2)	122.31(2)	As(4)-Eu(2)-As(4)#3	161.116(19)
As(7)-As(5)-Eu(2)	71.40(2)	N(1)-Eu(2)-As(5)	111.15(12)
As(3)-As(6)-As(5)	105.08(3)	N(2)-Eu(2)-As(5)	156.67(11)
As(3)-As(6)-As(7)	104.92(3)	N(3)-Eu(2)-As(5)	94.39(13)
As(5)-As(6)-As(7)	60.93(2)	As(2)-Eu(2)-As(5)	39.035(14)
As(4)-As(7)-As(6)	105.08(3)	As(3)#3-Eu(2)-As(5)	69.174(14)
As(4)-As(7)-As(5)	103.93(3)	As(4)-Eu(2)-As(5)	66.663(14)
As(6)-As(7)-As(5)	59.41(2)	As(4)#3-Eu(2)-As(5)	128.709(16)
N(1)-Eu(2)-N(2)	73.23(17)		

A.1.5 Rb_2AuAs_7

Table A.21: Crystal data and structure refinement for Rb_2AuAs_7.

Empirical formula	Rb_2AuAs_7
Formula weight / $g \cdot mol^{-1}$	892.35
Temperature / K	123(2)
Crystal system; space group	Monoclinic; $I2/a$
Lattice constants / $Å$	$a = 7.4747(3)$
	$b = 12.6250(6)$
	$c = 12.0006(6)$
	$\beta = 92.449(3)$ °
Volume / $Å^3$	1131.44(9)
Z; F(000); calc. density / $g \cdot cm^{-3}$	4; 1536; 5.239
Wavelength	$Mo_{K\alpha}(\lambda = 0.710\,73$ Å)
Crystal size / mm^3	0.100 × 0.020 × 0.010
Theta range for data collection / °	$3.169 \leq \theta \leq 27.477$
Limiting indices	$-9 \leq h \leq 9$; $-16 \leq k \leq 16$; $-15 \leq l \leq 15$
Reflections collected / unique	2531 / 1296
Completeness to $\theta = 25.242°$	99.3%
R_{int}	0.0473
Absorption coefficient / mm^{-1}	41.802; Semi-empirical from equivalents
Max. / min. transmission	0.3679 / 0.2048
Refinement method	Full-matrix least-squares on F^2
Data / restraints / parameters	1296 / 0 / 48
R indices (all data) R_1; wR_2	0.0666; 0.0955
R indices $[[n]I > 2\sigma(I)]$ R_1; wR_2	[939] 0.0389; 0.0868
Goodness-of-fit for F^2	1.025
Largest diff. peak / $e^- \cdot Å^{-3}$	+1.658
Largest diff. hole / $e^- \cdot Å^{-3}$	-2.107

Table A.22: Atomic coordinates ($\times 1 \times 10^4$) and equivalent isotropic displacement parameters U_{eq} / $Å^2$ $\times 1 \times 10^3$ for the independent atoms in the structure of Rb_2AuAs_7.

Atom	Wyck.	Site	x / a	y / b	z / c	U_{eq} / $Å^2$
Au(1)	4*b*	-1	0	0	5000	29(1)
As(1)	8*f*	1	2153(2)	1795(1)	6804(1)	19(1)
As(2)	8*f*	1	333(2)	2959(1)	5602(1)	20(1)
As(3)	8*f*	1	5050(2)	1717(1)	5955(1)	20(1)
As(4)	4*e*	2	2500	4186(1)	5000	22(1)
Rb(1)	8*f*	1	6665(2)	845(1)	2152(1)	22(1)

Table A.23: Anisotropic displacement parameters U_{ij} / $Å^2$ $\times 1 \times 10^3$ for the independent atoms in the structure of Rb_2AuAs_7.

Atom	U_{11}	U_{22}	U_{33}	U_{23}	U_{13}	U_{12}
Au(1)	45(1)	22(1)	19(1)	0(1)	7(1)	-7(1)
As(1)	25(1)	20(1)	13(1)	2(1)	1(1)	-2(1)
As(2)	22(1)	24(1)	14(1)	-1(1)	3(1)	2(1)
As(3)	24(1)	22(1)	15(1)	0(1)	1(1)	4(1)
As(4)	34(1)	15(1)	17(1)	0	1(1)	0
Rb(1)	23(1)	23(1)	22(1)	-2(1)	2(1)	1(1)

Table A.24: Selected bond lengths for Rb_2AuAs_7. Symmetry transformations used to generate equivalent atoms: #1: x-1/2,-y,z; #2: -x+1/2,y,-z+1; #3: x-1,y,z; #4: -x+1,-y,-z+1; #5: -x+1/2,-y+1/2,-z+3/2; #6: x-1,-y+1/2,z+1/2; #7: -x+1/2,-y+1/2,-z+1/2; #8: -x+3/2,y,-z+1; #9: x,-y+1/2,z+1/2; #10: x-1/2,y+1/2,z+1/2; #11: -x+1,y+1/2,-z+1/2.

Atoms 1, 2	Distance / $Å$	Atoms 1, 2	Distance / $Å$
Au(1)-As(3)#1	2.4514(12)	As(2)-As(3)#2	2.4470(16)
Au(1)-As(3)#2	2.4514(12)	As(2)-Rb(1)#6	3.7005(16)
Au(1)-Rb(1)#1	3.8385(11)	As(2)-Rb(1)#7	3.8738(16)
Au(1)-Rb(1)#2	3.8385(11)	As(2)-Rb(1)#2	4.1189(16)
Au(1)-Rb(1)#3	4.2789(12)	As(3)-Rb(1)#8	3.4535(17)
Au(1)-Rb(1)#4	4.2789(12)	As(3)-Rb(1)#9	3.5841(17)
As(1)-As(3)	2.4338(18)	As(3)-Rb(1)#4	4.1850(17)

continued on next page

Atoms 1, 2	Distance / Å	Atoms 1, 2	Distance / Å
As(1)-As(2)	2.4342(17)	As(4)-Rb(1)#10	3.4036(16)
As(1)-As(1)#5	2.481(2)	As(4)-Rb(1)#11	3.4036(16)
As(1)-Rb(1)#2	3.3848(16)	As(4)-Rb(1)#9	3.9589(12)
As(1)-Rb(1)#4	3.6557(17)	As(4)-Rb(1)#7	3.9589(12)
As(2)-As(4)	2.3754(16)		

Table A.25: Selected bond angles for Rb_2AuAs_7. Symmetry transformations used to generate equivalent atoms: #1: x-1/2,-y,z; #2: -x+1/2,y,-z+1; #5: -x+1/2,-y+1/2,-z+3/2.

Atoms 1, 2, 3	Angle / °	Atoms 1, 2, 3	Angle / °
As(3)#1-Au(1)-As(3)#2	180	As(4)-As(2)-As(3)#2	104.17(5)
As(3)-As(1)-As(2)	105.12(6)	As(1)-As(2)-As(3)#2	96.29(6)
As(3)-As(1)-As(1)#5	98.44(7)	As(1)-As(3)-As(2)#2	102.51(6)
As(2)-As(1)-As(1)#5	93.49(7)	As(1)-As(3)-Au(1)#2	103.62(5)
As(4)-As(2)-As(1)	101.71(6)	As(2)#2-As(4)-As(2)	98.63(8)

A.1.6 $Rb_3AuSe_2 \cdot 1.5\,NH_3$

Table A.26: Crystal data and structure refinement for$Rb_3AuSe_2 \cdot 1.5\,NH_3$. Crystal No.1 at 123 K. The figures were created on the basis of this data set.

Empirical formula	$Rb_3AuSe_2 \cdot 1.5\,NH_3$
Formula weight / $g \cdot mol^{-1}$	636.85
Temperature / K	123(2)
Crystal system; space group	Monoclinic; $P2_1/n$
Lattice constants / $Å$	$a = 9.8531(4)$
	$b = 10.5173(4)$
	$c = 10.6144(4)$
	$\beta = 110.838(2)$ °
Volume / $Å^3$	1028.00(7)
Z; F(000); calc. density / $g \cdot cm^{-3}$	4; 1112; 4.170
Wavelength	$Mo_{K\alpha}(\lambda = 0.710\,73$ Å)
Crystal size / mm^3	0.188 × 0.142 × 0.070
Theta range for data collection / °	$2.940 \leq \theta \leq 33.293$
Limiting indices	$-15 \leq h \leq 15$; $-16 \leq k \leq 16$; $-16 \leq l \leq 16$
Reflections collected / unique	7001 / 3898
Completeness to $\theta = 25.242°$	99.0%
R_{int}	0.0488
Absorption coefficient / mm^{-1}	35.433; Semi-empirical from equivalents
Refinement method	Full-matrix least-squares on F^2
Data / restraints / parameters	3898 / 0 / 74
R indices (all data) R_1; wR_2	0.0653; 0.1256
R indices $[[n]I > 2\sigma(I)]$ R_1; wR_2	[3898] 0.0482; 0.1183
Goodness-of-fit for F^2	1.029
Extinction coefficient	0.0038(3)
Largest diff. peak / $e^- \cdot Å^{-3}$	+3.459
Largest diff. hole / $e^- \cdot Å^{-3}$	-3.183

Table A.27: Atomic coordinates ($\times 1 \times 10^4$) and equivalent isotropic displacement parameters U_{eq} / $Å^2$ $\times 1 \times 10^3$ for the independent atoms in the structure of $Rb_3AuSe_2 \cdot 1.5\,NH_3$. Crystal No.1 at 123 K.

Atom	Wyck.	Site	*SOF*	*x* / *a*	*y* / *b*	*z* / *c*	U_{eq} / $Å^2$
Au(1)	4*e*	1		5543(1)	6562(1)	3102(1)	17(1)
Se(1)	4*e*	1		3102(1)	6963(1)	2971(1)	24(1)
Se(2)	4*e*	1		7926(1)	6043(1)	3132(1)	21(1)
Rb(1)	4*e*	1		5442(1)	3353(1)	3496(1)	23(1)
Rb(2)	4*e*	1		6989(1)	4119(1)	282(1)	26(1)
Rb(3)	4*e*	1		8930(1)	5452(1)	6449(1)	18(1)
N(1)	4*e*	1		4076(8)	3132(7)	308(7)	23(1)
N(2)	4*e*	1	0.5	10004(16)	5390(16)	384(16)	27(3)

Table A.28: Anisotropic displacement parameters U_{ij} / $Å^2$ $\times 1 \times 10^3$ for the independent atoms in the structure of $Rb_3AuSe_2 \cdot 1.5\,NH_3$. Crystal No.1 at 123 K.

Atom	U_{11}	U_{22}	U_{33}	U_{23}	U_{13}	U_{12}
Au(1)	22(1)	10(1)	13(1)	1(1)	0(1)	-2(1)
Se(1)	22(1)	34(1)	15(1)	5(1)	6(1)	-9(1)
Se(2)	25(1)	18(1)	16(1)	-2(1)	-1(1)	7(1)
Rb(1)	36(1)	14(1)	15(1)	1(1)	4(1)	-5(1)
Rb(2)	46(1)	13(1)	16(1)	-1(1)	7(1)	1(1)
Rb(3)	24(1)	14(1)	18(1)	0(1)	10(1)	1(1)
N(1)	35(4)	17(3)	16(3)	4(2)	8(3)	1(3)
N(2)	26(6)	25(8)	32(8)	-12(6)	14(6)	-10(6)

Table A.29: Selected bond lengths for $Rb_3AuSe_2 \cdot 1.5\,NH_3$. Crystal No.1 at 123 K. Crystal No.1 at 123 K. Symmetry transformations used to generate equivalent atoms: #1: -x+3/2,y+1/2,-z+1/2; #2: -x+1,-y+1,-z; #3: x-1/2,-y+3/2,z-1/2; #4: -x+1,-y+1,-z+1; #5: -x+1/2,y+1/2,-z+1/2; #6: -x+2,-y+1,-z+1; #7: -x+3/2,y-1/2,-z+1/2; #8: x-1/2,-y+1/2,z-1/2; #9: -x+2,-y+1,-z.

Atoms 1, 2	Distance / $Å$	Atoms 1, 2	Distance / $Å$
Au(1)-Se(1)	2.3964(9)	Se(2)-Rb(1)#1	3.6680(12)
Au(1)-Se(2)	2.3997(8)	Se(2)-Rb(1)	3.8483(12)
Au(1)-Rb(1)	3.4064(9)	Rb(1)-N(1)	3.174(7)

continued on next page

Atoms 1, 2	Distance / Å	Atoms 1, 2	Distance / Å
Au(1)-Rb(2)#1	3.6225(9)	Rb(1)-N(2)#7	3.419(16)
Au(1)-Rb(2)#2	3.6421(9)	Rb(1)-Rb(2)	4.2789(12)
Au(1)-Rb(3)#3	3.6721(8)	Rb(1)-Rb(3)	4.3408(11)
Au(1)-Rb(1)#4	4.0600(9)	Rb(1)-Rb(3)#4	4.5079(11)
Au(1)-Rb(3)	4.0851(8)	Rb(1)-Rb(3)#8	4.5443(11)
Se(1)-Rb(3)#3	3.4068(11)	Rb(2)-N(1)	3.062(8)
Se(1)-Rb(3)#4	3.4225(11)	Rb(2)-N(1)#2	3.063(8)
Se(1)-Rb(1)#4	3.5215(11)	Rb(2)-N(2)	3.224(14)
Se(1)-Rb(1)#5	3.5906(12)	Rb(2)-N(2)#9	3.321(13)
Se(1)-Rb(2)#2	3.6067(12)	Rb(2)-Rb(2)#2	4.1814(18)
Se(2)-Rb(3)	3.3593(11)	Rb(2)-Rb(3)#7	4.2300(11)
Se(2)-Rb(3)#6	3.3595(11)	Rb(3)-N(2)#6	3.267(17)
Se(2)-Rb(2)	3.4796(11)	Rb(3)-Rb(3)#6	4.4080(14)
Se(2)-Rb(2)#1	3.6349(12)	N(2)-N(2)#9	1.15(3)

Table A.30: Selected bond angles for $Rb_3AuSe_2 \cdot 1.5\,NH_3$. Crystal No.1 at 123 K.

Atoms 1, 2, 3	Angle / °
Se(1)-Au(1)-Se(2)	176.16(3)

Table A.31: Crystal data and structure refinement for$Rb_3AuSe_2 \cdot 1.5\,NH_3$. Crystal No.2 at 150 K. The figures were created on the basis of this data set.

Empirical formula	$Rb_3AuSe_2 \cdot 1.5\,NH_3$
Formula weight / $g \cdot mol^{-1}$	636.85
Temperature / K	150(2)
Crystal system; space group	Monoclinic; $P2_1/n$
Lattice constants / $Å$	$a = 9.8937(6)$
	$b = 10.5795(8)$
	$c = 10.6636(6)$
	$\beta = 110.812(4)$ °
Volume / $Å^3$	1043.33(12)
Z; F(000); calc. density / $g \cdot cm^{-3}$	4; 1092; 4.054
Wavelength	$Mo_{K\alpha}(\lambda = 0.710\,73\,Å)$
Crystal size / mm^3	0.058 x 0.054 x 0.050
Theta range for data collection / °	$2.925 \leq \theta \leq 27.473$
Limiting indices	$-12 \leq h \leq 12$; $-11 \leq k \leq 11$; $-13 \leq l \leq 13$
Reflections collected / unique	7152 / 2333
Completeness to $\theta = 25.242°$	98.9%
R_{int}	0.1144
Absorption coefficient / mm^{-1}	34.908; Semi-empirical from equivalents
Max. / min. transmission	0.2208/ 0.1855
Refinement method	Full-matrix least-squares on F^2
Data / restraints / parameters	2333 / 0 / 74
R indices (all data) R_1; wR_2	0.1244; 0.1055
R indices $[[n]I > 2\sigma(I)]$ R_1; wR_2	[1255] 0.0478; 0.0851
Goodness-of-fit for F^2	0.880
Extinction coefficient	0.00118(14)
Largest diff. peak / $e^- \cdot Å^{-3}$	+1.872
Largest diff. hole / $e^- \cdot Å^{-3}$	-2.143

Table A.32: Anisotropic displacement parameters U_{ij} / $Å^2$ $\times 1 \times 10^3$ for the independent atoms in the structure of $Rb_3AuSe_2 \cdot 1.5\,NH_3$. Crystal No.2 at 100 K.

Atom	U_{11}	U_{22}	U_{33}	U_{23}	U_{13}	U_{12}
Au(1)	24(1)	16(1)	18(1)	1(1)	1(1)	-2(1)
Se(1)	23(1)	38(1)	21(1)	3(1)	6(1)	-9(1)
Se(2)	29(1)	21(1)	21(1)	-2(1)	0(1)	5(1)
Rb(1)	35(1)	20(1)	18(1)	0(1)	5(1)	-4(1)
Rb(2)	50(1)	18(1)	20(1)	-2(1)	9(1)	2(1)
Rb(3)	24(1)	20(1)	23(1)	0(1)	10(1)	1(1)
N(1)	49(8)	21(8)	17(6)	-1(5)	15(6)	-10(6)
N(2)	1(10)	50(20)	32(17)	-25(12)	5(11)	-1(11)

Table A.33: Anisotropic displacement parameters U_{ij} / $Å^2$ $\times 1 \times 10^3$ for the independent atoms in the structure of $Rb_3AuSe_2 \cdot 1.5\,NH_3$. Crystal No.2 at 110 K.

Atom	U_{11}	U_{22}	U_{33}	U_{23}	U_{13}	U_{12}
Au(1)	26(1)	16(1)	20(1)	1(1)	2(1)	-2(1)
Se(1)	25(1)	37(1)	23(1)	5(1)	6(1)	-7(1)
Se(2)	29(1)	23(1)	21(1)	-2(1)	0(1)	7(1)
Rb(1)	37(1)	21(1)	20(1)	1(1)	3(1)	-4(1)
Rb(2)	49(1)	18(1)	21(1)	-2(1)	8(1)	1(1)
Rb(3)	25(1)	21(1)	25(1)	0(1)	10(1)	2(1)
N(1)	28(6)	21(7)	25(7)	1(5)	7(6)	1(6)
N(2)	28(6)	21(7)	25(7)	1(5)	7(6)	1(6)

Table A.34: Anisotropic displacement parameters U_{ij} / $Å^2$ $\times 1 \times 10^3$ for the independent atoms in the structure of $Rb_3AuSe_2 \cdot 1.5\,NH_3$. Crystal No.2 at 120 K.

Atom	U_{11}	U_{22}	U_{33}	U_{23}	U_{13}	U_{12}
Au(1)	27(1)	18(1)	20(1)	1(1)	2(1)	-2(1)
Se(1)	26(1)	39(1)	24(1)	5(1)	7(1)	-8(1)
Se(2)	31(1)	25(1)	24(1)	-2(1)	2(1)	6(1)
Rb(1)	40(1)	23(1)	22(1)	1(1)	5(1)	-5(1)

continued on next page

Atom	U_{11}	U_{22}	U_{33}	U_{23}	U_{13}	U_{12}
Rb(2)	50(1)	21(1)	25(1)	-2(1)	9(1)	1(1)
Rb(3)	30(1)	23(1)	26(1)	1(1)	13(1)	2(1)
N(1)	43(10)	24(10)	23(9)	-9(8)	2(8)	-13(8)
N(2)	60(30)	30(30)	50(30)	-9(18)	20(20)	-10(20)

Table A.35: Anisotropic displacement parameters U_{ij} / $Å^2$ $\times 1 \times 10^3$ for the independent atoms in the structure of $Rb_3AuSe_2 \cdot 1.5\,NH_3$. Crystal No.2 at 130 K.

Atom	U_{11}	U_{22}	U_{33}	U_{23}	U_{13}	U_{12}
Au(1)	27(1)	18(1)	20(1)	1(1)	2(1)	-2(1)
Se(1)	26(1)	40(1)	23(1)	3(1)	8(1)	-7(1)
Se(2)	29(1)	25(1)	23(1)	-3(1)	1(1)	7(1)
Rb(1)	41(1)	23(1)	21(1)	1(1)	6(1)	-4(1)
Rb(2)	48(1)	23(1)	23(1)	-2(1)	9(1)	1(1)
Rb(3)	28(1)	22(1)	27(1)	1(1)	13(1)	2(1)
N(1)	48(8)	19(8)	11(6)	-4(5)	-5(6)	-10(6)
N(2)	45(15)	6(15)	48(19)	2(12)	29(14)	15(13)

Table A.36: Anisotropic displacement parameters U_{ij} / $Å^2$ $\times 1 \times 10^3$ for the independent atoms in the structure of $Rb_3AuSe_2 \cdot 1.5\,NH_3$. Crystal No.2 at 140 K.

Atom	U_{11}	U_{22}	U_{33}	U_{23}	U_{13}	U_{12}
Au(1)	27(1)	19(1)	21(1)	2(1)	3(1)	-2(1)
Se(1)	27(1)	42(1)	26(1)	4(1)	10(1)	-8(1)
Se(2)	32(1)	27(1)	23(1)	-1(1)	2(1)	6(1)
Rb(1)	43(1)	24(1)	23(1)	1(1)	6(1)	-5(1)
Rb(2)	48(1)	23(1)	25(1)	-1(1)	9(1)	1(1)
Rb(3)	30(1)	24(1)	27(1)	1(1)	12(1)	2(1)
N(1)	45(8)	29(8)	19(7)	-3(6)	-1(6)	-4(6)
N(2)	19(12)	60(20)	31(18)	-20(13)	3(13)	0(15)

Table A.37: Anisotropic displacement parameters U_{ij} / $Å^2$ $\times 1 \times 10^3$ for the independent atoms in the structure of $Rb_3AuSe_2 \cdot 1.5\,NH_3$. Crystal No.2 at 150 K.

Atom	U_{11}	U_{22}	U_{33}	U_{23}	U_{13}	U_{12}
Au(1)	29(1)	21(1)	23(1)	1(1)	4(1)	-2(1)
Se(1)	31(1)	41(1)	28(1)	4(1)	11(1)	-6(1)
Se(2)	31(1)	28(1)	26(1)	-2(1)	3(1)	6(1)
Rb(1)	44(1)	28(1)	24(1)	1(1)	6(1)	-6(1)
Rb(2)	49(1)	25(1)	27(1)	-2(1)	10(1)	1(1)
Rb(3)	32(1)	25(1)	30(1)	0(1)	14(1)	2(1)
N(1)	50(8)	26(8)	13(6)	-3(6)	-4(6)	0(7)
N(2)	25(12)	50(20)	23(16)	6(13)	12(12)	21(14)

Table A.38: Anisotropic displacement parameters U_{ij} / $Å^2$ $\times 1 \times 10^3$ for the independent atoms in the structure of $Rb_3AuSe_2 \cdot 1.5\,NH_3$. Crystal No.2 at 160 K.

Atom	U_{11}	U_{22}	U_{33}	U_{23}	U_{13}	U_{12}
Au(1)	31(1)	24(1)	25(1)	1(1)	5(1)	-1(1)
Se(1)	33(1)	45(1)	30(1)	3(1)	12(1)	-7(1)
Se(2)	32(1)	32(1)	28(1)	-3(1)	3(1)	6(1)
Rb(1)	48(1)	30(1)	27(1)	0(1)	7(1)	-4(1)
Rb(2)	49(1)	28(1)	30(1)	-2(1)	11(1)	0(1)
Rb(3)	36(1)	28(1)	31(1)	1(1)	15(1)	2(1)
N(1)	38(7)	45(10)	20(6)	-7(6)	-1(6)	-7(7)
N(2)	19(11)	27(19)	52(19)	-13(13)	9(12)	-1(13)

A.1.7 $K_{10}CuSe_8Cl \cdot NH_3$

Table A.39: Crystal data and structure refinement for $K_{10}CuSe_8Cl \cdot NH_3$.

Empirical formula	$K_{10}CuSe_8Cl \cdot NH_3$
Formula weight / $g \cdot mol^{-1}$	1138.70
Temperature / K	123(2)
Crystal system; space group	Orthorhombic; *Pbcn*
Lattice constants / $Å$	$a = 13.0315(3)$
	$b = 11.9464(4)$
	$c = 16.8078(5)$
Volume / $Å^3$	2616.63(13)
Z; F(000); calc. density / $g \cdot cm^{-3}$	4; 2072; 2.891
Wavelength	$Mo_{K\alpha}(\lambda = 0.710\,73\,Å)$
Crystal size / mm^3	0.082 × 0.050 × 0.047
Theta range for data collection / °	$3.126 \leq \theta \leq 27.488$
Limiting indices	$-16 \leq h \leq 16$; $-15 \leq k \leq 15$; $-21 \leq l \leq 21$
Reflections collected / unique	5427 / 2977
Completeness to $\theta = 25.242°$	99.2%
R_{int}	0.0445
Absorption coefficient / mm^{-1}	13.645; Semi-empirical from equivalents
Refinement method	Full-matrix least-squares on F^2
Data / restraints / parameters	2977 / 0 / 102
R indices (all data) R_1; wR_2	0.0670; 0.0648
R indices $[[n]I > 2\sigma(I)]R_1$; wR_2	[1960] 0.0331; 0.0576
Goodness-of-fit for F^2	0.953
Largest diff. peak / $e^- \cdot Å^{-3}$	+0.872
Largest diff. hole / $e^- \cdot Å^{-3}$	-0.735

Table A.40: Atomic coordinates ($\times 1 \times 10^4$) and equivalent isotropic displacement parameters U_{eq} / $Å^2$ $\times 1 \times 10^3$ for the independent atoms in the structure of $K_{10}CuSe_8Cl \cdot NH_3$.

Atom	Wyck.	Site	*SOF*	*x* / *a*	*y* / *b*	*z* / *c*	U_{eq} / $Å^2$
Cu(1)	4*a*	-1		5000	5000	0	15(1)
Se(1)	8*d*	1		6551(1)	4216(1)	65(1)	15(1)
Se(2)	8*d*	1		6977(1)	6835(1)	2035(1)	15(1)
Se(3)	8*d*	1		7770(1)	8082(1)	2978(1)	16(1)
Se(4)	8*d*	1		5195(1)	9015(1)	5001(1)	16(1)
K(1)	8*d*	1		8314(1)	4544(1)	1413(1)	16(1)
K(2)	8*d*	1		8260(1)	5473(1)	3658(1)	16(1)
K(3)	8*d*	1		7836(1)	1895(1)	12(1)	19(1)
K(4)	8*d*	1		5512(1)	7183(1)	3590(1)	20(1)
K(5)	8*d*	1		9438(1)	7725(1)	1548(1)	24(1)
Cl(1)	4*c*	.2.		10000	5428(2)	2500	20(1)
N(2)	8*d*	1	0.5	9943(8)	9707(6)	2793(5)	30(3)

Table A.41: Anisotropic displacement parameters U_{ij} / $Å^2$ $\times 1 \times 10^3$ for the independent atoms in the structure of $K_{10}CuSe_8Cl \cdot NH_3$.

Atom	U_{11}	U_{22}	U_{33}	U_{23}	U_{13}	U_{12}
Cu(1)	12(1)	16(1)	18(1)	1(1)	0(1)	1(1)
Se(1)	12(1)	16(1)	18(1)	1(1)	0(1)	2(1)
Se(2)	16(1)	16(1)	15(1)	-1(1)	1(1)	1(1)
Se(3)	17(1)	15(1)	15(1)	-1(1)	0(1)	1(1)
Se(4)	16(1)	18(1)	13(1)	-1(1)	0(1)	2(1)
K(1)	17(1)	17(1)	15(1)	-1(1)	-2(1)	0(1)
K(2)	15(1)	16(1)	17(1)	-1(1)	2(1)	0(1)
K(3)	25(1)	17(1)	16(1)	0(1)	-2(1)	4(1)
K(4)	15(1)	29(1)	16(1)	-4(1)	0(1)	1(1)
K(5)	20(1)	33(1)	19(1)	5(1)	2(1)	7(1)
Cl(1)	12(1)	34(1)	15(1)	0	0(1)	0
N(2)	23(5)	17(5)	50(7)	-2(4)	-3(7)	10(4)

Table A.42: Selected bond lengths for $K_{10}CuSe_8Cl \cdot NH_3$. Symmetry transformations used to generate equivalent atoms: #1: -x+1,-y+1,-z; #2: x,-y+1,z-1/2; #3: -x+1,y,-z+1/2; #5: -x+3/2,y+1/2,z; #6: -x+3/2,y-1/2,z; #8: x,-y+1,z+1/2; #9: -x+2,y,-z+1/2; #10: -x+1,-y+2,-z+1; #11: -x+3/2,-y+3/2,z+1/2; #12: x-1/2,-y+3/2,-z+1; #13: x-1/2,y+1/2,-z+1/2.

Atoms 1, 2	Distance / *Å*	Atoms 1, 2	Distance / *Å*
Cu(1)-Se(1)#1	2.2301(5)	Se(3)-K(2)	3.3804(12)
Cu(1)-Se(1)	2.2301(5)	Se(3)-K(3)#8	3.4197(13)
Se(1)-K(3)	3.2405(12)	Se(3)-K(1)#5	3.4588(12)
Se(1)-K(1)	3.2508(12)	Se(3)-K(5)#9	3.7494(13)
Se(1)-K(2)#2	3.2695(12)	Se(4)-Se(4)#10	2.4076(10)
Se(1)-K(4)#2	3.2815(12)	Se(4)-K(4)	3.2525(12)
Se(1)-K(3)#5	3.2999(12)	Se(4)-K(5)#11	3.3635(13)
Se(1)-K(5)#6	3.3229(12)	Se(4)-K(2)#12	3.4373(12)
Se(2)-Se(3)	2.4075(7)	Se(4)-K(1)#13	3.4714(12)
Se(2)-K(4)	3.2631(12)	Se(4)-K(2)#5	3.4899(12)
Se(2)-K(1)	3.4089(12)	Se(4)-K(1)#11	3.5179(12)
Se(2)-K(3)#5	3.4105(13)	Se(4)-K(3)#8	3.6090(12)
Se(2)-K(1)#5	3.4223(12)	K(1)-Cl(1)	3.0460(13)
Se(2)-K(4)#3	3.4355(12)	K(2)-Cl(1)	2.9896(11)
Se(2)-K(5)	3.4768(13)	K(4)-N(2)#6	3.301(8)
Se(2)-K(2)	3.5890(12)	K(5)-N(2)#9	2.736(8)
Se(3)-K(5)	3.2692(12)	K(5)-N(2)	3.228(8)
Se(3)-K(4)	3.2963(13)	K(5)-Cl(1)	3.260(2)
Se(3)-K(2)#5	3.3569(12)		

Table A.43: Selected bond angles for $K_{10}CuSe_8Cl \cdot NH_3$. Symmetry transformations used to generate equivalent atoms: #1: -x+1,-y+1,-z.

Atoms 1, 2, 3	Angle / °
Se(1)#1-Cu(1)-Se(1)	180

A.1.8 $K_2[AuSe]Se \cdot NH_3$

Table A.44: Crystal data and structure refinement for$K_2[AuSe]Se \cdot NH_3$. Refinement for the hexagonal cell.

Empirical formula	$K_2[AuSe]Se \cdot NH_3$
Formula weight / $g \cdot mol^{-1}$	450.12
Temperature / K	123(2)
Crystal system; space group	Hexagonal; $P6_3$
Lattice constants / $Å$	$a = b = 11.6455(12)$
	$c = 6.2657(7)$
Volume / $Å^3$	735.90(17)
Z; F(000); calc. density / $g \cdot cm^{-3}$	4; 780; 4.063
Wavelength	$Mo_{K\alpha}(\lambda = 0.710\,73\,Å)$
Crystal size / mm^3	$0.21 \times 0.022 \times 0.014$
Theta range for data collection / °	$2.019 \leq \theta \leq 31.093$
Limiting indices	$-16 \leq h \leq 16$; $-16 \leq k \leq 15$; $-8 \leq l \leq 8$
Reflections collected / unique	12656 / 1448
Completeness to $\theta = 25.242°$	100.0%
R_{int}	0.0774
Absorption coefficient / mm^{-1}	30.896; Semi-empirical from equivalents
Refinement method	Full-matrix least-squares on F^2
Data / restraints / parameters	1448 / 1 / 37
R indices (all data) R_1; wR_2	0.0991; 0.2291
R indices $[[n]I > 2\sigma(I)]$ R_1; wR_2	[1114] 0.0630; 0.1721
Goodness-of-fit for F^2	1.191
Absolute structure parameter	0.47(6)
Largest diff. peak / $e^- \cdot Å^{-3}$	+8.692
Largest diff. hole / $e^- \cdot Å^{-3}$	-8.680

Table A.45: Atomic coordinates ($\times 1 \times 10^4$) and equivalent isotropic displacement parameters U_{eq} / $Å^2$ $\times 1 \times 10^3$ for the independent atoms in the structure of K_2[AuSe]Se· NH_3 in hexagonal setting.

Atom	Wyck.	Site	x / a	y / b	z / c	U_{eq} / $Å^2$
Au(1)	6c	1	25(1)	5005(2)	1286(3)	16(1)
Se(1)	6c	1	499(3)	6783(2)	3658(8)	16(1)
Se(2)	2a	3..	0	10000	6845(10)	19(2)
K(2)	6c	1	566(6)	7886(6)	8668(16)	25(1)
K(1)	2b	3..	3333	6667	4123(17)	20(3)
N(1)	2b	3..	3333	6667	8290(70)	18(9)

Table A.46: Anisotropic displacement parameters U_{ij} / $Å^2$ $\times 1 \times 10^3$ for the independent atoms in the structure of K_2[AuSe]Se· NH_3 in hexagonal setting.

Atom	U_{11}	U_{22}	U_{33}	U_{23}	U_{13}	U_{12}
Au(1)	20(1)	19(1)	11(1)	-1(1)	-2(1)	11(1)
Se(1)	25(1)	18(1)	9(1)	-3(2)	-1(2)	13(1)
Se(2)	24(2)	24(2)	10(3)	0	0	12(1)
K(2)	38(3)	22(3)	8(2)	-9(4)	-4(4)	10(3)
K(1)	24(3)	24(3)	14(7)	0	0	12(2)

Table A.47: Selected bond lengths for K_2[AuSe]Se· NH_3 in hexagonal setting. Symmetry transformations used to generate equivalent atoms: #1: -x,-y+1,z-1/2; #2: -x,-y+1,z+1/2; #3: x,y,z-1; #4: y-1,-x+y,z-1/2; #5: x-y+1,x+1,z-1/2; #6: -x+y-1,-x+1,z; #7: -y+1,x-y+2,z; #8: -x,-y+2,z-1/2; #9: x-y+1,x+1,z+1/2; #10: y-1,-x+y,z+1/2.

Atoms 1, 2	Distance / $Å$	Atoms 1, 2	Distance / $Å$
Au(1)-Se(1)	2.379(4)	Se(1)-K(2)#5	3.830(7)
Au(1)-Se(1)#1	2.479(4)	Se(2)-K(2)#6	3.069(8)
Au(1)-Au(1)#2	3.1333(3)	Se(2)-K(2)#7	3.069(8)
Au(1)-Au(1)#1	3.1333(4)	Se(2)-K(2)	3.069(8)
Au(1)-K(2)#1	3.423(7)	Se(2)-K(2)#5	3.475(9)
Au(1)-K(2)#3	3.498(8)	Se(2)-K(2)#4	3.475(9)
Au(1)-K(1)#1	3.648(4)	Se(2)-K(2)#8	3.475(9)
Au(1)-K(1)	3.780(5)	K(2)-K(2)#9	4.234(4)

continued on next page

Atoms 1, 2	Distance / Å	Atoms 1, 2	Distance / Å
Se(1)-K(2)#3	3.366(11)	K(2)-K(2)#10	4.234(4)
Se(1)-K(2)	3.379(10)	K(2)-K(2)#5	4.234(4)
Se(1)-K(1)	3.383(3)	K(2)-K(2)#4	4.234(4)
Se(1)-K(2)#4	3.400(6)	K(1)-N(1)	2.61(5)
Se(2)-Se(2)#5	3.1333(3)		

Table A.48: Selected bond angles for K_2[AuSe]Se· NH_3 in hexagonal setting. Symmetry transformations used to generate equivalent atoms: #1: -x,-y+1,z-1/2; #2: -x,-y+1,z+1/2.

Atoms 1, 2, 3	Angle / °	Atoms 1, 2, 3	Angle / °
Se(1)-Au(1)-Se(1)#1	176.77(19)	Au(1)#2-Au(1)-Au(1)#1	178.02(8)
Au(1)-Se(1)-Au(1)#2	80.30(7)		

Table A.49: Crystal data and structure refinement for $K_4[AuSe]_3Se \cdot NH_3$. Refinement for the monoclinic cell.

Empirical formula	$K_4[AuSe]_3Se \cdot NH_3$
Formula weight / $g \cdot mol^{-1}$	1093.15
Temperature / K	123(2)
Crystal system; space group	Monoclinic; $P2_1$
Lattice constants / $Å$	$a = 11.6594(8)$
	$b = 6.2610(3)$
	$c = 11.6532(8)$
	$\beta = 120.018(2)$ °
Volume / $Å^3$	736.57(8)
Z; F(000); calc. density / $g \cdot cm^{-3}$	2; 928; 4.929
Wavelength	$Mo_{K\alpha}(\lambda = 0.710\,73$ Å)
Crystal size / mm^3	0.064 x 0.05 x 0.06
Theta range for data collection / °	$2.017 \leq \theta \leq 26.949$
Limiting indices	$-14 \leq h \leq 14$; $-7 \leq k \leq 7$; $-14 \leq l \leq 14$
Reflections collected / unique	11511 / 3136
Completeness to $\theta = 25.242°$	100.0%
R_{int}	0.0651
Absorption coefficient / mm^{-1}	40.781; Semi-empirical from equivalents
Refinement method	Full-matrix least-squares on F^2
Data / restraints / parameters	3136 / 115 / 102
R indices (all data) R_1; wR_2	0.0708; 0.1181
R indices $[[n]I > 2\sigma(I)]$ R_1; wR_2	[2550] 0.0493; 0.1054
Goodness-of-fit for F^2	1.078
Absolute structure parameter	0.499 (15)
Largest diff. peak / $e^- \cdot Å^{-3}$	+2.756
Largest diff. hole / $e^- \cdot Å^{-3}$	-2.832

Table A.50: Atomic coordinates ($\times 1 \times 10^4$) and equivalent isotropic displacement parameters U_{eq} / $Å^2$ $\times 1 \times 10^3$ for the independent atoms in the structure of K_2[AuSe]Se· NH_3 in monoclinic setting.

Atom	Wyck.	Site	x / a	y / b	z / c	U_{eq} / $Å^2$
Au(1)	2a	1	5018(4)	7425(11)	10016(5)	10(1)
Au(2)	2a	1	10002(5)	7427(15)	4981(6)	19(1)
Au(3)	2a	1	15(4)	2404(10)	-7(4)	9(1)
Se(1)	2a	1	5508(7)	9770(30)	8714(7)	10(2)
Se(2)	2a	1	1267(7)	-230(30)	1797(7)	9(2)
Se(3)	2a	1	8245(8)	9933(15)	4536(8)	16(2)
Se(4)	2a	1	5075(11)	2944(3)	5026(15)	10(1)
K(1)	2a	1	5727(12)	4800(40)	7818(14)	13(3)
K(2)	2a	1	7020(15)	4860(50)	4557(16)	22(3)
K(3)	2a	1	2312(15)	4850(30)	2836(13)	4(2)
K(4)	2a	1	8269(19)	270(10)	11499(12)	4(2)
N(1)	2a	1	8310(70)	4400(40)	11550(50)	4(2)

Table A.51: Anisotropic displacement parameters U_{ij} / $Å^2$ $\times 1 \times 10^3$ for the independent atoms in the structure of K_4[AuSe]$_3$Se· NH_3 in monoclinic setting.

Atom	U_{11}	U_{22}	U_{33}	U_{23}	U_{13}	U_{12}
Au(1)	16(2)	4(2)	18(2)	-1(1)	14(1)	0(1)
Au(2)	25(2)	23(2)	14(2)	5(1)	14(2)	6(1)
Au(3)	7(1)	7(2)	9(1)	-2(1)	1(1)	-1(1)
Se(1)	14(2)	5(2)	11(2)	0(1)	6(1)	0(1)
Se(2)	9(2)	1(2)	9(2)	0(1)	-1(1)	0(1)
Se(3)	17(2)	11(2)	19(2)	-1(1)	8(1)	0(1)
Se(4)	11(2)	11(2)	10(2)	-1(1)	6(1)	-1(1)
K(1)	14(3)	11(3)	13(3)	0(1)	6(2)	0(1)
K(2)	22(3)	21(3)	23(3)	0(1)	11(2)	0(1)
K(3)	4(2)	4(2)	4(2)	0(1)	2(1)	0(1)
K(4)	4(2)	4(2)	4(2)	0(1)	2(1)	0(1)
N(1)	4(2)	4(2)	4(2)	0(1)	2(1)	0(1)

Table A.52: Selected bond lengths for $K_4[AuSe]_3Se \cdot NH_3$ in monoclinic setting. Symmetry transformations used to generate equivalent atoms: #1: -x+1,y-1/2,-z+2; #2: -x+1,y+1/2,-z+2; #3: x,y+1,z; #11: -x+1,y+1/2,-z+1.

Atoms 1, 2	Distance / *Å*	Atoms 1, 2	Distance / *Å*
Au(1)-Se(1)	2.377(13)	Se(1)-K(1)#3	3.37(3)
Au(1)-Se(1)#1	2.498(14)	Se(1)-K(2)#11	3.462(16)
Au(1)-Au(1)#2	3.1308(2)	Se(1)-K(3)#11	3.784(18)
Au(1)-Au(1)#1	3.1308(2)	K(4)-N(1)	2.59(2)
Se(7)-Se(7)#1	3.1343(10)		

Table A.53: Selected bond angles for $K_4[AuSe]_3Se \cdot NH_3$ in monoclinic setting. Symmetry transformations used to generate equivalent atoms: #1: -x+1,y-1/2,-z+2; #2: -x+1,y+1/2,-z+2.

Atoms 1, 2, 3	Angle / °	Atoms 1, 2, 3	Angle / °
Se(1)-Au(1)-Se(1)#1	176.3(6)	Au(1)-Se(1)-Au(1)#2	79.9(2)
Au(1)#2-Au(1)-Au(1)#1	178.5(4)		

A.1.9 $NH_4Fe_2S_3$

Table A.54: Crystal data and structure refinement for $NH_4Fe_2S_3$.

Empirical formula	$NH_4Fe_2S_3$
Formula weight / $g \cdot mol^{-1}$	225.92
Temperature / K	123(2)
Crystal system; space group	Orthorhombic; $Cmcm$
Lattice constants / $Å$	$a = 9.0986(15)$
	$b = 10.982(2)$
	$c = 5.4440(8)$
Volume / $Å^3$	543.97(16)
Z; F(000); calc. density / $g \cdot cm^{-3}$	4; 444; 2.759
Wavelength	$Mo_{K\alpha}(\lambda = 0.710\,73\,Å)$
Crystal size / mm^3	0.222 × 0.012 × 0.012
Theta range for data collection / °	$3.711 \leq \theta \leq 27.501$
Limiting indices	$-11 \leq h \leq 11$; $-14 \leq k \leq 14$; $-7 \leq l \leq 7$
Reflections collected / unique	605 / 365
Completeness to $\theta = 25.242°$	99.7%
R_{int}	0.0618
Absorption coefficient / mm^{-1}	6.322; Semi-empirical from equivalents
Max. / min. transmission	0.928 / 0.334
Refinement method	Full-matrix least-squares on F^2
Data / restraints / parameters	365 / 0 / 20
R indices (all data) R_1; wR_2	0.0770; 0.0993
R indices $[[n]I > 2\sigma(I)]$ R_1; wR_2	[240] 0.0416; 0.0900
Goodness-of-fit for F^2	0.974
Largest diff. peak / $e^- \cdot Å^{-3}$	+1.176
Largest diff. hole / $e^- \cdot Å^{-3}$	-0.951

Table A.55: Atomic coordinates ($\times 1 \times 10^4$) and equivalent isotropic displacement parameters U_{eq} / $Å^2$ $\times 1 \times 10^3$ for the independent atoms in the structure of $NH_4Fe_2S_3$.

Atom	Wyck.	Site	x / a	y / b	z / c	U_{eq} / $Å^2$
Fe(1)	8*e*	2..	6483(1)	5000	5000	12(1)
S(1)	4*c*	m2m	5000	3823(3)	2500	12(1)
S(2)	8*g*	..m	7802(2)	3849(2)	7500	17(1)
N(1)	4*c*	m2m	10000	3316(9)	2500	21(2)

Table A.56: Anisotropic displacement parameters U_{ij} / $Å^2$ $\times 1 \times 10^3$ for the independent atoms in the structure of $NH_4Fe_2S_3$.

Atom	U_{11}	U_{22}	U_{33}	U_{23}	U_{13}	U_{12}
Fe(1)	12(1)	16(1)	8(1)	0(1)	0	0
S(1)	12(1)	14(2)	10(1)	0	0	0
S(2)	15(1)	23(1)	13(1)	0	0	-4(1)
N(1)	17(5)	32(6)	14(5)	0	0	0

Table A.57: Selected bond lengths and angles for $NH_4Fe_2S_3$. Symmetry transformations used to generate equivalent atoms: #1: x,-y+1,-z+1; #2: -x+3,-y+1,-z+1; #3: x,y,-z+3/2; #4: x,y,-z+1/2.

Atoms 1, 2	Distance / $Å$	Atoms 1, 2, 3	Angle / °
Fe(1)-S(2)	2.2119(17)	S(2)-Fe(1)-S(2)#1	114.26(11)
Fe(1)-S(2)#1	2.2119(17)	S(2)-Fe(1)-S(1)#2	105.91(5)
Fe(1)-S(1)#2	2.3114(18)	S(2)#1-Fe(1)-S(1)#2	111.07(8)
Fe(1)-S(1)	2.3114(18)	S(2)-Fe(1)-S(1)	111.07(8)
Fe(1)-Fe(1)#2	2.698(2)	S(2)#1-Fe(1)-S(1)	105.91(5)
Fe(1)-Fe(1)#3	2.7220(4)	S(1)#2-Fe(1)-S(1)	108.58(7)
Fe(1)-Fe(1)#4	2.7220(4)	Fe(1)#2-Fe(1)-Fe(1)#4	90
		Fe(1)#3-Fe(1)-Fe(1)#4	180

A.1.10 $NH_4Fe_2Se_3$

Table A.58: Crystal data and structure refinement for $NH_4Fe_2Se_3$.

Empirical formula	$NH_4Fe_2Se_3$
Formula weight / g·mol^{-1}	366.62
Temperature / K	123(2)
Crystal system; space group	Orthorhombic; $Cmcm$
Lattice constants / $Å$	$a = 9.4101(7)$
	$b = 11.4689(10)$
	$c = 5.6377(5)$
Volume / Å^3	608.44(9)
Z; F(000); calc. density / g·cm^{-3}	4; 660; 4.002
Wavelength	$Mo_{K\alpha}(\lambda = 0.710\,73\,Å)$
Crystal size / mm^3	0.208 × 0.008 × 0.004
Theta range for data collection / °	$3.553 \leq \theta \leq 27.468$
Limiting indices	$-11 \leq h \leq 12$; $-14 \leq k \leq 14$; $-7 \leq l \leq 7$
Reflections collected / unique	5014 / 409
Completeness to $\theta = 25.242°$	99.7%
R_{int}	0.1583
Absorption coefficient / mm^{-1}	45.0240; Analytical
	from equivalents
Max. / min. transmission	0.8342 / 0.1033
Refinement method	Full-matrix least-squares on F^2
Data / restraints / parameters	409 / 7 / 26
R indices (all data) R_1; wR_2	0.0696; 0.0811
R indices $[[n]I > 2\sigma(I)]$ R_1 R_1; wR_2	[287] 0.0365; 0.0705
Goodness-of-fit for F^2	1.004
Largest diff. peak / $e^- \cdot Å^{-3}$ Å^{-3}	+1.282
Largest diff. hole / $e^- \cdot Å^{-3}$	-1.237

Table A.59: Atomic coordinates ($\times 1 \times 10^4$) and equivalent isotropic displacement parameters U_{eq} / $Å^2$ $\times 1 \times 10^3$ for the independent atoms in the structure of $NH_4Fe_2Se_3$.

Atom	Wyck.	Site	x / a	y / b	z / c	U_{eq} / $Å^2$
Fe(1)	8*e*	2..	6462(1)	5000	5000	16(1)
Se(1)	4*c*	m2m	5000	3756(1)	2500	16(1)
Se(2)	8*g*	..m	7824(1)	3815(1)	7500	19(1)
N(1)	4*c*	m2m	10000	3356(15)	2500	37(4)
H(1N1)	8*g*	..m	10720(90)	2870(70)	2500	130(80)
H(2N1)	8*f*	m..	10000	3610(180)	1000(200)	220(140)

Table A.60: Anisotropic displacement parameters U_{ij} / $Å^2$ $\times 1 \times 10^3$ for the independent atoms in the structure of $NH_4Fe_2Se_3$.

Atom	U_{11}	U_{22}	U_{33}	U_{23}	U_{13}	U_{12}
Fe(1)	17(1)	20(1)	11(1)	0(1)	0	0
Se(1)	18(1)	18(1)	12(1)	0	0	0
Se(2)	22(1)	23(1)	12(1)	0	0	5(1)
N(1)	36(9)	42(9)	31(9)	0	0	0

Table A.61: Selected bond lengths and angles for $NH_4Fe_2Se_3$. Symmetry transformations used to generate equivalent atoms: #1: x,-y+1,z-1/2; #2: -x+1,-y+1,-z+1; #3: x,y,-z+3/2; #4: x,y,-z+1/2; #5: -x+2,y,-z+1/2.

Atoms 1, 2	Distance / $Å$	Atoms 1, 2, 3	Angle / °
Fe(1)-Se(2)#1	2.3401(10)	Se(2)#1-Fe(1)-Se(2)	113.61(6)
Fe(1)-Se(2)	2.3401(10)	Se(2)#1-Fe(1)-Se(1)	107.549(19)
Fe(1)-Se(1)	2.4322(10)	Se(2)-Fe(1)-Se(1)	108.54(3)
Fe(1)-Se(1)#2	2.4322(10)	Se(2)#1-Fe(1)-Se(1)#2	108.55(3)
Fe(1)-Fe(1)#2	2.752(2)	Se(2)-Fe(1)-Se(1)#2	107.550(19)
Fe(1)-Fe(1)#3	2.8189(3)	Se(1)-Fe(1)-Se(1)#2	111.08(5)
Fe(1)-Fe(1)#4	2.8189(3)	Fe(1)#2-Fe(1)-Fe(1)#4	90
N(1)-H(1N1)	0.88(10)	Fe(1)#3-Fe(1)-Fe(1)#4	180
N(1)-H(2N1)	0.88(10)		

continued on next page

Atoms 1, 2	Distance / $\AA$	Atoms 1, 2, 3	Angle / °
N(1)-H(2N1)#5	0.88(10)		
N(1)-H(1N1)#5	0.88(10)		

A.1.11 $[Mn_2(HPO_3)_2(C_2H_8N_2)]$

Table A.62: Crystal data and structure refinement for$MnPO_3H\cdot$ en.

Empirical formula	$MnPO_3H\cdot$ en
Formula weight / $g \cdot mol^{-1}$	329.94
Temperature / K	123(2)
Crystal system; space group	Orthorhombic; $Pnnm$
Lattice constants / $Å$	$a = 15.6111(7)$
	$b = 4.9811(2)$
	$c = 6.0109(2)$
Volume / $Å^3$	467.41(3)
Z; F(000); calc. density / $g \cdot cm^{-3}$	2; 328; 2.344
Wavelength	$Mo_{K\alpha}(\lambda = 0.710\,73\,Å)$
Crystal size / mm^3	0.630 × 0.072 × 0.020
Theta range for data collection / °	$3.632 \leq \theta \leq 27.441$
Limiting indices	$-19 \leq h \leq 19$; $-6 \leq k \leq 6$; $-7 \leq l \leq 7$
Reflections collected / unique	999 / 587
Completeness to $\theta = 25.242°$	99.8%
R_{int}	0.0113
Absorption coefficient / mm^{-1}	3.048; Semi-empirical from equivalents
Refinement method	Full-matrix least-squares on F^2
Data / restraints / parameters	587 / 0 / 51
R indices (all data) R_1; wR_2	0.0279; 0.0690
R indices $[[n]I > 2\sigma(I)]$ R_1; wR_2	[555] 0.0261; 0.0684
Goodness-of-fit for F^2	1.265
Largest diff. peak / $e^- \cdot Å^{-3}$	+0.365
Largest diff. hole / $e^- \cdot Å^{-3}$	-0.454

Table A.63: Atomic coordinates ($\times 1 \times 10^4$) and equivalent isotropic displacement parameters U_{eq} / $Å^2$ $\times 1 \times 10^3$ for the independent atoms in the structure of $MnPO_3H \cdot$ en.

Atom	Wyck.	Site	x / a	y / b	z / c	U_{eq} / $Å^2$
Mn(1)	4g	..m	2672(1)	2004(1)	5000	14(1)
P(1)	4g	..m	3520(1)	1437(2)	0	13(1)
O(1)	8h	1	3138(1)	51(3)	2054(3)	15(1)
O(2)	4g	..m	3431(2)	4458(5)	0	17(1)
N(1)	4g	..m	3773(2)	4965(6)	5000	15(1)
C(1)	4g	..m	4660(2)	3923(7)	5000	18(1)
H3	8h	1	3698	5844	3905	
H2	8h	1	4736	2872	3694	
H1	4g	..m	4346	781	0	

Table A.64: Anisotropic displacement parameters U_{ij} / $Å^2$ $\times 1 \times 10^3$ for the independent atoms in the structure of $MnPO_3H \cdot$ en.

Atom	U_{11}	U_{22}	U_{33}	U_{23}	U_{13}	U_{12}
Mn(1)	16(1)	12(1)	14(1)	0	0	0(1)
P(1)	14(1)	12(1)	12(1)	0	0	0(1)
O(1)	21(1)	11(1)	13(1)	0(1)	2(1)	0(1)
O(2)	18(1)	11(1)	21(1)	0	0	1(1)
N(1)	16(2)	14(1)	15(2)	0	0	-1(1)
C(1)	16(2)	14(2)	22(2)	0	0	0(2)

Table A.65: Selected bond lengths for $MnPO_3H \cdot$ en. Symmetry transformations used to generate equivalent atoms: #1: -x+1/2,y-1/2,-z+1/2; #2: x,y,-z+1; #3: -x+1/2,y+1/2,z+1/2; #4: -x+1/2,y+1/2,-z+1/2; #5: x,y,-z; #6: -x+1,-y+1,-z+1.

Atoms 1, 2	Distance / $Å$	Atoms 1, 2	Distance / $Å$
Mn(1)-O(2)#1	2.138(3)	P(1)-O(1)#5	1.5354(18)
Mn(1)-O(1)#2	2.1476(18)	P(1)-H(1)	1.33(4)
Mn(1)-O(1)	2.1476(18)	N(1)-C(1)	1.479(5)
Mn(1)-N(1)	2.265(3)	N(1)-H(3)	0.80(3)

continued on next page

Atoms 1, 2	Distance / Å	Atoms 1, 2	Distance / Å
Mn(1)-O(1)#3	2.3290(18)	N(1)-H(3)#2	0.80(3)
Mn(1)-O(1)#4	2.3290(18)	C(1)-C(1)#6	1.509(7)
Mn(1)-P(1)#4	2.8875(10)	C(1)-H(2)	0.95(3)
P(1)-O(2)	1.511(3)	C(1)-H(2)#2	0.95(3)
P(1)-O(1)	1.5354(18)		

Table A.66: Selected bond angles for $MnPO_3H\cdot$ en. Symmetry transformations used to generate equivalent atoms: #1: -x+1/2,y-1/2,-z+1/2; #2: x,y,-z+1; #3: -x+1/2,y+1/2,z+1/2; #4: -x+1/2,y+1/2,-z+1/2; #5: x,y,-z; #6: -x+1,-y+1,-z+1.

Atoms 1, 2, 3	Angle / °	Atoms 1, 2, 3	Angle / °
O(2)#1-Mn(1)-O(1)#2	90.24(6)	O(2)-P(1)-O(1)	114.33(9)
O(2)#1-Mn(1)-O(1)	90.25(6)	O(2)-P(1)-O(1)#5	114.33(9)
O(1)#2-Mn(1)-O(1)	111.09(10)	O(1)-P(1)-O(1)#5	107.04(14)
O(2)#1-Mn(1)-N(1)	175.74(11)	O(2)-P(1)-H(1)	109(2)
O(1)#2-Mn(1)-N(1)	92.16(7)	O(1)-P(1)-H(1)	105.5(11)
O(1)-Mn(1)-N(1)	92.16(7)	O(1)#5-P(1)-H(1)	105.5(11)
O(2)#1-Mn(1)-O(1)#3	87.11(7)		
O(1)#2-Mn(1)-O(1)#3	92.41(4)		
O(1)-Mn(1)-O(1)#3	156.37(8)		
N(1)-Mn(1)-O(1)#3	89.28(8)		
O(2)#1-Mn(1)-O(1)#4	87.11(7)		
O(1)#2-Mn(1)-O(1)#4	156.37(8)		
O(1)-Mn(1)-O(1)#4	92.41(4)		
N(1)-Mn(1)-O(1)#4	89.28(8)		
O(1)#3-Mn(1)-O(1)#4	64.02(9)		

A.1.12 $K_9Se_{2.88}(Se_2)_{1.12}OH$

Table A.67: Crystal data and structure refinement for $K_9Se_{2.88}(Se_2)_{1.12}OH$.

Empirical formula	$K_9Se_{2.88}(Se_2)_{1.12}OH$
Formula weight / $g \cdot mol^{-1}$	763.71
Temperature / K	123(2)
Crystal system; space group	Monoclinic; $C2/m$
Lattice constants / $Å$	$a = 9.2535(3)$
	$b = 16.5172(5)$
	$c = 18.0434(7)$
	$\beta = 98.595(2)$ °
Volume / $Å^3$	2726.82(16)
Z; F(000); calc. density / $g \cdot cm^{-3}$	4; 2036; 2.723
Wavelength	$Mo_{K\alpha}(\lambda = 0.710\,73$ Å)
Crystal size / mm^3	0.128 × 0.056 × 0.007
Theta range for data collection / °	$2.922 \leq \theta \leq 27.487$
Limiting indices	$-12 \leq h \leq 12$; $-21 \leq k \leq 21$; $-23 \leq l \leq 23$
Reflections collected / unique	5397 / 3141
Completeness to $\theta = 25.242°$	97.7%
R_{int}	0.0512
Absorption coefficient / mm^{-1}	12.544; Semi-empirical from equivalents
Refinement method	Full-matrix least-squares on F^2
Data / restraints / parameters	3141 / 0 / 123
R indices (all data) R_1; wR_2	0.0683; 0.1141
R indices $[[n]I > 2\sigma(I)]$ R_1; wR_2	[2311] 0.0436; 0.1048
Goodness-of-fit for F^2	1.000
Largest diff. peak / $e^- \cdot Å^{-3}$	+1.610
Largest diff. hole / $e^- \cdot Å^{-3}$	-1.401

Table A.68: Atomic coordinates ($\times 1 \times 10^4$) and equivalent isotropic displacement parameters U_{eq} / $Å^2$ $\times 1 \times 10^3$ for the independent atoms in the structure of $K_9Se_{2.88}(Se_2)_{1.12}OH$.

Atom	Wyck.	Site	*SOF*	*x* / *a*	*y* / *b*	*z* / *c*	U_{eq} / $Å^2$
Se(1)	8*j*	1		1549(1)	1817(1)	3910(1)	14(1)
Se(2)	4*i*	m		6028(1)	0	3919(1)	14(1)
Se(3)	8*j*	1		2410(1)	3661(1)	851(1)	18(1)
Se(4)	8*j*	1		2084(1)	2987(1)	2005(1)	15(1)
Se(5)	4*i*	m	0.8848	2879(1)	0	1443(1)	19(1)
Se(6)	4*i*	m	0.1152	3374(10)	0	2165(6)	24(3)
Se(7)	4*i*	m	0.1152	2232(11)	0	887(6)	27(3)
O(1)	4*i*	m		9515(9)	0	3188(5)	36(2)
K(1)	8*j*	1		4347(2)	1568(1)	2959(1)	24(1)
K(2)	4*h*	2		5000	1708(1)	5000	21(1)
K(3)	8*j*	1		3251(2)	3492(1)	4141(1)	21(1)
K(4)	4*i*	m		2743(2)	0	4279(1)	19(1)
K(5)	8*j*	1		435(2)	1197(1)	2104(1)	18(1)
K(6)	4*i*	m		6522(2)	0	2093(1)	20(1)
K(7)	2*b*	2/m		5000	0	0	20(1)
K(8)	8*j*	1		3802(2)	1832(1)	900(1)	19(1)
K(9)	2*a*	2/m		0	0	0	47(1)
HO(1)	4*i*	m		8424	0	3372	

Table A.69: Anisotropic displacement parameters U_{ij} / $Å^2$ $\times 1 \times 10^3$ for the independent atoms in the structure of $K_9Se_{2.88}(Se_2)_{1.12}OH$.

Atom	U_{11}	U_{22}	U_{33}	U_{23}	U_{13}	U_{12}
Se(1)	12(1)	12(1)	19(1)	0(1)	3(1)	0(1)
Se(2)	13(1)	11(1)	17(1)	0	3(1)	0
Se(3)	20(1)	14(1)	18(1)	1(1)	2(1)	2(1)
Se(4)	14(1)	13(1)	20(1)	0(1)	3(1)	1(1)
Se(5)	17(1)	13(1)	28(1)	0	9(1)	0
Se(6)	22(5)	15(5)	37(7)	0	10(4)	0

continued on next page

Atom	U_{11}	U_{22}	U_{33}	U_{23}	U_{13}	U_{12}
Se(7)	32(6)	37(6)	11(6)	0	-1(5)	0
O(1)	33(5)	43(5)	32(5)	0	2(4)	0
K(1)	19(1)	29(1)	26(1)	11(1)	9(1)	9(1)
K(2)	18(1)	21(1)	23(1)	0	2(1)	0
K(3)	14(1)	14(1)	37(1)	3(1)	8(1)	1(1)
K(4)	17(1)	13(1)	26(1)	0	0(1)	0
K(5)	16(1)	15(1)	23(1)	0(1)	4(1)	1(1)
K(6)	28(1)	13(1)	19(1)	0	7(1)	0
K(7)	24(2)	14(1)	22(2)	0	1(1)	0
K(8)	20(1)	16(1)	20(1)	-2(1)	2(1)	2(1)
K(9)	63(3)	46(3)	32(2)	0	5(2)	0

Table A.70: Selected bond lengths for $K_9Se_{2.88}(Se_2)_{1.12}OH$. Symmetry transformations used to generate equivalent atoms: #9: x+1/2,y+1/2,z.

Atoms 1, 2	Distance / *Å*	Atoms 1, 2	Distance / *Å*
Se(6)-Se(7)	2.389(15)	Se(3)-K(9)#9	3.7545(7)
Se(3)-Se(4)	2.4179(10)	Se(4)-K(8)	3.3294(16)
Se(1)-K(3)	3.1795(16)	Se(4)-K(5)	3.3440(16)
Se(1)-K(5)	3.4245(18)	Se(5)-K(9)	3.4348(13)
Se(2)-K(4)	3.201(2)	Se(5)-K(9)	3.4348(13)
Se(2)-K(1)	3.3649(17)	Se(6)-K(5)	3.351(7)
Se(2)-H1	2.5584/10)	Se(6)-K(8)	3.847(7)
Se(2)-O(1)	3.6637(10)	Se(7)-K(9)	2.417(10)
Se(3)-Se(4)	2.4179(10)	Se(7)-K(7)	3.217(10)
Se(3)-K(8)	3.2792(16)		

Table A.71: Selected bond angles for $K_9Se_{2.88}(Se_2)_{1.12}OH$. Symmetry transformations used to generate equivalent atoms: #8: x-1/2,y+1/2,z; #9: x+1/2,y+1/2,z.

Atoms 1, 2, 3	Angle / °	Atoms 1, 2, 3	Angle / °
Se(6)-Se(7)-K(9)	148.3(5)	Se(4)-Se(3)-K(9)#9	142.43(3)

continued on next page

Atoms 1, 2, 3	Angle / °	Atoms 1, 2, 3	Angle / °
Se(6)-Se(7)-K(7)	102.1(4)	Se(2)-O(1)-H(1)	174.82(3)
Se(3)-Se(4)-K(1)	126.94(4)	Se(4)-Se(3)-K(7)#8	122.59(3)

A.1.13 As_3NS_3

Table A.72: Crystal data and structure refinement forAs_3NS_3 at 293 K prior to heating to 373 K.

Empirical formula	As_3NS_3
Formula weight / $g \cdot mol^{-1}$	334.95
Temperature / K	293(2)
Crystal system; space group	Hexagonal; $P6_3/m$
Lattice constants / $\AA$	$a = b = 10.7386(6)$
	$c = 3.2941(2)$
Volume / $\AA^3$	328.97(4)
Z; F(000); calc. density / $g \cdot cm^{-3}$	2; 308; 3.381
Wavelength	$Mo_{K\alpha}(\lambda = 0.710\,73\,\text{Å})$
Crystal size / mm^3	0.028 × 0.028 × 0.010
Theta range for data collection / °	$3.795 \leq \theta \leq 27.368$
Limiting indices	-13 ≤ h ≤ 13; -11 ≤ k ≤ 11; -4 ≤ l ≤ 4
Reflections collected / unique	998 / 294
Completeness to $\theta = 25.242°$	99.6%
R_{int}	0.0495
Absorption coefficient / mm^{-1}	15.974; Semi-empirical from equivalents
Refinement method	Full-matrix least-squares on F^2
Data / restraints / parameters	294 / 0 / 15
R indices (all data) R_1; wR_2	0.0555; 0.0858
R indices $[[n]I > 2\sigma(I)]$ R_1; wR_2	[218] 0.0340; 0.0795
Goodness-of-fit for F^2	1.063
Largest diff. peak / $e^- \cdot \AA^{-3}$	+1.464
Largest diff. hole / $e^- \cdot \AA^{-3}$	-0.601

Table A.73: Atomic coordinates ($\times 1 \times 10^4$) and equivalent isotropic displacement parameters U_{eq} / $Å^2$ $\times 1 \times 10^3$ for the independent atoms in the structure of As_3NS_3 at 293 K prior to heating to 373 K.

Atom	Wyck.	Site	x / a	y / b	z / c	U_{eq} / $Å^2$
As	6*h*	m..	4999(1)	3451(1)	7500	24(1)
S	6*h*	m..	3749(2)	1830(2)	2500	26(1)
N	2*c*	-6..	6667	3333	7500	21(3)

Table A.74: Anisotropic displacement parameters U_{ij} / $Å^2$ $\times 1 \times 10^3$ for the independent atoms in the structure of As_3NS_3 at 293 K prior to heating to 373 K.

Atom	U_{11}	U_{22}	U_{33}	U_{23}	U_{13}	U_{12}
As	28(1)	26(1)	20(1)	0	0	16(1)
S	27(1)	28(1)	19(1)	0	0	10(1)
N	19(4)	19(4)	23(7)	0	0	10(2)

Table A.75: Selected bond lengths and angles for As_3NSe_3 at 293 K prior to heating to 373 K. Symmetry transformations used to generate equivalent atoms: #1: x,y,z+1; #2: x,y,z-1; #3: -y+1,x-y,z; #4: -x+y+1,-x+1,z.

Atoms 1, 2	Distance / $Å$	Atoms 1, 2, 3	Angle / °
As-N	1.8575(9)	N-As-S	99.63(6)
As-S	2.2817(16)	N-As-S#1	99.63(6)
As-S#1	2.2818(16)	S-As-S#1	92.41(8)
		As-S-As#2	92.41(8)
		As#3-N-As#4	120
		As#3-N-As	120
		As#4-N-As	120

Table A.76: Crystal data and structure refinement forAs_3NS_3 at 373 K.

Empirical formula	As_3NS_3
Formula weight / $g \cdot mol^{-1}$	334.95
Temperature / K	373(2)
Crystal system; space group	Hexagonal; $P6_3/m$
Lattice constants / $\AA$	$a = b = 10.7517(7)$
	$c = 3.2844(3)$
Volume / $\AA^3$	328.81(5)
Z; F(000); calc. density / $g \cdot cm^{-3}$	2; 308; 3.383
Wavelength	$Mo_{K\alpha}(\lambda = 0.710\,73\,\text{Å})$
Crystal size / mm^3	$0.028 \times 0.028 \times 0.010$
Theta range for data collection / °	$3.790 \leq \theta \leq 27.394$
Limiting indices	$-13 \leq h \leq 13$; $-11 \leq k \leq 11$; $-4 \leq l \leq 4$
Reflections collected / unique	998 / 294
Completeness to $\theta = 25.242°$	99.6%
R_{int}	0.0619
Absorption coefficient / mm^{-1}	15.982; Semi-empirical from equivalents
Refinement method	Full-matrix least-squares on F^2
Data / restraints / parameters	294 / 0 / 15
R indices (all data) R_1; wR_2	0.0735; 0.0987
R indices $[[n]I > 2\sigma(I)]$ R_1; wR_2	[206] 0.0408; 0.0887
Goodness-of-fit for F^2	1.015
Largest diff. peak / $e^- \cdot \AA^{-3}$	+1.266
Largest diff. hole / $e^- \cdot \AA^{-3}$	-0.767

Table A.77: Atomic coordinates ($\times 1 \times 10^4$) and equivalent isotropic displacement parameter U_{eq} / $Å^2$ $\times 1 \times 10^3$ for the independent atoms in the structure of As_3NS_3 at 373 K.

Atom	Wyck.	Site	*SOF*	*x / a*	*y / b*	*z / c*	U_{eq} / $Å^2$
As	6*h*	m..		8452(1)	5003(1)	7500	32(1)
S	6*h*	m..		8100(3)	6263(3)	2500	34(1)
N	2*c*	-6..		6667	3333	7500	30(3)

Table A.78: Anisotropic displacement parameters U_{ij} / $Å^2$ $\times 1 \times 10^3$ for the independent atoms in the structure of As_3NS_3 at 373 K.

Atom	U_{11}	U_{22}	U_{33}	U_{23}	U_{13}	U_{12}
As	32(1)	37(1)	25(1)	0	0	16(1)
S	46(2)	39(1)	21(1)	0	0	23(1)
N	31(4)	31(4)	27(8)	0	0	16(2)

Table A.79: Selected bond lengths and angles for As_3NSe_3 at 373 K. Symmetry transformations used to generate equivalent atoms: #1: x,y,z+1; #2: x,y,z-1; #3: -x+y+1,-x+1,z; #4: -y+1,x-y,z.

Atoms 1, 2	Distance / $Å$	Atoms 1, 2, 3	Angle / °
As-N	1.8609(9)	N-As-S#1	100.12(7)
As-S#1	2.2778(18)	N-As-S	100.12(7)
As-S	2.2778(18)	S#1-As-S	92.27(9)
		As#2-S-As	92.27(9)
		As-N-As#3	120
		As-N-As#4	120
		As#3-N-As#4	120

Table A.80: Crystal data and structure refinement for As_3NS_3 at 293 K after heating to 373 K.

Empirical formula	As_3NS_3
Formula weight / $g \cdot mol^{-1}$	334.95
Temperature / K	293(2)
Crystal system; space group	Hexagonal; $P6_3/m$
Lattice constants / $Å$	$a = b = 10.7334(6)$
	$c = 3.2809(3)$
Volume / $Å^3$	327.34(5)
Z; F(000); calc. density / $g \cdot cm^{-3}$	2; 308; 3.398
Wavelength	$Mo_{K\alpha}(\lambda = 0.710\,73\,Å)$
Crystal size / mm^3	$0.028 \times 0.028 \times 0.010$
Theta range for data collection / °	$3.790 \leq \theta \leq 27.394$
Limiting indices	$-13 \leq h \leq 13$; $-11 \leq k \leq 11$; $-4 \leq l \leq 4$
Reflections collected / unique	991 / 294
Completeness to $\theta = 25.242°$	99.6%
R_{int}	0.0562
Absorption coefficient / mm^{-1}	16.054; Semi-empirical from equivalents
Refinement method	Full-matrix least-squares on F^2
Data / restraints / parameters	294 / 0 / 15
R indices (all data) R_1; wR_2	0.0587; 0.0776
R indices $[[n]I > 2\sigma(I)]$ R_1; wR_2	[216] 0.0346; 0.0713
Goodness-of-fit for F^2	1.035
Largest diff. peak / $e^- \cdot Å^{-3}$	+1.131
Largest diff. hole / $e^- \cdot Å^{-3}$	-0.718

Table A.81: Atomic coordinates ($\times 1 \times 10^4$) and equivalent isotropic displacement parameters U_{eq} / $Å^2$ $\times 1 \times 10^3$ for the independent atoms in the structure of As_3NS_3 at 293 K after heating to 373 K.

Atom	Wyck.	Site	*SOF*	*x* / *a*	*y* / *b*	*z* / *c*	U_{eq} / $Å^2$
As	6*h*	m..		4992(1)	3449(1)	7500	27(1)
S	6*h*	m..		3730(2)	1833(2)	2500	29(1)
N	2*c*	-6..		6667	3333	7500	28(3)

Table A.82: Anisotropic displacement parameters U_{ij} / $Å^2$ $\times 1 \times 10^3$ for the independent atoms in the structure of As_3NS_3 at 293 K after heating to 373 K.

Atom	U_{11}	U_{22}	U_{33}	U_{23}	U_{13}	U_{12}
As	31(1)	30(1)	21(1)	0	0	17(1)
S	32(1)	30(1)	19(1)	0	0	12(1)
N	29(4)	29(4)	25(6)	0	0	14(2)

Table A.83: Selected bond lengths and angles for As_3NSe_3 at 293 K after heating to 373 K. Symmetry transformations used to generate equivalent atoms: #1: x,y,z+1; #2: x,y,z-1; #3: -y+1,x-y,z; #4: -x+y+1,-x+1,z.

Atoms 1, 2	Distance / $Å$	Atoms 1, 2, 3	Angle / °
As-N	1.8631(8)	N-As-S#1	100.12(6)
As-S#1	2.2820(15)	N-As-S	100.12(6)
As-S	2.2820(15)	S#1-As-S	92.40(8)
		As#2-S-As	92.40(8)
		As#3-N-As	120
		As#3-N-As#4	120
		As-N-As#4	120.000(1)

A.1.14 As_3NSe_3

Table A.84: Crystal data and structure refinement forAs_3NS_3 at 123 K.

Empirical formula	As_3NSe_3
Formula weight / $g \cdot mol^{-1}$	475.65
Temperature / K	123(2)
Crystal system; space group	Hexagonal; $P6_3/m$
Lattice constants / $\AA$	$a = b = 10.8641(16)$
	$c = 3.4651(12)$
Volume / $\AA^3$	354.19(16)
Z; F(000); calc. density / $g \cdot cm^{-3}$	2; 416; 4.460
Wavelength	$Mo_{K\alpha}(\lambda = 0.710\,73\,\text{Å})$
Crystal size / mm^3	0.050 × 0.008 × 0.008
Theta range for data collection / °	$2.165 \leq \theta \leq 27.590$
Limiting indices	$-14 \leq h \leq 14$; $-14 \leq k \leq 14$; $-4 \leq l \leq 4$
Reflections collected / unique	4880 / 316
Completeness to $\theta = 25.242°$	98.8%
R_{int}	0.2436
Absorption coefficient / mm^{-1}	29.387; Semi-empirical from equivalents
Refinement method	Full-matrix least-squares on F^2
Data / restraints / parameters	316 / 0 / 17
R indices (all data) R_1; wR_2	0.1222; 0.1705
R indices $[[n]I > 2\sigma(I)]$ R_1; wR_2	[198] 0.0640; 0.1417
Goodness-of-fit for F^2	1.002
Largest diff. peak / $e^- \cdot \AA^{-3}$	+2.892
Largest diff. hole / $e^- \cdot \AA^{-3}$	-2.609

Table A.85: Atomic coordinates ($\times 1 \times 10^4$) and equivalent isotropic displacement parameters U_{eq} / $Å^2$ $\times 1 \times 10^3$ for the independent atoms in the structure of As_3NSe_3 at 123 K.

Atom	Wyck.	Site	*SOF*	*x / a*	*y / b*	*z / c*	U_{eq} / $Å^2$
As	6*h*	m..		5066(3)	1536(3)	7500	13(1)
Se	6*h*	m..		3712(3)	1884(3)	2500	13(1)
N	2*c*	-6..		6667	3333	7500	13(8)

Table A.86: Anisotropic displacement parameters U_{ij} / $Å^2$ $\times 1 \times 10^3$ for the independent atoms in the structure of As_3NSe_3 at 123 K.

Atom	U_{11}	U_{22}	U_{23}	U_{13}	U_{12}
As	15(1)	13(1)	0	0	6(1)
Se	15(1)	15(1)	0	0	7(1)
N	13(11)	13(11)	0	0	7(5)

Table A.87: Selected bond lengths and angles for As_3NSe_3 at 123 K. Symmetry transformations used to generate equivalent atoms: #1: x,y,z+1; #2: x,y,z-1; #3: -x+y+1,-x+1,z; #4: -y+1,x-y,z.

Atoms 1, 2	Distance / $Å$	Atoms 1, 2, 3	Angle / °
As-N	1.855(3)	N-As-Se	99.12(10)
As-Se	2.422(3)	N-As-Se#1	99.12(10)
As-Se#1	2.422(3)	Se-As-Se#1	91.33(13)
		As-Se-As#2	91.33(13)
		As#3-N-As	120.001(2)
		As#3-N-As#4	120
		As-N-As#4	119.999(2)

A.1.15 $Rb_5(AsSe_3)Se\cdot 2\,NH_3$

Table A.88: Crystal data and structure refinement for $Rb_5(AsSe_3)Se\cdot 2\,NH_3$.

Empirical formula	$Rb_5(AsSe_3)Se\cdot 2\,NH_3$
Formula weight / $g\cdot mol^{-1}$	846.13
Temperature / K	123(2)
Crystal system; space group	Orthorhombic; $P2_12_12_1$
Lattice constants / $Å$	a = 8.7877(7)
	b = 10.7419(7)
	c = 17.4683(10)
Volume / $Å^3$	1648.95(19)
Z; F(000); calc. density / $g\cdot cm^{-3}$	4; 1472; 3.408
Wavelength	$Mo_{K\alpha}(\lambda = 0.710\,73$ Å)
Crystal size / mm^3	0.130 × 0.070 × 0.030
Theta range for data collection / °	$2.995 \leq \theta \leq 27.491$
Limiting indices	$-11 \leq h \leq 11$; $-13 \leq k \leq 13$; $-22 \leq l \leq 22$
Reflections collected / unique	6352 / 3616
Completeness to $\theta = 25.242°$	99.1%
R_{int}	0.1621
Absorption coefficient / mm^{-1}	25.519; Semi-empirical from equivalents
Refinement method	Full-matrix least-squares on F^2
Data / restraints / parameters	3616 / 0 / 100
R indices (all data) R_1; wR_2	0.1784; 0.2086
R indices $[[n]I > 2\sigma(I)]$ R_1; wR_2	[1776] 0.0796; 0.1692
Goodness-of-fit for F^2	0.936
Largest diff. peak / $e^-\cdot Å^{-3}$	+2.459
Largest diff. hole / $e^-\cdot Å^{-3}$	-2.862

Table A.89: Atomic coordinates ($\times 1 \times 10^4$) and equivalent isotropic displacement parameters U_{eq} / $Å^2$ $\times 1 \times 10^3$ for the independent atoms in the structure of $Rb_5(AsSe_3)Se \cdot 2\,NH_3$.

Atom	Wyck.	Site	x / a	y / b	z / c	U_{eq} / $Å^2$
Se(1)	4*a*	1	2774(5)	3815(4)	530(2)	19(1)
Se(2)	4*a*	1	7081(6)	5497(3)	2495(2)	21(1)
Se(3)	4*a*	1	7967(5)	3653(4)	4260(2)	24(1)
Se(4)	4*a*	1	7171(6)	1981(3)	2419(2)	21(1)
As(1)	4*a*	1	8481(5)	3734(4)	2909(2)	23(1)
N(1)	4*a*	1	7740(40)	3880(30)	635(17)	28(8)
N(2)	4*a*	1	7540(40)	8660(40)	850(18)	32(8)
Rb(1)	4*a*	1	5114(4)	6160(3)	4185(2)	21(1)
Rb(2)	4*a*	1	6293(5)	8719(4)	2572(2)	27(1)
Rb(3)	4*a*	1	4788(4)	6365(3)	900(2)	21(1)
Rb(4)	4*a*	1	4852(5)	8371(3)	6073(2)	23(1)
Rb(5)	4*a*	1	136(6)	5750(3)	1230(2)	26(1)

Table A.90: Anisotropic displacement parameters U_{ij} / $Å^2$ $\times 1 \times 10^3$ for the independent atoms in the structure of $Rb_5(AsSe_3)Se \cdot 2\,NH_3$.

Atom	U_{11}	U_{22}	U_{33}	U_{23}	U_{13}	U_{12}
Se(1)	22(2)	13(2)	22(2)	2(2)	-4(2)	3(2)
Se(2)	28(3)	16(2)	18(2)	-2(2)	1(2)	1(2)
Se(3)	38(3)	11(2)	24(2)	-1(2)	-11(2)	-4(2)
Se(4)	29(3)	12(2)	23(2)	-2(2)	-2(2)	-1(2)
As(1)	25(2)	15(2)	30(2)	1(2)	-1(2)	-1(2)
Rb(1)	22(2)	21(2)	19(2)	-1(2)	1(2)	-1(2)
Rb(2)	40(3)	20(2)	21(2)	-1(2)	-4(2)	0(2)
Rb(3)	22(2)	19(2)	22(2)	-1(2)	0(2)	-4(2)
Rb(4)	25(3)	18(2)	24(2)	-1(1)	-1(2)	-1(2)
Rb(5)	30(3)	16(2)	33(2)	-7(1)	3(2)	0(2)

Table A.91: Selected bond lengths for $Rb_5(AsSe_3)Se \cdot 2\,NH_3$. Symmetry transformations used to generate equivalent atoms: #1: -x+1,y-1/2,-z+1/2; #2: -x+1/2,-y+1,z-1/2; #3: x+1,y,z; #4: x+1/2,-y+3/2,-z+1; #5: -x+3/2,-y+1,z+1/2; #6: -x+3/2,-y+1,z-1/2; #7: x,y-1,z; #8: -x+1,y+1/2,-z+1/2; #9: x+1/2,-y+3/2,-z.

Atoms 1, 2	Distance / *Å*	Atoms 1, 2	Distance / *Å*
Se(1)-Rb(3)	3.324(5)	Se(3)-Rb(1)	3.683(6)
Se(1)-Rb(5)	3.345(6)	Se(4)-As(1)	2.367(6)
Se(1)-Rb(2)#1	3.418(5)	Se(4)-Rb(3)#1	3.468(6)
Se(1)-Rb(4)#2	3.426(6)	Se(4)-Rb(4)#6	3.538(6)
Se(1)-Rb(1)#1	3.440(5)	Se(4)-Rb(1)#1	3.558(5)
Se(1)-Rb(1)#2	3.458(5)	Se(4)-Rb(2)#1	3.571(6)
Se(1)-Rb(4)#1	3.524(6)	Se(4)-Rb(5)#1	3.594(6)
Se(2)-As(1)	2.372(6)	Se(4)-Rb(2)#7	3.597(5)
Se(2)-Rb(5)#3	3.487(7)	As(1)-Rb(5)#1	3.743(6)
Se(2)-Rb(1)	3.495(5)	As(1)-Rb(4)#4	3.780(5)
Se(2)-Rb(2)#1	3.528(6)	As(1)-Rb(5)#3	3.925(6)
Se(2)-Rb(2)	3.533(5)	As(1)-Rb(4)#6	4.189(5)
Se(2)-Rb(3)	3.563(5)	N(1)-Rb(5)#3	3.09(3)
Se(2)-Rb(4)#4	3.698(6)	N(1)-Rb(1)#6	3.16(3)
Se(3)-As(1)	2.403(5)	N(1)-Rb(4)#6	3.30(4)
Se(3)-Rb(3)#1	3.461(6)	N(2)-Rb(2)	3.20(3)
Se(3)-Rb(3)#5	3.478(5)	N(2)-Rb(3)	3.45(4)
Se(3)-Rb(5)#1	3.638(6)	N(2)-Rb(1)#8	3.55(4)
Se(3)-Rb(4)#4	3.647(5)	N(2)-Rb(3)#9	3.64(3)

Table A.92: Selected bond angles for $Rb_5(AsSe_3)Se \cdot 2\,NH_3$.

Atoms 1, 2, 3	Angle / °
Se(4)-As(1)-Se(2)	105.8(2)
Se(4)-As(1)-Se(3)	103.6(2)
Se(2)-As(1)-Se(3)	103.4(2)

A.1.16 $[Mn(NH_3)_6][As_4S_6]\cdot NH_3$

Table A.93: Crystal data and structure refinement for$[Mn(NH_3)_6][As_4S_6]\cdot NH_3$.

Empirical formula	$[Mn(NH_3)_6][As_4S_6]\cdot NH_3$
Formula weight / $g \cdot mol^{-1}$	666.22
Temperature / K	123(2)
Crystal system; space group	Orthorhombic; $Pmn2_1$
Lattice constants / $Å$	$a = 8.1474(2)$
	$b = 11.5618(3)$
	$c = 10.8145(3)$
Volume / $Å^3$	1018.71(5)
Z; F(000); calc. density / $g \cdot cm^{-3}$	2; 646; 2.172
Wavelength	$Mo_{K\alpha}(\lambda = 0.710\,73\,Å)$
Crystal size / mm^3	$0.200 \times 0.104 \times 0.100$
Theta range for data collection / °	$3.059 \leq \theta \leq 27.455$
Limiting indices	$-10 \leq h \leq 10$; $-14 \leq k \leq 14$; $-14 \leq l \leq 14$
Reflections collected / unique	8064 / 2353
Completeness to $\theta = 25.242°$	99.2%
R_{int}	0.1301
Absorption coefficient / mm^{-1}	7.704; numerical (spherical)
Max. / min. transmission	0.6460/ 0.6422
Refinement method	Full-matrix least-squares on F^2
Data / restraints / parameters	2353 / 1 / 99
R indices (all data) R_1; wR_2	0.0454; 0.1068
R indices $[[n]I > 2\sigma(I)]$ R_1; wR_2	[2260] 0.0440; 0.1052
Goodness-of-fit for F^2	1.067
Extinction coefficient	0.0084(19)
Absolute structure parameter	0.020(14)
Largest diff. peak / $e^- \cdot Å^{-3}$	+1.352
Largest diff. hole / $e^- \cdot Å^{-3}$	-1.063

Table A.94: Atomic coordinates ($\times 1 \times 10^4$) and equivalent isotropic displacement parameters U_{eq} / $Å^2$ $\times 1 \times 10^3$ for the independent atoms in the structure of $[Mn(NH_3)_6][As_4S_6]\cdot NH_3$.

Atom	Wyck.	Site	x / a	y / b	z / c	U_{eq} / $Å^2$
As(1)	2*a*	m..	5000	5696(1)	6789(1)	18(1)
As(2)	4*b*	1	3425(1)	4679(1)	4072(1)	18(1)
As(3)	2*a*	m..	5000	1914(1)	4550(1)	18(1)
Mn(1)	2*a*	m..	0	8547(1)	4487(2)	18(1)
N(1)	2*a*	m..	5000	7940(10)	880(11)	33(2)
N(2)	4*b*	1	1996(9)	9172(7)	5793(7)	29(2)
N(3)	2*a*	m..	0	6828(8)	5483(11)	29(2)
N(4)	4*b*	1	2045(8)	7941(6)	3209(7)	22(1)
N(5)	2*a*	m..	0	10322(10)	3551(15)	43(3)
S(1)	2*a*	m..	5000	6982(2)	5338(3)	23(1)
S(2)	4*b*	1	2950(2)	4492(2)	6111(2)	19(1)
S(3)	4*b*	1	2940(2)	2846(2)	3500(2)	20(1)
S(4)	2*a*	m..	5000	240(2)	3678(3)	22(1)

Table A.95: Anisotropic displacement parameters U_{ij} / $Å^2$ $\times 1 \times 10^3$ for the independent atoms in the structure of $[Mn(NH_3)_6][As_4S_6]\cdot NH_3$.

Atom	U_{11}	U_{22}	U_{33}	U_{23}	U_{13}	U_{12}
As(1)	17(1)	23(1)	13(1)	-2(1)	0	0
As(2)	20(1)	20(1)	13(1)	0(1)	-2(1)	3(1)
As(3)	19(1)	22(1)	12(1)	1(1)	0	0
Mn(1)	17(1)	22(1)	14(1)	-3(1)	0	0
N(1)	40(6)	34(5)	25(5)	-7(4)	0	0
N(2)	25(3)	43(4)	20(4)	-7(3)	-1(3)	-4(3)
N(3)	34(6)	29(5)	23(5)	6(4)	0	0
N(4)	19(3)	30(3)	17(3)	-2(3)	5(3)	-3(3)
N(5)	57(8)	28(6)	45(7)	4(5)	0	0
S(1)	24(1)	24(1)	22(1)	3(1)	0	0
S(2)	18(1)	24(1)	15(1)	-1(1)	2(1)	-4(1)

continued on next page

Atom	U_{11}	U_{22}	U_{33}	U_{23}	U_{13}	U_{12}
S(3)	16(1)	25(1)	18(1)	-3(1)	-2(1)	-1(1)
S(4)	24(1)	19(1)	21(1)	1(1)	0	0

Table A.96: Selected bond lengths for $[Mn(NH_3)_6][As_4S_6]\cdot NH_3$. Symmetry transformations used to generate equivalent atoms: #1: -x+1,y,z; #2: -x,y,z.

Atoms 1, 2	Distance / Å	Atoms 1, 2	Distance / Å
As(1)-S(1)	2.162(3)	As(3)-S(3)#1	2.295(2)
As(1)-S(2)#1	2.295(2)	Mn(1)-N(3)	2.261(10)
As(1)-S(2)	2.295(2)	Mn(1)-N(2)	2.272(7)
As(2)-S(3)	2.244(2)	Mn(1)-N(2)#2	2.272(7)
As(2)-S(2)	2.249(2)	Mn(1)-N(4)#2	2.275(7)
As(2)-As(2)#1	2.5660(15)	Mn(1)-N(4)	2.275(7)
As(3)-S(4)	2.154(3)	Mn(1)-N(5)	2.288(12)
As(3)-S(3)	2.295(2)		

Table A.97: Selected bond angles for $[Mn(NH_3)_6][As_4S_6]\cdot NH_3$. Symmetry transformations used to generate equivalent atoms: #1: -x+1,y,z; #2: -x,y,z.

Atoms 1, 2, 3	Angle / °	Atoms 1, 2, 3	Angle / °
S(1)-As(1)-S(2)#1	100.67(8)	N(2)-Mn(1)-N(4)#2	178.6(3)
S(1)-As(1)-S(2)	100.67(8)	N(2)#2-Mn(1)-N(4)#2	87.2(3)
S(2)#1-As(1)-S(2)	93.43(10)	N(3)-Mn(1)-N(4)	91.1(3)
S(3)-As(2)-S(2)	98.57(8)	N(2)-Mn(1)-N(4)	87.2(3)
S(3)-As(2)-As(2)#1	100.15(5)	N(2)#2-Mn(1)-N(4)	178.6(3)
S(2)-As(2)-As(2)#1	99.92(5)	N(4)#2-Mn(1)-N(4)	94.2(4)
S(4)-As(3)-S(3)	101.83(8)	N(3)-Mn(1)-N(5)	177.8(5)
S(4)-As(3)-S(3)#1	101.83(8)	N(2)-Mn(1)-N(5)	89.4(4)
S(3)-As(3)-S(3)#1	94.01(10)	N(2)#2-Mn(1)-N(5)	89.4(4)
N(3)-Mn(1)-N(2)	89.1(3)	N(4)#2-Mn(1)-N(5)	90.4(3)
N(3)-Mn(1)-N(2)#2	89.1(3)	N(4)-Mn(1)-N(5)	90.4(3)
N(2)-Mn(1)-N(2)#2	91.4(4)	As(2)-S(2)-As(1)	97.44(8)

continued on next page

Atoms 1, 2, 3	Angle / °	Atoms 1, 2, 3	Angle / °
N(3)-Mn(1)-N(4)#2	91.1(3)	As(2)-S(3)-As(3)	100.25(8)

A.1.17 $[Mn(NH_3)_6][As_2Se_6]$

Table A.98: Crystal data and structure refinement for$[Mn(NH_3)_6][As_2Se_6]$.

Empirical formula	$[Mn(NH_3)_6][As_2Se_6]$
Formula weight / $g \cdot mol^{-1}$	780.74
Temperature / K	123(2)
Crystal system; space group	Monoclinic; $P2_1/n$
Lattice constants / $Å$	$a = 6.7484(4)$
	$b = 12.3781(8)$
	$c = 10.8297(6)$
	$\beta = 102.940(4)$ °
Volume / $Å^3$	881.66(9)
Z; F(000); calc. density / $g \cdot cm^{-3}$	2; 710; 2.941
Wavelength	$Mo_{K\alpha}(\lambda = 0.710\,73\,Å)$
Crystal size / mm^3	0.039 × 0.020 × 0.012
Theta range for data collection / °	$3.262 \leq \theta \leq 27.462$
Limiting indices	$-8 \leq h \leq 8$; $-16 \leq k \leq 16$; $-14 \leq l \leq 13$
Reflections collected / unique	5599 / 1835
Completeness to $\theta = 25.242°$	93.1%
R_{int}	0.0788
Absorption coefficient / mm^{-1}	16.843; Semi-empirical
Max. / min. transmission	1.0163/ 0.8677
Refinement method	Full-matrix least-squares on F^2
Data / restraints / parameters	1835 / 0 / 74
R indices (all data) R_1; wR_2	0.0781; 0.0992
R indices $[[n]I > 2\sigma(I)]$ R_1; wR_2	[1283] 0.0431; 0.0883
Goodness-of-fit for F^2	1.015
Extinction coefficient	0.0031(4)
Largest diff. peak / $e^- \cdot Å^{-3}$	+1.007
Largest diff. hole / $e^- \cdot Å^{-3}$	-0.881

Table A.99: Atomic coordinates ($\times 1 \times 10^4$) and equivalent isotropic displacement parameters U_{eq} / $\AA^2$ $\times 1 \times 10^3$ for the independent atoms in the structure of $[Mn(NH_3)_6][As_2Se_6]$.

Atom	Wyck.	Site	x / a	y / b	z / c	U_{eq} / $\AA^2$
As(1)	4*e*	1	7571(1)	3860(1)	5421(1)	21(1)
Mn(1)	2*b*	-1	5000	5000	0	18(1)
N(1)	4*e*	1	7712(11)	5649(6)	-717(7)	25(2)
N(2)	4*e*	1	4855(10)	6631(5)	891(7)	23(2)
N(3)	4*e*	1	2957(11)	5632(6)	-1841(7)	30(2)
Se(1)	4*e*	1	9367(1)	3248(1)	7378(1)	22(1)
Se(2)	4*e*	1	7807(1)	5742(1)	5978(1)	23(1)
Se(3)	4*e*	1	5742(1)	6526(1)	4168(1)	22(1)

Table A.100: Anisotropic displacement parameters U_{ij} / $\AA^2$ $\times 1 \times 10^3$ for the independent atoms in the structure of $[Mn(NH_3)_6][As_2Se_6]$.

Atom	U_{11}	U_{22}	U_{33}	U_{23}	U_{13}	U_{12}
As(1)	20(1)	20(1)	22(1)	-1(1)	4(1)	1(1)
Mn(1)	19(1)	14(1)	19(1)	0(1)	1(1)	2(1)
N(1)	27(4)	24(4)	24(4)	0(3)	4(4)	4(3)
N(2)	18(4)	29(4)	19(4)	1(3)	-1(3)	0(3)
N(3)	26(4)	28(4)	32(5)	-2(3)	-4(4)	1(3)
Se(1)	19(1)	19(1)	25(1)	1(1)	0(1)	2(1)
Se(2)	22(1)	19(1)	25(1)	1(1)	-4(1)	-2(1)
Se(3)	19(1)	21(1)	23(1)	4(1)	1(1)	-2(1)

Table A.101: Selected bond lengths for $[Mn(NH_3)_6][As_2Se_6]$. Symmetry transformations used to generate equivalent atoms: #1: -x+1,-y+1,-z+1; #2: -x+1,-y+1,-z.

Atoms 1, 2	Distance / $\AA$	Atoms 1, 2	Distance / $\AA$
As(1)-Se(1)	2.3204(13)	N(1)-H(1A)	0.91
As(1)-Se(2)	2.4037(12)	N(1)-H(1B)	0.91
As(1)-Se(3)#1	2.4229(12)	N(1)-H(1C)	0.91
Mn(1)-N(2)	2.249(7)	N(2)-H(2A)	0.91

continued on next page

Atoms 1, 2	Distance / Å	Atoms 1, 2	Distance / Å
Mn(1)-N(2)#2	2.249(7)	N(2)-H(2B)	0.91
Mn(1)-N(1)	2.288(7)	N(2)-H(2C)	0.91
Mn(1)-N(1)#2	2.288(7)	N(3)-H(3A)	0.91
Mn(1)-N(3)	2.293(7)	N(3)-H(3B)	0.91
Mn(1)-N(3)#2	2.293(7)	N(3)-H(3C)	0.91
Se(2)-Se(3)	2.3461(13)		

Table A.102: Selected bond angles for $[Mn(NH_3)_6][As_2Se_6]$. Symmetry transformations used to generate equivalent atoms: #1: -x+1,-y+1,-z+1; #2: -x+1,-y+1,-z.

Atoms 1, 2, 3	Angle / °	Atoms 1, 2, 3	Angle / °
Se(1)-As(1)-Se(2)	95.44(5)	N(3)-Mn(1)-N(3)#2	180
Se(1)-As(1)-Se(3)#1	94.73(4)	Mn(1)-N(1)-H(1A)	109.5
Se(2)-As(1)-Se(3)#1	99.00(4)	Mn(1)-N(1)-H(1B)	109.5
N(2)-Mn(1)-N(2)#2	180	H(1A)-N(1)-H(1B)	109.5
N(2)-Mn(1)-N(1)	86.9(2)	Mn(1)-N(1)-H(1C)	109.5
N(2)#2-Mn(1)-N(1)	93.1(2)	H(1A)-N(1)-H(1C)	109.5
N(2)-Mn(1)-N(1)#2	93.1(2)	H(1B)-N(1)-H(1C)	109.5
N(2)#2-Mn(1)-N(1)#2	86.9(2)	Mn(1)-N(2)-H(2A)	109.5
N(1)-Mn(1)-N(1)#2	180.00(17)	Mn(1)-N(2)-H(2B)	109.5
N(2)-Mn(1)-N(3)	89.5(3)	H(2A)-N(2)-H(2B)	109.5
N(2)#2-Mn(1)-N(3)	90.5(3)	Mn(1)-N(2)-H(2C)	109.5
N(1)-Mn(1)-N(3)	87.5(3)	H(2A)-N(2)-H(2C)	109.5
N(1)#2-Mn(1)-N(3)	92.5(3)	H(2B)-N(2)-H(2C)	109.5
N(2)-Mn(1)-N(3)#2	90.5(3)	Mn(1)-N(3)-H(3A)	109.5
N(2)#2-Mn(1)-N(3)#2	89.5(3)	Mn(1)-N(3)-H(3B)	109.5
N(1)-Mn(1)-N(3)#2	92.5(3)	H(3A)-N(3)-H(3B)	109.5
N(1)#2-Mn(1)-N(3)#2	87.5(3)	Mn(1)-N(3)-H(3C)	109.5
Se(3)-Se(2)-As(1)	101.37(5)	H(3A)-N(3)-H(3C)	109.5
Se(2)-Se(3)-As(1)#1	99.48(4)	H(3B)-N(3)-H(3C)	109.5

B.1 Powder Diffraction Pattern

B.1.1 Ba_3As_2O

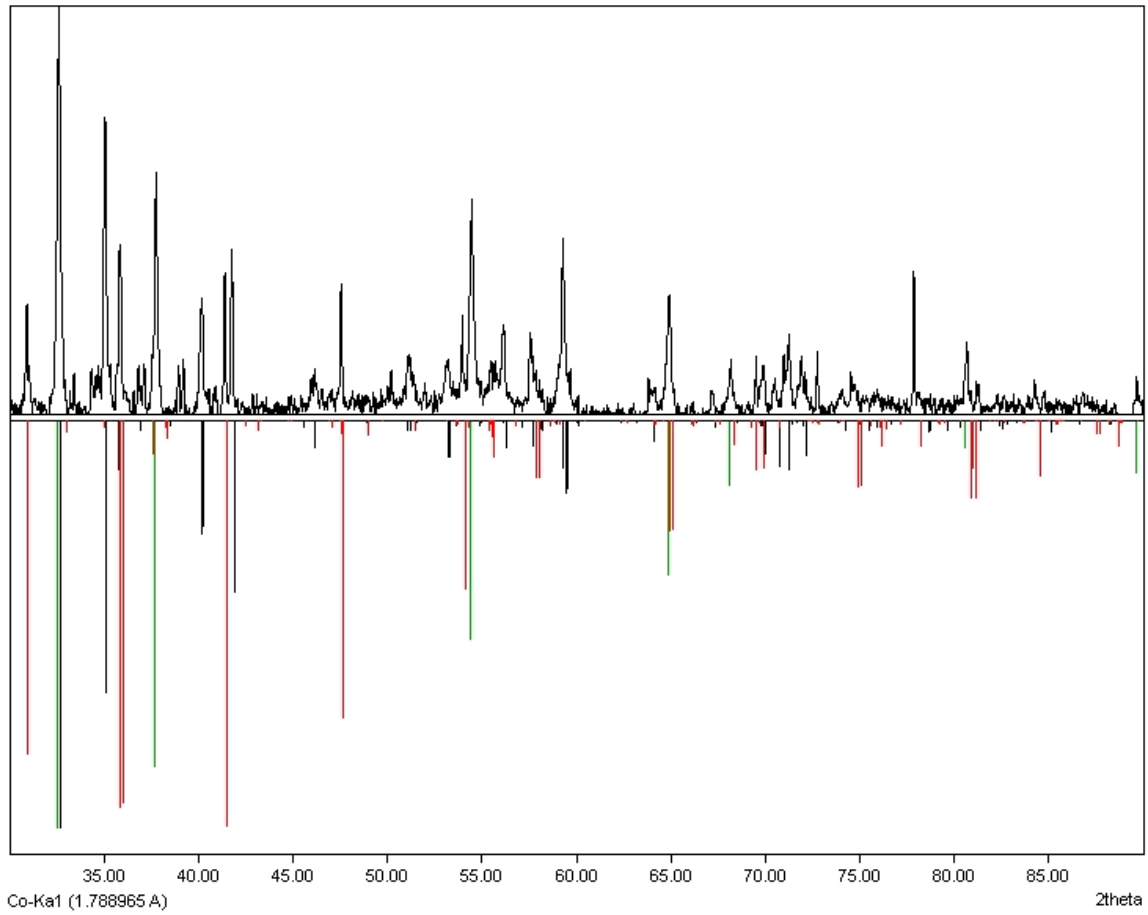

Figure B.1: Powder diffraction pattern of Ba_3As_2O at top, compared with the reflection positions calculated from single crystal data at bottom (black), reflexes calculated from the single crystal data of Ba_3As_4(red) and the database entry of BaO [220] (green).

The powder diffraction pattern indicates, that Ba_3As_2O is present in the phase triangle of Ba_3As_4 and BaO.

B.1.2 Ba_3As_4

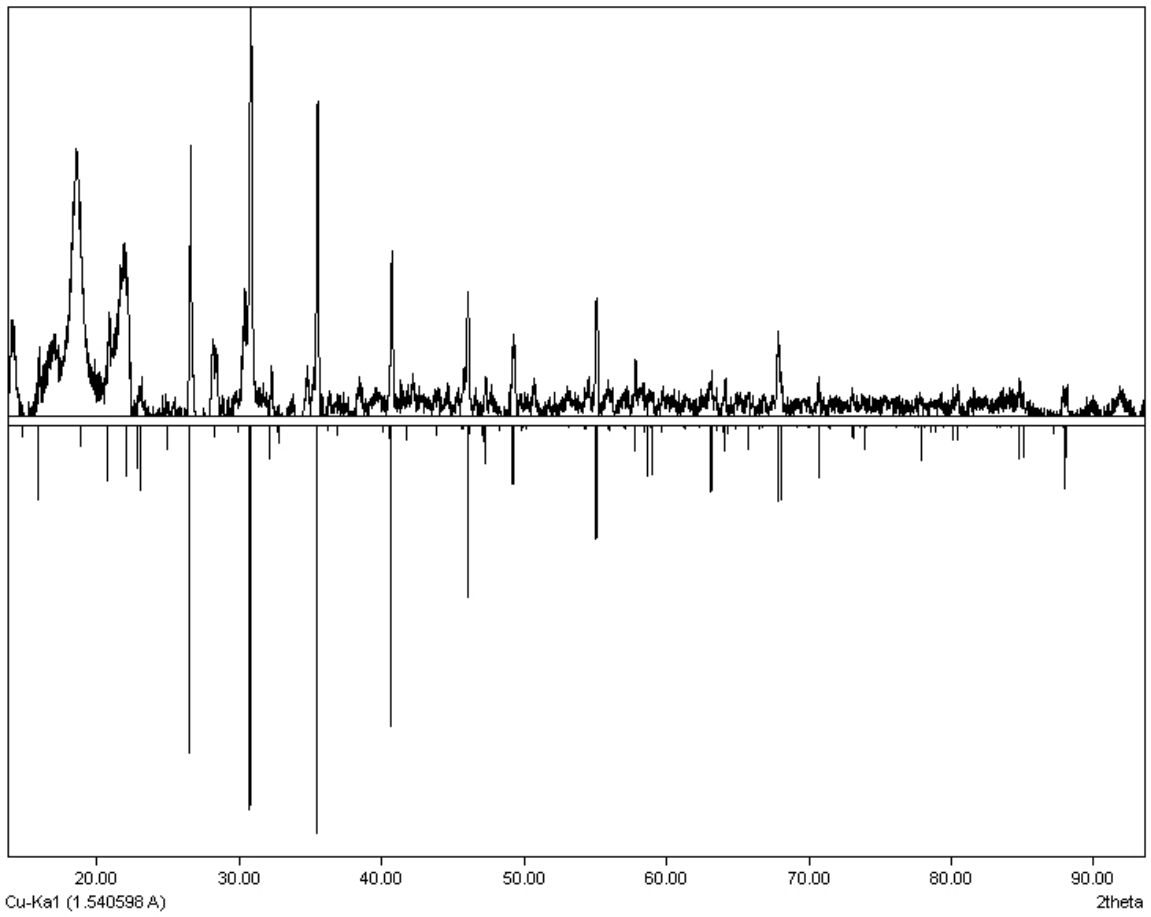

Figure B.2: Powder diffraction pattern of Ba_3As_4, with the reflection positions calculated from single crystal data at bottom. Top: measured reflections of Ba_3As_4; bottom: calculated reflections of Ba_3As_4 with DIAMOND [131]. Scotch Magic Tape was used to protect the substance against oxidation. Reflexes up to $\theta = 26°$ and one reflex at $\theta = 50°$ were caused by the scotch tape (Appendix: B.1.5).

B.1.3 $NH_3Fe_2S_3$

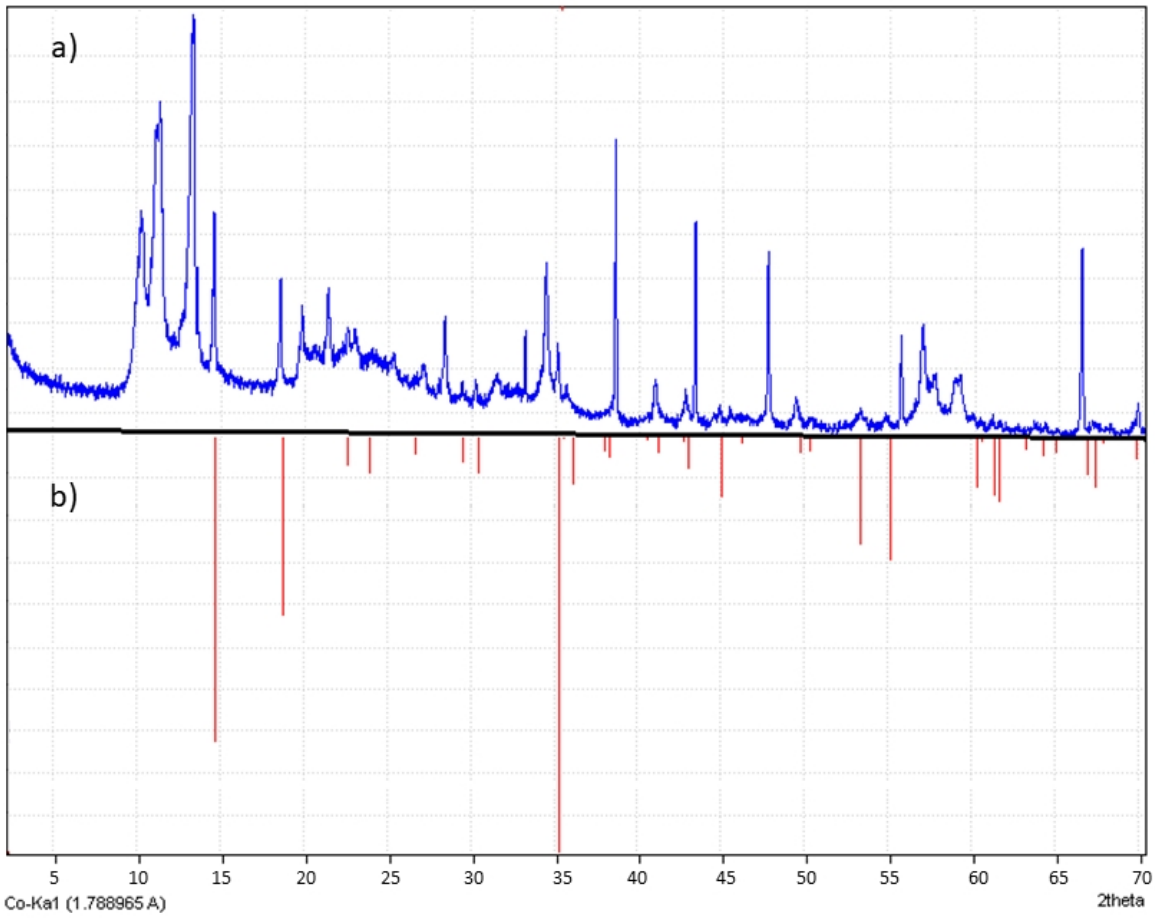

Figure B.3: a) Experimental powder diffraction pattern and b) simulated powder diffraction pattern of $(NH_4)Fe_2S_3$

The simulated powder diffraction pattern was created with the program Diamond 4[131], using the structural data obtained from the single crystal X-ray data. The reflections of the simulated powder diffraction pattern are present in the experimental pattern. The unknown reflexes show that the desired product is not the main component of the powder studied. Reflections with a high intensity at $10° < 2\theta < 14°$ cannot be assigned to the reflections of the simulated powder diffraction pattern. Besides $(NH_4)Fe_2S_3$, other substances could not be identified. However, the reactants used, iron and crystalline sulphur can be excluded as minor phases. Since the product was first mortared in air, it is assumed that the unknown by-product could have formed by rapid ageing of $(NH_4)Fe_2S_3$ in air.

B.1.4 $NH_3Fe_2Se_3$

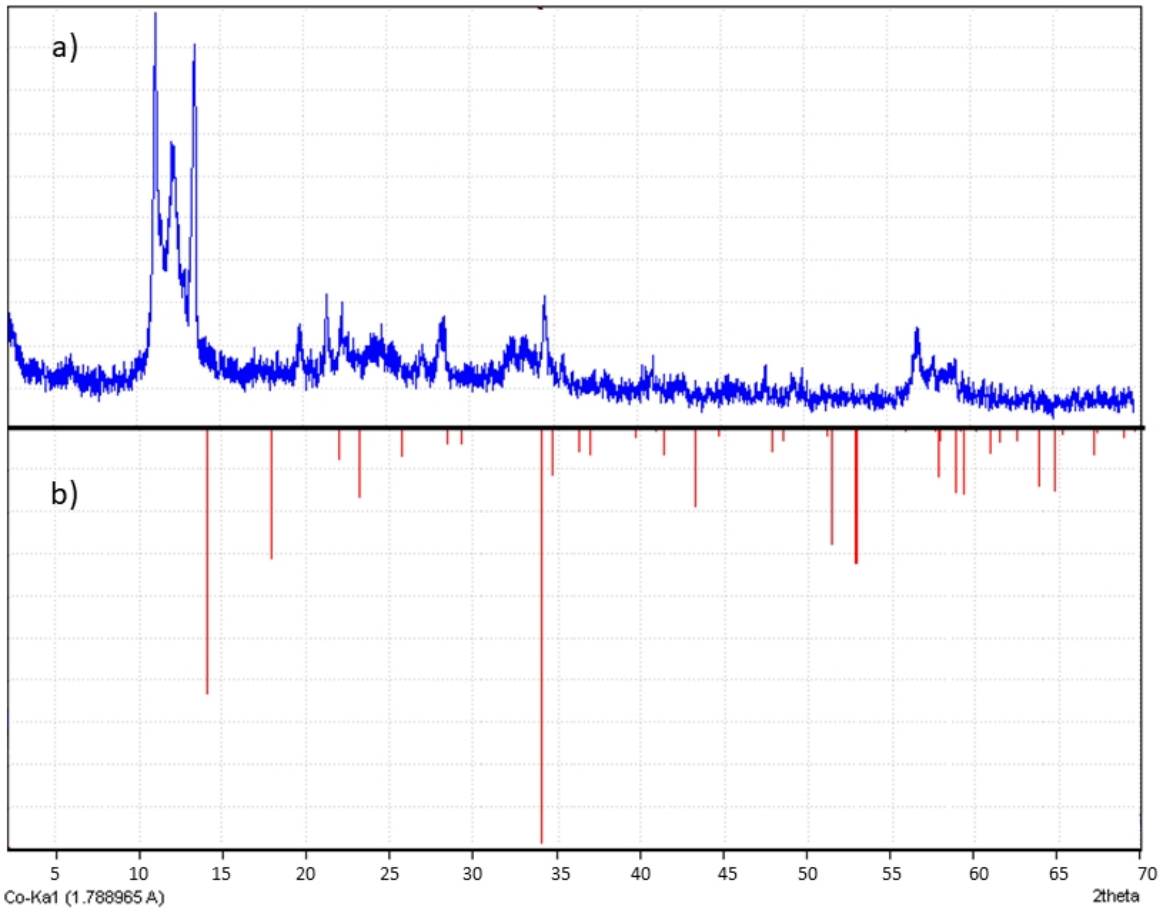

Figure B.4: a) Experimental powder diffraction pattern and b) simulated powder diffraction pattern of $(NH_4)Fe_2Se_3$.

The reflections of the simulated powder diffraction pattern are present in the experimental diffraction pattern. However, in addition to the reflections that can be assigned to $(NH_4)Fe_2Se_3$, further reflections of unknown compounds are present. The relection with the highest relative intensity of the simulated powder diffraction pattern at $2\theta = 34.03°$, has a much lower intensity in the experimental powder diffraction pattern. Therefore, the relative amount of $(NH_4)Fe_2S_3$ in the sample powder is low. However, no statement can be made about the exact composition of the powder.

B.1.5 ScotchMagicTape

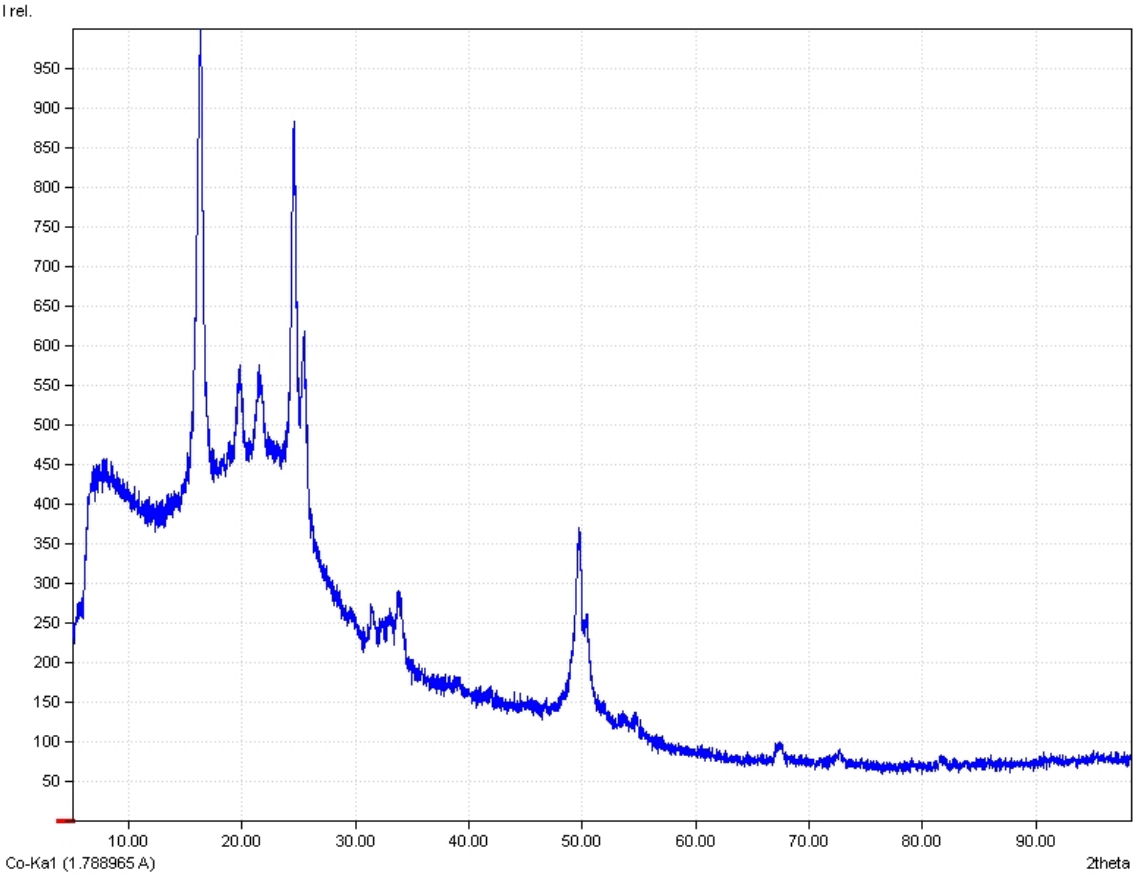

Figure B.5: Powder diffraction pattern of the Scotch Magic Tape, used as sample protecting film.

C.1 Energy Dispersive X-Ray Spectroscopy (EDX)

C.1.1 Ba_3As_2O

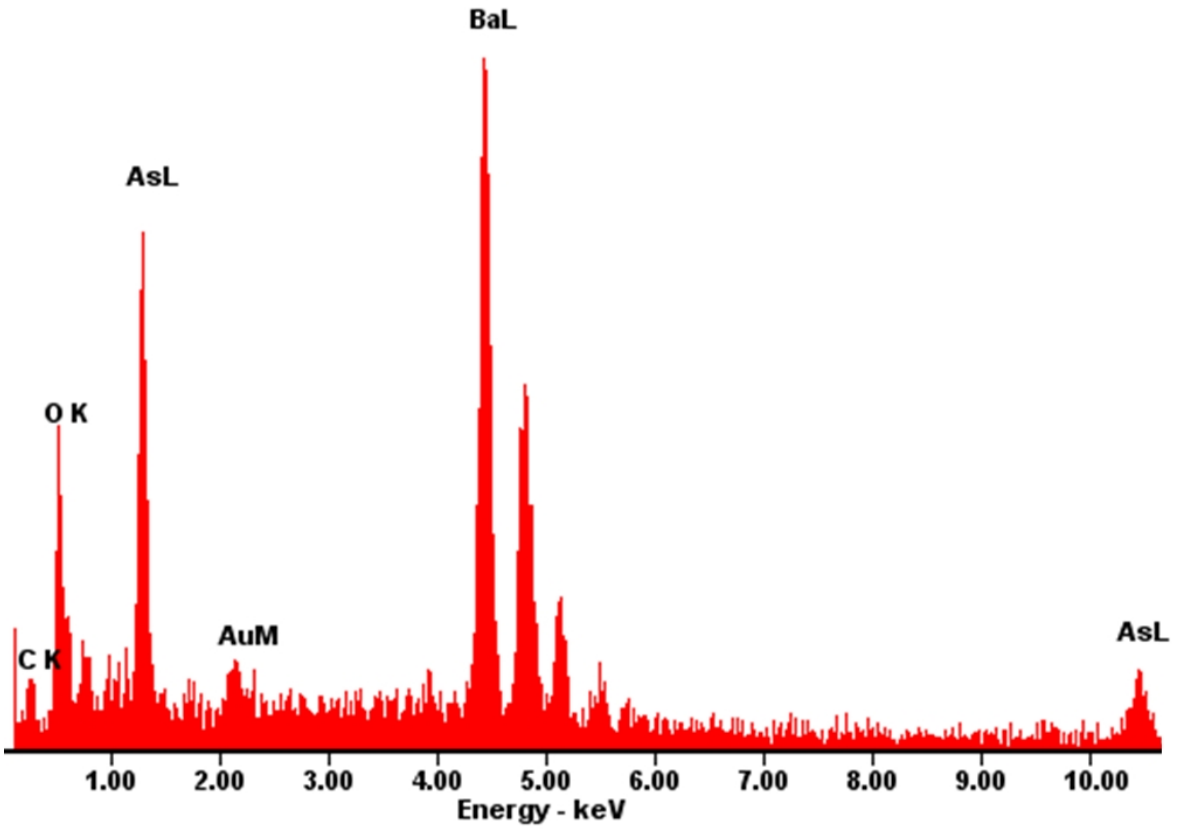

Figure C.1: EDX spectrum of a spot analysis of a crystal of Ba_3As_2O. The sample was sputtered with gold to increase conductivity.

Table C.1: EDX measurements of Ba_3As_2O in atomic percent with standardised and expected values.

Element /Emission Line	Atomic %	standardised	expected values
Ba L	36,08	3,00	3
As L	24,24	2,02	2
O K	39,69	3,31	1

C.1.2 $K_3Ba_7(As_3)_3O$

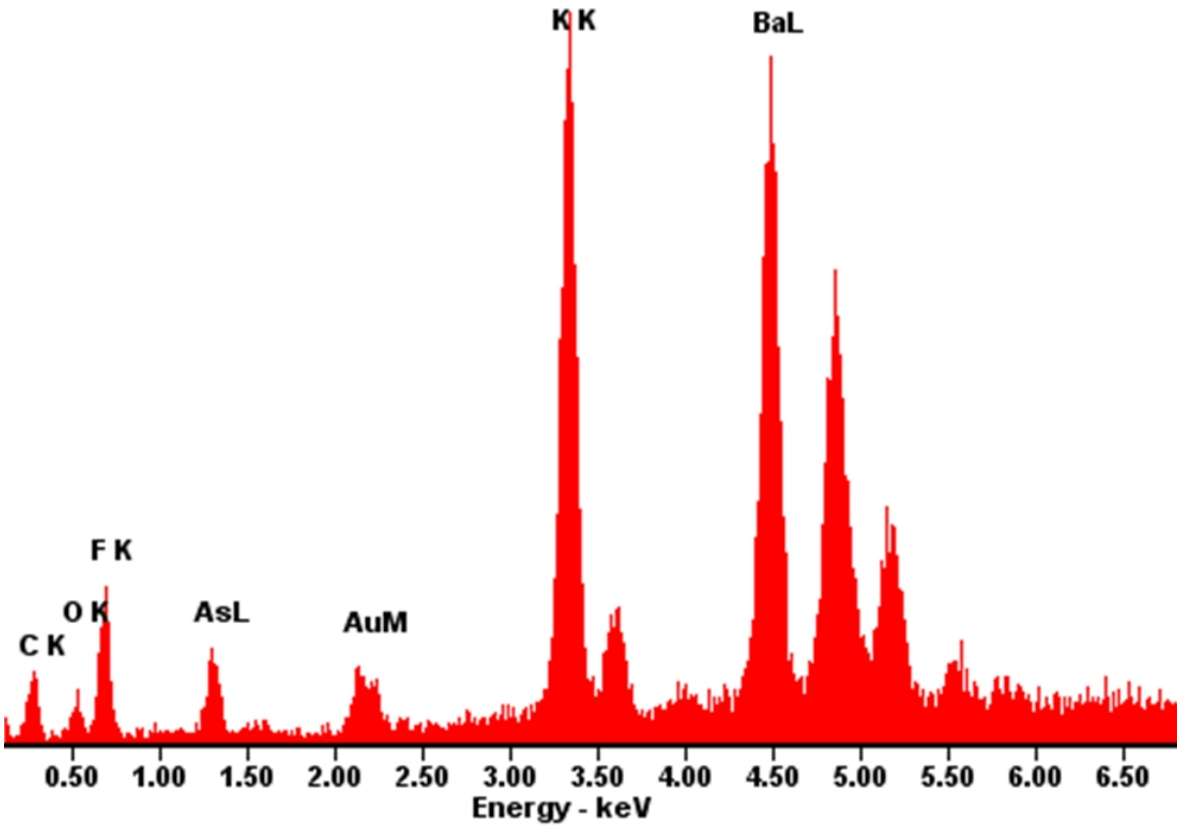

Figure C.2: EDX spectrum of a spot analysis of a crystal of $K_3Ba_7(As_3)_3O$. The sample was sputtered with gold to increase conductivity.

Table C.2: EDX measurements of $K_3Ba_7(As_3)_3O$ in atomic percent with standardised and expected values.

Element /Emission Line	Atomic %	standardised	expected values
K K	7.34	3.00	3
Ba L	27.66	11.3	7
As L	25.47	10.41	9
O K	39.53	16.15	1

C.1.3 Ba_3As_4

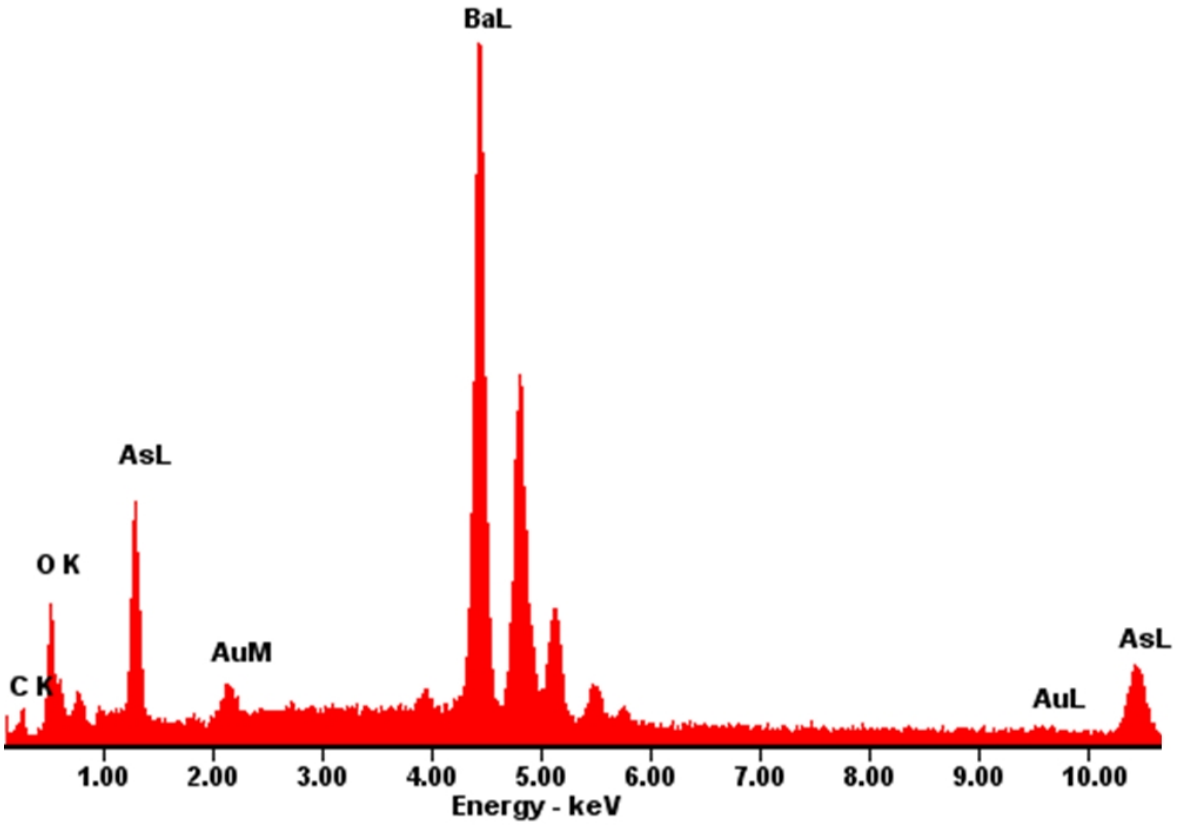

Figure C.3: EDX spectrum of a spot analysis of a crystal of Ba_3As_4. The sample was sputtered with gold to increase conductivity.

Table C.3: EDX measurements of Ba_3As_4 in atomic percent with standardised and expected values.

Element /Emission Line	Atomic %	standardised	expected values
Ba L	43.14	3	3
As L	56.86	3.95	4

C.1.4 $[Eu(NH_3)_8]_2[Eu(NH_3)_3(As_7)_2]$

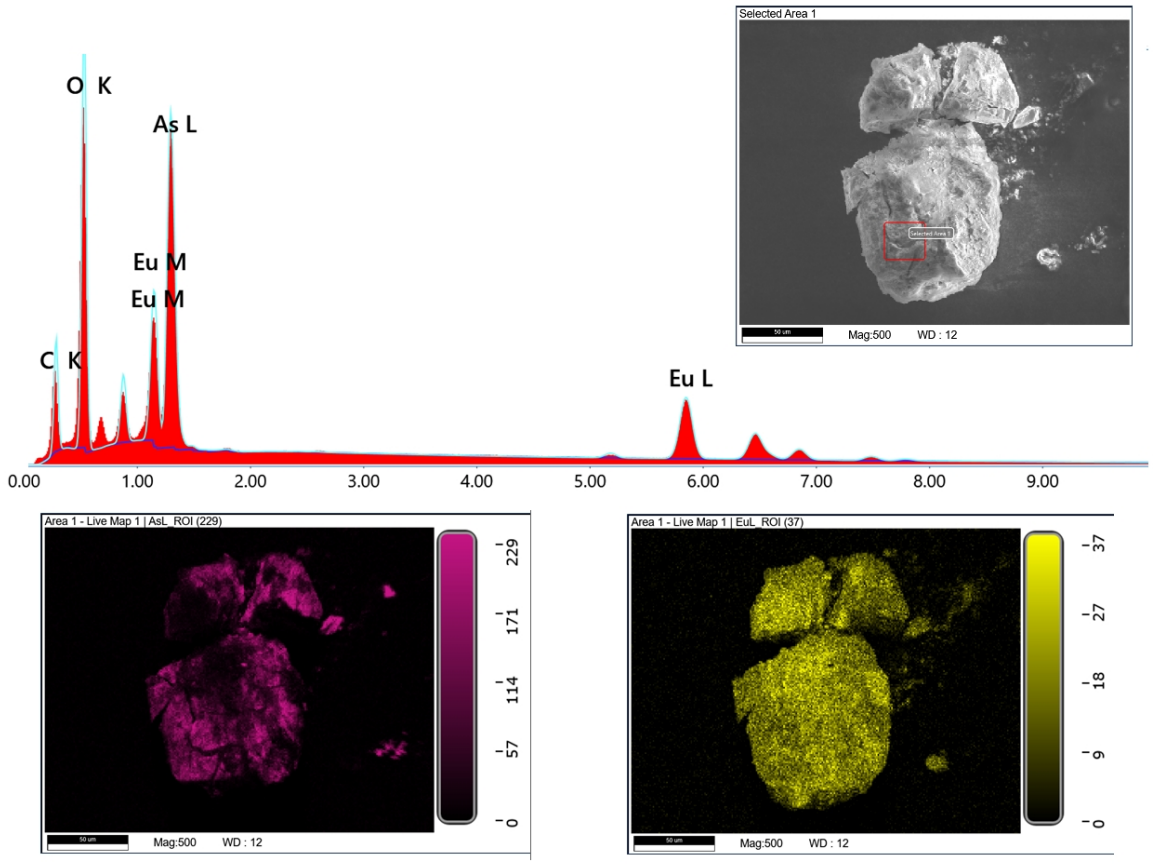

Figure C.4: EDX spectrum of a spot analysis of a crystal of $[Eu(NH_3)_8]_2[Eu(NH_3)_3(As_7)_2]$. A REM-image of the measured, but already decomposed crystal is shown at the top right. Below are the REM-live maps with the distribution of As (violet) and Eu (yellow). It can be clearly seen that As and Eu are not evenly distributed in the decomposed crystal.

Table C.4: EDX measurements of $[Eu(NH_3)_8]_2[Eu(NH_3)_3(As_7)_2]$ in atomic percent with standardised and expected values.

Element /Emission Line	Atomic %	standardised	expected values
C K	36.5		
O K	44.7		
As L	10.8	4.1	14
Eu L	7.9	3	3

$[Eu(NH_3)_8]_2[Eu(NH_3)_3(As_7)_2]$ decomposed at room temperature and released a garlic smell, which could indicate the formation of AsH_3, which resulted in an under-representation of As in the EDX analysis.

C.1.5 Rb_2AuAs_7

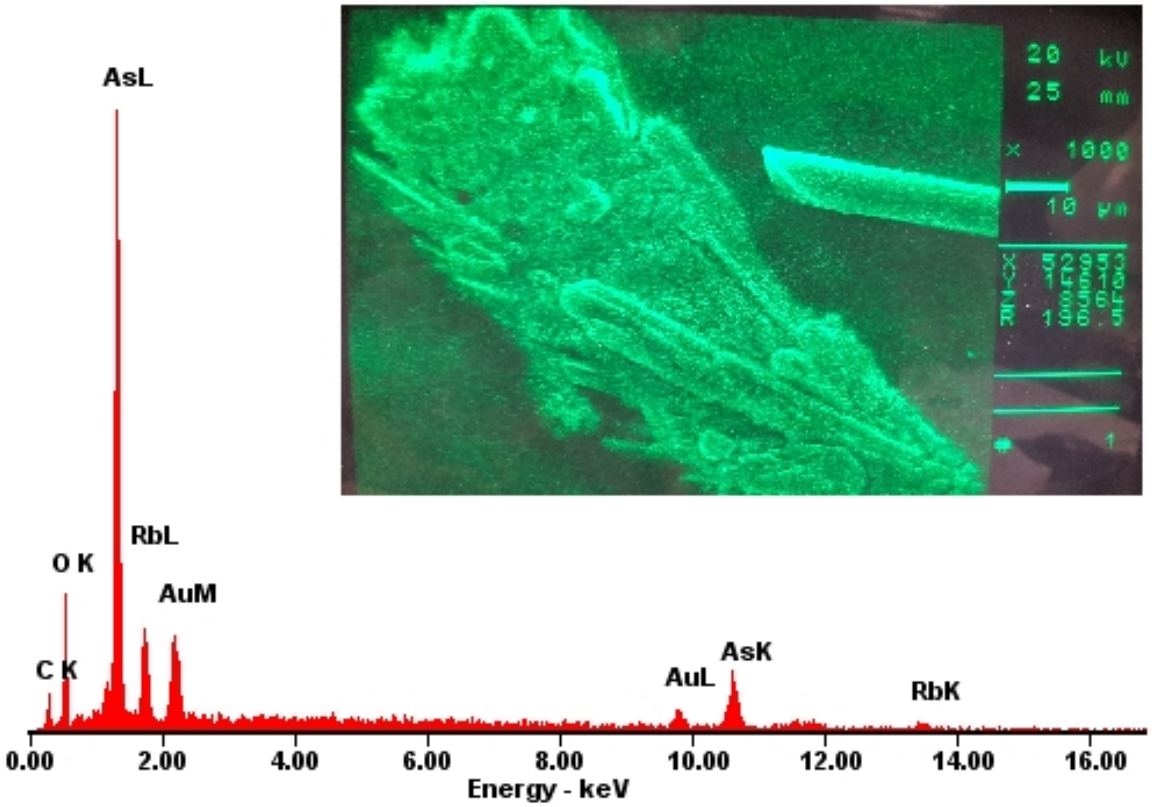

Figure C.5: EDX spectrum of a spot analysis of a crystal of Rb_2AuAs_7. A REM-image of the measured crystal is shown at the top right.

Table C.5: EDX measurements of Rb_2AuAs_7 in atomic percent with standardised and expected values.

Element /Emission Line	Atomic %	standardised	expected values
Rb L	18.50	1.65	3
Au M	11.20	1.00	1
As L	70.30	6.28	7

C.1.6 $Rb_3AuSe_2 \cdot 1.5\,NH_3$

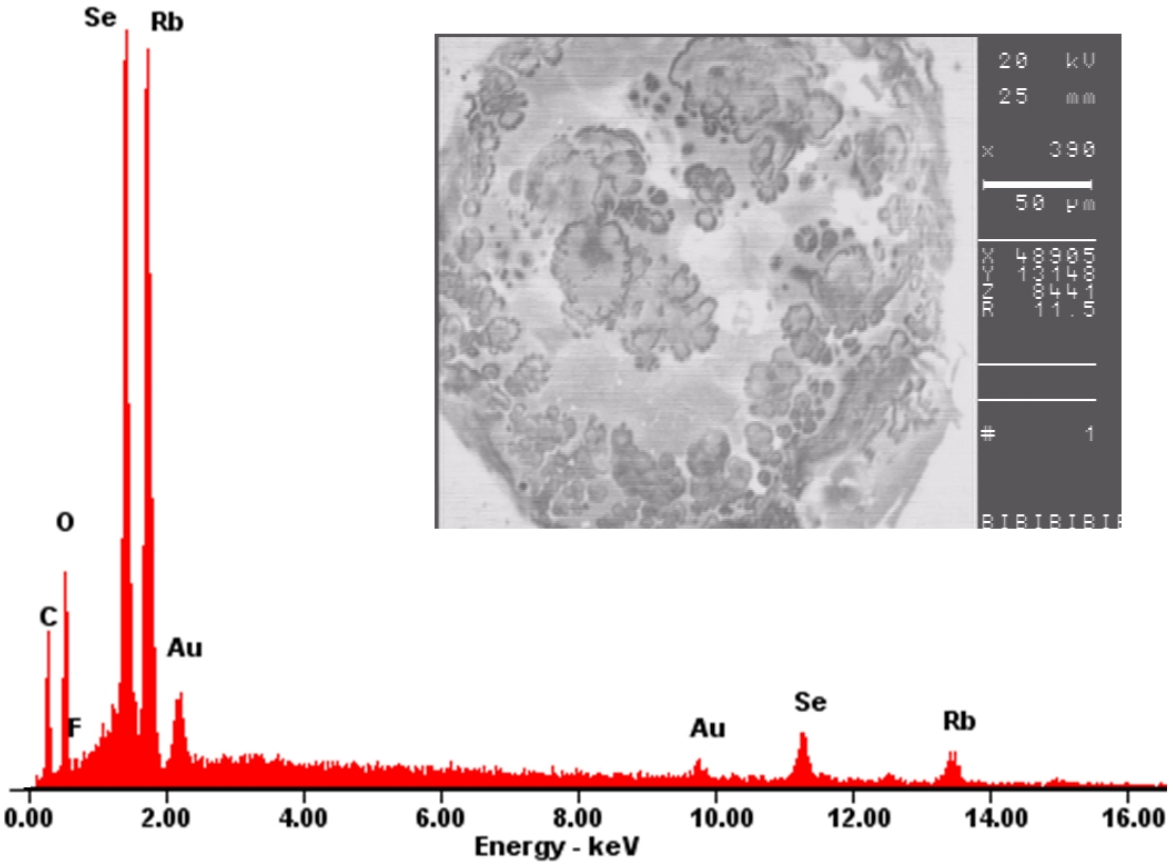

Figure C.6: EDX spectrum of a spot analysis of a crystal of $Rb_3AuSe_2 \cdot 1.5\,NH_3$. A REM-BSE-image of the measured, decomposed crystal is shown at the top right.

Table C.6: EDX measurements of $Rb_3AuSe_2 \cdot 1.5\,NH_3$ in atomic percent with standardised and expected values.

Element /Emission Line	Atomic %	standardised	expected values
Rb L	53.26	5.24	3
Au L	10.16	1.00	1
Se L	36.58	3.60	2

C.1.7 $K_{10}CuSe_8Cl \cdot NH_3$

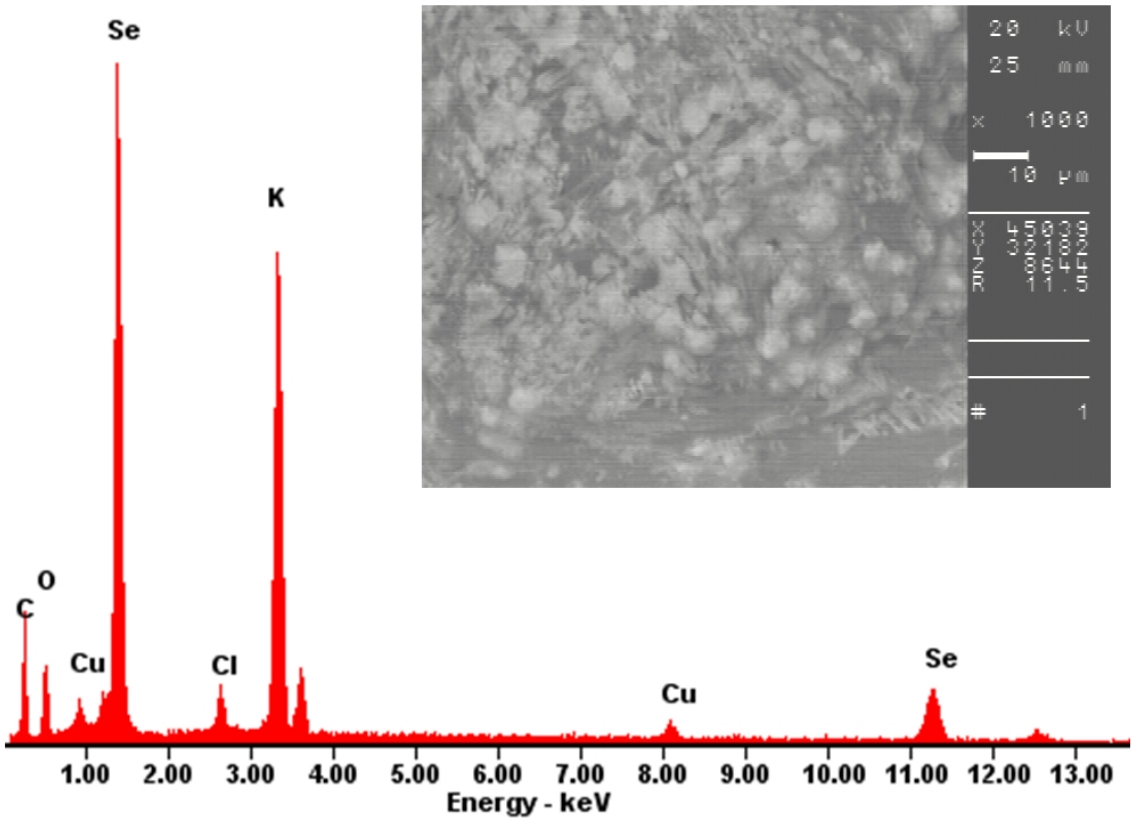

Figure C.7: EDX spectrum of a spot analysis of a crystal of $K_{10}CuSe_8Cl \cdot NH_3$. A REM-BSE-image of the measured, already decomposed crystal is shown at the top right.

Table C.7: EDX measurements of $K_{10}CuSe_8Cl \cdot NH_3$ in atomic percent with standardised and expected values.

Element /Emission Line	Atomic %	standardised	expected values
K K	42.32	12.92	10
Cu K	3.28	1.00	1
Se K	36.11	11.02	10
Cl K	4.01	1.22	1

C.1.8 $K_2[AuSe]Se \cdot NH_3$

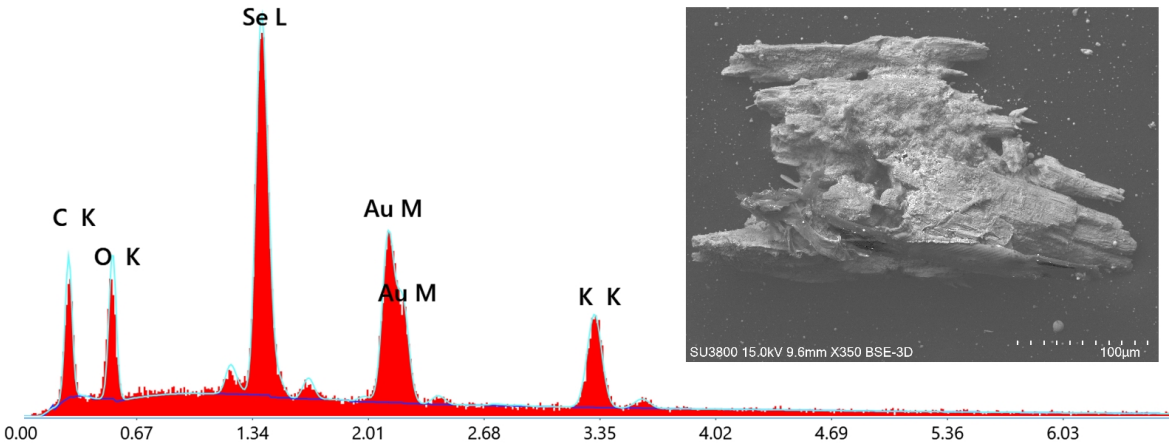

Figure C.8: EDX spectrum of a spot analysis of a crystal of $K_2[AuSe]Se \cdot NH_3$. A REM-image of the measured, already decomposed crystal is shown at the top right.

Table C.8: EDX measurements of $K_2[AuSe]Se \cdot NH_3$ in atomic percent with standardised and expected values.

Element /Emission Line	Atomic %	standardised	expected values
C K	32.4		
O K	30.8		
K K	13.5	1.75	2
Se L	15.6	2.03	2
Au M	7.7	1	1

C.1.9 $NH_4Fe_2S_3$

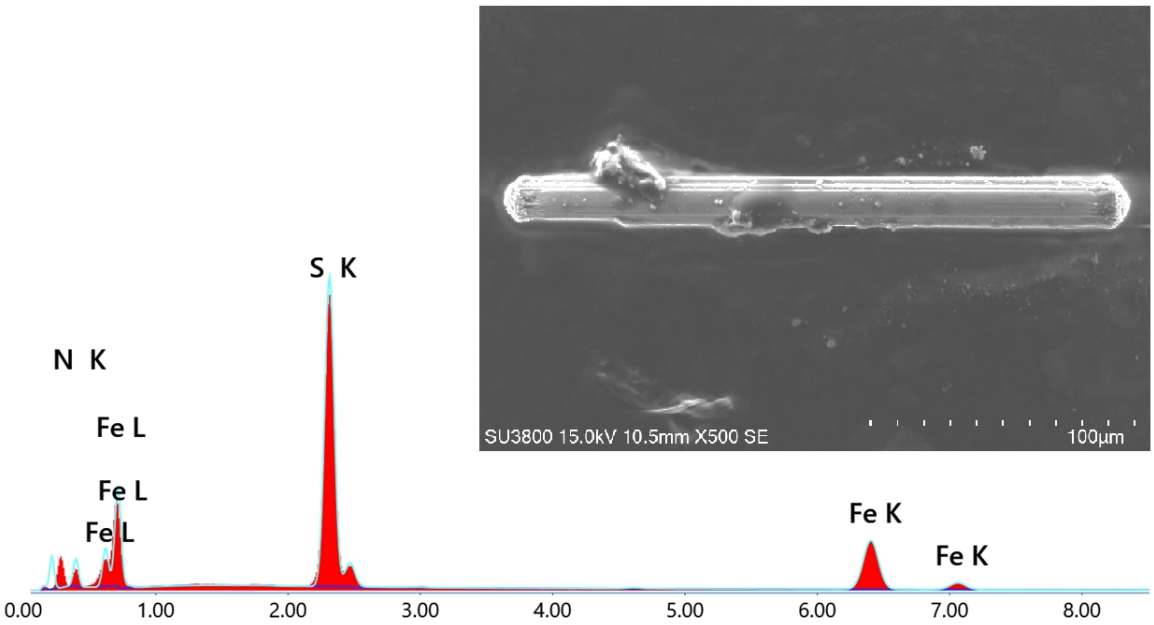

Figure C.9: EDX spectrum of a spot analysis of a crystal of $(NH_4)Fe_2S_3$. A REM-image of the measured crystal is shown at the top right.

Table C.9: EDX measurements of $(NH_4)Fe_2S_3$ in atomic percent with standardised and expected values.

Element /Emission Line	Atomic %	standardised	expected values
N K	40.6	3.78	1
Fe K	21.5	2.00	2
S K	37.8	3.52	3

C.1.10 $NH_4Fe_2Se_3$

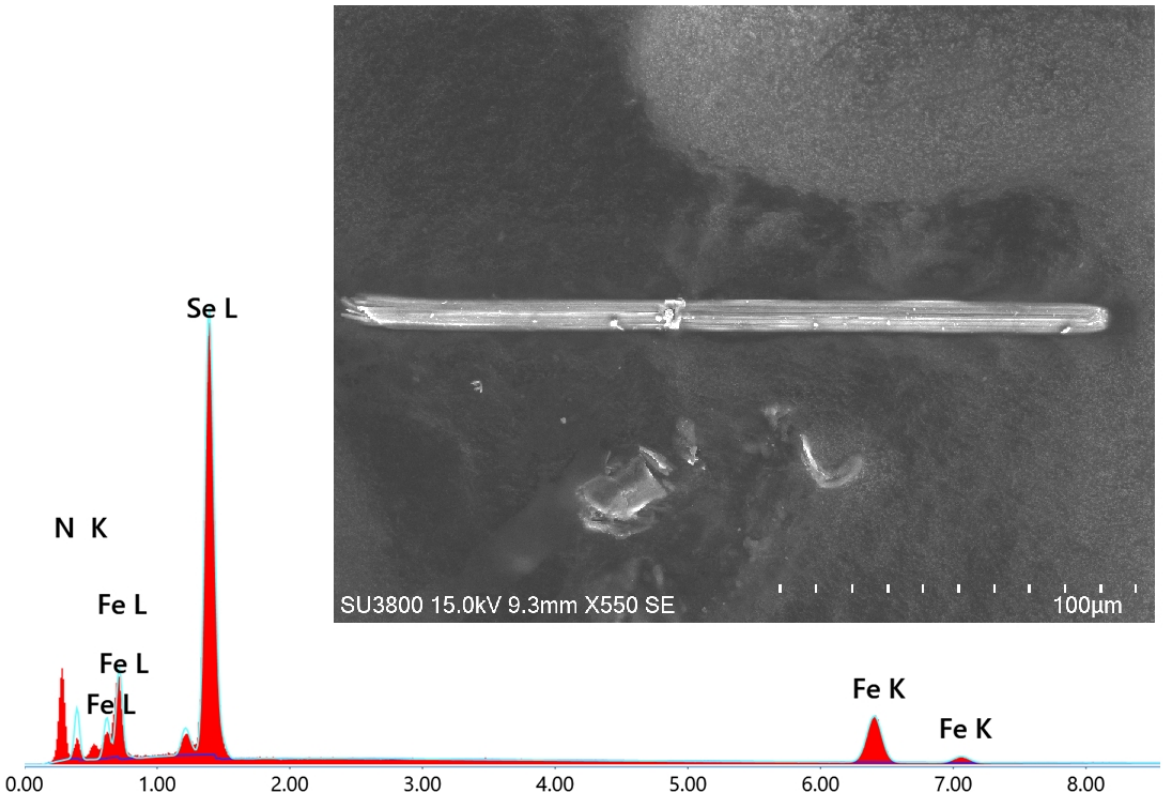

Figure C.10: EDX spectrum of a spot analysis of a crystal of $(NH_4)Fe_2Se_3$. A REM-image of the measured crystal is shown at the top right.

Table C.10: EDX measurements of $(NH_4)Fe_2Se_3$ in atomic percent with standardised and expected values.

Element /Emission Line	Atomic %	standardised	expected values
N K	44.2	4.17	1
Fe K	21.2	2.00	2
Se L	34.7	3.27	3

C.1.11 $[Mn_2(HPO_3)_2(C_2H_8N_2)]$

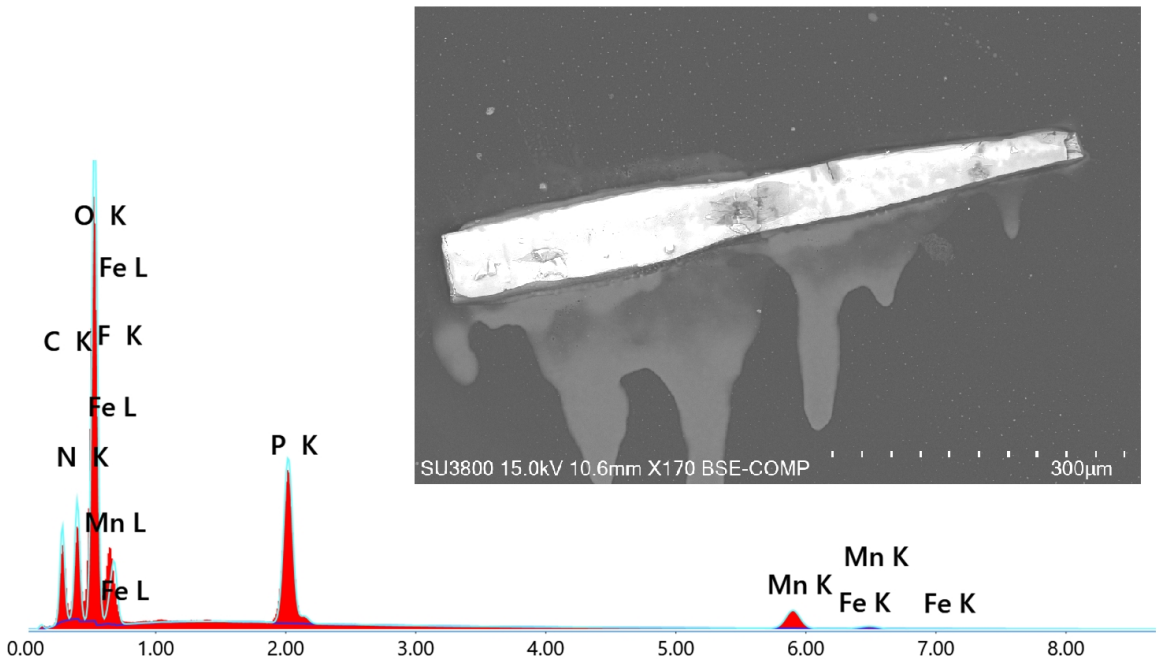

Figure C.11: EDX spectrum of a spot analysis of a crystal of $[Mn_2(HPO_3)_2(C_2H_8N_2)]$. A REM-image of the measured crystal is shown at the top right.

Table C.11: EDX measurements of $[Mn_2(HPO_3)_2(C_2H_8N_2)]$ in atomic percent with standardised and expected values. The crystal was moistened with polyfluorinated oil for the previous X-ray measurement. Therefore, the values for the proportion of carbon, nitrogen, oxygen and fluorine do not provide any information about the actual composition of the compound. From the analysis, the ratio of phosphorus to manganese is 2:1, but the ratio of phosphorus to manganese in the compound should be 1:1. Since phosphorus is a light element, the values do not provide an exact quantitative composition.

Element /Emission Line	Atomic %	standardised	expected values
C K	16.8	4.80	2
N K	18.3	5.23	2
O K	44	12.57	6
F K	11.4		
P K	6	1.71	1
Mn K	3.5	1.00	1
Fe K	0.1		

C.1.12 $K_9Se_{2.88}(Se_2)_{1.12}OH$

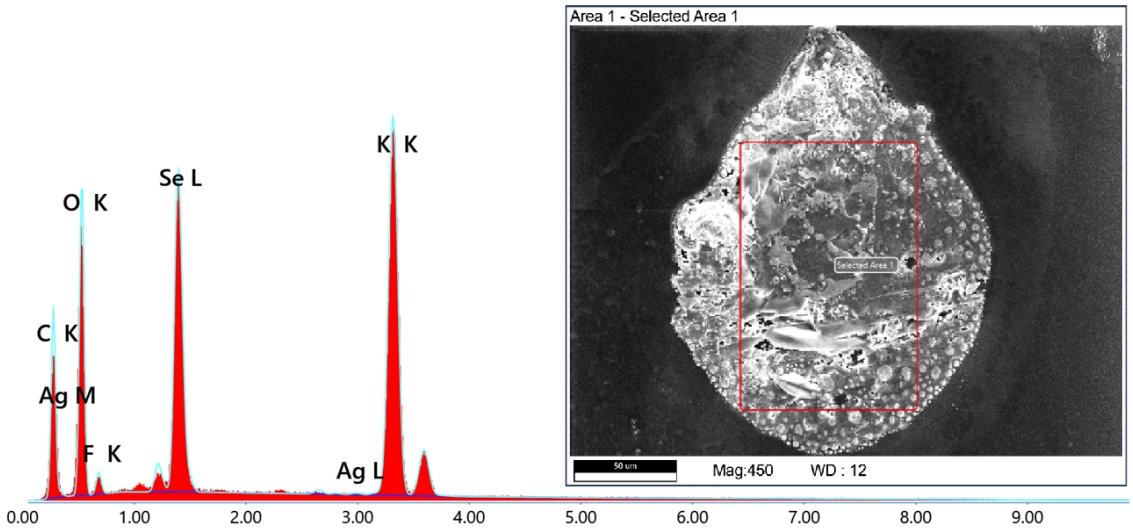

Figure C.12: EDX spectrum of a spot analysis of a crystal of $K_9Se_{2.88}(Se_2)_{1.12}OH$. A REM-image of the measured crystal is shown at the top right.

Table C.12: EDX measurements of $K_9Se_{2.88}(Se_2)_{1.12}OH$ in atomic percent with standardised and expected values.

Element /Emission Line	Atomic %	standardised	expected values
C K	24.3		
O K	49.1		
F K	2.6		
K K	18.8	9.00	9
Se L	5.1	2.44	4
Ag L	0		

C.1.13 As_3NS_3

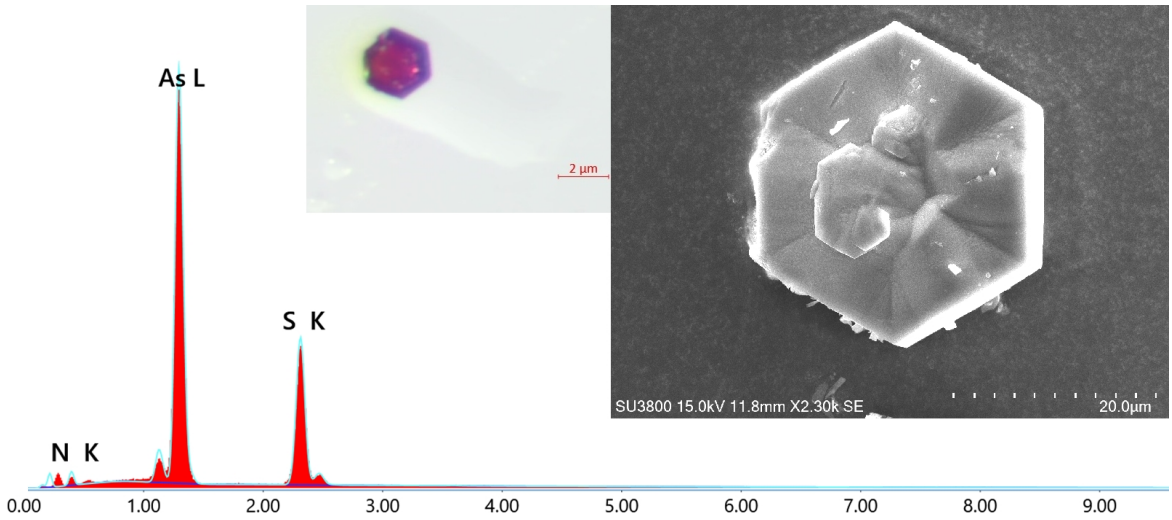

Figure C.13: EDX spectrum of a spot analysis of a crystal of As_3NS_3. A REM-image of the measured crystal is shown at the top right next to a picture of the red hexagonal crystal of As_3NS_3. From the analysis, the ratio of N:S:As is 2:3:3, but the ratio was expected be 1:3:3. Since nitrogen is a light element, the values do not provide an exact quantitative composition.

Table C.13: EDX measurements of As_3NS_3 in atomic percent with standardised and expected values.

Element /Emission Line	Atomic %	standardised	expected values
N K	23.5	1.74	1
S K	35.9	2.65	3
As L	40.6	3.00	3

C.1.14 As_3NSe_3

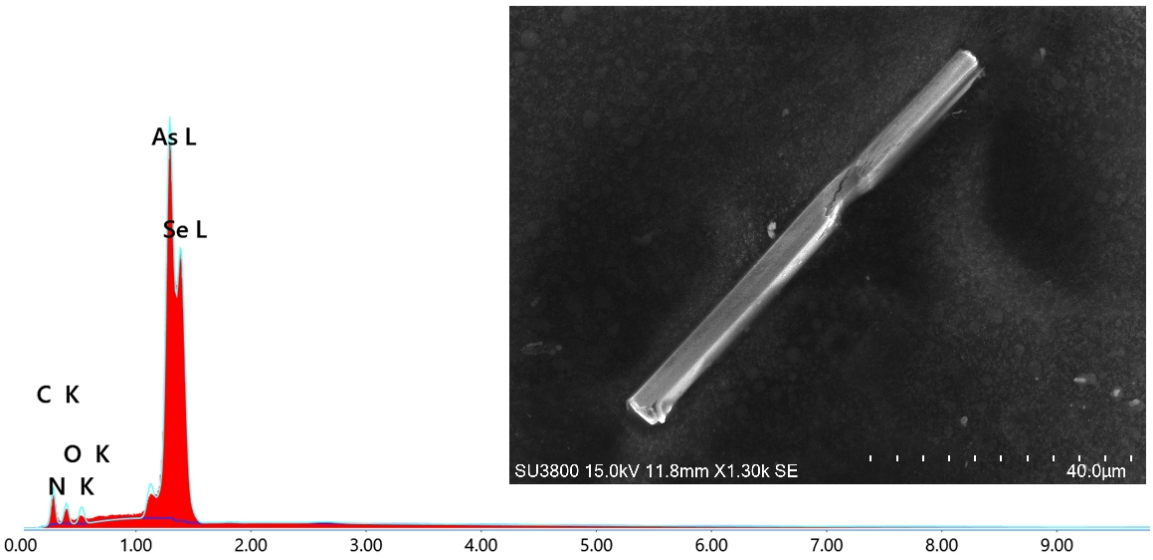

Figure C.14: EDX spectrum of a spot analysis of a crystal of As_3NSe_3. A REM-image of the measured crystal is shown at the top right. From the analysis, the ratio of N:S:As is 2:3:2, but the ratio was expected be 1:3:3. Since nitrogen is a light element, the values do not provide an exact quantitative composition.

Table C.14: EDX measurements of As_3NSe_3 in atomic percent with standardised and expected values.

Element /Emission Line	Atomic %	standardised	expected values
C K	44.6		
O K	3.7		
N K	13.7	1.92	1
As L	21.4	3.00	3
Se L	16.6	2.33	3

C.1.15 $Rb_5(AsSe_3)Se\cdot 2\,NH_3$

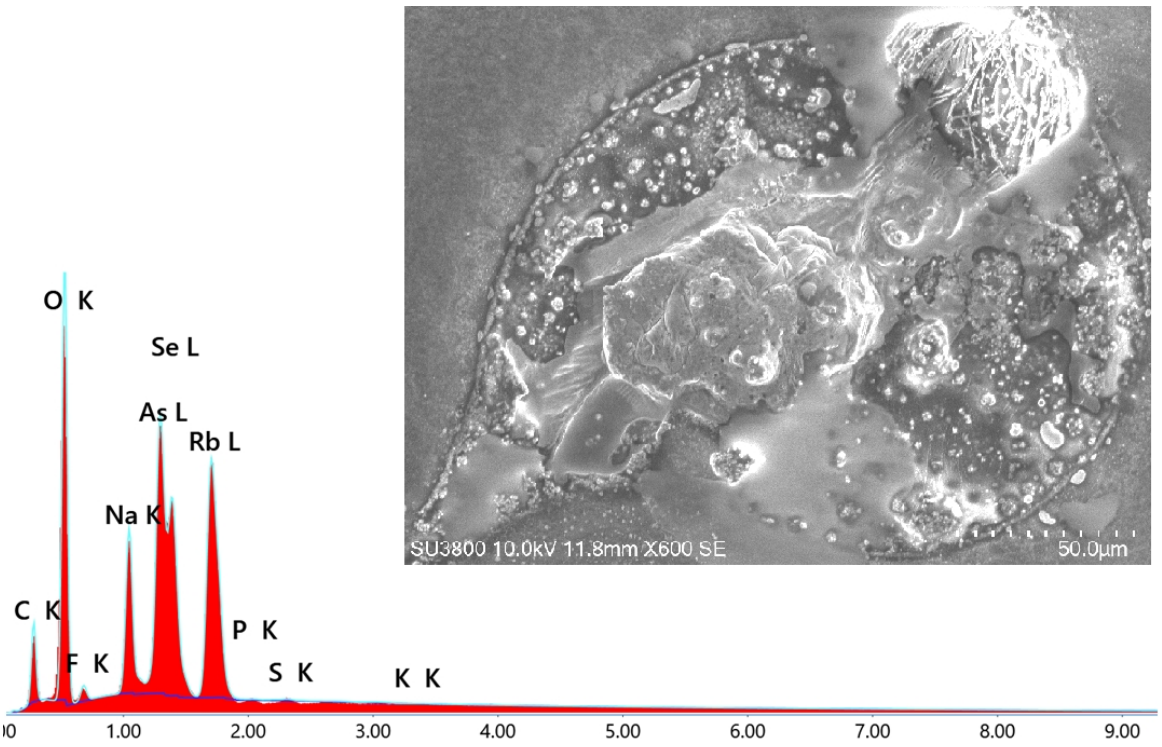

Figure C.15: EDX spectrum of a spot analysis of a crystal of $Rb_5(AsSe_3)Se\cdot 2\,NH_3$. A REM-image of the measured, decomposed crystal is shown at the top right. According to the EDX analysis, the selenium was contaminated with traces of sulphur.

Table C.15: EDX measurements of $Rb_5(AsSe_3)Se\cdot 2\,NH_3$ in atomic percent with standardised and expected values.

Element /Emission Line	Atomic %	standardised	expected values
C K	64.30		
O K	20.30		
F K	4.30		
Na K	2.00		
S K	0.30		
Rb L	2.70	1.80	5
As L	1.50	1.00	1
Se L	4.70	3.13	4

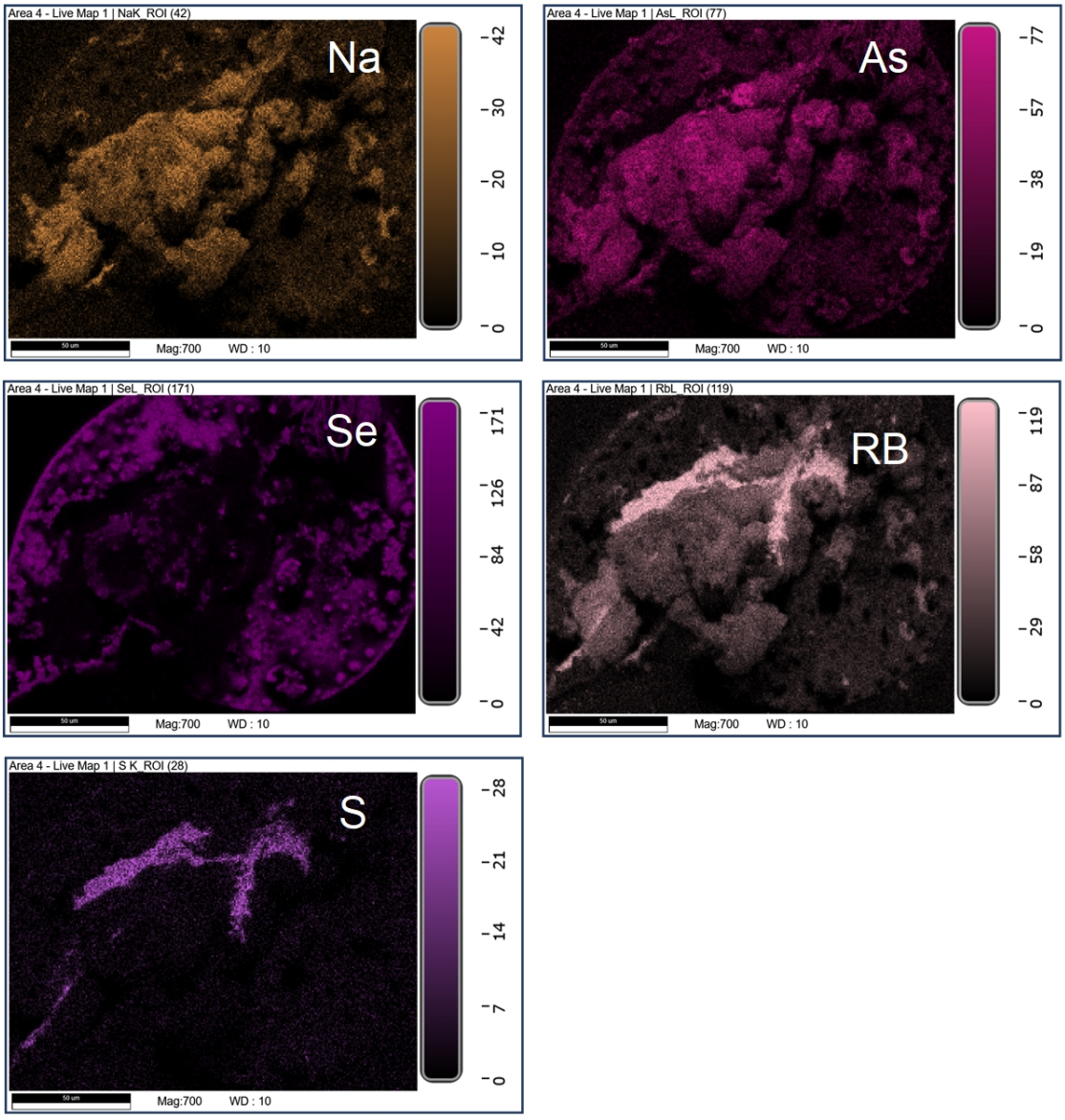

Figure C.16: The REM-live maps of the decomposed crystal $Rb_5(AsSe_3)Se \cdot 2\,NH_3$ show the distribution of the elements.

C.1.16 $[Mn(NH_3)_6][As_4S_6]\cdot NH_3$

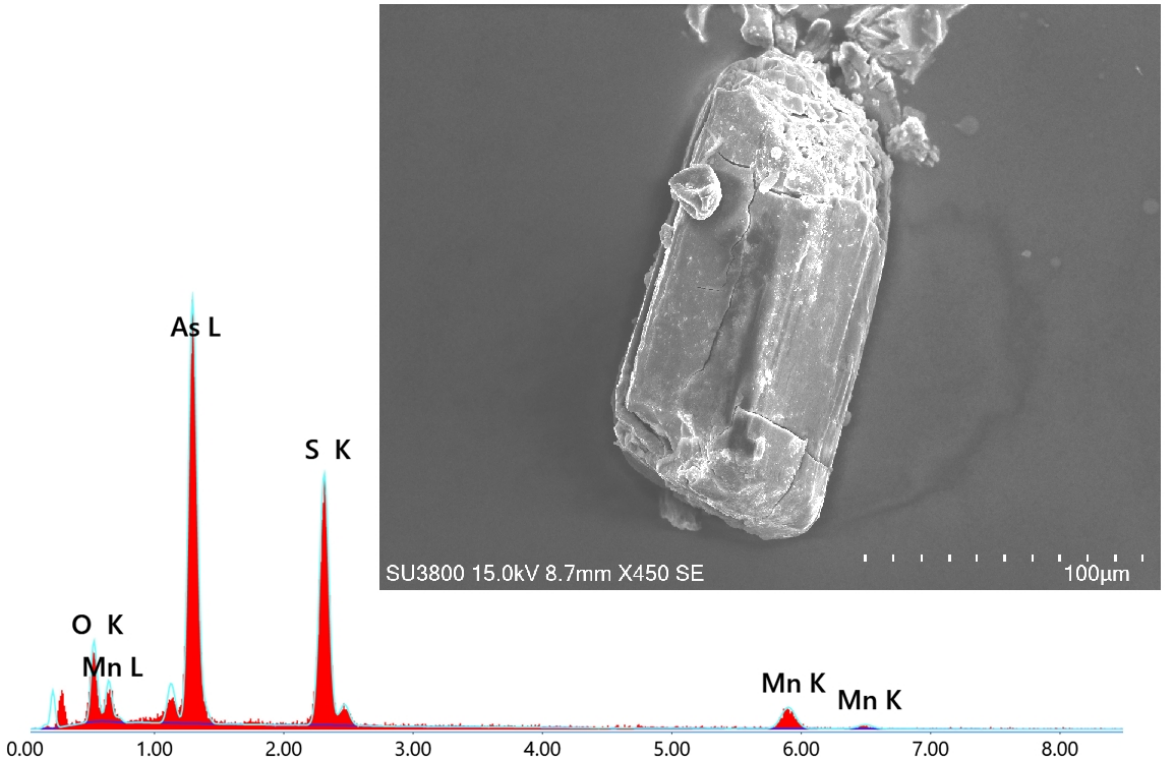

Figure C.17: EDX spectrum of a spot analysis of a crystal of $[Mn(NH_3)_6][As_4S_6]\cdot NH_3$. A REM-image of the measured crystal is shown at the top right.

Table C.16: EDX measurements of $[Mn(NH_3)_6][As_4S_6]\cdot NH_3$ in atomic percent with standardised and expected values.

Element /Emission Line	Atomic %	standardised	expected values
O K	28.3		
Mn K	7.5	1.05	1
As L	28.5	4.00	4
S K	35.7	5.01	6

D.1 Raman spectrum of $[Mn(NH_3)_6][As_4S_6]\cdot NH_3$

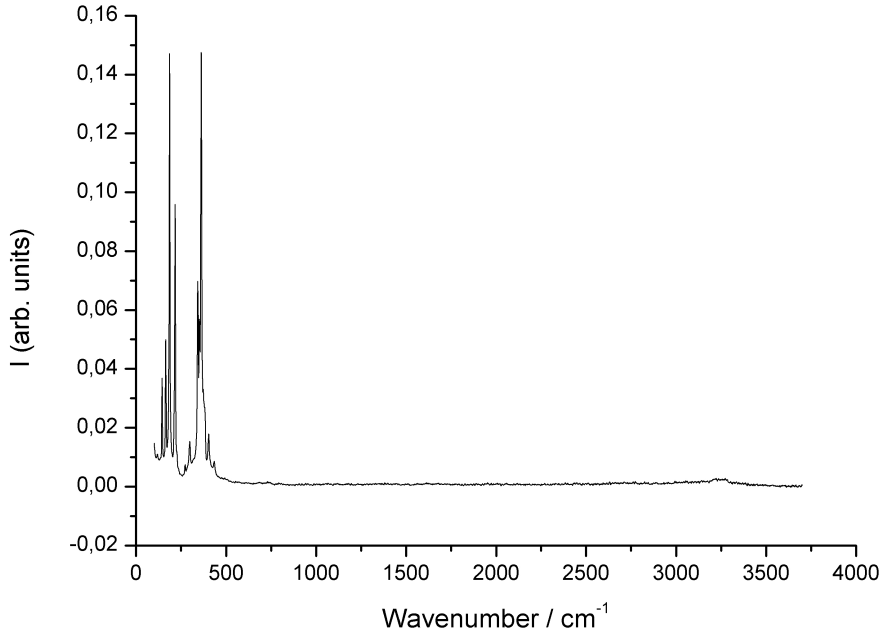

Figure D.1: The Raman spectrum of $[Mn(NH_3)_6][As_4S_6]$ in the full range of $100 - 4000$ cm^{-1}.

Bibliography

[1] W. Weyl, *Ann. Phys.* **1864**, *197*, 601–612.

[2] W. Weyl, *Ann. Phys.* **1864**, *199*, 350–367.

[3] G. Gibson, W. Argo, *J. Am. Chem. Soc.* **1918**, *40*, 1327–1361.

[4] A. C. Joannis, *C. R. Acad. Sci.* **1891**, *113*, 795.

[5] A. C. Joannis, *C. R. Acad. Sci.* **1892**, *114*, 587.

[6] C. A. Kraus, *J. Am. Chem. Soc.* **1907**, *29*, 1557–1571.

[7] C. A. Kraus, *J. Am. Chem. Soc.* **1922**, *44*, 1216–1239.

[8] F. H. Smyth, *J. Am. Chem. Soc.* **1917**, *39*, 1299–1312.

[9] E. Zintl, J. Goubean, W. Dullenkopf, *Z. Phys. Chem.* **1931**, *154*, 1–46.

[10] E. Zintl, W. Dallenkopf, *Z. Phys. Chem.* **1932**, *16*, 195–205.

[11] F. Laves in *Sci. Nat.* . Springer, **1941**, pp. 244–256.

[12] J. D. Corbett, *Angew. Chem.* **2000**, *112*, 682–704.

[13] W. Klemm, E. Busmann, *Z. Anorg. Allg. Chem.* **1963**, *319*, 297–311.

[14] E. Zintl, *Angew. Chem.* **1939**, *52*, 1–6.

[15] G. N. Lewis, *J. Am. Chem. Soc.* **1916**, *38*, 762–785.

[16] W. Kossel, *Ann. Phys.* **1916**, *354*, 229–362.

[17] H. Schäfer, B. Eisenmann, W. Müller, *Angew. Chem.* **1973**, *85*, 742–760.

[18] W. Pearson, *Acta Crystallogr.* **1964**, *17*, 1–15.

[19] G. Cordier, G. Savelsberg, H. Schäfer, *Z. Naturforsch. B* **1982**, *37*, 975–980.

[20] R. Nesper, *Prog. Solid State Chem.* **1990**, *20*, 1–45.

[21] M. Martinez-Ripoll, A. Haase, G. Brauer, *Acta Crystallogr. Sect. B* **1973**, *29*, 1715–1717.

[22] M. Martinez-Ripoll, A. Haase, G. Brauer, *Acta Crystallogr. Sect. B* **1974**, *30*, 2003–2004.

[23] B. Eisenmann, K. Deller, *Z. Naturforsch. B* **1975**, *30*, 66–72.

[24] B. Better, A. Hutz, G. Nagorsen, *Z. Metallkd.* **1976**, *67*, 118–119.

[25] Y. Wang, L. Calvert, E. Gabe, J. Taylor, *Acta Crystallogr. Sect. B* **1977**, *33*, 3122–3125.

[26] D. Balz, K. Plieth, *Z. Elektrochem.* **1955**, *59*, 545–551.

[27] W. Stassen, M. Sato, L. Calvert, *Acta Crystallogr. Sect. B* **1970**, *26*, 1534–1540.

[28] Y. Wang, L. Calvert, J. Taylor, *Acta Crystallogr. Sect. B* **1980**, *36*, 220–221.

[29] H.-G. von Schnering, M. Wittmann, D. Sommer, *Z. Anorg. Allg. Chem.* **1984**, *510*, 61–71.

[30] M. Boss, F. Pickhard, M. Zumdick, C. Röhr, *Acta Crystallogr. Sect. C* **2001**, *57*, 503–504.

[31] C. Hoch, P. Zönnchen, C. Röhr, 20^{th} *European Crystallographic Meeting*, **1998**.

[32] S. Hoffmann, T. F. Fässler, C. Hoch, C. Röhr, *Angew. Chem.* **2001**, *40*, 4398–4400.

[33] J. Nuss, M. Jansen, *Z. Anorg. Allg. Chem.* **2003**, *629*, 387–393.

[34] E. A. Leon-Escamilla, J. D. Corbett, *Chem. Mater* **2006**, *18*, 4782–4792.

[35] H. Mattausch, O. Oeckler, A. Simon, *Z. Anorg. Allg. Chem.* **1999**, *625*, 297–301.

[36] H. Mattausch, A. Simon, *Angew. Chem.* **1998**, *37*, 499–502.

[37] S. Hoffmann, T. F. Fässler, C. Hoch, C. Röhr, *Angew. Chem.* **2001**, *113*, 4527–4529.

[38] D. Kummer, L. Diehl, *Angew. Chem.* **1970**, *82*, 881–882.

[39] S. C. Critchlow, J. D. Corbett, *J. Am. Chem. Soc.* **1983**, *105*, 5715–5716.

[40] J. D. Corbett, *Chem. Rev.* **1985**, *85*, 383–397.

[41] E. A. Leon-Escamilla, J. D. Corbett, *J. Alloys Compd.* **1994**, *206*, L15–L17.

[42] B. Zhou, M. S. Denning, D. L. Kays, J. M. Goicoechea, *J. Am. Chem. Soc.* **2009**, *131*, 2802–2803.

[43] N. Lichtenberger, Y. J. Franzke, W. Massa, F. Weigend, S. Dehnen, *Eur. J. Chem.* **2018**, *24*, 12022–12030.

[44] T. Kottke, D. Stalke, *J. Appl. Crystallogr.* **1993**, *26*, 615–619.

[45] N. Korber, A. Fleischmann, *J. Am. Chem. Soc.* **2001**, 383–385.

[46] R. Nesper, *Z. Anorg. Allg. Chem.* **2014**, *640*, 2639–2648.

[47] E. Larsson, *Ark. Kemi* **1965**, *23*, 335.

[48] D. T. Cromer, *Acta Crystallogr.* **1959**, *12*, 36–41.

[49] N. Kinomura, K. Terao, S. Kikkawa, H. Horiuchi, M. Koizumi, H. Setoguchi, *Mater. Res. Bull.* **1983**, *18*, 53–57.

[50] W. Hönle, J. Buresch, K. Peters, J. Chang, H.-G. von Schnering, *Z. Kristallogr. NCS* **2002**, *217*, 485–486.

[51] K. Janzon, H. Schäfer, A. Weiss, *Z. Naturforsch. B* **1968**, *23*, 1544–1544.

[52] J. Evers, *J. Solid State Chem.* **1978**, *24*, 199–207.

[53] U. Scholz, W. Jeitschko, *Z. Anorg. Allg. Chem.* **1986**, *540*, 234–242.

[54] U. Scholz, W. Jeitschko, M. Reehuis, *J. Solid State Chem.* **1988**, *74*, 260–267.

[55] K. Deller, B. Eisenmann, *Z. Naturforsch. B* **1976**, *31*, 1023–1027.

[56] E. Ahmed, M. Ruck, *Coord. Chem. Rev.* **2011**, *255*, 2892–2903.

[57] O. Kysliak, M. Marcus, T. Bredow, J. Beck, *Inorg. Chem.* **2013**, *52*, 8327–8333.

[58] E. Wiberg, *Lehrbuch der anorganischen Chemie*, Walter de Gruyter GmbH & Co KG, **2019**.

[59] S. Rondinini, P. Longhi, P. Mussini, T. Mussini, **1987**.

[60] H. Jacobs, D. Schmidt, *Curr. Top. Mater. Sci.* **1982**, *8*, 387–427.

[61] H. Xiang, *J. Phys. Chem. Ref. Data* **2004**, *33*, 1005–1011.

[62] T. M. Richter, R. Niewa, *Inorganics* **2014**, *2*, 29–78.

[63] E. W. Lemmon, Thermophysical properties of fluid systems, `http://webbook.nist.gov/chemistry/fluid/`, (Accessed: 18 May 2022), **1998**.

[64] D. Ehrentraut, E. Meissner, M. Bockowski, *Technology of gallium nitride crystal growth, Vol. 133*, Springer Science & Business Media, **2010**.

[65] B. Wang, M. J. Callahan, *Cryst. Growth Des.* **2006**, *6*, 1227–1246.

[66] M. H. Moeller, W. Jeitschko, *Inorg. Chem.* **1981**, *20*, 828–833.

[67] O. Osters, T. Nilges, *Acta Crystallogr. Sect. E* **2011**, *67*, i62–i62.

[68] S. Lange, M. Bawohl, R. Weihrich, T. Nilges, *Angew. Chem.* **2008**, *120*, 5736–5739.

[69] W. Bauhofer, M. Wittmann, H.-G. von Schnering, *J. Phys. Chem. Solids* **1981**, *42*, 687–695.

[70] K. Schaefer, K. Koehler, F. Baumer, R. Poettgen, T. Nilges, *Z. Naturforsch. B* **2016**, *71*, 603–609.

[71] A. Iandelli, E. Franceschi, *J. Less-Common Met.* **1973**, *30*, 211–216.

[72] M. Wang, A. Mar, *Acta Crystallogr. Sect. C* **2000**, *56*, 138–139.

[73] S. Burtzlaff, M. Hołyńska, S. Dehnen, *Z. Anorg. Allg. Chem.* **2010**, *636*, 1691–1693.

[74] F. Emmerling, C. Röhr, *Z. Naturforsch. B* **2002**, *57*, 963–975.

[75] N. Mandel, J. Donohue, *Acta Crystallogr. Sect. B* **1971**, *27*, 2288–2289.

[76] W. Hönle, J. Buresch, K. Peters, J. Chang, H.-G. von Schnering, *Z. Kristallogr. NCS* **2002**, *217*, 487–488.

[77] W. Hönle, J. Buresch, J. Wolf, K. Peters, J.-H. Chang, H.-G. von Schnering, *Z. Kristallogr. NCS* **2002**, *217*, 489–490.

[78] A. Hinz, J. M. Goicoechea, *Angew. Chem.* **2016**, *55*, 8536–8541.

[79] F. Emmerling, C. Röhr, *Z. Anorg. Allg. Chem.* **2003**, *629*, 467–472.

[80] T. Hanauer, J. C. Aschenbrenner, N. Korber, *Inorg. Chem.* **2006**, *45*, 6723–6727.

[81] F. Emmerling, D. Petri, C. Röhr, *Z. Anorg. Allg. Chem.* **2004**, *630*, 2490–2501.

[82] F. Kraus, T. Hanauer, N. Korber, *Inorg. Chem.* **2006**, *45*, 1117–1123.

[83] W. Hönle, G. Krogull, K. Peters, H.-G. von Schnering, *Z. Kristallogr. NCS* **1999**, *214*, 17–18.

[84] W. Schmettow, H.-G. von Schnering, *Angew. Chem.* **1977**, *16*, 857–857.

[85] W. Wichelhaus, H.-G. von Schnering, *Sci. Nat.* **1972**, *59*, 78–79.

[86] N. Tian, Y. Yang, D. Liu, X. Liu, P.-H. Tan, D. Zhang, K. Chang, H. Li, M. Zhao, J. R. Li, et al., *ACS Nano* **2018**, *12*, 1712–1719.

[87] M. Meier, V. Faupel, N. Korber, *Z. Anorg. Allg. Chem.* **2014**, *640*, 2659–2662.

[88] M. Moller, W. Jeitschko, *Z. Anorg. Allg. Chem.* **1982**, *491*, 225–236.

[89] W. Wichelhaus, H.-G. von Schnering, *Sci. Nat. .* **1975**, *62*, 180–180.

[90] R. C. Haushalter, B. W. Eichhorn, A. L. Rheingold, S. J. Geib, *J. Chem. Soc. D* **1988**, 1027–1028.

[91] M. J. Moses, J. C. Fettinger, B. W. Eichhorn, *Science* **2003**.

[92] H.-G. von Schnering, W. Hönle, *Chem. Rev.* **1988**, *88*, 243–273.

[93] C. Hirschle, C. Röhr, *Z. Anorg. Allg. Chem.* **2000**, *626*, 1992–1998.

[94] L. G. Perla, A. G. Oliver, S. C. Sevov, *Inorg. Chem.* **2015**, *54*, 872–875.

[95] T. Hanauer, N. Korber, *Z. Anorg. Allg. Chem.* **2006**, *632*, 1135–1140.

[96] B. Weinert, A. R. Eulenstein, R. Ababei, S. Dehnen, *Angew. Chem.* **2014**, *53*, 4704–4708.

[97] N. K. Chaki, S. Mandal, A. C. Reber, M. Qian, H. M. Saavedra, P. S. Weiss, S. N. Khanna, A. Sen, *ACS Nano* **2010**, *4*, 5813–5818.

[98] M. Qian, A. C. Reber, A. Ugrinov, N. K. Chaki, S. Mandal, H. M. Saavedra, S. N. Khanna, A. Sen, P. S. Weiss, *ACS Nano* **2010**, *4*, 235–240.

[99] S. Mandal, A. C. Reber, M. Qian, P. S. Weiss, S. N. Khanna, A. Sen, *Acc. Chem. Res.* **2013**, *46*, 2385–2395.

[100] W. J. Peer, J. Lagowski, *J. Am. Chem. Soc.* **1978**, *100*, 6260–6261.

[101] T. Hanauer, M. Grothe, M. Reil, N. Korber, *Helv. Chim. Acta* **2005**, *88*, 950–961.

[102] M. Driess, K. Merz, H. Pritzkow, R. Janoschek, *Angew. Chem.* **1996**, *35*, 2507–2510.

[103] K. Hubler, G. Becker, *Z. Anorg. Allg. Chem.* **1998**, *624*, 483–496.

[104] M. Somer, W. Hönle, H.-G. von Schnering, *Z. Naturforsch. B* **1989**, *44*, 296–306.

[105] N. Korber, H.-G. von Schnering, *Z. Kristallogr. NCS* **1997**, *212*, 85–86.

[106] Y. Park, M. G. Kanatzidis, *Angew. Chem.* **1990**, *102*, 945–947.

[107] K. O. Klepp, C. Weithaler, M. Sing, *J. Alloys Compd.* **1998**, *269*, 92–97.

[108] K. Klepp, C. Weithaler, *J. Alloys Compd.* **1996**, *243*, 1–5.

[109] Y. Park, M. G. Kanatzidis, *J. Alloys Compd.* **1997**, *257*, 137–145.

[110] N. S. Hartig, P. K. Dorhout, S. M. Miller, *J. Solid State Chem.* **1994**, *113*, 88–93.

[111] K. O. Klepp, C. Weithaler, *Z. Naturforsch. B* **1995**, *50*, 1791–1793.

[112] O. Tiedje, E. Krasovskii, W. Schattke, P. Stoll, C. Näther, W. Bensch, *Phys. Rev. B* **2003**, *67*, 134105.

[113] G. Savelsberg, *Z. Naturforsch. B* **1978**, *33*, 370–373.

[114] K. Klepp, W. Bronger, *J. Less-Common Met.* **1987**, *128*, 65–71.

[115] K. Klepp, C. Weithaler, *Z. Kristallogr. – Cryst. Mater.* **1995**, *210*, 221–221.

[116] K. Klepp, C. Weithaler, *Z. Kristallogr. – Cryst. Mater.* **1996**, *211*, 549–549.

[117] W. Bronger, H. Kathage, *J. Alloys Compd.* **1992**, *184*, 87–94.

[118] K. Klepp, C. Weithaler, *Eur. j. solid state inorg. chem.* **1998**, *35*, 101–110.

[119] U. Müller, M.-L. Ha-Eierdanz, G. Kräuter, K. Dehnicke, *Z. Naturforsch. B* **1990**, *45*, 1128–1132.

[120] J. Cusick, M. L. Scudder, D. C. Craig, I. G. Dance, *Polyhedron* **1989**, *8*, 1139–1141.

[121] M. G. Kanatzidis, S. P. Huang, *Inorg. Chem.* **1989**, *28*, 4667–4669.

[122] S. P. Huang, M. G. Kanatzidis, *Inorg. Chem.* **1991**, *30*, 3572–3575.

[123] *STOE Win XPOW v1.05*, STOE & Cie GmbH, Darmstadt, **1999**.

[124] K. Brandenburg, *Match v. 2.4.7*, Crystal Impact GbR, Bonn, **2016**.

[125] B. Nonius, *Nonius BV Delft The Netherlands* **1999**.

[126] Z. Otwinowski, W. Minor, *Methods Enzymol.* **1997**, *276*, 307–326.

[127] G. M. Sheldrick, *Acta Crystallogr. Sect. A* **2008**, *64*, 112–122.

[128] S. Bruker, B. A. SMART, *Acta Crystallogr. Sect. A* **2008**, *64*, 112.

[129] R. Blessing, *Acta Crystallogr. Sect. A* **1995**, *51*, 33–38.

[130] L. J. Farrugia, *J. Appl. Crystallogr.* **2012**, *45*, 849–854.

[131] K. Brandenburg, *Diamond 4.6.4*, Crystal Impact GbR, Bonn, **2020**.

[132] A. Rabenau, *Angew. Chem.* **1985**, *24*, 1026–1040.

[133] Y. Cao, Bachelor Thesis, Universität Bonn, **2017**.

[134] C. Hadenfeldt, H.-U. Terschüren, *Z. Anorg. Allg. Chem.* **1991**, *597*, 69–78.

[135] M. Pinsky, D. Avnir, *Inorg. Chem.* **1998**, *37*, 5575–5582.

[136] M. Llunell, *SHAPE v2.1*, Electronic Structure group, Barcelona, **2013**.

[137] J. Brous, *Acta. Cryst* **1953**, *6*, 67–70.

[138] J. Lin, W. Hönle, H.-G. von Schnering, *J. Alloys Compd.* **1992**, *178*, 455–465.

[139] F. Gascoin, S. C. Sevov, *J. Solid State Chem.* **2003**, *175*, 306–309.

[140] F. Emmerling, D. Petri, C. Roehr, *ChemInform* **2005**, *36*.

[141] Y. Wang, L. Calvert, M. Smart, J. Taylor, E. Gabe, *Acta Crystallogr. Sect. B* **1979**, *35*, 2186–2188.

[142] K. Deller, B. Eisenmann, *Z. Naturforsch. B* **1977**, *32*, 1368–1370.

[143] H.-G. von Schnering, M. Wittmann, D. Sommer, *Z. Anorg. Allg. Chem.* **1984**, *510*, 61–71.

[144] R. Nesper, H.-G. von Schnering, *Tschermaks Min. Petr. Mitt.* **1983**, *32*, 195–208.

[145] N. Korber, J. Daniels, *Z. Anorg. Allg. Chem.* **1999**, *625*, 189–191.

[146] S. S. Rudel, T. Graubner, A. J. Karttunen, F. Kraus, *Z. Anorg. Allg. Chem.* **2020**, *646*, 1396–1402.

[147] P. Woidy, A. J. Karttunen, T. G. Müller, F. Kraus, *Z. Naturforsch. B* **2014**, *69*, 1141–1148.

[148] S. Westman, P.-E. Werner, T. Schuler, W. Raldow, *Acta Chem. Scand. A* **1981**, *35*.

[149] S. Lysgaard, A. L. Ammitzbøll, R. E. Johnsen, P. Norby, U. J. Quaade, T. Vegge, *Int. J. Hydrog. Energy* **2012**, *37*, 18927–18936.

[150] C. Haigh, *Polyhedron* **1995**, *14*, 2871–2878.

[151] D. Blight, D. Kepert, *Inorg. Chem.* **1972**, *11*, 1556–1561.

[152] W. Hönle, H.-G. von Schnering, *Z. Anorg. Allg. Chem.* **1978**, *440*, 171–182.

[153] L. Rothe, Bachelor Thesis, Universität Bonn, **2018**.

[154] C. Mues, H.-U. Schuster, *Z. Naturforsch. B* **1980**, *35*, 1055–1058.

[155] B. Eisenmann, J. Klein, M. Somer, *J. Alloys Compd.* **1992**, *178*, 431–439.

[156] V. Petříček, M. Dušek, L. Palatinus, *Z. Kristallogr. – Cryst. Mater.* **2014**, *229*, 345–352.

[157] J. Graf, Dissertation, Universität Kaiserslautern, **2003**.

[158] S. Joseph, C. Suchentrunk, N. Korber, *Z. Naturforsch. B* **2010**, *65*, 1059–1065.

[159] J. D. Dunitz, E. F. Maverick, K. N. Trueblood, *Angew. Chem.* **1988**, *100*, 910–926.

[160] J. Beck, *Z. Anorg. Allg. Chem.* **1990**, *585*, 157–167.

[161] H. Föppl, E. Busmann, F.-K. Frorath, *Z. Anorg. Allg. Chem.* **1962**, *314*, 12–20.

[162] P. Böttcher, J. Getzschmann, R. Keller, *Z. Anorg. Allg. Chem.* **1993**, 476–488.

[163] SHELXTL Software Reference Manual, version 269-0159xx, BRUKER AXS Inc., November 1997.

[164] W. Bronger, H. Kathage, C. Sauer, *Journal of alloys and compounds* **1992**, *187*, 351–362.

[165] C. Graf, A. Assoud, O. Mayasree, H. Kleinke, *Molecules* **2009**, *14*, 3115–3131.

[166] K. Stöwe, *J. Solid State Chem.* **2000**, *149*, 123–132.

[167] G. Thiele, L. Vondung, C. Donsbach, S. Pulz, S. Dehnen, *Z. Anorg. Allg. Chem.* **2014**, *640*, 2684–2700.

[168] P. Lemp, Bachelor Thesis, Universität Bonn, **2020**.

[169] J. R. Clark, G. Brown, *Am. Mineral.* **1980**, *65*, 477–482.

[170] H. Takahashi, A. Sugimoto, Y. Nambu, T. Yamauchi, Y. Hirata, T. Kawakami, M. Avdeev, K. Matsubayashi, F. Du, C. Kawashima, et al., *Nat. Mater.* **2015**, *14*, 1008–1012.

[171] Y. Zhang, L. Lin, J.-J. Zhang, E. Dagotto, S. Dong, *Phys. Rev. B* **2017**, *95*, 115154.

[172] H. Hong, H. Steinfink, *J. Solid State Chem.* **1972**, *5*, 93–104.

[173] J. Caron, J. Neilson, D. Miller, K. Arpino, A. Llobet, T. McQueen, *Phys. Rev. B* **2012**, *85*, 180405.

[174] R. H. Mitchell, K. C. Ross, E. G. Potter, *J. Solid State Chem.* **2004**, *177*, 1867–1872.

[175] K. Klepp, W. Sparlinek, H. Boller, *J. Alloys Compd.* **1996**, *238*, 1–5.

[176] T. Balić-Žunić, L. Karanović, D. Poleti, *Acta Chim. Slov.* **2008**, *55*, 801–809.

[177] B. Riedel, C. Janiak, *Anorganische Chemie*, Walter de Gruyter Verlag, **2007**.

[178] P. W. Atkins, J. de Paula, *Physikalische Chemie*, WILEY-VCH, **2007**.

[179] B. Krebs, G. Henkel, *Angew. Chem.* **1991**, *103*, 785–804.

[180] A. Ludi, *Chem. Unserer Zeit* **1988**, *22*, 123–127.

[181] W. Reiff, I. Grey, A. Fan, Z. Eliezer, H. Steinfink, *J. Solid State Chem.* **1975**, *13*, 32–40.

[182] J. Hoggins, H. Steinfink, *Inorg. Chem.* **1976**, *15*, 1682–1685.

[183] J. B. Goodenough, *Mater. Res. Bull.* **1978**, *13*, 1305–1314.

[184] M. Atanasov, R. Potze, G. Sawatzky, *J. Solid State Chem.* **1995**, *119*, 380–393.

[185] R. Roß, Master Thesis, Universität Bonn, **2021**.

[186] R. Dovesi, V. Saunders, C. Roetti, R. Orlando, C. Zicovich-Wilson, F. Pascale, B. Civalleri, K. Doll, N. Harrison, I. Bush, et al., **2017**.

[187] M. F. Peintinger, D. V. Oliveira, T. Bredow, *J. Comput. Chem.* **2013**, *34*, 451–459.

[188] Y. Zhao, D. G. Truhlar, *Theor. Chem. Acc.* **2008**, *120*, 215–241.

[189] J. Moellmann, S. Grimme, *J. Phys. Chem. C* **2014**, *118*, 7615–7621.

[190] S. Fernández, J. L. Mesa, J. L. Pizarro, L. Lezama, M. I. Arriortua, R. Olazcuaga, T. Rojo, *Chem. Mater* **2000**, *12*, 2092–2098.

[191] U.-C. Chung, J. L. Mesa, J. L. Pizarro, V. Jubera, L. Lezama, M. I. Arriortua, T. Rojo, *J. Solid State Chem.* **2005**, *178*, 2913–2921.

[192] J. Li, Z. Chen, R.-J. Wang, D. M. Proserpio, *Coord. Chem. Rev.* **1999**, *190*, 707–735.

[193] T. van Almsick, A. Loose, W. S. Sheldrick, *Z. Anorg. Allg. Chem.* **2005**, *631*, 21–23.

[194] P. Böttcher, *Z. Kristallogr. Cryst. Mater.* **1979**, *150*, 65–74.

[195] V. Müller, G. Frenzen, K. Dehnicke, D. Fenske, *Z. Naturforsch. B* **1992**, *47*, 205–210.

[196] U. Kretschmann, P. Böttcher, *Z. Naturforsch. B* **1985**, *40*, 895–899.

[197] F. Allen, O. Kennard, D. Watson, L. Brammer, A. Orpen, R. Taylor in *International Tables for Crystallography, Volume C*, (Ed.: A. Wilson), Kluwer Academic Publishers, Netherlands, **1992**, pp. 685–706.

[198] A. Lobato, H. Osman, M. Salvadó, M. Taravillo, V. Baonza, J. Recio, *Phys. Chem. Chem. Phys.* **2019**, *21*, 12585–12596.

[199] N. Morimoto, *Mineral. Mag.* **1954**, *1*, 160–169.

[200] J. Spinks, *Z. Phys. Chem.* **1934**, *88*, 511–514.

[201] M. Ceppatelli, D. Scelta, M. Serrano-Ruiz, K. Dziubek, M. Morana, V. Svitlyk, G. Garbarino, T. Poręba, M. Mezouar, M. Peruzzini, *Angew. Chem.* **2022**, *134*, e202114191.

[202] A. Jockisch, H. Schmidbaur, *Z. Naturforsch. B* **1999**, *54*, 1529–1531.

[203] W. Bronger, A. Donike, D. Schmitz, *Z. Anorg. Allg. Chem.* **1998**, *624*, 553–554.

[204] R. Eßmann, G. Kreiner, A. Niemann, D. Rechenbach, A. Schmieding, T. Sichla, U. Zachwieja, H. Jacobs, *Z. Anorg. Allg. Chem.* **1996**, *622*, 1161–1166.

[205] H. Jacobs, J. Bock, C. Stüve, *J. Less-Common Met.* **1987**, *134*, 207–214.

[206] R. Blachnik, A. Fehlker, *Z. Kristallogr. NCS* **2001**, *216*, 223–224.

[207] E. Porter, G. Sheldrick, *J. Chem. Soc. A* **1971**, 3130–3132.

[208] H. Rijnberk, C. Näther, W. Bensch, *Z. Kristallogr. NCS* **1998**, *213*, 616–618.

[209] D.-D. Yang, Y. Song, B. Zhang, N.-N. Shen, G.-L. Xu, W.-W. Xiong, X.-Y. Huang, *Cryst. Growth Des.* **2018**, *18*, 3255–3262.

[210] D. M. Smith, C.-W. Park, J. A. Ibers, *Inorg. Chem.* **1996**, *35*, 6682–6687.

[211] K. Sommer, M. Becke-Goehring, *Z. Anorg. Allg. Chem.* **1965**, *339*, 182–190.

[212] S. Grimme, J. Antony, S. Ehrlich, H. Krieg, *J. Chem. Phys.* **2010**, *132*, 154104.

[213] S. Grimme, S. Ehrlich, L. Goerigk, *J. Comput. Chem.* **2011**, *32*, 1456–1465.

[214] F. Weigend, R. Ahlrichs, *Phys. Chem. Chem. Phys.* **2005**, *7*, 3297–3305.

[215] F. Weigend, *Phys. Chem. Chem. Phys.* **2006**, *8*, 1057–1065.

[216] T. A. Guiton, C. G. Pantano, *Chem. Mater.* **1989**, *1*, 558–563.

[217] M.-L. Fu, G.-C. Guo, X. Liu, B. Liu, L.-Z. Cai, J.-S. Huang, *Inorg. Chem. Comm.* **2005**, *8*, 18–21.

[218] D. Jia, J. Zhao, Y. Pan, W. Tang, B. Wu, Y. Zhang, *Inorg. Chem.* **2011**, *50*, 7195–7201.

[219] D. M. Smith, M. A. Pell, J. A. Ibers, *Inorg. Chem.* **1998**, *37*, 2340–2343.

[220] W. Burgers, *Z. Phys* **1933**, *80*, 352–360.

Danksagung

Ich bedanke mich herzlich bei meinem Doktorvater Herrn Prof. Dr. Beck für die Betreuung meiner Arbeit, sowie die Freiheiten während meiner Forschung und dass er mich auf das Gebiet der Synthesen in flüssigem Ammoniak gelenkt hat.

Herrn Prof. Dr. Glaum danke ich für die freundliche Übernahme des Korreferats. Mein Dank geht auch an die gesamte Prüfungskommission.

Mein besonderer Dank geht an Dr. Jörg Daniels und Dr. Christian Landvogt für die durchgeführten Einkristallmessungen. Dr. Daniels möchte ich besonders danken für die Ausdauer in den teils tagelangen Bemühungen, geeignete Kristalle unter Tieftemperaturbedingungen zu finden. Ich möchte ihm und Dr. Gregor Schnakenburg für die Unterstützung bei den teils sehr kniffligen Strukturlösungen danken. Zusätzlich möchte ich mich bei Dr. Schnakenburg für die Berechnung des Ramanspektrums bedanken.

Dr. Jürgen Tirrée danke ich vielmals für die Durchführung der Ramanmessungen.

Weiterhin möchte ich mich bei Dr. Ralf Weisbarth für EDX-Messungen bedanken und auch dafür, dass ich durch seine Anleitung eigenständig die Proben analysieren konnte.

Mein Dank geht auch an Norbert Wagner, Klaus Armbruster, Volker Bendisch und Simone Weisbarth für die Unterstützung bei der Instandhaltung der Glove Box, den Experimenten am HF-Ofen, der Bereitstellung von Chemikalien, Mikroskop-Bildern, und den freundlichen Unterhaltungen. Meinen BachelorantInnen Yuanyuan Cao, Leon Rothe und Pauline Lemp möchte ich für die motivierte und gute Mitarbeit danken.

Ebenso möchte ich mich für das gute Arbeitsklima, die vielen Gespräche und die Ratschläge bei meinen KollegInnen im Arbeitskreis bedanken. Besonders möchte ich dabei die unterhaltsame Zeit an der Ammoniakanlage mit Dominik Offermanns erwähnen. Durch seine positive Einstellung war so mancher Frust über geplatzte Ampullen schnell wieder vergessen.

Abseits der Chemie möchte ich meinen Freunden danken, die mich über Jahre begleitet haben. Vielen Dank an Cordt und Camille für das Korrekturlesen meiner Dissertation.

Zum Ende möchte ich meiner Familie danken. Ganz besonders meiner Frau Theresa, die mich über das ganze Studium unterstützt, begleitet, ertragen und wenn nötig auch angetrieben hat. Ich wünsche mir noch viele weitere glückliche Jahre mit dir.

Eidesstattliche Erklärung

Hiermit erkläre ich, Frederik Hermann, dass die von mir eingereichte Dissertation mit dem Titel "Pnictogenide and Chalcogenide Zintl Phases via Solid State and Solvothermal Syntheses" und die darin vorgestellten Arbeiten mein eigen sind. Hiermit erkläre ich an Eides statt:

- Die von mir eingereichte Dissertation habe ich selbstständig und ohne unzulässige fremde Hilfe verfasst. Hierbei habe ich weder Textstellen von Dritten oder aus eigenen Prüfungsarbeiten noch Grafiken oder sonstige Materialien ohne Kennzeichnung übernommen.
- Es sind ausschließlich die von mir angegebenen Quellen und Hilfsmittel verwendet worden.
- Sämtliche wörtliche und nicht wörtliche Zitate aus anderen Werken sind gemäß den wissenschaftlichen Zitierregeln kenntlich gemacht.
- Die von mir vorgelegte Arbeit ist bisher noch nicht oder an der nachstehend aufgeführten Stelle vollständig/auszugsweise veröffentlicht. (s. Anlage)
- Die von mir vorgelegte Arbeit ist bisher noch in keiner Form als Bestandteil einer Prüfungs-/Qualifikationsleistung vorgelegt worden.
- Ich bin nicht zweimal in einem Promotionsverfahren an einer deutschen Hochschule aufgrund einer Ablehnung der Dissertation oder nicht bestandener Prüfungsleistungen gescheitert.
- Die von mir eingereichte Dissertation habe ich unter Beachtung der Grundsätze zur Sicherung guter wissenschaftlicher Praxis erstellt.
- Über die Bedeutung und die strafrechtlichen Folgen einer falschen eidesstattlichen Erklärung gemäß § 156 StGB bin ich mir bewusst.
- Meine Angaben entsprechen der Wahrheit und ich habe diese nach bestem Wissen und Gewissen gemacht.

Bonn, _____ _____

(Datum) (Frederik Hermann)